Low-Noise Avalanche Photodiodes

A Dissertation

Presented to

the Faculty of the School of Engineering and Applied Science

University of Virginia

In Partial Fulfillment of the

Requirements for the Degree of

Doctor of Philosophy

By

Yuan Yuan

December 2019

APPROVAL SHEET

This Dissertation
is submitted in partial fulfillment of the requirements
for the degree of
Doctor of Philosophy

Author Signature: ___________________

This dissertation has been read and approved by the examining committee:

Advisor: Joe C. Campbell ___________________________

Committee Chair: Andreas Beling ___________________________

Committee Member: Arthur W. Lichtenberger ___________________________

Committee Member: Stephen J. McDonnell ___________________________

Committee Member: Xu Yi ___________________________

Accepted for the School of Engineering and Applied Science:

Craig H. Benson, School of Engineering and Applied Science

December 2019

This dissertation is dedicated to my parents and my girlfriend

Contents

Acknowledgement

First of all, I would like to express my deepest gratitude to my advisor, Dr. Joe C Campbell, whose patient instruction and guidance are beneficial to me. Thanks to his friendliness and support, these years is one of best times in my life. Thanks to his insight and encouragement, I was able to finish my study. His enthusiasm for scientific research has set an example for me to learn for the rest of my life. I feel so lucky and honored to be a student of such knowledgeable scientist.

I would like to thank my proposal committee, Dr. Andreas Beling, Dr. Arthur W. Lichtenberger, Dr. Stephen J. McDonnell, and Dr. Xu Yi. They have given me a lot of valuable suggestions and helped me improve my research.

I feel so grateful to our group members: Dr. Min Ren, Dr. Keye Sun, Dr. Jiyuan Zheng, Dr. Yang Shen, Dr. Xingjun Xue, Dr. Nan Ye, Dr. Qinglong Li, Dr. Madison Woodson, Dr. Zhanyu Yang, Dr. Jizhao Zang, Dr. Bassem M. Tossoun, Andrew H. Jones, Qianhuan Yu, Jesse S. Morgan, Yiwei Peng, Fengxin Yu, Ta-Ching Tzu, Junyi Gao, Junming Mao, Ze Wang, Dekang Chen, Bintian Guo, and Tasneem Fatema for being wonderful colleagues and friends. Especially, Dr. Min Ren, Dr. Keye Sun, and Dr. Jiyuan Zheng, who gave me a lot of help in both scientific research and personal life like elder brothers.

I would like to thank the staff of the Microfabrication Lab at University of Virginia, Alex Lobo, Michael Stogoski, and Joseph Beatrice. Thanks for their contributions in student training and instrument maintenance of the cleanroom. I will also thank Dr. Seth R. Bank, Ann Kathryn Rockwell, and Stephen D. March at University of Texas Austin; Dr. John E. Bowers, Dr. Daehwan Jung at University of California Santa Barbara; Dr. Zhihong Huang, Dr. Binhao Wang, Dr. Xiaoge Zheng, and Dr. Di Liang at Hewlett Packard Labs; Dr. Eric Harmon at LightSpin Technology; Dr. Christopher Pinzone at Thorlab Quantum Electronics for their support and collaboration.

Last but not least, I would thank my family: my father Guobiao Yuan, my mother Hongmei Sun, and my girlfriend Wanshi Hong. Without their love and encouragement, I could not finish my PhD study. I love you forever.

Yuan Yuan

University of Virginia

December 2019

Abstract

Avalanche photodiodes (APDs) have been widely used in many applications, including long-haul telecommunication, quantum communication, light detection and ranging (LIDAR), data centers, high-performance computers, imaging, and biological and chemical agent detection. Owing to the internal multiplication gain, APDs have a higher sensitivity than conventional p-i-n photodiodes. However, the multiplication mechanism, impact ionization, is a stochastics process. This is the source of an additional noise, referred to as the excess noise. This thesis focuses on low-noise performance, and includes several types APDs.

Conventional III-V APDs have numerous benefits, they have direct bandgap, high absorption coefficients, wide spectral response regions, and flexible, complex structure design. Previously the excess noise was not as low as silicon APDs. However, four years ago, our group collaborated with Prof. Seth Bank's group in the University of Texas at Austin showed that AlInAsSb digital alloy APDs exhibit comparable low excess noise to silicon APDs. This breakthrough makes opens the potential for wider deployment of low-noise APDs. Different from multi quantum well (MQW) and superlattice materials, digital alloys have extremely thin periods, only a few monolayers (MLs) thick, which allows the wave functions to couple through several wells by the resonant tunneling effect. The digital alloy growth method may be the origin of low noise in AlInAsSb digital alloy APDs. Recently, Prof. John P. R. David's group at the University of Sheffield has demonstrated an extremely low excess noise AlAsSb digital alloy APDs [1]. They proposed that large phonon scattering and large hole effective mass caused by Sb may explain the low excess noise. In Chapters 3 to 5, I report the characteristics of $Al_{0.7}InAsSb$ binary digital alloy, $Al_{0.7}InAsSb$ ternary digital alloy, $Al_{0.8}InAsSb$ digital alloy, InAlAs digital alloy, AlGaAs digital alloy and InGaAs digital alloy APDs. Only the $Al_{0.7}InAsSb$, $Al_{0.8}InAsSb$, and InAlAs digital alloys exhibit smaller

excess noise than their random alloy counterparts. In order to further explore this low-noise performance, temperature measurements and ionization coefficient measurements have been done, and the experimental results are consistent with Dr. Jiyuan Zheng's simulations. Recently, Ann Kathryn Rockwell, one of Professor Seth Bank's graduate students, has grown an $Al_{0.7}InAsSb$ "random-digital alloy" by changing the periods from 4ML to 16ML. The average is 10ML. The $Al_{0.7}InAsSb$ random-digital alloy shows higher excess noise than the $Al_{0.7}InAsSb$ digital alloy. In Chapter 6, I describe the characteristics of digital alloy $Al_{0.7}InAsSb$ APDs in Geiger-mode operation, to achieve single photon detection. These single photon avalanche diodes (SPADs) achieve higher single photon detection efficiency and lower dark count rate than reported InGaAs-InAlAs SPADs.

Another promising research area is low-noise APDs in silicon photonics. Chapters 8 and 9 introduce the low-noise III-V APD and Si-Ge APD on silicon. We demonstrated the first III-V APD grown by heteroepitaxy on silicon. This InGaAs-InAlAs APD exhibits the same small excess noise as the APDs on InP substrate. In the future, high-bandwidth-density optical interconnects, high bandwidth, and high sensitivity APDs are desirable owing to the need for high data rates and low power consumption. I demonstrated a low-voltage, high-speed Si-Ge waveguide APD that shows superior high-temperatures performance with 100% internal quantum efficiency. Its breakdown voltage, bandwidth, and gain-bandwidth product are also very insensitive to temperature. The excellent temperature characteristics of this Si-Ge APD demonstrates its potential to be used in a high-operating-temperature optical link for future energy-efficient data centers and high-performance computers. Moreover, this Si-Ge APD can obtain higher sensitivity by adding a distributed Bragg reflector (DBR).

List of Figures

List of Tables

Chapter 1. Introduction

Recently, there has been a widespread interest and considerable research and development efforts in avalanche photodiodes (APDs). The driving force is the huge demand for high-sensitivity optical receivers [2]. Silicon APDs have been near-ideal optical detectors for wavelengths below 1.1 μm owing to their low excess noise and high material quality [3]. For longer wavelength, there has been a lot of work to develop III-V semiconductors, for example InGaAs/InP [3, 4], InGaAs/InAlAs [5–7] at telecommunication wavelengths. However, these III-V APDs have much higher excess noise than silicon APDs. Low-noise APDs with performance comparable to silicon have been sought for decades.

1.1 Avalanche photodiodes and applications

A photodiode is a semiconductor that exploits the photoelectric effect to convert optical signals to electrical signals. Relative to conventional p-i-n photodiodes, APDs can provide higher receiver sensitivity owing to their internal gain, which originates from impact ionization. In a high electric field, free carriers are accelerated to achieve higher energy, once their energy is higher than the threshold energy, E_i, impact ionization can occur. The threshold energy, E_i, can be estimated from momentum and energy conservation. Typically, the required electric field for III-V compounds is $> 10^5$ kV/cm at room temperature. The impact ionization process is a three-body collision process, as shown in Fig. 1-1 (a). The primary electron in the conduction band, e_1, has sufficient energy to impact with the lattice, and promote electron e_2 from the valance band into the conduction band, and leaves a hole, h_2', in the valance band. The resultant electrons are expressed as e_1' and e_2'. The average distance for electrons and holes to accelerate to obtain sufficient energy can be denoted as *1/α* and *1/β*, respectively. This is illustrated in Fig. 1-1 (b). The reciprocals of the average distances, α and β, are respectively defined as the impact ionization coefficients for electrons and holes [9].

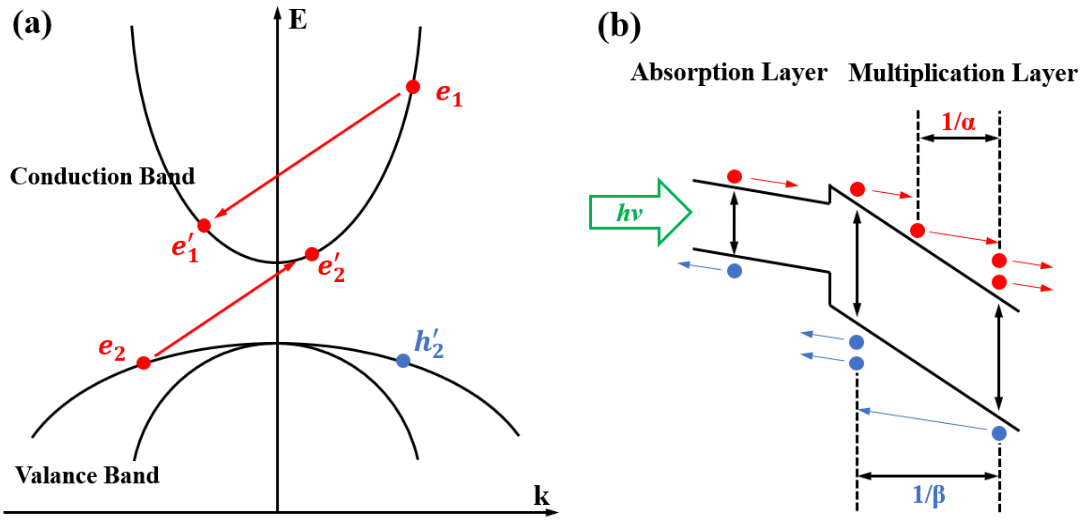

Figure 1-1. Impact ionization process in (a) E-k band structure, and (b) band diagram.

The internal gain in APDs enables detection of weak optical signals. Owing to the significant improvement of sensitivity, APDs have been widely used in commercial, research, and military applications including long-haul telecommunications [10], three-dimensional imaging cameras [11], light detection and ranging (LIDAR) [12], quantum communication [13], quantum computing [14], and data centers [15]. Figure 1-2 illustrates a generic gain versus reverse voltage curve. At very low bias voltage, the photocurrent increases with voltage because of the increase of depletion region. As the unintentional doping (UID) layer has been fully depleted, the photocurrent is nearly a constant, which is the unity gain region (M ~ 1) in Fig. 1-2; and conventional p-i-n photodiodes operate at this region. As the bias voltage increases, free carriers gain sufficient energy to impact ionize, the source of the APD gain. This region is referred to as the linear mode because the output electrical signal is proportional to the optical intensity. Once the bias voltage exceeds the breakdown voltage, V_{bd}, the APD operates in the Geiger mode. The breakdown voltage is defined as the voltage with infinite gain. In Geiger mode, the output electrical signal no longer varies with the light intensity. Even a single photon-generated carrier can initiate a self-sustaining avalanche. Essentially it functions as an optical switch. The device turns on when triggered by photons. Owing to single photon level detection, the Geiger mode APDs are frequently referred to single photon avalanche diodes (SPADs). In summary, by changing the bias voltage, APDs can provide high performance for a wide range of applications.

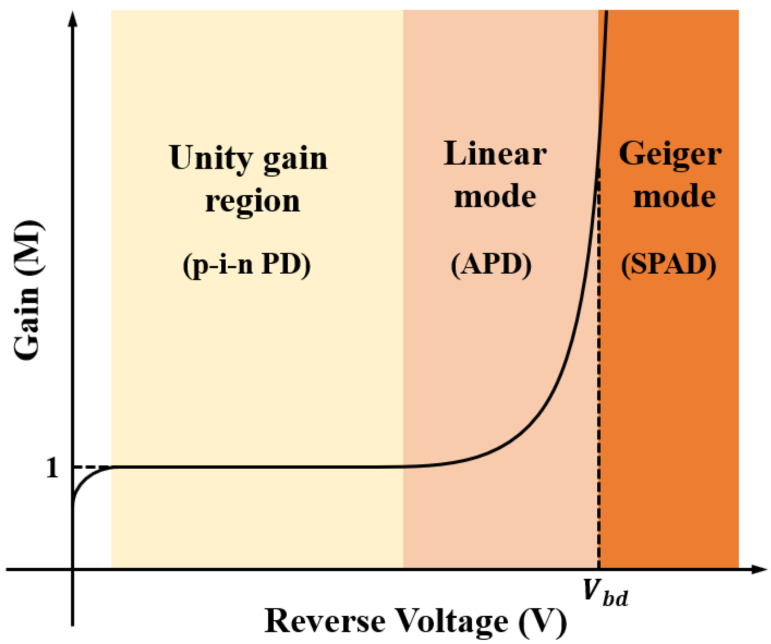

Figure 1-2. Gain versus reverse voltage curve for APDs.

1.2 Motivation for low-noise APDs

As a result of their internal gain, APDs can achieve higher sensitivity than p-i-n photodiodes. However, the stochastic nature of the multiplication mechanism, impact ionization, results in gain fluctuations, a source of noise that is typically expressed as the excess noise factor, $F(M)$, which is incorporated as a multiplicative of the shot noise:

$$\left\langle i_{shot}^{2} \right\rangle = 2q\left(I_{photo} + I_{dark}\right)M^{2}F(M)\Delta f \ , \tag{1.1}$$

where I_{photo} is photocurrent, I_{dark} is dark current, M is average gain, and Δf is bandwidth. The tradeoff between the benefit of internal gain and the detriment of gain-linked noise is illustrated by the signal to noise ratio, SNR,

$$SNR = \frac{I_{photo}^2}{2qI_{total}F(M)\Delta f + \frac{\sigma_{circuit}^2}{M^2}}, \tag{1.2}$$

where the $\sigma_{circuit}^2$ is the RMS noise current of the following electronic circuitry. The APD gain effectively suppresses the circuit noise until it reaches the point where the APD noise is comparable to that of the circuit. Thus, it is beneficial to minimize $F(M)$, which is a function of the average gain and k, the ratio of hole, β, to electron, α, ionization coefficients. For bulk multiplication regions where, non-local effects can be ignored, the excess noise factor is given by [16]:

$$F(M) = kM + (1-k)(2-1/M)\,. \tag{1.3}$$

The excess noise factor increases with increasing gain but increases slower for the lower value of k.

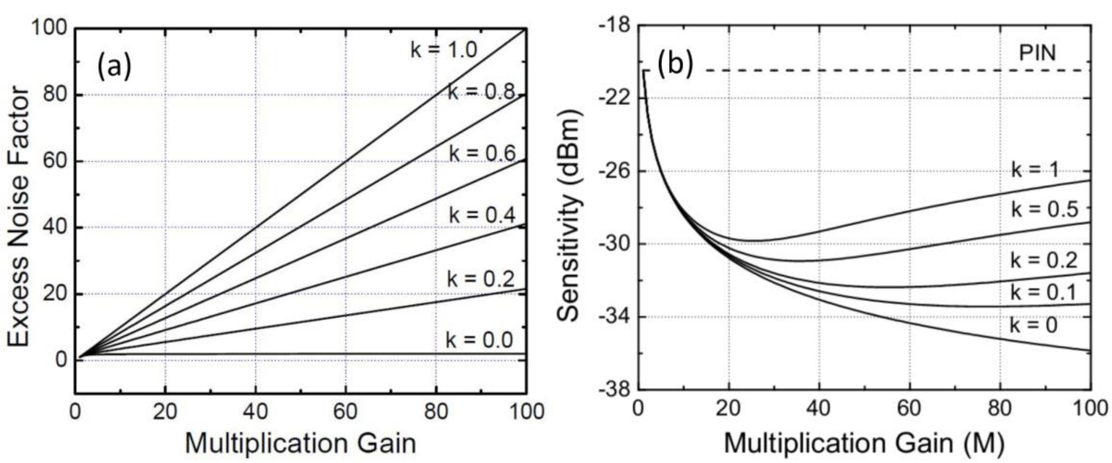

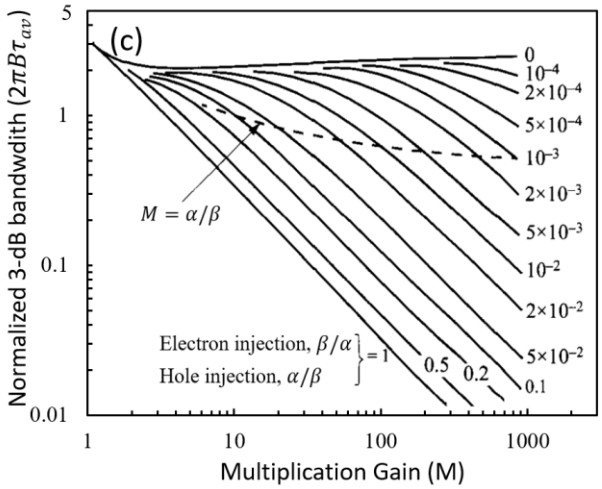

Figure 1-3. (a) Excess noise factor, (b) sensitivity, and (c) normalized 3-dB bandwidth in APDs with different *k* values [16, 17].

In the local field model, the variation of $F(M)$ with different *k* is shown in Fig. 1-3 (a). For fixed gain, low *k* results in lower noise and thus higher sensitivity. The relation between sensitivity and *k* value is shown in Fig. 1-3 (b), where with a lower *k* value, higher receiver sensitivity can be obtained [18]. Therefore, APDs with low *k* are highly desirable.

Another important figure of merit is the gain-bandwidth product (GBP), Emmons [18] has shown that lower *k* also enables higher gain-bandwidth products as shown in Fig. 1-3 (c). For 1550 nm wavelength, the InGaAs/InP separate absorption, charge, and multiplication (SACM) APDs have been widely deployed in optical receivers. However, InP has a relatively high *k* ~ 0.5, which results in high excess noise and GBP < 100 GHz. Recently, Nada et al. [8] have reported InGaAs/InAlAs SACM APDs, where the *k* of the InAlAs multiplication layer is ~ 0.2. These APDs achieved 270 GHz GBP. The champion multiplication material candidate is silicon, whose *k* is only ~ 0.02. The best Ge/Si SACM APDs have achieved GBP > 340 GHz [19]. However, owing to lattice mismatch between Ge and Si, the high dark current becomes the dominate limitation of the sensitivity. Recently, Zhou et al. [20] and Xie et al. [21] have reported that AlGaAsSb APDs, whose k value is ~ 0.1, exhibit a high GBP of 424 GHz.

1.3 Dissertation organization

This work focuses on low excess noise APDs, include $Al_xIn_{1-x}As_ySb_{1-y}$ (henceforth referred to as AlInAsSb) digital alloys lattice-matched to GaSb [21-25], $In_{0.52}Al_{0.48}As$ (henceforth referred to as InAlAs) digital alloy on InP [26, 27], InAlAs random alloy on Si [28, 29], and Ge/Si APDs. It is organized as follows: Chapter 2 introduces APDs fundamentals, experimental techniques and fabrication processes; Chapters 3, 4, and 5 respectively describe the $Al_{0.7}$InAsSb, $Al_{0.8}$InAsSb, and InAlAs digital alloy APDs. Chapter 6 demonstrates the measurements of single photon detection. Chapter 7 reports the InAlAs random alloy with triple-mesa design. A III-V compound APD on Si substrate and a Ge/Si SACM APD are investigated in Chapters 8 and 9. Chapter 10 is the summary and future work.

Chapter 2. Fundamentals, fabrication, and characterization

2.1 APD characteristics and measurement techniques

The performance of APDs is evaluated through a number of characteristics, which include dark current, multiplication gain, responsivity and quantum efficiency, bandwidth, and excess noise. However, there are always tradeoffs between these factors. Therefore, the APD design needs to be optimized for the application. This section introduces all of the above characteristics and also the corresponding measurement techniques.

2.1.1 Dark current

The dark current is the current that is measured in the absence of illumination. In our lab, the dark current is measured with a semiconductor parameter analyzer (HP4145) or source meter (Keithley 2400). Dark current is a key performance parameter. It is a noise source that originates from thermal generation of electron-hole pairs. As shown in Eq. 1.1, the SNR decreases with higher dark current. There are several components of the dark current. They can be analyzed through their dependence on temperature and bias voltage [31]. First is the diffusion current. It can be expressed as:

$$J_{diff} \propto \exp\left(-\frac{E_g}{K_B T}\right)\left[\exp\left(\frac{qV}{K_B T}\right)-1\right], \tag{2.1}$$

where E_g is the bandgap of semiconductor, K_B is the Boltzmann constant, q is the elementary charge, V is the applied bias, and T is the absolute temperature. The internal and surface generation-recombination (GR) dark current are given by Eqs. 2.2 and 2.3, respectively:

$$J_{internal\text{-}GR} \propto \sqrt{V_{built} - V} \exp\left(-\frac{E_g}{2K_BT}\right)\left[\exp\left(\frac{qV}{2K_BT}\right) - 1\right], \tag{2.2}$$

$$J_{surface\text{-}GR} \propto \sqrt{V_{built} - V} \exp\left(-\frac{E_g}{4K_BT}\right), \tag{2.3}$$

where V_{built} is the built-in voltage in the junction. The trap-assisted tunneling (TAT) dark current is another important mechanism, due to high electric field in APDs. The TAT current is relatively independent of temperature. The relationship between TAT current and electric field is given by [32]:

$$J_{TAT} \propto \frac{q^2 E}{36\pi\hbar^2} \sqrt{\frac{2m^*}{E_g}} \exp\left[-\frac{4\sqrt{2m^*} E_g^{3/2}}{3q\hbar E}\right], \tag{2.4}$$

where E is the average electric field, $\hbar$ is the reduced Planck constant ($\hbar = h/2\pi$), m^* is the effective mass, which is relative to the effective electron and hole masses, m_e^* and m_h^*:

$$m^* = 2\left(\frac{1}{m_e^*} + \frac{1}{m_h^*}\right)^{-1} . \tag{2.5}$$

At low bias voltage, the TAT current can be ignored, and the temperature dependence of the total dark current obeys the relation:

$$J_{total} \approx J_{diff} + J_{internal\text{-}GR} + J_{surface\text{-}GR} \propto \exp\left(-\frac{E_a}{K_BT}\right) , \tag{2.6}$$

where E_a is the thermal activation energy. By measuring the dark current versus temperature, E_a of APDs can extracted from fitting Eq. 2.6, and the dominate dark current mechanisms can be determined.

In addition to classifying the dark current by physical mechanisms, the dark current can also be separated into two categories, bulk and surface dark current. The method to distinguish bulk and surface dark current to measure the dark current versus device diameter, d. Bulk dark current is proportional to the device area, which scales quadratically with d, $J_{bulk} \propto d^2$. The surface dark current scales linearly with the device perimeter, hence $J_{surface} \propto d$. Typically, the electron-hole pairs from bulk dark current can achieve multiplication, while surface dark current cannot. Consequently, the total dark current at gain, M, is given by:

$$J_{total}(M) \approx J_{bulk} M + J_{surface} \quad . \tag{2.7}$$

In general, the bulk dark current arises from the defects and traps in the crystal that cannot be address in the fabrication process. However, the surface dark current, which is caused by dangling bonds and high surface electric field, can be reduced by effective surface passivation. Many surface passivation methods have been explored to eliminate dangling bonds with insulating materials, such as Benzocyclobutene (BCB), SU8, SiN_x, and SiO_2 [33]. Tailoring the mesa structure can also reduce the surface electric field, e.g., tapered-mesa, double-mesa, and recent triple-mesa. These mesa structures will be discussed in detail in Chapter 6.

2.1.2 Multiplication gain

The multiplication gain of APDs can be calculated from the photocurrent versus bias voltage. The measured method is same as the dark current measurement. The gain value at certain voltage equals to the ratio of the photocurrent at this bias voltage, $I_{photo}(V)$, to the unity gain photocurrent, $I_{photo}(V_0)$:

$$M(V) = \frac{I_{photo}(V)}{I_{photo}(V_0)} = \frac{I_{total}(V) - I_{dark}(V)}{I_{total}(V_0) - I_{dark}(V_0)} \quad , \tag{2.8}$$

where V_0 is the voltage at unity gain. As discussed in Section 1.1, the mechanism of multiplication gain is impact ionization, which depends on the ionization coefficients, α and β. For most semiconductor materials $\alpha \neq \beta$, therefore, multiplication relies on the injection of primary carriers.

Depending on the types of primary injected carriers, there are three situations: pure electron injection, pure hole injection, and mixed injection. For simple p-i-n APDs, the gain value for pure electron and pure hole injection can be calculated with α and β [9]:

$$M_e = \left\{1 - \int_0^W \alpha \exp\left[-\int_0^x (\alpha - \beta) dx'\right] dx\right\}^{-1} , \tag{2.9}$$

$$M_h = \left\{1 - \int_0^W \beta \exp\left[\int_x^W (\alpha - \beta) dx'\right] dx\right\}^{-1} , \tag{2.10}$$

where M_e is the gain for pure electron injection, M_h is the gain for pure hole injection, and W is the depletion width. On the other hand, the α and β can be extracted if M_e and M_h are known.

2.1.3 Responsivity and quantum efficiency

The responsivity is defined as the ratio of the generated photocurrent to the incident optical power at unity gain, and can be expressed as:

$$R = \frac{I_{photo}(V_0)}{P} = \frac{I_{total}(V_0) - I_{dark}(V_0)}{P} , \tag{2.11}$$

where R is the responsivity, P is the incident optical power. The responsivity is expressed in units of A/W. There is another way to express the photo-response, quantum efficiency (QE), which defines the probability that one photon converts into one electron-hole pair. There are two types QE that are regularly used in photodiodes, external and internal QE. As the name indicates, external QE considers the number of photons incident on the device, whereas, internal QE refers to those photons absorbed in the detector. The external QE can be defined as:

$$\eta_{external} = \frac{N_{e-h}}{N_{photon}} = \frac{I_{photo}(V_0)/q}{P/h\upsilon} = R\frac{h\upsilon}{q}, \tag{2.12}$$

where $\eta_{external}$ is external QE, N_{e-h} is the number of photogenerated electro-hole pairs, N_{photon}

is the number of illuminated photons, h is the Plank constant, and υ is the frequency of light. The external QE simply equals the responsivity R times the ratio of the photon energy to electron elementary charge.

The internal QE does not consider the propagation loss or coupling loss, it is only determined by the device internal properties and can be written as:

$$\eta_{\text{internal}} = (1-R)(1-\Gamma)\left[1-\exp\left(-\gamma(\lambda)L_{absorber}\right)\right] , \tag{2.13}$$

where R is the surface reflectivity; Γ represents the loss of carriers in the device, such as recombination and scattering; $\gamma(\lambda)$ is the absorption coefficient at wavelength λ; and the $L_{absorber}$ is the absorption length. Based on the definition, the relationship between external QE and internal QE is given by:

$$\eta_{external} = (1-\eta_{loss})\eta_{internal} , \tag{2.14}$$

where η_{loss} is the light loss before photons are absorbed. For the vertically-illuminated APDs, the main loss is the light reflection at the interface between air and semiconductor, which can be calculated by $(n_1 - n_2)^2/(n_1 + n_2)^2$, n_1 and n_2 are refractive indexes of air and semiconductor, respectively. Typically, the reflection ~ 30 % between air and semiconductor. By using anti-reflective coating (ARC) this 30 % reflection can be greatly reduced. One of the simplest anti-reflection coatings is a thin film with refractive index, $n_{ARC} = \sqrt{n_1 n_2}$ and thickness is one quarter of the light wavelength, $\mathrm{T} = \lambda/4$. There are several other ways to improve the QE, such as dual path, waveguide structure, photonic crystal, and resonate cavity [34].

The experimental setup to measure the external quantum efficiency is shown in Fig. 2.1. A tungsten-halogen lamp is used as the light source to provide a continuous light spectrum. The SPEX 1681 spectrometer selects the desired wavelength from the broad-band spectrum. A chopper and a lock-in amplifier decouple the photocurrent and dark current, then amplify the photocurrent.

A long pass filter is used to block the output light with second-order frequency. Depending on the working wavelength, commercial, calibrated Si or InGaAs photodiodes are measured. Since their QE is known, they function as reference diodes. Then the APD is measured at unity gain and the photocurrent values from the lock-in amplifier are recorded. Finally, the responsivity and QE are determined by comparing the APD and reference photodiode.

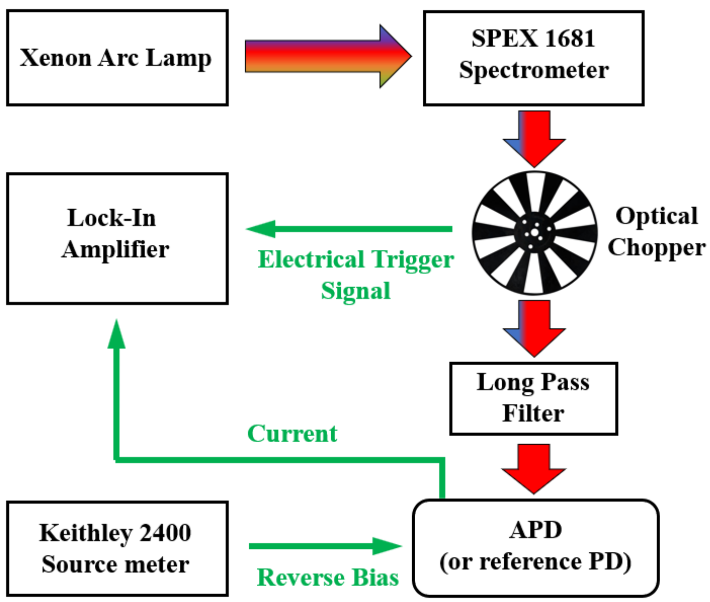

Figure 2-1. Experimental setup for responsivity and quantum efficiency measurement.

2.1.4 Bandwidth

Typically, the 3-dB bandwidth is used to evaluate the speed of APDs, which is the frequency where the RF output power drops by 3 dB compared to its low-frequency output value. There are three factors that limit the bandwidth of APDs: the RC response time, the carrier transit time, and the avalanche build-up time. The RC response time originates from the internal capacitance and resistance of APDs, the equivalent circuit is illustrated in Fig. 2-2 below, where I is the output current; C_j is the junction capacitance; R_j is the junction resistance, which depends on the device structure, it varies from a few hundred Ohms to several kilo-Ohms; R_s is the series resistance, including the metal contact resistance and the sheet resistance; and R_L is the load resistance, which for most cases is 50 Ω.

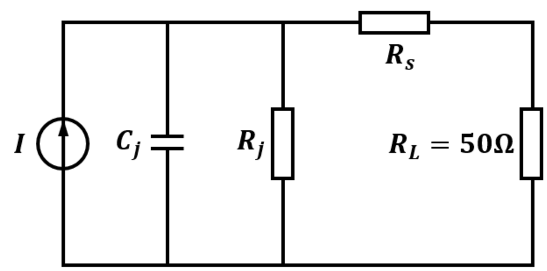

Figure 2-2. The equivalent circuit of APDs.

Based on the equivalent circuit, when $R_j \gg R_s + R_L$, the RC response-limited bandwidth, f_{RC}, is given by:

$$f_{RC} = \frac{1}{2\pi C_j (R_s + R_L)} . \tag{2.15}$$

The smaller the junction capacitance and metal contact resistance, the higher is the RC bandwidth that can be achieved. The junction capacitance $C_j = \varepsilon_0 \varepsilon_r A / W_D$, where ε_0 is the vacuum permittivity, ε_r is the relative permittivity, A is the active area, and W_D is the depletion width. As a result, a small device with low ohmic contact resistance is needed for high RC-limited bandwidth.

The carrier transit time is determined by the time required for the photon generated carriers to be collected. The transit time limited bandwidth f_{tr} can be approximately calculated using the relations [35]:

$$f_{tr} = \frac{3.5\bar{v}}{2\pi L_{tr}} , \tag{2.16}$$

$$\bar{v} = \sqrt[4]{2\left(\frac{1}{v_e^4} + \frac{1}{v_h^4}\right)^{-1}} , \tag{2.17}$$

where $\bar{v}$ is the effective average drift velocity, L_{tr} is the carrier transit length, v_e is the electron drift velocity, and v_h is the hole drift velocity. In contrast to the RC bandwidth, narrow devices exhibit higher transit-time bandwidth.

At unity gain, there is no build-up time limitation, and the 3-dB bandwidth for the RC response time and the transit time is:

$$f_{3-dB} = \sqrt{\frac{1}{\frac{1}{f_{RC}^{\ 2}} + \frac{1}{f_{tr}^{\ 2}}}}, \tag{2.18}$$

for which there is a trade-off between f_{RC} and f_{tr}. A thick depletion width can improve f_{RC}, while at the same time reducing f_{tr}. Thus, optimization of device thickness is needed for a high-speed design.

At low gain, $M < \alpha/\beta$, the bandwidth can be estimated by Eq. 2.18. When the gain increases above α/β, the build-up time dominates the bandwidth. The bandwidth decreases with higher gain, and is determined by the gain-bandwidth product (GBP). As shown in Fig. 1-3(c), the GBP depends on the semiconductor properties. The GBP is higher with for lower values of k [18], and for thinner multiplication regions.

The bandwidth measurement setups are shown in Fig. 2-3. Based on the wavelength and bandwidth, there are two setups. Figure 2-3(a) is the setup with direct modulation. A vertical-cavity surface-emitting laser (VCSEL) is directly modulated with an analog signal generator, and then coupled into the APD. The output electrical RF signal is monitored by an electrical spectrum analyzer (ESA). In this method, a high-speed photodiode with known frequency response should also be tested to calibrate the loss from the laser, bias tee, and coaxial cables. This method is suitable for the devices that work at wavelengths consistent with those of high-speed semiconductor lasers or do not have extremely high speed.

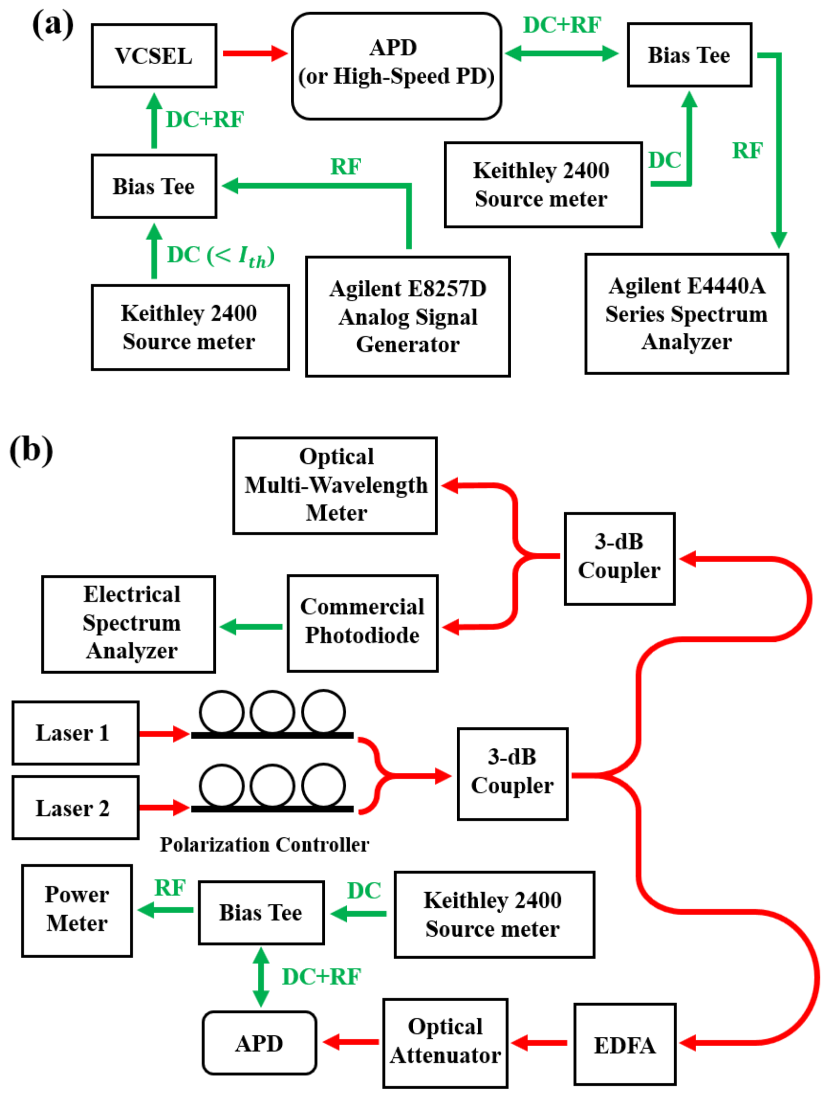

Figure 2-3. The bandwidth measurement setups based on (a) direct modulation and (b) optical heterodyne.

Another method utilizes the optical heterodyne setup shown in Fig. 2-3(b) [36]. The outputs of two continuous wave (CW) lasers with similar wavelengths are combined through a 3-dB coupler. By changing the temperature of one of the lasers, the wavelengths can be tuned, and thus change the frequency difference between the two CW lasers. This frequency difference is the modulation frequency, which is referred to as the beat frequency. To ensure 100 % modulation, the two CW lasers should exhibit same intensity and polarization, which can be easily achieved with polarization controllers and by adjusting the laser drive currents and. The heterodyne signal is split into two branches, the top branch is used to monitor the beat frequency. This is measured with an optical multi-wavelength meter for ultra-high-speed frequency (> 50 GHz) or a commercial photodiode with ESA is used for frequency < 50 GHz. The bottom branch is coupled into the APDs through an erbium-doped fiber amplifier and an optical attenuator. The output RF signal is measured with an ESA. The optical heterodyne setup is suitable for high-bandwidth measurements that can be tuned from low frequency to hundreds GHz. However, the frequency resolution is not as precise as direct modulation, which is limited by the resolution of the wavelength, ~ 0.008 nm.

2.1.5 Excess noise

As noted above, the excess noise is due to gain fluctuations. The excess noise factor, $F(M)$, for the local-field model is expressed in Eq. 1.3 [16]. The k value is determined by the ionization coefficients of the electron, α, and the hole, β, which are material parameters affected by the semiconductor band structure. A small k value is always desired for low $F(M)$, as shown in Fig. 1-3(a). The physical explanation of the positive relationship between k value and excess noise can be illustrated in Fig. 2-4. The top one represents the electron injection ionization event for the APD with $\beta \sim 0$, i.e., $k \sim 0$, which means holes do not impact ionize. In this situation, ionization of electrons determines the gain. This is fundamentally a single pass process. The bottom figure, however, illustrates the opposite case; $\beta \sim \alpha$ and $k \sim 1$. Electrons and holes have equal probability to ionize. The injected initial electron ionizes creating the first electron-hole pair, the hole in this pair can ionize the second pair, and so on. This is a chain-like process. If one carrier does not impact ionize, it will prevent subsequent events, which leads to a larger fluctuations in the gain. Therefore, the feedback loop will generate higher stochasticity and longer build-up time compare to the single pass path at $k \sim 0$.

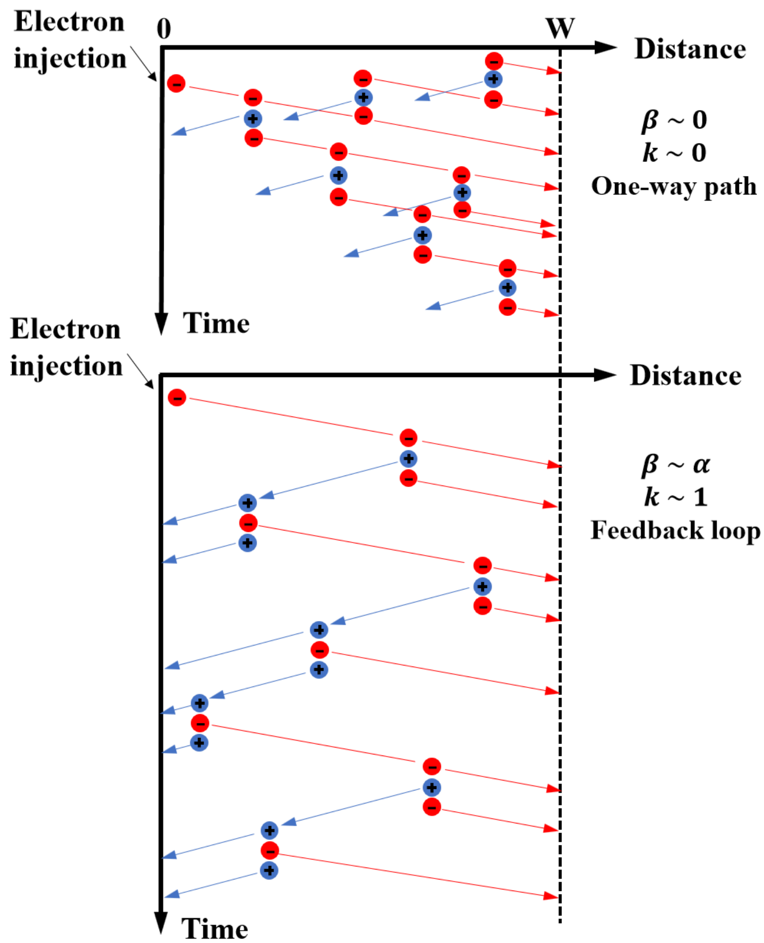

Figure 2-4. The excess noise measurement setup.

As Eq. 1.1 shows, the shot noise is proportional to the excess noise factor, which provides a way to measure $F(M)$. The shot noise contributed by the photocurrent can be expressed as:

$$\left\langle i_{shot-photo}^{2}(M)\right\rangle = \left\langle i_{shot-total}^{2}(M)\right\rangle - \left\langle i_{shot-dark}^{2}(M)\right\rangle = 2qI_{photo}M^{2}F(M)\Delta f \ . \tag{2.19}$$

When $M = 1$, $F(M) = k + (1-k)(2-1) = 1$ and the shot noise is:

$$\left\langle i_{shot-photo}^{2}(M=1)\right\rangle = 2qI_{photo}\Delta f \ . \tag{2.20}$$

Based on these two equations, $F(M)$ can be simply expressed as:

$$F(M) = \frac{1}{M^{2}} \frac{\left\langle i_{shot-photo}^{2}(M)\right\rangle}{\left\langle i_{shot-photo}^{2}(M=1)\right\rangle} = \frac{1}{M^{2}} \frac{2qI_{photo}M^{2}F(M)\Delta f}{2qI_{photo}\Delta f} , \tag{2.21}$$

which can be calculated with measurements of the photogenerated shot noise density at gain of 1 and M. The shot noise at different gain values can be measured with the setup in Fig. 2-4. Before the measurement, a noise source is used to calibrated a noise figure meter. Then, a CW laser is used to generate a DC photocurrent from the APD. The AC signal comes from the noise. By using an optical chopper, the dark noise and total noise can be measured by the noise figure meter, respectively. As Eq. 2.19 shows, the noise from the circuit can be eliminated by subtracting the dark noise from total noise. Finally, $F(M)$ can be calculated from Eq. 2.21.

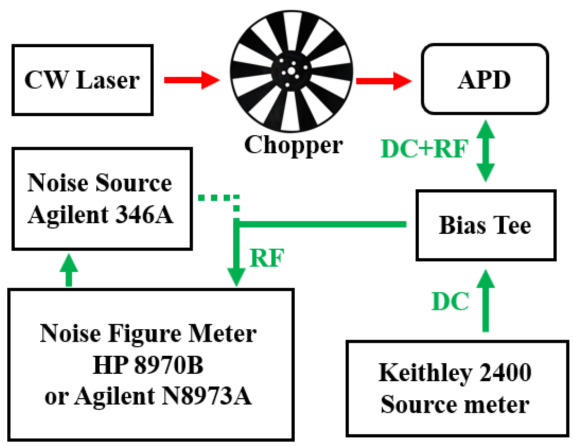

Figure 2-5. The excess noise measurement setup.

In the excess noise measurement, the initial injected carriers are very important due the importance of pure carrier injection. For most material, owing to the fact that $k > 0$, both electrons and holes can impact ionize. For p-i-n APDs, a short-wavelength laser is needed to ensure that all the light is absorbed in an undepleted layer adjacent to the multiplication region. On the other hand, for SACM APDs, the epitaxial layer configuration is designed so that light is absorbed in a narrow bandgap layer and the carrier with the highest ionization coefficient is injected into the multiplication region. The laser spot should be focused on the center of the APD to avoid edge illumination, because edge illumination will allow other layers to absorb light, and result in mixed carrier injection.

2.2 Fabrication process

The fabrication process is important for APDs, because it affects the dark current, gain, QE, and bandwidth. Typically, I first use a simple mask that enables easy fabrication and provides high yield. A suitable etching method and the verification of wafer quality can be determined by this method. Figure 2-6 displays an optical image of a simple APD mask and schematic cross section of a processed device. First, I use a wet etch or dry etch to form the mesa. The metal is deposited on the top p-contact and bottom n-contact layers. Finally, an SU8 coating (the purple region) is spun on the sidewall as a passivation to suppress the surface leakage.

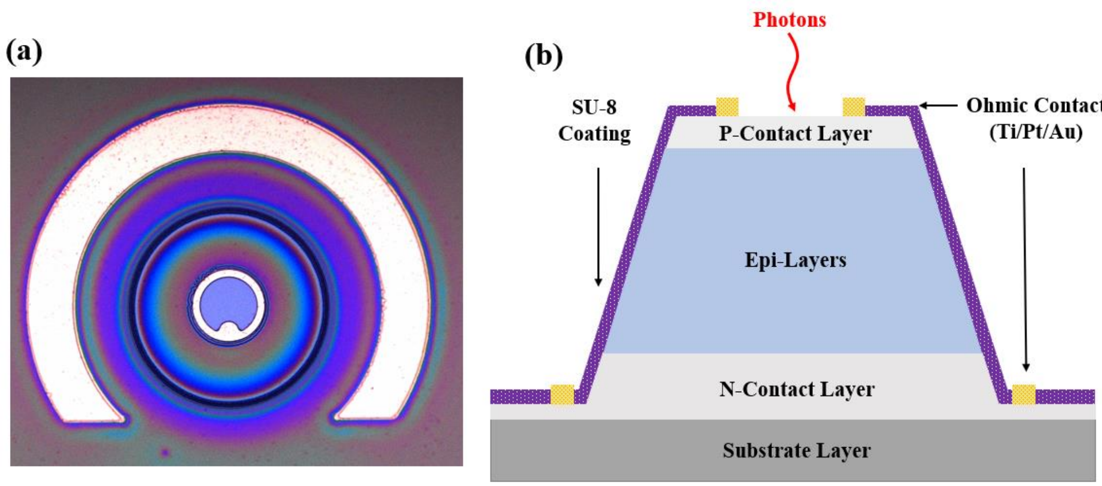

Figure 2-6. (a) Optical image and (b) schematic cross section of simple-mask APDs.

For high-speed APDs, a small mesa area is needed to reduce capacitance and improve the RC-limited bandwidth. In addition, a coplanar waveguide (CPW) ground-signal-ground (GSG) pad with 50 Ω impendence is needed for impendence matching, which can reduce RF reflection. Therefore, small APDs with an airbridge structure are used. The complete fabrication process is shown in Fig. 2-7.

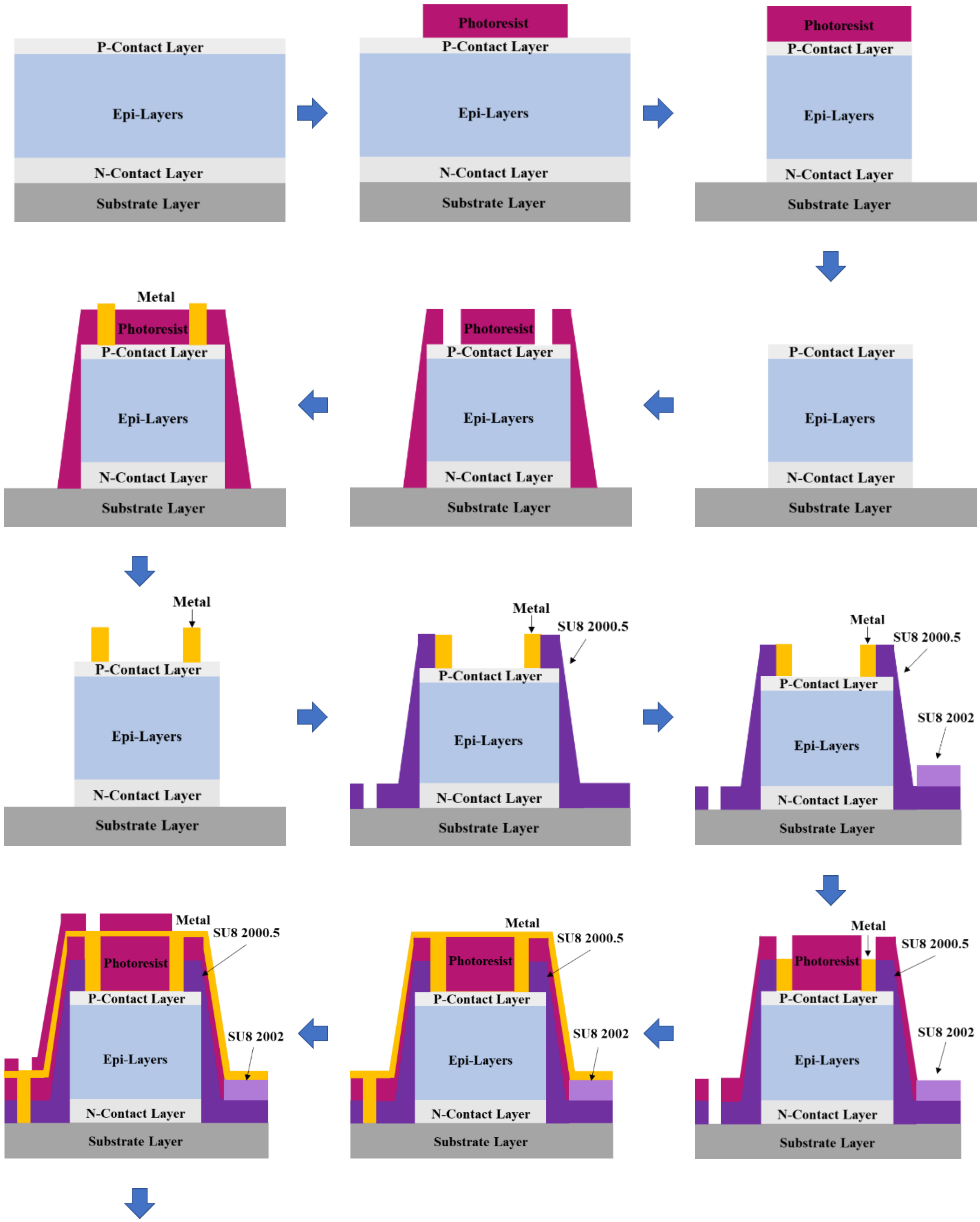
P-Contact Layer
Epi-Layers
N-Contact Layer
Substrate Layer
Photoresist
P-Contact Layer
Epi-Layers
N-Contact Layer
Substrate Layer
Photoresist
P-Contact Layer
Epi-Layers
N-Contact Layer
Substrate Layer
Metal
Photoresist
P-Contact Layer
Epi-Layers
N-Contact Layer
Substrate Layer
Photoresist
P-Contact Layer
Epi-Layers
N-Contact Layer
Substrate Layer
P-Contact Layer
Epi-Layers
N-Contact Layer
Substrate Layer
Metal
P-Contact Layer
Epi-Layers
N-Contact Layer
Substrate Layer
Metal
SU8 2000.5
P-Contact Layer
Epi-Layers
N-Contact Layer
Substrate Layer
Metal
SU8 2000.5
SU8 2002
P-Contact Layer
Epi-Layers
N-Contact Layer
Substrate Layer
Metal
SU8 2000.5
Photoresist
P-Contact Layer
SU8 2002
Epi-Layers
N-Contact Layer
Substrate Layer
Metal
SU8 2000.5
Photoresist
P-Contact Layer
SU8 2002
Epi-Layers
N-Contact Layer
Substrate Layer
Metal
Photoresist
SU8 2000.5
P-Contact Layer
SU8 2002
Epi-Layers
N-Contact Layer
Substrate Layer

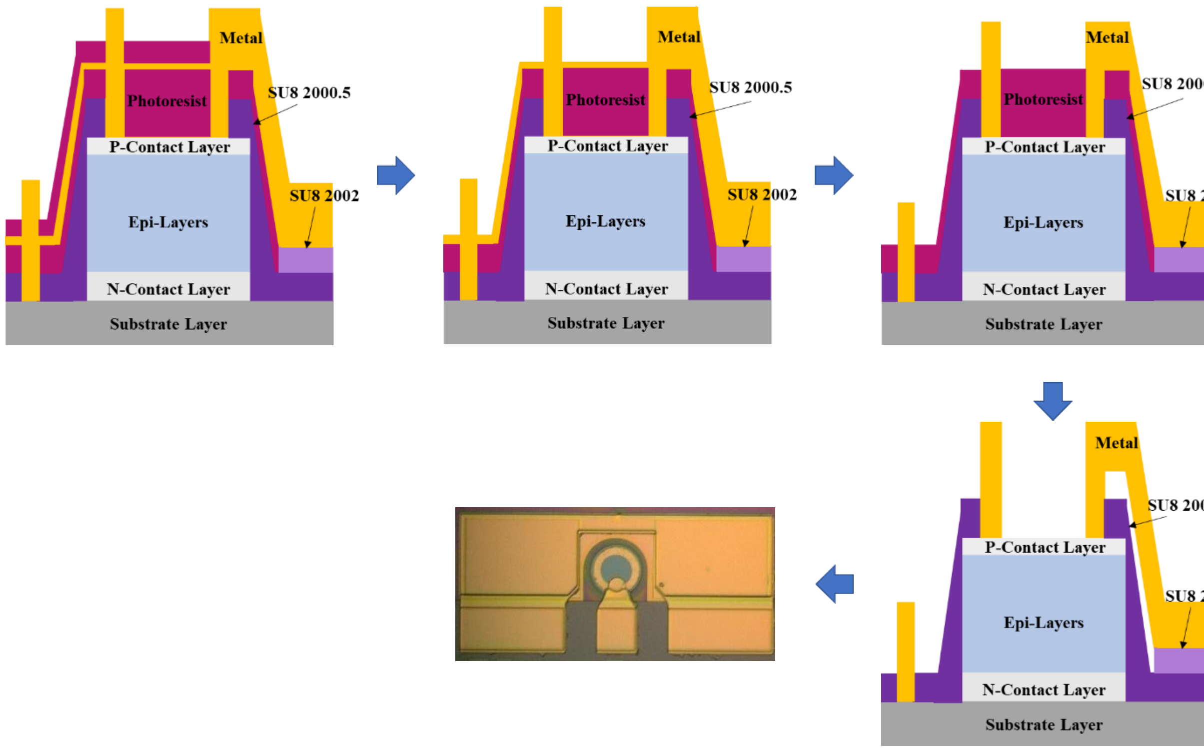

Figure 2-7. Fabrication process flow of airbridge APDs.

The first step uses standard photolithography to form mesa patterns. Depending on the etching method, an AZ5214, AZ4330, or SiO_2 mask (from soft to hard), is needed to protect the mesas. For the AZ5214 mask, I spin HMDS at 4000 rpm for 30 s, spin AZ5214 at 4000 rpm for 30 s, and pre-bake at 100 °C for 1 min. Then the wafer is exposed under MJB4 channel 1 for 1 min and developed in 300 MIF for 25 s. For the AZ4330 mask, it is spun HMDS at 4000 rpm for 40 s, spun AZ4330 at 2500 rpm for 30 s, and pre-bake at 110 °C for 2 min. Then exposed under MJB4 for 100 s, developed in H_2O: AZ400K (4: 1) solution for 2 min, post-baked at 110 °C for 10 min, and exposed with 50 % duty cycle UV light for 30 min. For the SiO_2 mask, I use a plasma-enhanced chemical vapor deposition (PECVD) to grow SiO_2, and use an inductively coupled plasma (ICP) etch or a buffered oxide etch (BOE) to fabricate a hard mask. The etching methods include wet etching and dry etching. There are several wet etching solutions that I use for different semiconductors, such as H_2SO_4: H_2O_2: H_2O (1: 8: 80), H_3PO_4: H_2O_2: H_2O (1: 1: 8), HCl: H_2O_2: H_2O (1: 1: 10), HCl: H_2O (1: 1), and Critic acid: H_2O: H_2O_2: H_3PO_4 (10 g: 60 ml: 4 ml: 8 ml). The dry etching uses 300 W N_2 and Cl_2 ICP in a reactive ion etching (RIE) chamber.

After forming the mesas, the top metal contacts are deposited. In order to ensure the success of the lift-off, I spin LOR 10B at 4000 rpm for 30 s, pre-bake at 180 °C for 15 min, cool down for 2 min, spin AZ5214 at 4000 rpm for 30 s, pre-bake again at 100 °C for 2 min, expose 60 s, develop in 300 MIF for 25 s, and post-bake at 110 °C for 50 s. Then the wafer is loaded into the e-beam evaporator to deposit the top contact, which is usually Ti/Pt/Au. Ti is the metal bonding layer between the semiconductor and other metals; Pt is the blocking layer to avoid Au diffusion into the semiconductor at high temperature, such as the annealing process; and Au is the contact layer because it has excellent electrical conductivity and does not oxidize. Acetone is used to lift-off extra metal, and AZ400K is used to remove the LOR 10B.

The next step is passivation. I normally use SU8 2000.5 to reduce the number of dangling bonds due to its stability and universality. The recipe is the following: spin SU8 2000.5 at 5000 rpm for 40 s, pre-bake at 90 °C for 70 s, expose 10 s, then post-bake at 90 °C for 70 s. The wafer is allowed to cool for 2 min. Finally, the SU8 is developed for 1 min. An RF pad stage is needed to procedure a complete isolation between the GSG RF pad and the n-type contact layer. SU8 2002 is spun as the RF pad stage. Its recipe is same as SU8 2000.5 above.

A seed layer metal is required for the electroplating step. An AZ5214 mask is used to form the seed layer patterns by using the recipe described above. Ti/Au is deposited by the e-beam evaporation. An AZ5214 mask is used again to create airbridge layer patterns, and I use electroplating to grow ~ 2 μm Au. Eventually, the top AZ5214 photoresist is removed by a 200 W O_2-plasma; the Au seed layer is removed by Au etchant HG1200 ~ 1min; and acetone in ultrasonication is used to lift-off the metals. A cross section of the completed device and an optical image of the airbridge APD is shown at the bottom of Fig. 2-7.

Chapter 3. $Al_{0.7}InAsSb$ digital alloy APDs

3.1 Device structure

AlInAsSb digital alloy materials are grown on n-type Te-doped GaSb (001) substrate by solid-source molecular-beam epitaxy (MBE). For the AlInAsSb digital alloy period, we chose a nominal period thickness of 10 monolayers (ML) or 3.05 nm [37]. The AlInAsSb lattice matched to GaSb and bright-field transmission electron microscopy (TEM) of an $Al_{0.5}In_{0.5}As_{0.5}Sb_{0.5}$ digital alloy wafer are shown in Fig. 3.1(a) and (b), respectively [21, 37]. Since the thickness of each layer is ~ one to two MLs, which is sufficiently thin that the electron and hole wavefunctions overlap multiple layers, the features of digital alloys differ from those of a random alloy with the same average composition.

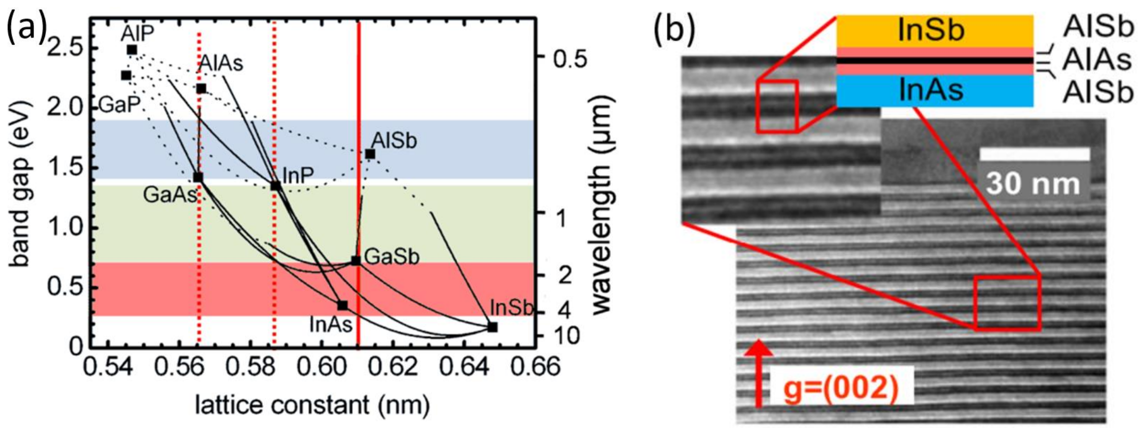

Figure 3-1. (a) Bandgap versus the lattice constant and (b) bright-field transmission electron microscopy for a 300 nm-thick $Al_{0.5}In_{0.5}As_{0.5}Sb_{0.5}$ film [21, 37].

A difficulty with crystal growth of the AlInAsSb material system is that there is a miscibility gap that is particularly severe for high Al concentrations. Vaughn et al. [39] demonstrated that stable AlInAsSb could be grown within the miscibility gap as a digital alloy of the constituent binaries: AlAs, AlSb, InAs, and InSb, however, the Al fractions were limited from 0% to 40%.

Recently, Prof. Seth Bank's group at the University of Texas in Austin reported stable AlInAsSb digital alloys with Al fractions ranging from 0% to 80%. In this chapter, I report the characteristics of $Al_{0.7}In_{0.3}As_{0.3}Sb_{0.7}$ APDs. In the following the AlInAsSb digital alloys will be designated by their Al content, e.g., $Al_{0.7}$InAsSb, with the assumption of lattice-matching to GaSb. All the wafers were grown by Prof. Seth Bank's group.

In previous work, it was found that $Al_{0.7}$InAsSb digital alloy APDs, exhibit low excess noise comparable to Si [24]. This $Al_{0.7}$InAsSb digital alloys consists of the binaries AlAs, AlSb, InAs, and InSb and will be referred to as the binary digital alloy. A possible explanation for low noise observed in the binary $Al_{0.7}$InAsSb digital alloys involves modifications of the valence band transport that suppress hole ionization while having minimal effect on electron ionization. In order to verify this explanation, a new $Al_{0.7}$InAsSb structure was grown, which is comprised of InAs, InSb, and the ternary $AlAs_{0.1}Sb_{0.9}$, this will be denoted as the ternary digital alloy (even though it contains two binaries). The primary purpose of this ternary $Al_{0.7}$InAsSb digital alloy is to eliminate the largest portion of the valence band offset, due to the asymmetric bowing between the conduction band and valence band edges, which should greatly reduce miniband formation and alteration of the hole transport.

The binary and ternary digital alloys were grown on GaSb and InAs substrates, respectively. The period thicknesses of these two $Al_{0.7}$InAsSb digital alloys are both 10 monolayers (ML), and the fundamental periods are shown in Fig. 3-2.

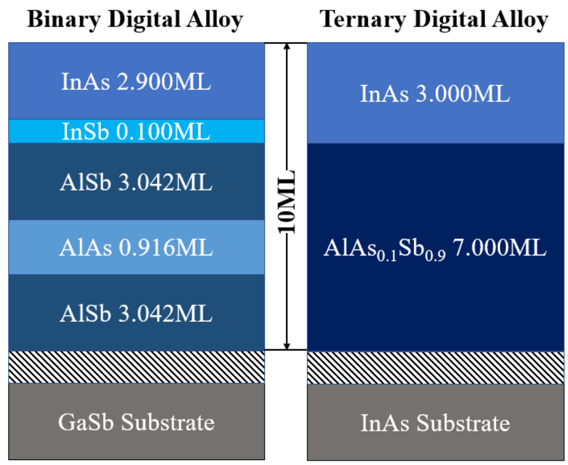

Figure 3-2. Schematic cross sections of binary and ternary $Al_{0.7}InAsSb$ digital alloys.

Binary and ternary $Al_{0.7}InAsSb$ digital alloys APDs with p-i-n and n-i-p structures with the same multiplication region thickness were grown in order to determine the ionization coefficients through measurements with pure electron and pure hole injection. The layer structures are shown in Table 3-1. The p-type and n-type layers are doped with Be and Te, respectively. All four mesa types were defined by standard photolithography and formed by dry etching followed by a brief wet etch to suppress surface dark current. RIE and ICP were used to etch approximately 1µm. The mesa etch was completed with a critic acid solution, which is described in Section 2.2. Ti/Au was deposited as top and bottom contacts by electron-beam evaporation. SU8 was spun on the sidewall as a surface passivation.

Table 3-1. Structures of $Al_{0.7}InAsSb$ digital alloy APDs.

Types	Material	Doping (cm^{-3})	Thickness(nm)	Types	Material	Doping (cm^{-3})	Thickness(nm)
Binary digital alloy p-i-n APD	GaSb	p: 1×10^{19}	100	Ternary digital alloy p-i-n APD	InAs	p: 1×10^{19}	100
	$Al_{0.7}InAsSb$	p: 2×10^{18}	100		$Al_{0.7}InAsSb$	p: 2×10^{18}	100
	$Al_{0.7}InAsSb$	UID	1000		$Al_{0.7}InAsSb$	UID	1000
	$Al_{0.7}InAsSb$	n: 2×10^{18}	200		$Al_{0.7}InAsSb$	n: 2×10^{18}	200
	GaSb	n: 2×10^{18}	300		InAs	n: 2×10^{18}	300
	GaSb	n: 1×10^{17}	substrate		InAs	n: 1×10^{17}	substrate
Binary digital alloy n-i-p APD	GaSb	n: 1×10^{19}	100	Ternary digital alloy n-i-p APD	InAs	n: 1×10^{19}	100
	$Al_{0.7}InAsSb$	n: 2×10^{18}	100		$Al_{0.7}InAsSb$	n: 2×10^{18}	100
	$Al_{0.7}InAsSb$	UID	1000		$Al_{0.7}InAsSb$	UID	1000
	$Al_{0.7}InAsSb$	p: 2×10^{18}	200		$Al_{0.7}InAsSb$	p: 2×10^{18}	200
	GaSb	p: 2×10^{18}	300		InAs	p: 2×10^{18}	300
	GaSb	p: 1×10^{17}	substrate		InAs	p: 1×10^{17}	substrate

3.2 Experimental characteristics

All measurements were carried out with 100 μm-diameter APDs. Figure 3-3 shows the total current, dark current, and multiplication gain versus bias voltage for the four types of APDs. All were illuminated with a 543 nm He-Ne CW laser for pure electron injection gain, M_e, and pure hole injection gain, M_h. The gain curves indicate that $\alpha > \beta$ in both the binary and ternary digital alloys since $M_e > M_h$ at fixed voltage. The gain characteristics of the APDs vary with the depletion width. Capacitance-voltage measurements were carried out to ensure the depletion region thicknesses of the p-i-n and n-i-p APDs are same. In Fig. 3-4, the capacitances for these APDs are all ~ 0.8 pF when fully depleted, which means that the electric fields are comparable for the same voltages.

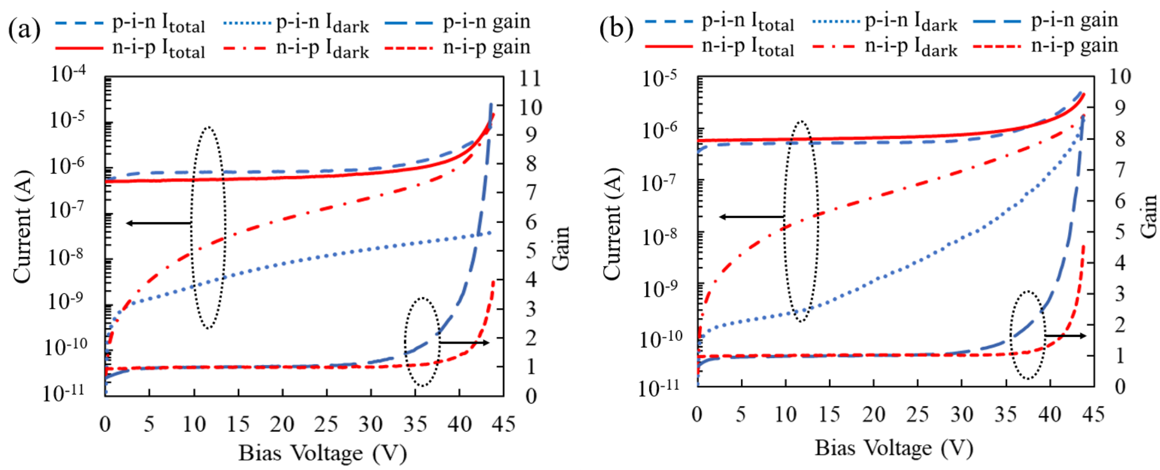

Figure 3-3. Total current, dark current, and gain versus bias voltage for (a) binary digital alloy p-i-n and n-i-p APDs, and (b) ternary digital alloy p-i-n and n-i-p APDs.

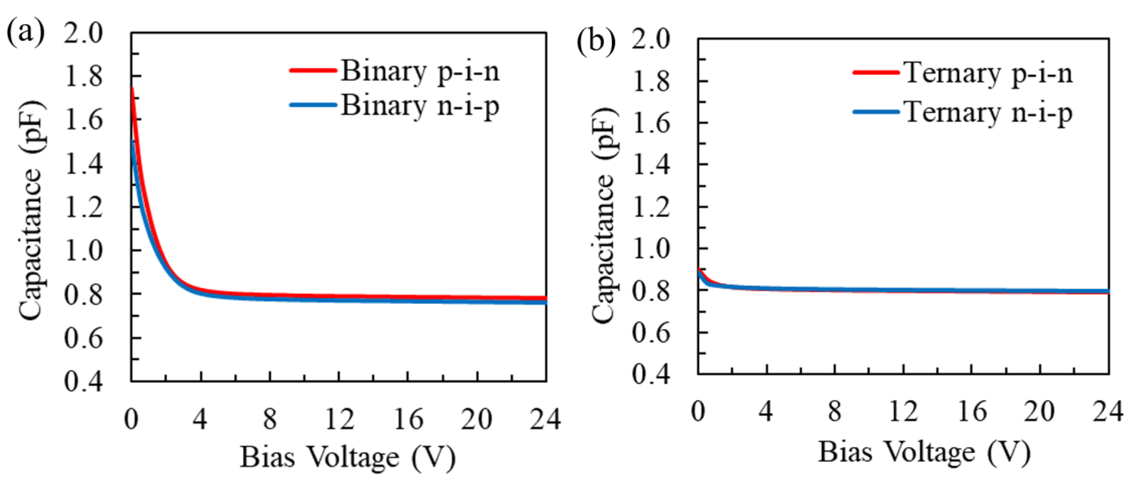

Figure 3-4. Capacitance-voltage measurements for (a) binary and (b) ternary digital alloy APDs.

The forward current-voltage characteristics for the p-i-n APDs from 213 K to 313 K are shown in Figs. 3-5(a) and3-5 (b). The ideality factor, *n,* at different temperatures can be fitted using Eq. 3.1 below [40]:

$$J_f \propto \exp\left(\frac{qV}{nK_BT}\right) - 1, \tag{3.1}$$

where J_f is the forward current density, K_B is the Boltzmann constant, and T is the absolute temperature. The fitted dashed lines agree well with the experimental results, and the ideality factors of the binary and ternary diodes are plotted in Fig. 3-5(c). The forward current density of a p-i-n junction can be expressed as [41]:

$$J_f = J_{d0}(e^{qV/K_BT} - 1) + J_{nr0}(e^{qV/2K_BT} - 1) + J_{r0}(e^{qV/K_BT} - 1), \tag{3.2}$$

where the first term is the diffusion current density with an ideality factor n = 1, the second term represents the Schottky-Read-Hall (SRH) recombination current density with ideality factor n = 2, and the last term is the radiative recombination current density in the depletion region with n = 1. From Fig. 3-5(c), we see that in the ternary material, the SRH recombination current density dominates. Also, the ideality factors decrease with increasing temperature.

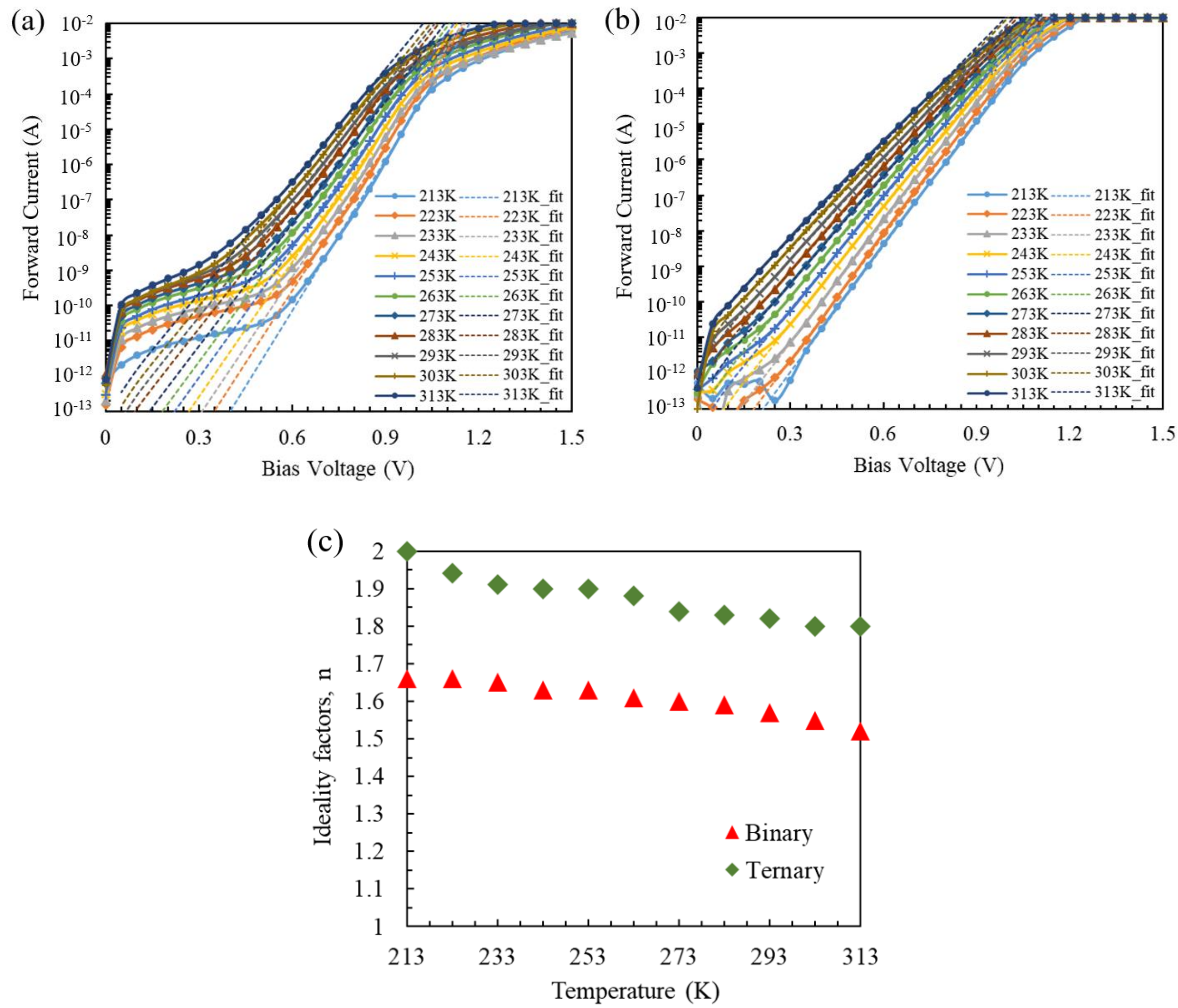

Figure 3-5. Forward current-voltage characteristics at different temperatures for the (a) binary and (b) ternary digital alloy p-i-n APDs. (c) Ideality factors versus temperature.

From the temperature variation of the dark current, the activation energy E_a can be determined by using Eq. 2.6 in Section 2.1.1. Figure 3-6 shows the dark current fits using this equation at reverse bias 5 V, 10 V, and 15 V. The activation energies for the binary and ternary digital alloys are 0.14 eV and 0.23 eV, respectively, at all three bias voltages. It appears that the dominant generation-recombination center of the ternary material is deeper than that of the binary material.

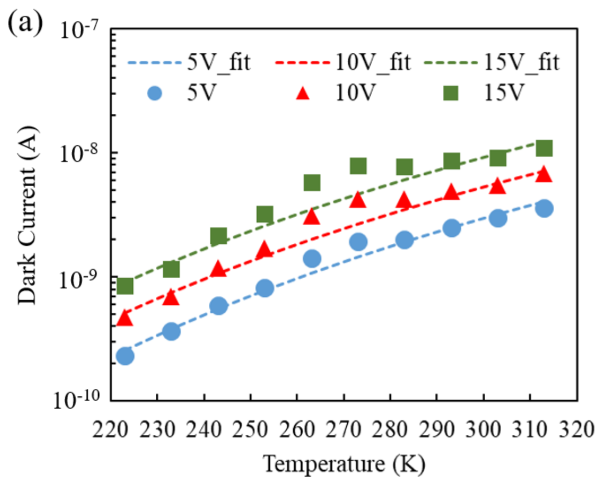

Figure 3-6. Dark current versus temperature for (a) binary and (b) ternary digital alloy p-i-n APD.

The temperature stability of APDs is an important figure of merit. This is due to the fact that phonon scattering increases with temperature, which causes carriers to require higher electric field in order to impact ionize. The temperature stability of APDs can be characterized by the breakdown voltage temperature coefficient, $\Delta V_{bd}/\Delta T$. In order to reduce the complexity and cost of the temperature control system, a smaller $\Delta V_{bd}/\Delta T$ is desirable. Recently, the digital alloy $Al_xInAsSb$ APDs have exhibited much smaller $\Delta V_{bd}/\Delta T$ than InP and random alloy InAlAs APDs [41, 42]. The breakdown voltages of these APDs were measured with a 543 nm He-Ne CW laser for pure electron injection. Figure 3-7(a) shows the breakdown voltage as a function of ambient temperature. The avalanche breakdown for the binary digital alloy occurs at lower electric field than that for the ternary. Recall that the thickness of the depletion region is the same for both types of APDs. From the slopes of the fitted functions, the $\Delta V_{bd}/\Delta T$ is 5.3 mV/K for the binary, and 3.9 mV/K for the ternary. A comparison of these two digital alloy materials to other conventional semiconductor materials is shown in Fig. 3-7(b). The temperature stability of the digital alloys is comparable to 100-nm thick AlGaAsSb and significantly lower than InP, InAlAs, and Si [44].

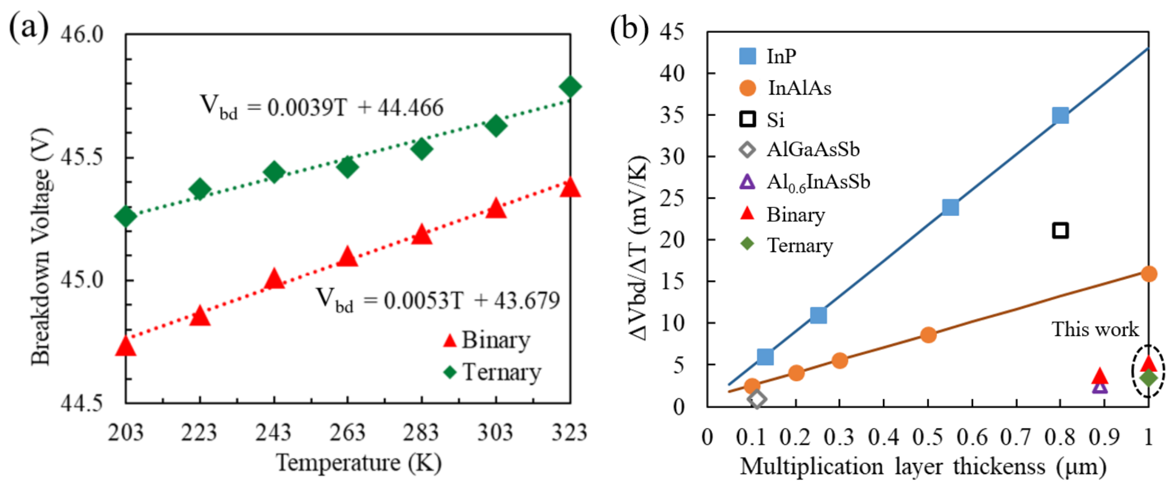

Figure 3-7. (a) Breakdown voltages versus temperature for both $Al_{0.7}InAsSb$ p-i-n APDs. (b) Temperature dependence of breakdown voltages for different materials APDs [19, 41, 43, 44].

APDs fabricated from binary $Al_{0.7}InAsSb$ lattice matched to GaSb have exhibited very low excess noise with k values ~ 0.01, which is comparable to Si APDs [23]. The excess noise for the binary and ternary p-i-n APDs were measured with an HP 8970B noise figure meter and a 543 nm He-Ne CW laser. As shown in Fig. 3-8(a), these two types of $Al_{0.7}InAsSb$ digital alloys exhibit the same excess noise characteristics. The excess noise factors for these two p-i-n APDs and AlGaAsSb [19, 45] , AlAsSb [47], InP [48], InAlAs [49], Si [50], and InAlAs digital alloy [27] APDs at $M = 10$ are plotted in Fig. 3-8 (b). Typically, thin multiplication layers exhibit lower noise than bulk materials due to the non-local effect [50-52]. Compared to other APDs, these two materials achieve very low excess noise factors even with thick multiplication regions.

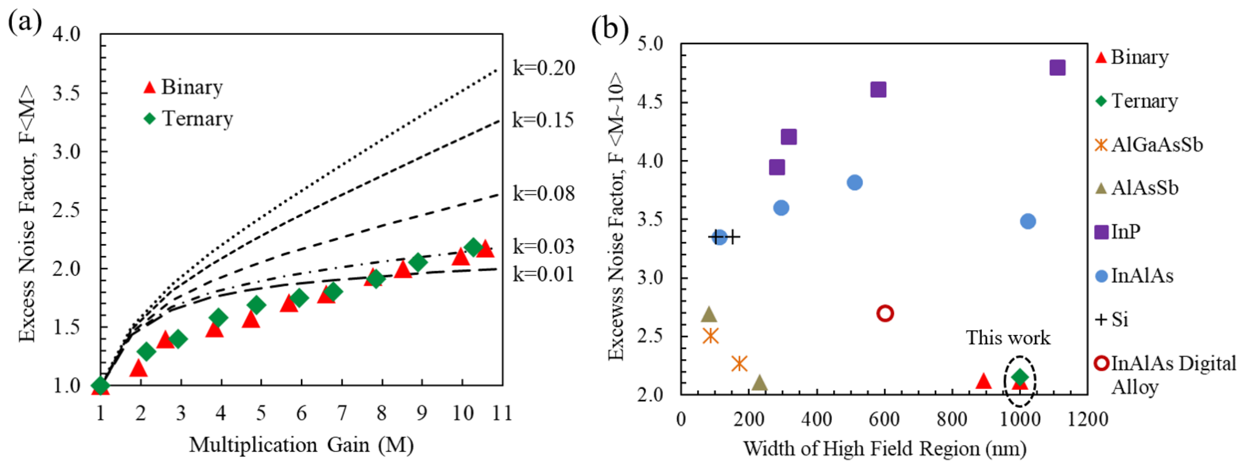

Figure 3-8. (a) Excess noise of binary and ternary digital alloy $Al_{0.7}InAsSb$ p-i-n APDs. (b) Comparison of excess noise factor at gain of 10 for different materials APDs [19, 23, 26, 45-49].

Figures 3-9(a) and (b) show the temperature variation of excess noise for the binary and ternary APDs, respectively. Figure 3-9(c) shows k versus temperature. Since the k value varies little with the multiplication gain, the k values plotted are those for $M = 11$. Similar to the digital alloy InAlAs APDs, the k values also decrease exponentially with decreasing temperature for both the binary and ternary materials. The temperature dependences of the binary and ternary APDs can be expressed as Eq. 3.3 and 3.4, respectively:

$$k = 4.0 \times 10^{-5} \times \exp(0.0247 \times T), \tag{3.3}$$

$$k = 1.5 \times 10^{-5} \times \exp(0.0247 \times T). \tag{3.4}$$

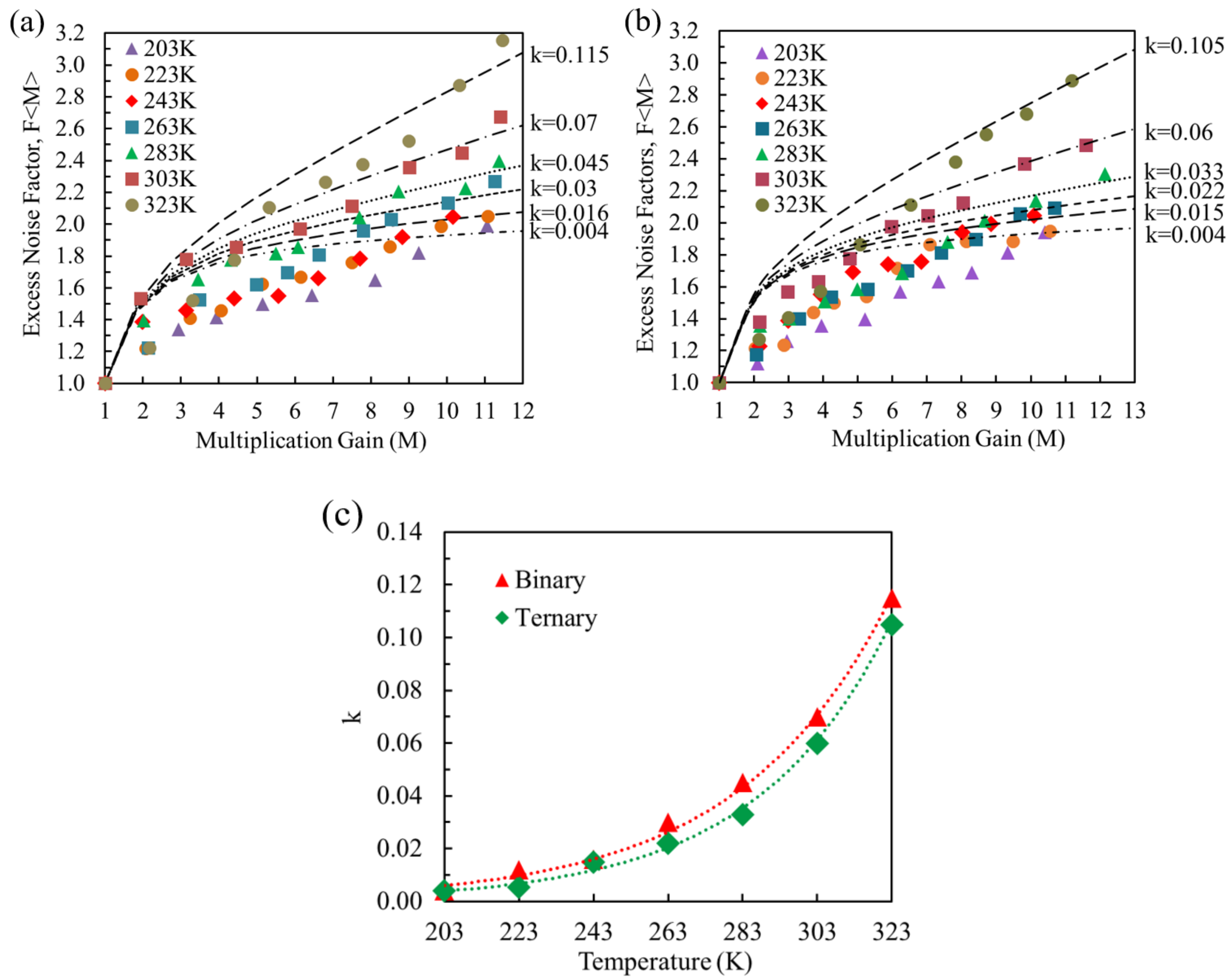

Figure 3-9. Temperature dependence of excess noise for (a) binary and (b) ternary digital alloy p-i-n APDs. (c) Ionization coefficient ratio *k* for binary and ternary digital alloy p-i-n APDs.

3.3 Impact ionization coefficients

In general, the impact ionization coefficients are determined by gain curves of pure electron and pure hole injection. Figure 3-3 shows the gain curves for p-i-n and n-i-p $Al_{0.7}InAsSb$ APDs under pure electron or hole injection. As noted above, the thicknesses of the depletion region, W_D, are exactly same for the p-i-n and n-i-p APDs. Using Eqs. 3.5 and 3.6 below [9]:

$$\alpha(E) = \frac{1}{W_D}\left[\frac{M_e(V)-1}{M_e(V)-M_h(V)}\right]\ln\left[\frac{M_e(V)}{M_h(V)}\right], \tag{3.5}$$

$$\beta(E) = \frac{1}{W_D}\left[\frac{M_h(V)-1}{M_h(V)-M_e(V)}\right]\ln\left[\frac{M_h(V)}{M_e(V)}\right], \tag{3.6}$$

the electric-field-dependent impact ionization coefficients for electrons (α) and holes (β) can be calculated. The calculations include the built-in voltage, V_{built}, in order to obtain accurate electric field values. The built-in voltage is estimated with equations [32]:

$$V_{built} = \frac{K_B T}{q}\ln\left(\frac{N_d N_a}{n_i^2}\right), \tag{3.7}$$

$$n_i = \sqrt{N_C N_V}\exp\left(\frac{-E_g}{2K_B T}\right), \tag{3.8}$$

where both of these materials have same bandgap energy, E_g, of 1.13 eV, and the values of N_C, N_V can be approximated with the parameters for $Ga_xInAsSb$ [54]: $N_C = 2.5 \times 10^{19} \times (0.022 + 0.03x - 0.012x^2)^{3/2}$, $N_V = 2.5 \times 10^{19} \times (0.41 + 0.16x + 0.23x^2)^{3/2}$, and $x = 0.7$. Therefore, V_{built} is approximately 1.14 V. The calculated results for α and β are plotted as open points in Fig. 3-10. The measurements can be fit to the following expressions for the binary digital alloy:

$$\alpha(E) = 3.5\times10^6 \times \exp(-2.4\times10^6 / E), \tag{3.9}$$

$$\beta(E) = 1.0\times10^7 \times \exp(-3.55\times10^6 / E), \tag{3.10}$$

and for the ternary digital alloy:

$$\alpha(E) = 4.0\times10^6 \times \exp(-2.5\times10^6 / E), \tag{3.11}$$

$$\beta(E) = 1.9\times10^8 \times \exp(-4.8\times10^6 / E). \tag{3.12}$$

The fits are plotted as solid lines in the figures.

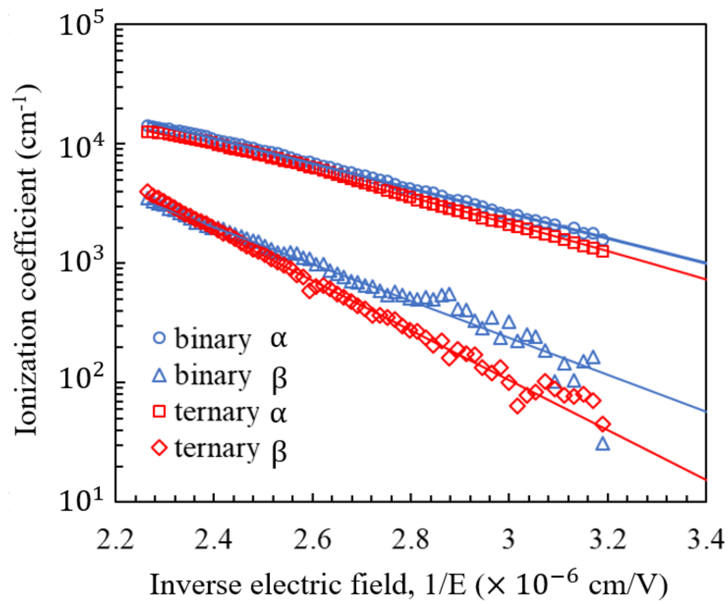

Figure 3-10. Ionization coefficients for $Al_{0.7}InAsSb$ binary and ternary digital alloy p-i-n APDs.

In Fig. 3-9(c), the k value changes exponentially with temperature. These k values were used to calculate the temperature dependence of the ionization coefficients using the following expressions:

$$\alpha(E) = \frac{\ln\left[k-(k-1)/M_e(V)\right]}{(k-1)\times W_D}, \tag{3.13}$$

$$\beta(E) = k \times \alpha(E). \tag{3.14}$$

As shown in Fig. 3-11, for both the binary and ternary alloys, the electron impact ionization coefficients display modest decrease with temperature, owing to increased phonon scattering at higher temperature. However, the hole impact ionization coefficients exhibit significant change; β increases rapidly with temperature. It follows that the observed decrease in excess noise with decreasing temperature is primarily due to the reduction of the hole ionization coefficient.

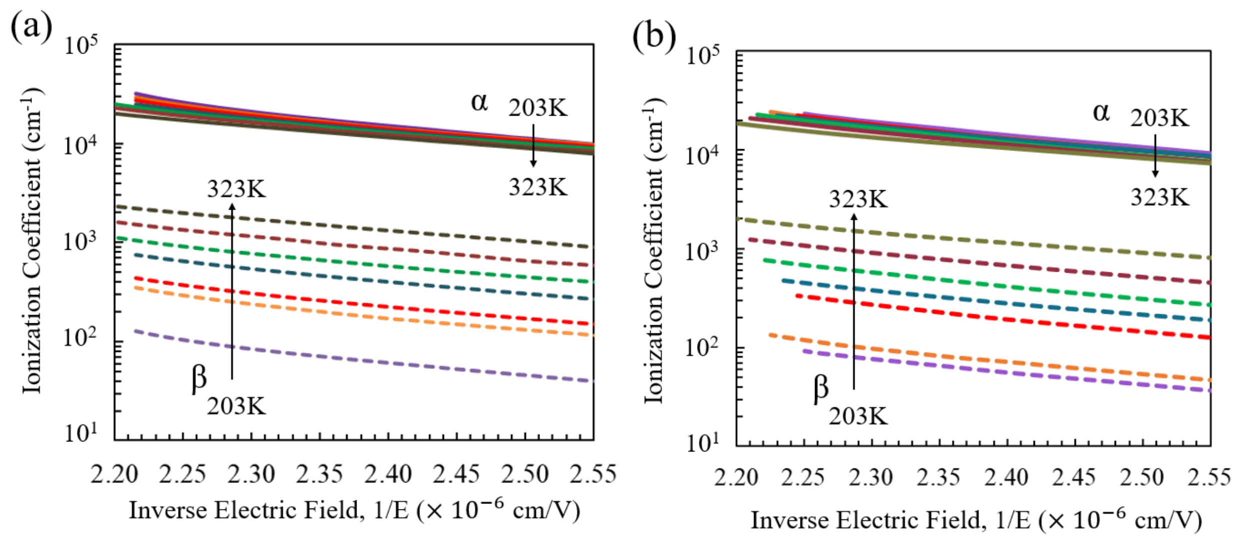

Figure 3-11. Temperature dependence of ionization coefficients for $Al_{0.7}InAsSb$ (a) binary and (b) ternary digital alloy p-i-n APD.

For binary $Al_{0.7}InAsSb$ digital alloy APDs, the optical characteristics were measured by spectroscopic ellipsometry. Ellipsometry measures two values Ψ and Δ, the amplitude ratio and phase difference between p-polarized and s-polarized light waves, respectively. The complex reflectance ratio, ρ, is given by the expression [55]:

$$\rho = \tan(\Psi)e^{i\Delta}. \tag{3.15}$$

The measured Ψ and Δ values at 60° incidence angle are shown in Fig. 3-12(a), where the solid lines are the measured reflection values using Eq. 3.15, and the dash lines are fitted curves. Here, the optical properties of the binary $Al_{0.7}InAsSb$ layers are approximated by effective medium approximations (EMA) with the Bruggeman analysis technique [56]. Figure 3-12(b) shows the real part, n, and the imaginary part, κ, of the deduced binary digital alloy $Al_{0.7}InAsSb$ complex refractive index. The absorption coefficients versus wavelength are plotted in Fig. 3-12(c). The measured external quantum efficiency (solid line) and the calculated efficiency ("○" data points) using the absorption coefficients are shown in Fig. 3-12(d). They agree for wavelengths up to ~900 nm. Hence the Bruggeman analysis technique using four binary semiconductors InAs, AlAs, InSb, and AlSb to calculate EMA optical properties, the long wavelength absorption coefficient near the bandgap edge might be not accurate, i.e., $\lambda > 900$ nm.

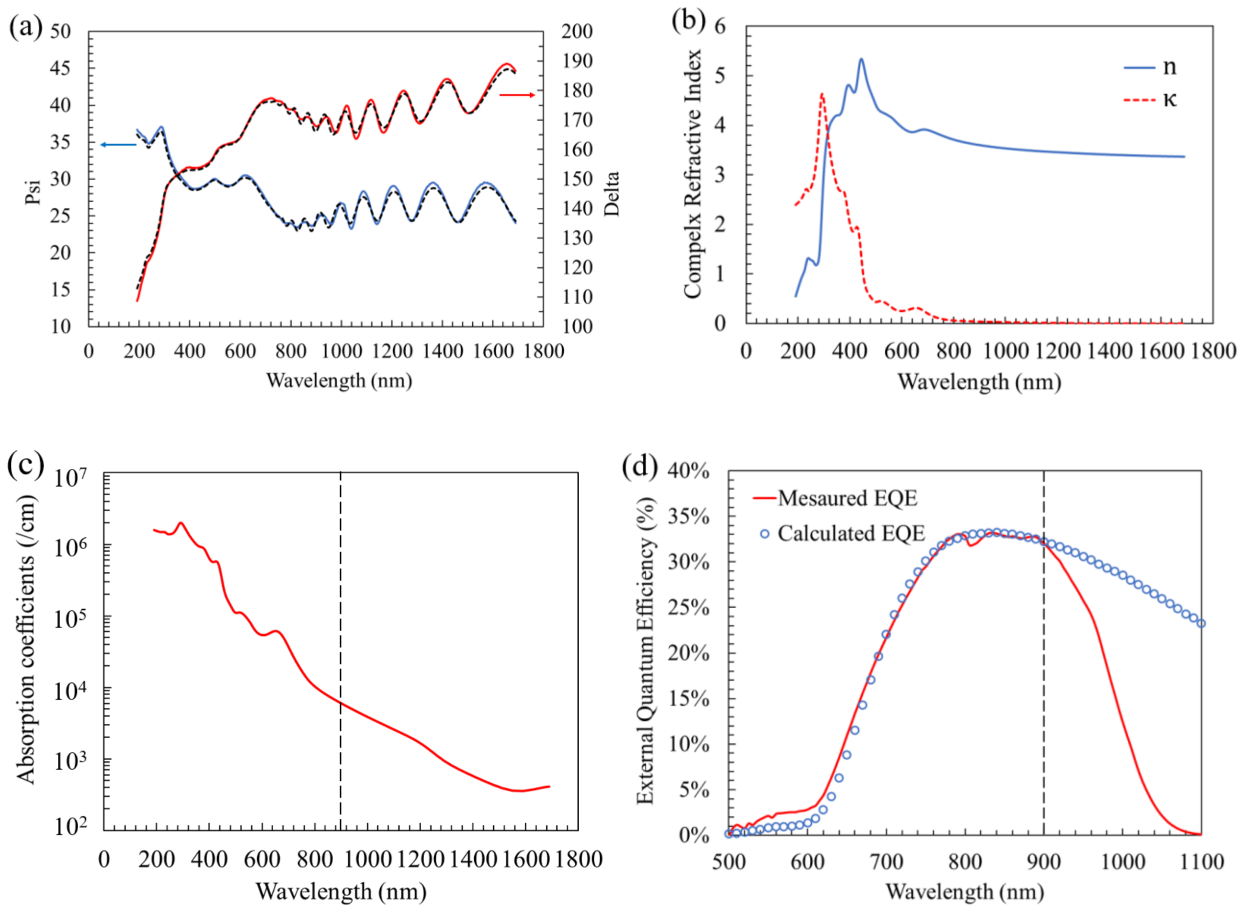

Figure 3-12. Optical characteristics of $Al_{0.7}InAsSb$ digital alloy as measured with spectroscopic ellipsometry: (a) reflection parameters versus wavelength, (b) complex refractive index, and (c) absorption coefficient versus wavelength. (d) Measured and calculated external quantum efficiencies of $Al_{0.7}InAsSb$ digital alloy.

The multiplication gain measurements of the binary $Al_{0.7}InAsSb$ APD are shown in Fig. 3-13. Using different wavelength lasers permits gain measurements corresponding to different carrier injection profiles. To determinate the ionization coefficients, the measurements used to obtain the ionization coefficients in Fig. 3-10 were based on pure electron and pure hole-initiated multiplication. However, in the absence of pure carrier injection, any two sets of gain measurements with known injection profiles can be used to obtain reliable ionization coefficients.

Compared to the mixed injection method, the pure carrier injection method requires fully symmetrical p-i-n and n-i-p APDs, or top and back illumination, which may, at times, be limited by material and processing issues. With the pure carrier injection method, it is also necessary to avoid photon recycling [57] and depletion edge movement [58]. In Fig. 3-13, the multiplication gain curves at 543 nm, 633 nm, and 850 nm provide three different injection profiles that can be used to determine the ionization coefficients. The gain curves move to higher bias voltages at longer illumination wavelength, which indicates that the electron ionization coefficient, α, is larger than the hole ionization coefficient, β [58, 59].

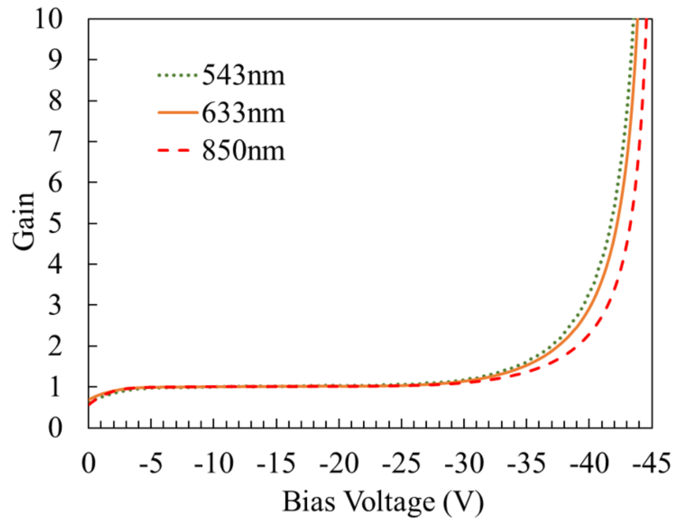

Figure 3-13. Multiplication gain versus voltage of an $Al_{0.7}InAsSb$ digital alloy APD.

Excess noise factor characteristics, $F(M)$, for $Al_{0.7}InAsSb$ digital alloy APD, again achieved at 543 nm, 633 nm, and 850 nm wavelengths, are plotted in Fig. 3-14. The excess noise factors measured at 543 nm laser are the lowest, since this wavelength produces pure electron injection. As the wavelength increases, there are more holes injected into the multiplication region, and the excess noise factor increases. This tendency is consistent with the conclusion that α is larger than β.

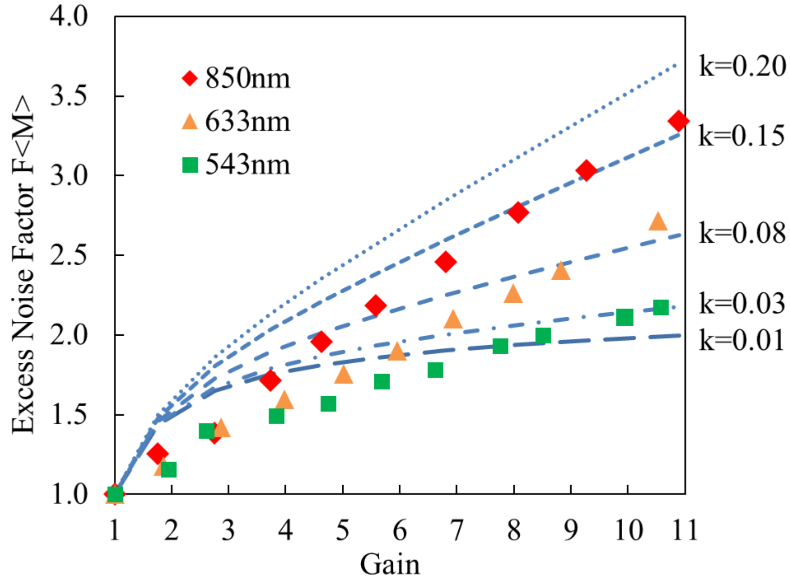

Figure 3-14. Excess noise factor versus gain for the binary $Al_{0.7}InAsSb$ digital alloy APD.

The mixed injection multiplication gain can be calculated using the following expressions [60, 61]:

$$M_{mix} = \frac{\int_0^W M(x)G(x)dx}{\int_0^W G(x)dx}, \tag{3.16}$$

$$G(x) \propto \exp(-\gamma x), \tag{3.17}$$

$$M(x) = \frac{(\alpha-\beta)\times\exp[-(\alpha-\beta)x]}{\alpha\times\exp[-(\alpha-\beta)W_D]-\beta}, \tag{3.18}$$

where W_D is depletion region width, γ is absorption coefficient, $G(x)$ is the carrier generation rate, and $M(x)$ is the gain for an electron-hole pair injected at position x. By using the equations above and the three wavelength multiplication gain sets, the ionization coefficients can be simulated. It can be seen in Fig. 3-13 that the avalanche gain starts at approximately -30 V. Figure 3-15 shows good agreement between the simulated gain and the measured gain values.

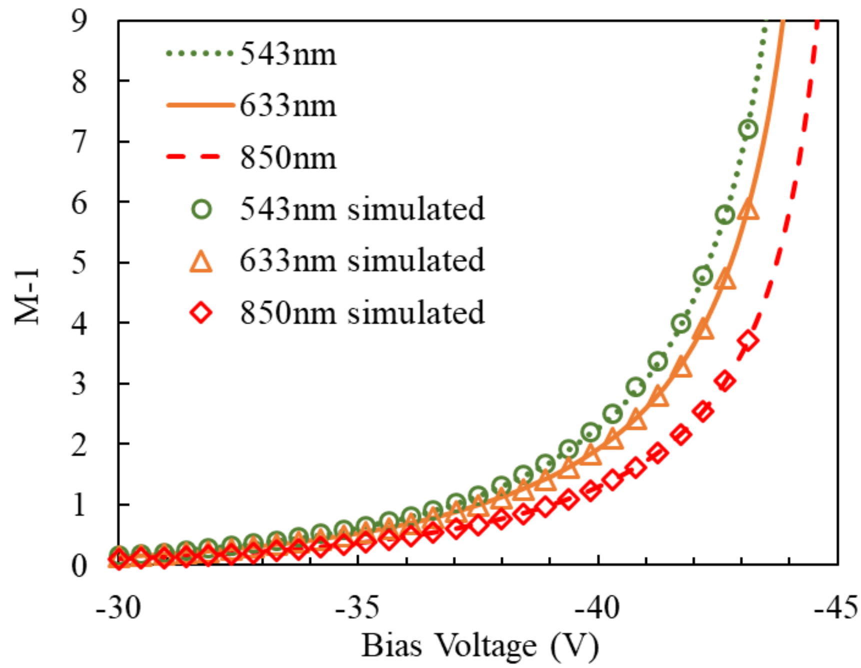

Figure 3-15. Measured (lines) and simulated (symbols) multiplication gain curves of an $Al_{0.7}InAsSb$ digital alloy APD.

Combined with the absorption coefficients for each layer, the gain and ionization coefficients of the binary $Al_{0.7}InAsSb$ digital alloy can be simulated. The absorption coefficients determined from the data in Fig. 3-12 (c) and the light absorption percentages in each layer (assuming 30% reflection at the interface between air and top GaSb layer) are shown in Table 3-2.

Table 3-2. Absorption coefficients and percentages of different layers.

Layers	543 nm (μm^{-1})	Absorption @ 543 nm	633 nm (μm^{-1})	Absorption @ 633 nm	850 nm (μm^{-1})	Absorption @ 850 nm
GaSb (p-type, 100nm)	41.21	69%	23.66	63%	4.42	25%
$Al_{0.7}InAsSb$ (p-type, 100nm)	9.26	1%	5.82	3%	0.77	3%
$Al_{0.7}InAsSb$ (UID, 1000nm)	9.26	0	5.82	4%	0.77	22%
$Al_{0.7}InAsSb$ (n-type, 200nm)	9.26	0	5.82	0	0.77	3%
GaSb (n-type, 300nm)	41.21	0	23.66	0	4.42	12%

The electric field calculation includes the built-in voltage, which is ~ 1.14 V. To assess the accuracy of the simulated results, the α (○) and β (△) determined from pure carrier injection by measuring the gain of the p-i-n and n-i-p APDs are also plotted in Fig. 3-16. The ionization coefficients simulated using the mix injection method are in good agreement with the results obtained from pure carrier injection. The agreement also supports the absorption coefficients of the $Al_{0.7}InAsSb$ digital alloy. The results of this study can be used to generate the following analytical expressions for the ionization coefficients, which are plotted as solid lines in Fig. 3-16:

$$\alpha(E) = 4.5\times10^{6} \times \exp(-2.5\times10^{6} / E)\,, \tag{3.19}$$

$$\beta(E) = 3.5\times10^{6} \times \exp(-3.2\times10^{6} / E)\,. \tag{3.20}$$

The ionization coefficients of Si [63] and InP [64] are also plotted in Fig. 3-16 for comparison. The AlInAsSb APD has comparable low excess noise to that of Si, because they exhibit similar large α/β values. Both α/β ratios are much larger than that of InP.

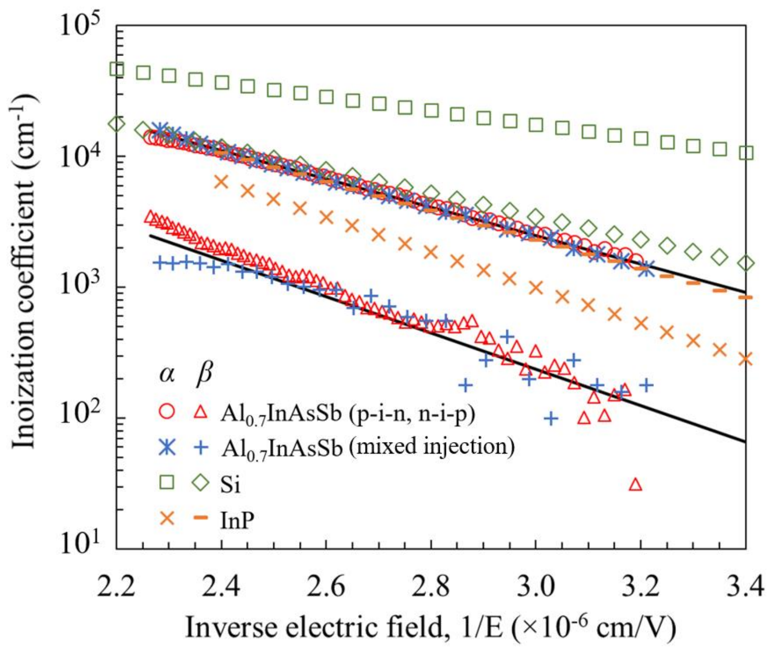

Figure 3-16. Ionization coefficients of the $Al_{0.7}InAsSb$ by using the pure carrier injection method and the mix injection method. Those for Si and InP are plotted for comparison [62, 63].

3.4 Random-digital alloy APDs

Recently, an $Al_{0.7}InAsSb$ "random-digital alloy" wafer has been grown to further verify the low excess noise of the digital alloy $Al_{0.7}InAsSb$ APDs. Instead of binary and ternary digital alloy periods shown in Fig. 3-2, the random-digital alloy is closer to a random alloy; the period is varied from 4ML to 16ML, but the average period is still 10ML. The $Al_{0.7}InAsSb$ random-digital alloy APD has exactly same structure as the binary and ternary digital alloy APDs in Table 3-1. Figure 3-17 is the current and gain versus bias voltage of the $Al_{0.7}InAsSb$ random-digital alloy APD. It was measured with a 543 nm laser.

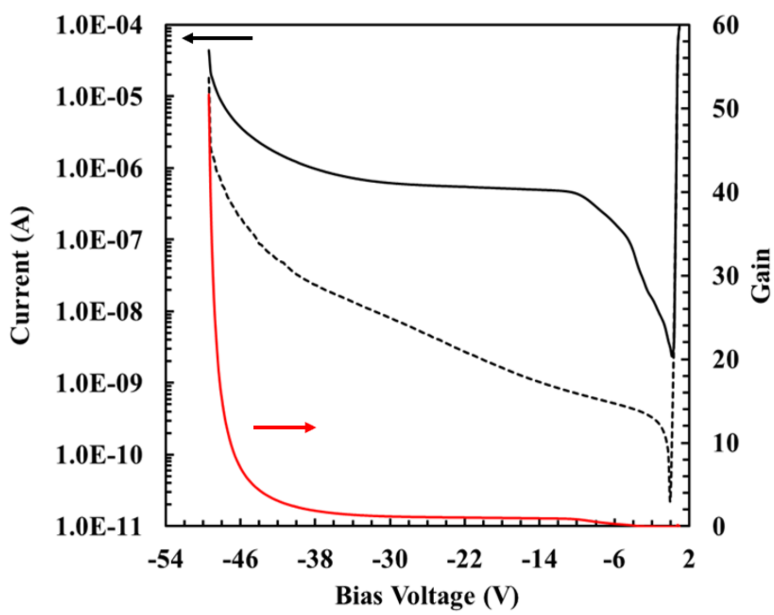

Figure 3-17. Current and gain versus voltage of an $Al_{0.7}InAsSb$ random-digital alloy APD.

The excess noise the random-digital alloy APD was measured with same method as the binary and ternary digital alloy APDs. The measured data are shown in Fig. 3-18, the $Al_{0.7}InAsSb$ random-digital alloy APD exhibits higher excess noise than the other two. The *k* is ~ 0.2. Without the periodic digital alloy structure, the $Al_{0.7}InAsSb$ APDs does not achieve the extremely low excess noise.

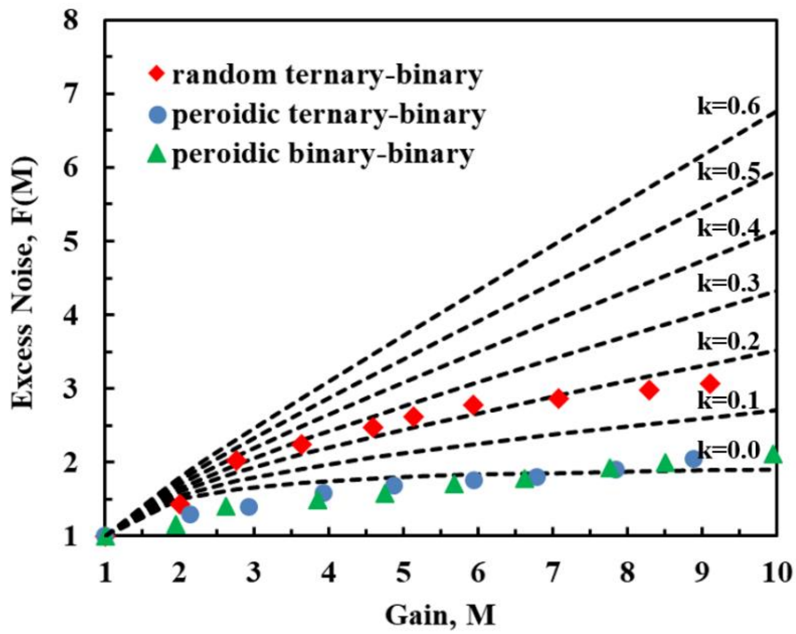

Figure 3-18. Comparison of excess noise of the $Al_{0.7}InAsSb$ random-digital alloy (◆), ternary digital alloy (●), and binary digital alloy (▲) APDs.

3.5 Conclusion

In conclusion, digital alloy $Al_{0.7}InAsSb$ APDs having two different periods, binary and ternary structures, have been studied. Both exhibit very low excess noise and high thermal stability. The excess noise performance at different temperatures exhibits an exponential relation with temperature. Moreover, the complex refractive indices and the absorption coefficients from 500 nm to 900 nm have been determined.

The impact ionization coefficients for these two types of $Al_{0.7}InAsSb$ APDs have also been measured by pure carrier injection and mixed injection methods, respectively. The results are consistent with each other, and it was found that the hole ionization coefficient exhibits significant reduction at lower temperature, while that of the electron is relatively independent of temperature.

Different from the binary and ternary digital alloy APDs, the $Al_{0.7}InAsSb$ random-digital alloy APD exhibits higher excess noise. The extremely low excess noise is not completely a result of high phonon scattering and large hole effective mass [23], but is also related to the periodicity of the digital alloy structures.

Chapter 4. $Al_{0.8}InAsSb$ digital alloy APDs

4.1 Device structure

The digital alloy AlInAsSb will transition from direct bandgap to indirect bandgap at the Al fraction of ~ 72% [37]. In Chapter 4, I report on the first $Al_{0.8}In_{0.2}As_{0.23}Sb_{0.77}$ p-i-n structure APD (written as $Al_{0.8}InAsSb$ in the following). The epitaxial layers were grown on n-type Te-doped GaSb (001) substrates by solid-source molecular beam epitaxy (MBE). The 10 monolayer (ML) period $Al_{0.8}InAsSb$ digital alloys consist of four binary alloys AlSb, AlAs, InSb, and InAs. The MBE shutter sequence was AlSb, AlAs, AlSb, InSb, InAs, Sb. A cross-sectional schematic of the $Al_{0.8}InAsSb$ p-i-n structure APD is shown in Fig. 4-1. The top three layers are p-type doped using Be, and the other layers are n-type doped with Te.

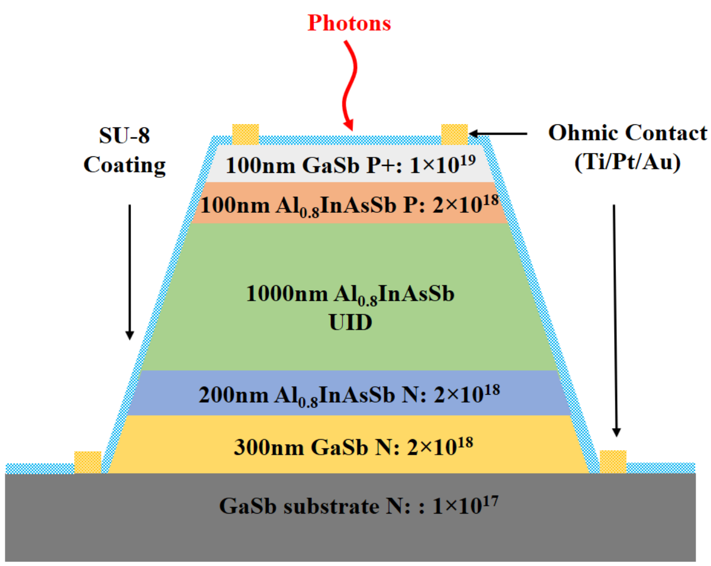

Figure 4-1. Schematic cross section of $Al_{0.8}InAsSb$ p-i-n APD.

The mesas were defined by standard photolithography with AZ5214 photoresist and formed by wet etching in a 5:1:5 solution of $HCl:H_2O_2:H_2O$. Ti/Pt/Au was deposited as the top and bottom contacts by electron-beam evaporation. After lift-off of the metals, SU-8 was spun on the sidewall as a surface passivation.

4.2 Experimental characteristics

All measurements were carried out at room temperature. Figure 4-2 shows the photocurrent, dark current, and gain versus bias voltage of a 100 μm-diameter $Al_{0.8}InAsSb$ p-i-n APD. The APD was illuminated with a 10 μW 850 nm laser, and the gain curve is plotted by choosing the unity gain point at -24.5 V. High gain of 489 was achieved at -32.5 V bias. There are three slopes in the photocurrent: the first gradual slope (from 0 to 11 V) may be caused by the heterojunction barrier [65], the second slope (from 11 to 24.5 V) is due to voltage-dependent carrier collection efficiency, and after 24.5 V the multiplication gain makes the third slope of the photocurrent steeper.

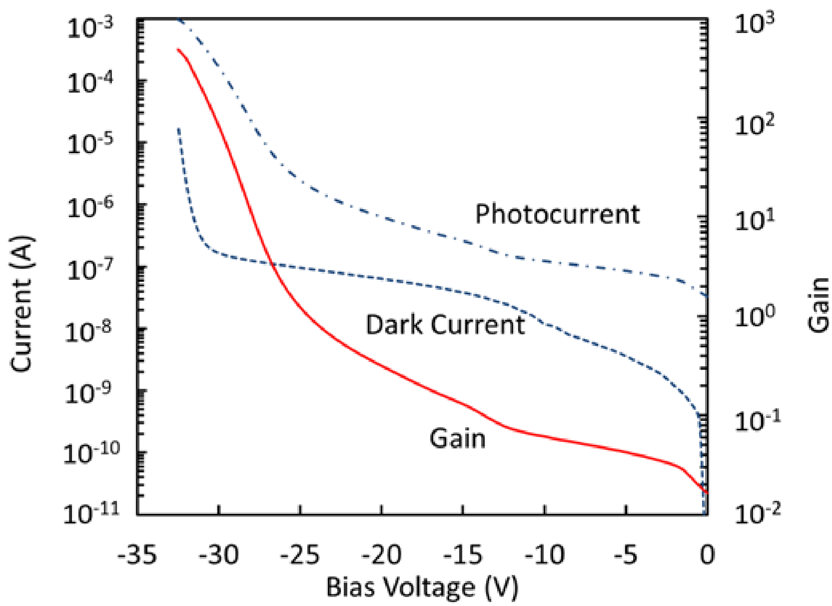

Figure 4-2. Photocurrent (solid line), dark current (dash dot line), and gain (dash line) versus bias voltage for a 100 μm-diameter $Al_{0.8}InAsSb$ p-i-n APD.

Since the photocurrent increases continuously with bias and does not exhibit a flat, voltage-independent region, the unity gain point is not obvious. The reason for this is voltage-dependent responsivity at lower bias. Owing to high background doping (~ 10^{17} cm^{-3}) in the 1000 nm-thick

$Al_{0.8}InAsSb$ p^- multiplication layer, shown in Fig. 4-3, the carrier collection efficiency improves with increasing bias as the depletion moves closer to the surface. This was confirmed by capacitance-voltage measurements, which were used to calculate the depletion width. Figure 4-4 shows the capacitance and depletion width versus voltage, where it is assumed that the dielectric constant of $Al_{0.8}InAsSb$ is approximately 14. Since the device was wet etched, its effective diameter was a little bit smaller than 100 µm. I used 98 µm to calculate the capacitance.

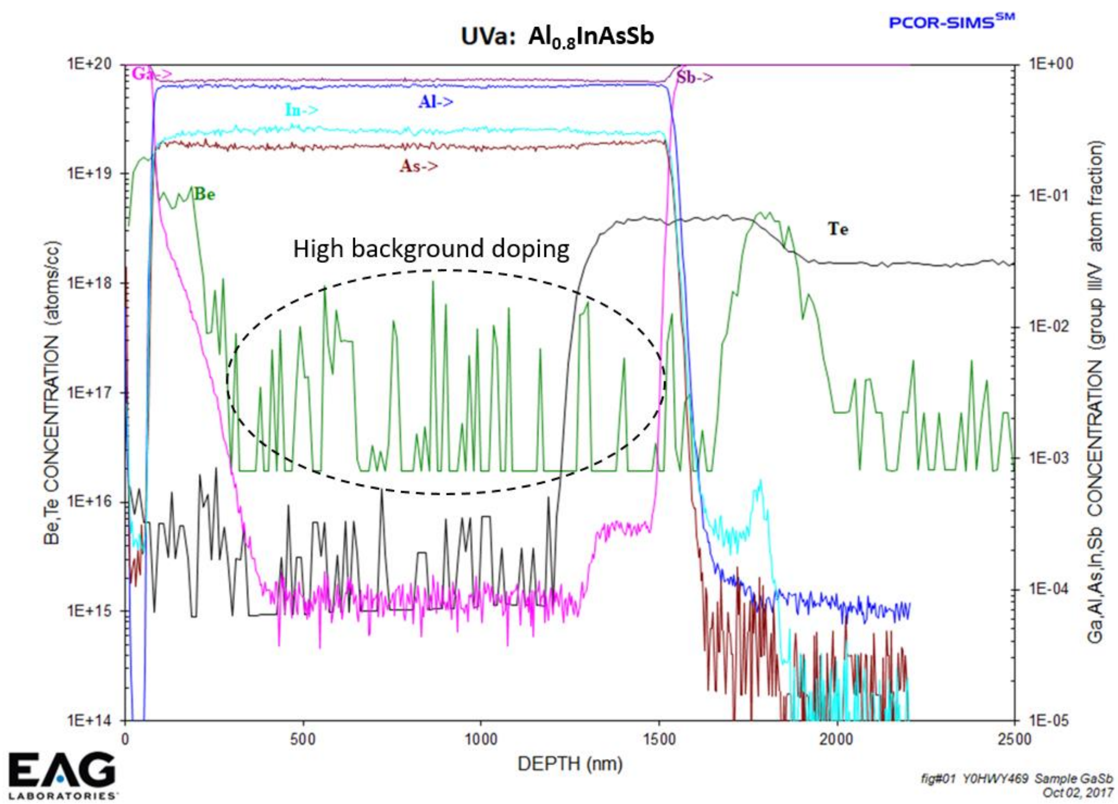

Figure 4-3. SIMS analysis of $Al_{0.8}InAsSb$ p-i-n APD.

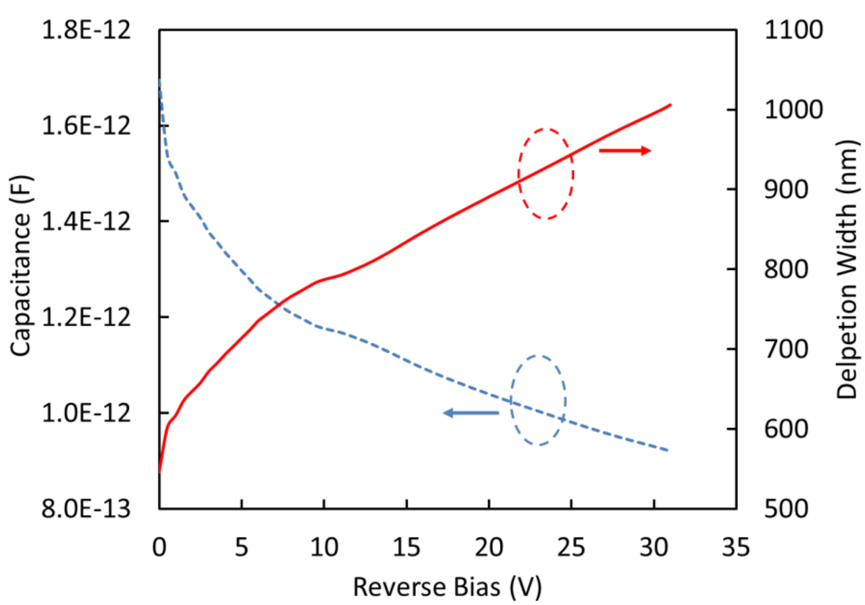

Figure 4-4. Capacitance and depletion width versus reverse bias of a 100 μm-diameter $Al_{0.8}InAsSb$ p-i-n APD.

In order to determine the gain curve in Fig. 4-2, I developed a model to fit the external quantum efficiency in order to find the unity gain point. Since the background doping in the multiplication layer is p-type, the edge of the depletion layer will move toward the surface with increasing reverse bias, which, in turn, will result in increased responsivity as more carriers are collected. This is illustrated in Fig. 4-5.

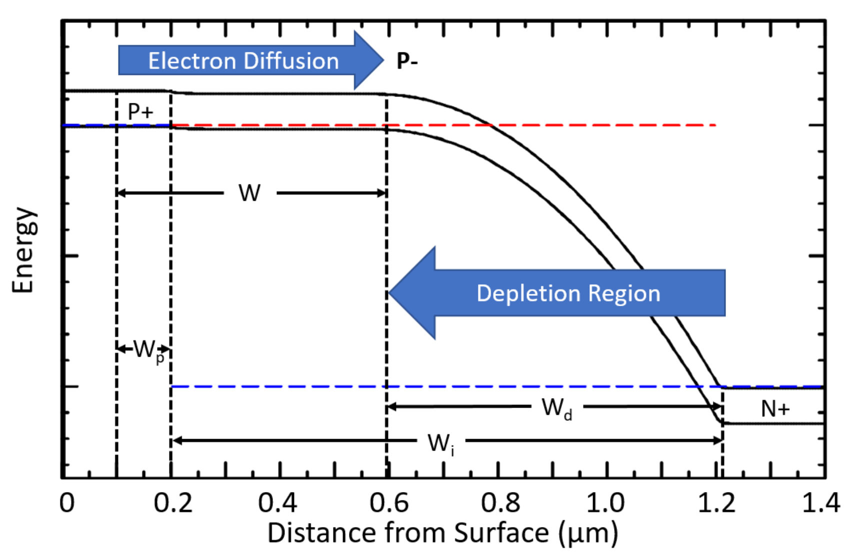

Figure 4-5. Illustration of mechanism for voltage-dependent responsivity.

The total current density of the device consists the drift current density that is generated in the depletion layer and the diffusion current density that is generated outside the depletion layer and collected by diffusion [32]. The current density can be expressed as:

$$J_{tot} = J_{dr} + J_{diff}\ , \tag{4.1}$$

$$J_{dr} = q\Phi_0[\exp(-\gamma W) - \exp(-\gamma W_p - \gamma W_i)], \tag{4.2}$$

$$J_{diff} = q\left[\frac{\Phi_0 \gamma L_n}{1-\gamma^2 L_n^2}\exp\left(-\frac{W}{L_n}\right) - \frac{\Phi_0 \gamma^2 L_n^2}{1-\gamma^2 L_n^2}\exp(-\gamma W)\right], \tag{4.3}$$

where the $\emptyset_0$ is the incident photon flux per unit area, γ is absorption coefficient and L_n is the electron diffusion length, The distance from the surface to the edge of the depletion region, W, can be expressed as $W = W_p + W_i - W_D$, where W_p *is* the thickness of the $Al_{0.8}InAsSb$ p-type layer, W_i is the thickness of the unintentionally-doped multiplication layer, and W_D is the depletion region thickness, respectively.

The total current density can be obtained by substituting Eqs. 4.2 and 4.3 into Eq. 4.1. The external quantum efficiency can then be calculated using the following equation:

$$\eta_{QE} = (1-R)(1-0.22)\left[\left(1-\frac{\gamma^2 L_n^2}{1-\gamma^2 L_n^2}\right)\exp(-\gamma W) + \frac{\gamma L_n}{1-\gamma^2 L_n^2}\exp\left(-\frac{W}{L_n}\right) - \exp(-\gamma W_p - \gamma W_i)\right], \tag{4.4}$$

where R is the reflection coefficient of the top surface, ~ 30%; and the fraction of 850 nm laser absorbed in the top GaSb layer is ~ 0.22 [66]. Figure 4.6 shows the measured external quantum efficiency of a 200 μm-diameter $Al_{0.8}InAsSb$ APD versus reverse bias from -1 V to -26 V in 1 V steps. Using Eq. 4.4 the efficiency at a specific wavelength can be fit with two parameters, γ and L_n.

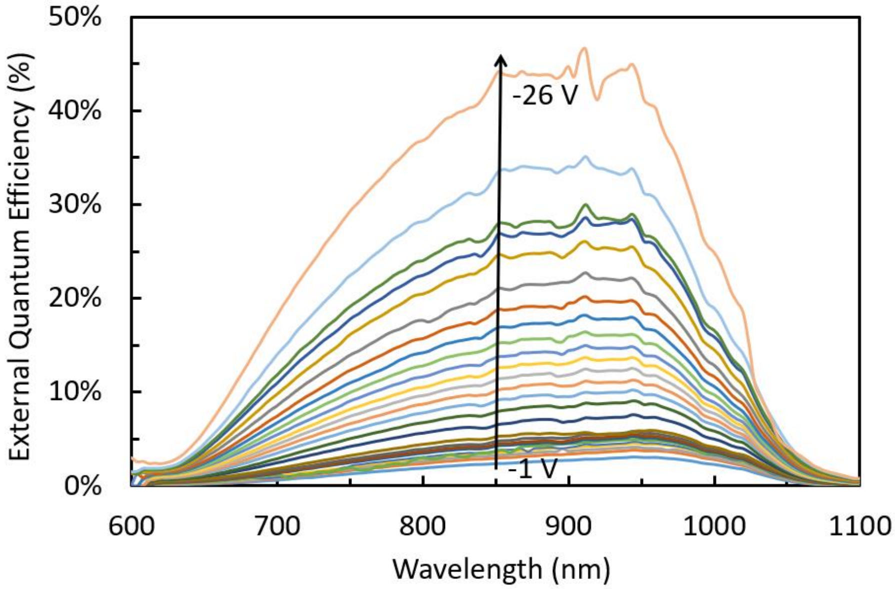

Figure 4-6. External quantum efficiency of a 200 μm-diameter $Al_{0.8}InAsSb$ p-i-n APD.

Figure 4-7 compares the measured and calculated external quantum efficiency at 850 nm for $\gamma = 5.4 \times 10^4\ cm^{-1}$, $L_n = 170\ nm$. Using two-parameter curve fitting, good agreement is achieved between the experimental and calculated quantum efficiency up to -24.5 V, which is marked by the dash line. At higher voltage, impact ionization causes the curves to diverge. Therefore, I have used -24.5 V as the unity gain point. After this bias voltage, the multiplication gain dominates the increment of the photocurrent, and the change caused by the extended depletion region can be ignored. At the unity gain point, the external quantum efficiency is approximately 30% at 850 nm wavelength. The external quantum efficiency is consistent with the responsivity from Fig. 4-2, which is approximately 0.2 A/W.

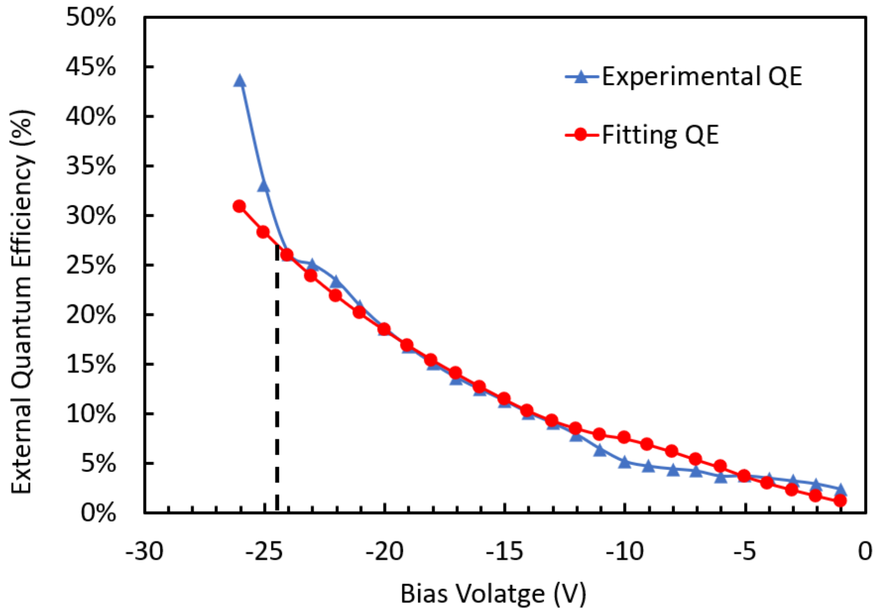

Figure 4-7. Two-parameter fit of the external quantum efficiency of a 200 µm-diameter $Al_{0.8}InAsSb$ p-i-n APD at 850 nm wavelength.

The unity gain point can be confirmed and the k value can be determined using a modification of the noise technique described in [67]. The noise power at any relative gain M_n can be expressed as:

$$S_n = 2qI_u\left(M_n M_{pt}\right)^2 F\left(M_n M_{pt}\right) R(\omega), \tag{4.5}$$

where I_u is the unity-gain photocurrent, $F(M)$ is the excess noise factor, $R(\omega)$ is the frequency dependent impedance, M_{pt} corresponds to the gain at the nominal unity-gain point voltage and M_n is the measured gain relative to M_{pt}. We note that M_{pt} may not be exactly unity and its actual value is determined by this procedure. The noise is measured for a series of M_n values and the following ratio is computed:

$$\frac{S_n}{S_{pt}} = M_n^2 \frac{F\left(M_n M_{pt}\right)}{F\left(M_{pt}\right)}. \tag{4.6}$$

The values of S_n and S_{pt} are measured, and the excess noise factors are calculated using the local field model: $F(M) = kM + (1-k)(2-1/M)$. For these measurements based on the discussion above, -24.5 V was selected as the M_{pt} reference point. Figure 4-8(a) shows the experimental values of S_n/S_{pt} and a fit using M_{pt} and k as adjustable parameters. The best fit was obtained for M_{pt} =1.0, which confirms that -24.5 V is the unity gain point, and $k = 0.05$.

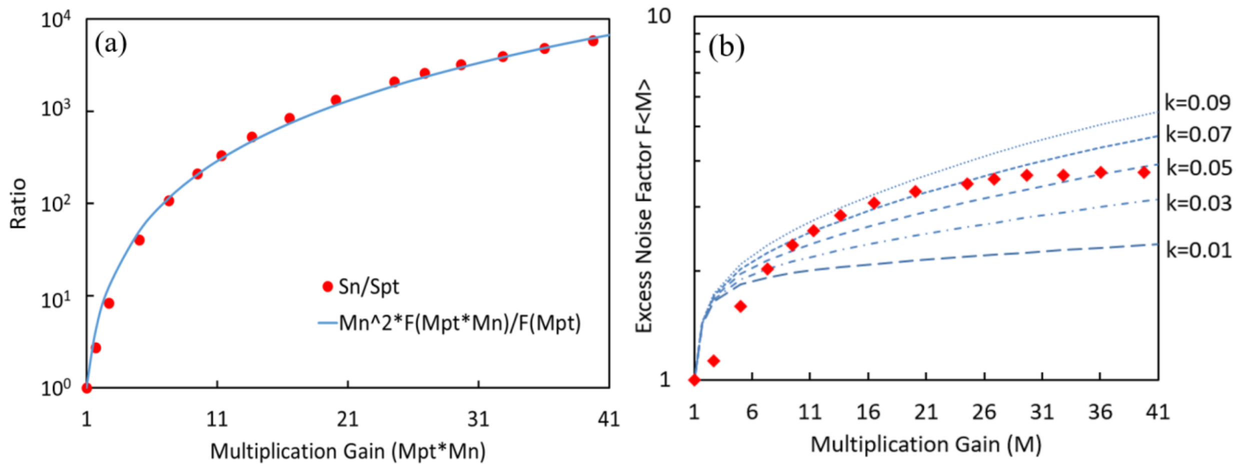

Figure 4-8. (a) Two-parameters fitting curve of the gain versus ratio of excess noise, and (b) excess noise factor versus gain of 100 µm-diameter $Al_{0.8}InAsSb$ p-i-n APD.

Using -24.5 V as the unity-gain reference, the excess noise was measured with an HP 8970 noise figure meter and a 543-nm He-Ne CW laser. The k value was obtained using the local-field model to plot and the gain values obtained as described above. The data points in Fig. 4-8(b) show the excess noise factor versus gain. The value of k is between 0.05 and 0.07, which is consistent with the fitting k value from the Fig. 4-8(a).

4.3 Conclusion

In this chapter, I report the first $Al_{0.8}InAsSb$ p-i-n structure APDs, fabricated using the digital alloy growth technique. These APDs exhibit gain as high as 489, low excess noise corresponding to $k = 0.05\sim0.07$, and external quantum efficiency of 30% at 850 nm wavelength. Furthermore, a new method is proposed to determine the unity gain point for the APDs with bias-dependent responsivity, which can be used in many APDs, such as undeleted APDs and SACM APDs.

Chapter 5. InAlAs digital alloy APDs

5.1 Comparison of excess noise

As shown in Chapters 3 and 4, the digital alloy AlInAsSb APDs exhibit excess noise as low as Si. In order to determine whether the low excess noise is a characteristic of digital alloys or we just got lucky with the AlInAsSb material system, digital alloy $In_{0.52}Al_{0.48}As$ (InAlAs in the following) and $Al_{0.74}Ga_{0.26}As$ (AlGaAs in the following) were grown by MBE, and their characteristics are compared with those of random alloy InAlAs and AlGaAs. A schematic cross section of the InAlAs APDs is shown in Fig. 5-1(a). The epitaxial layers were grown on n-type InP (001). A period of 8 monolayers (ML) or 2.44 nm of the binary alloys InAs and AlAs was used to fabricate the InAlAs digital alloy. The AlGaAs digital alloy APD was grown on n-type GaAs (001) substrate. The period of the binary alloys AlAs and GaAs for the $Al_{0.74}Ga_{0.26}As$ layers was 8.1 ML or 2.47 nm. A cross-section of the AlGaAs APD is shown in Fig. 5-1(b).

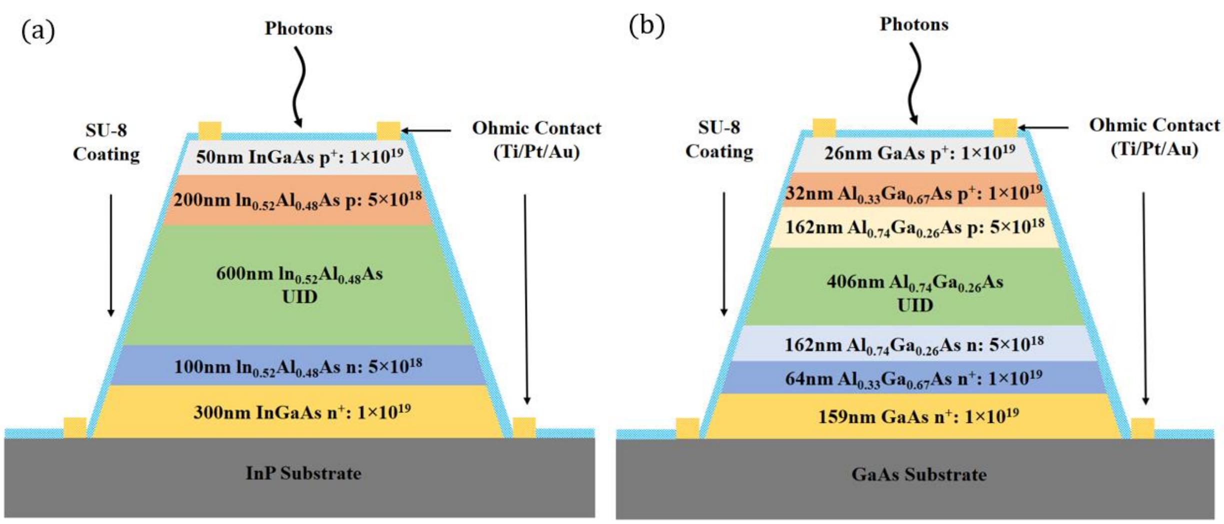

Figure 5-1. Schematic cross sections of (a) InAlAs APDs and (b) AlGaAs APDs.

Excess noise measurements were carried out at room temperature using a 543 nm He-Ne laser to ensure pure electron injection. Figure 5-2(a) shows the excess noise factor, $F(M)$, of the InAlAs random and digital alloy APDs. The excess noise of the random alloy is characterized by a k value of 0.2, which is consistent with previous reports [48, 67]. The k value for the digital alloy, on the other hand, is ~ 0.09. The excess noise for the random alloy AlGaAs with Al concentration from 20% to 90% [69] and the digital alloy are shown in Fig. 5-2(b); the excess noise of $Al_xGa_{1-x}As$ decreases with increasing Al concentration. We note that the noise of the digital alloy with Al concentration ~ 74%, ■, lies between the 60%, □, and 80%, ○, random alloys. We conclude that the digital alloy does not suppress the noise in AlGaAs.

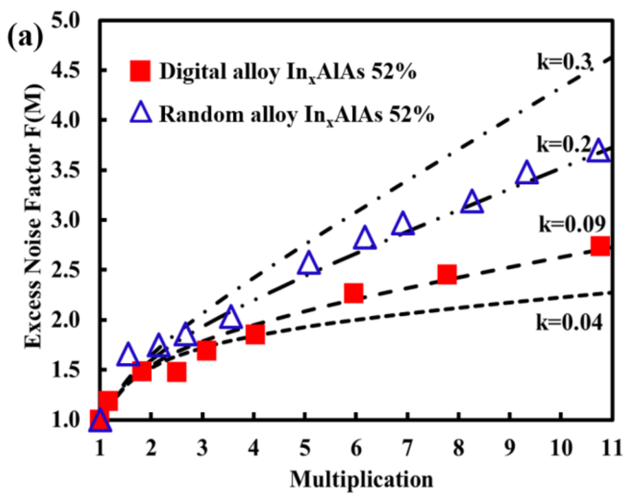

Figure 5-2. Excess noise factor, F(M), of (a) InAlAs digital and random alloy APDs, and (b) AlGaAs digital alloy APDs.

5.2 Temperature dependent characteristics

5.2.1 Excess noise variation

By using an environment-dependent tight binding model [27, 69], the band structures of digital and random alloys InAlAs were simulated by my colleague Dr. Jiyuan Zheng. Figure 5-3(a) shows how the supercells were chosen for zinc blende InAlAs. The supercell of the 8 ML digital alloy consists of 8 As, 4 In, and 4 Al atoms. Eight atoms comprise the random alloy supercell, 4 As, 2 In, and 2 Al atoms. In both structures the In and Al compositions are 50%. Figure 5-3(b) illustrated the reciprocal space positions chosen to calculate band structures, where Γ is the center of the first Brillouin zone, A and D are the boundaries of the first Brillouin zone along the growth direction and an in-plane direction, respectively; B is a random point between Γ and D; and C and E are the boundaries of the first Brillouin zone of B and D points along the growth direction.

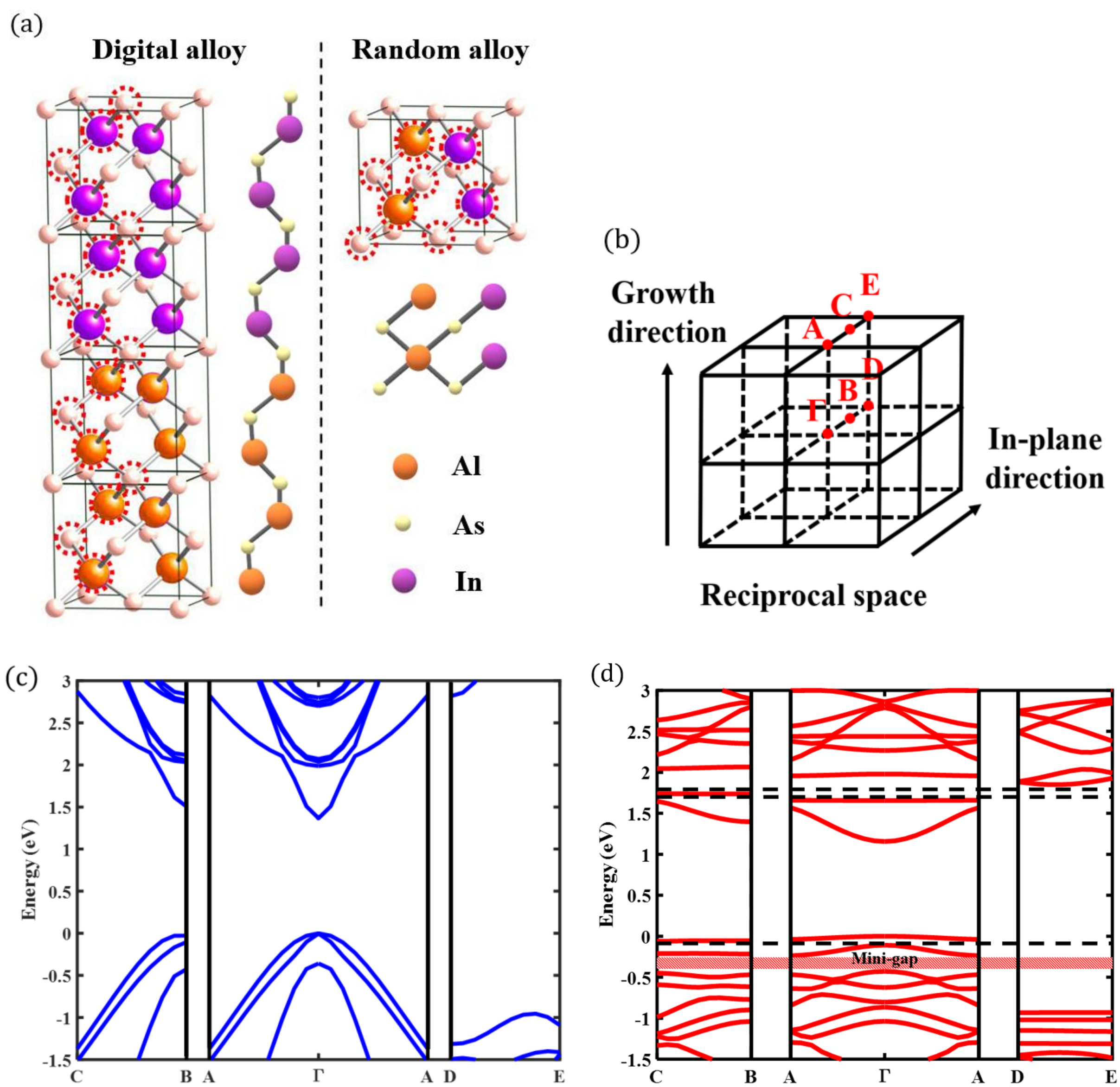

Figure 5-3. (a) InAlAs digital and random alloy supercells, (b) positions in reciprocal space, (c) band structures of InAlAs random alloy at different positions, and (d) band structures of InAlAs digital alloy at different positions. The mini-gap in the valance band is marked.

It can be seen from Fig. 5-3(c) and (d) that there are significant differences in the band structures of the InAlAs random and digital alloys. At the first Brillouin zone boundary of the InAlAs digital alloy, there is a mini-gap between the second and third valance bands. While, there are no gaps in the InAlAs random alloy. In the conduction band of the InAlAs digital alloy, the electrons can gain energy through in-plane scattering, however, there are not equivalent paths for holes in the valence bands. Therefore, the valence band mini-gap can impede holes from achieving sufficient energy to initiate impact ionization, particularly at low temperature. As the temperature decreases, the probability of phonon scattering to a higher-order valence band is reduced, which will suppress the hole ionization coefficient, β. It follows that the *k* value and thus the excess noise factor of InAlAs digital alloys should decrease with decreasing temperature.

In order to verify this hypothesis, I measured the excess noise from 203 K (-70 °C) to 323 K (50 °C). In Fig. 5-4(a), the excess noise factor of the InAlAs random alloy is plotted at different temperatures. As shown in Fig. 5-4(b) the *k* value is relatively independent of temperature and in the range 0.18 to 0.25, which is consistent with previous reports [68]. A fit to the temperature variation yields:

$$k = 0.2 + 6 \times 10^{-5} \times T \pm 0.04 , \tag{5.1}$$

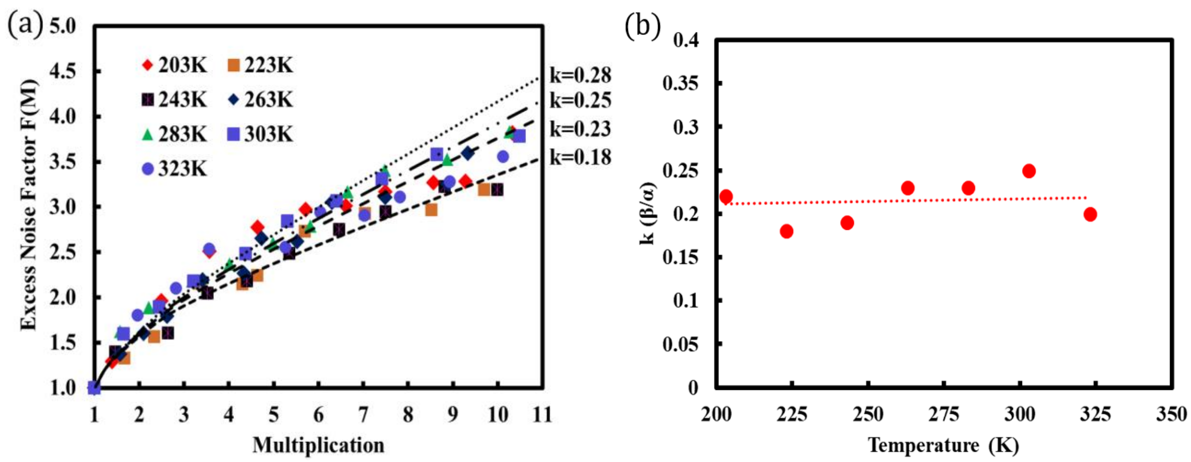

Figure 5-4. Temperature dependence of (a) excess noise factor and (b) ionization coefficient ratio k for InAlAs random alloy APD.

In contrast with the random alloy, the excess noise of the InAlAs digital alloy APDs exhibits strong temperature dependence as shown in Fig. 5-5(a). This is reflected by the variation of the k value with temperature (Fig. 5-5 (b)); the k value increases exponentially with temperature, and can be expressed as:

$$k = 0.0012 \times \exp(0.0147 \times T) . \tag{5.2}$$

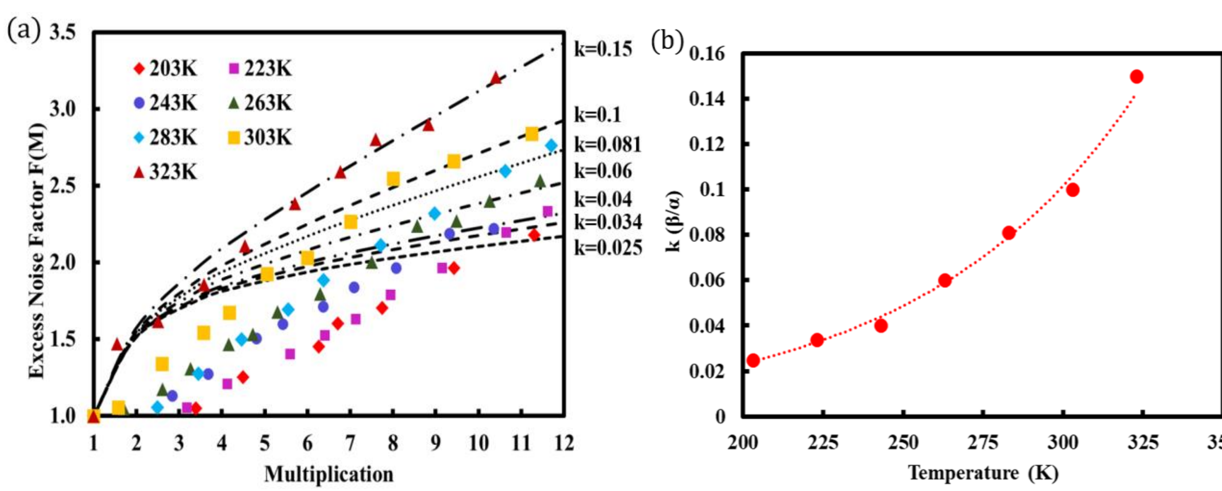

Figure 5-5. Temperature dependence of (a) excess noise factor and (b) ionization coefficient ratio k for InAlAs digital alloy APD.

The band structures of AlGaAs random and digital alloys are shown in Fig. 5-6(a) and 5-6(b), respectively. The band structures are similar. Therefore, the AlGaAs random and digital alloys are expected to have similar excess noise performance. For the digital alloy, there are no mini-gaps; the highest energy of the third valance band is the same as the lowest energy of the second valance band. This enables strong intraband scattering, which helps holes to achieve higher energy. Thus, the impact ionization probability of holes in AlGaAs digital alloy material is not projected to be strongly affected by temperature.

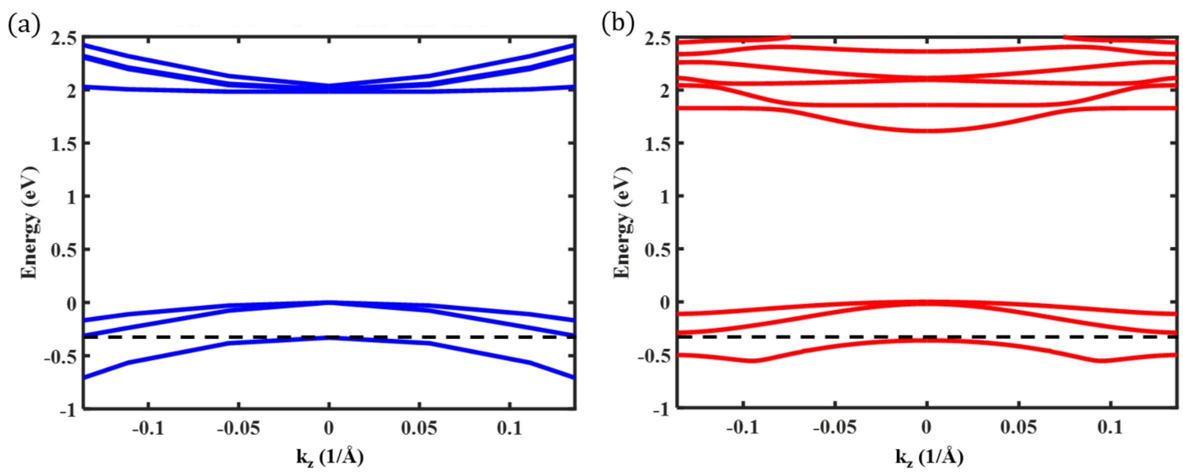

Figure 5-6. Band structures of (a) AlGaAs random alloy and (b) AlGaAs digital alloy.

I measured the excess noise of the AlGaAs APDs from 203 K (-70 °C) to 303 K (30 °C). The excess noise of the digital alloy is plotted at different temperatures in Fig. 5-7(a). The results are similar to those for the InAlAs random alloy APD, i.e., the variation of excess noise with temperature is small. This is consistent with reported measurements on $Al_xGa_{1-x}As$ random alloy APDs [70, 71]. Figure 5-7(b) shows that as the temperature changes, k remains in the range 0.1 to 0.15, and obeys the relation:

$$k = 0.11 + 5 \times 10^{-5} \times T \pm 0.04\,. \tag{5.3}$$

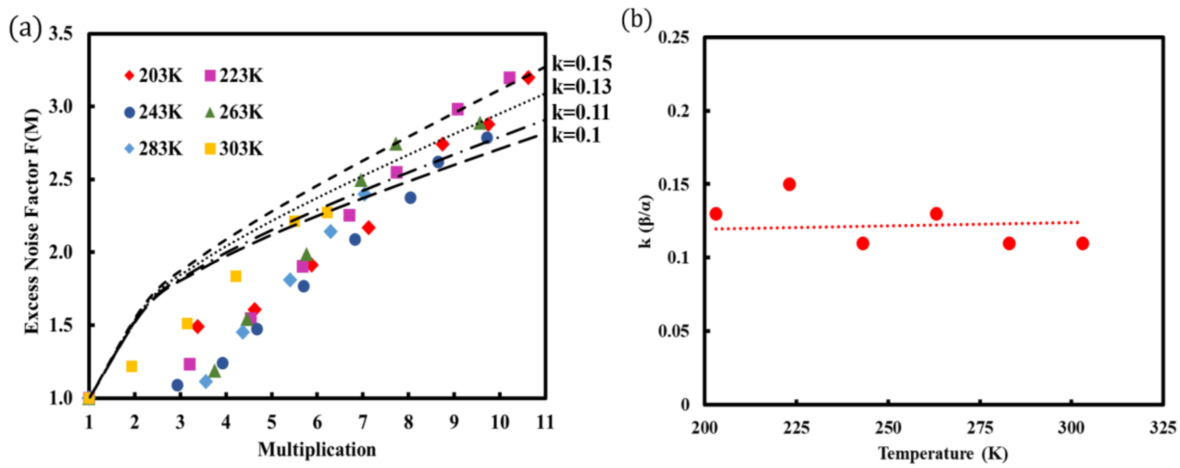

Figure 5-7. Temperature dependence of (a) excess noise factor and (b) ionization coefficient ratio k for AlGaAs digital alloy p-i-n APD.

5.2.2 Ionization coefficients variation

The approximate ionization coefficients can be determined from the pure electron injection gain versus voltage at different temperatures by using Eqs. 3.13 and 3.14. The relation between the electric field and gain is obtained from photocurrent versus bias measurements. Figures 5-8(a), 5-8(b), and 5-8(c) show the ionization coefficients versus the inverse electric field, 1/E, at different temperature for InAlAs random, InAlAs digital, and AlGaAs digital alloys, respectively.

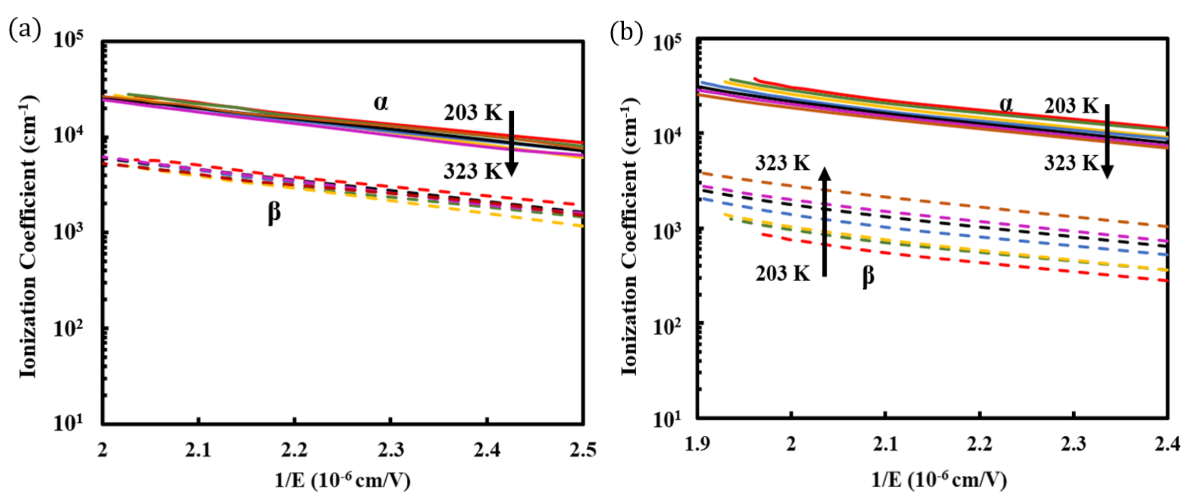

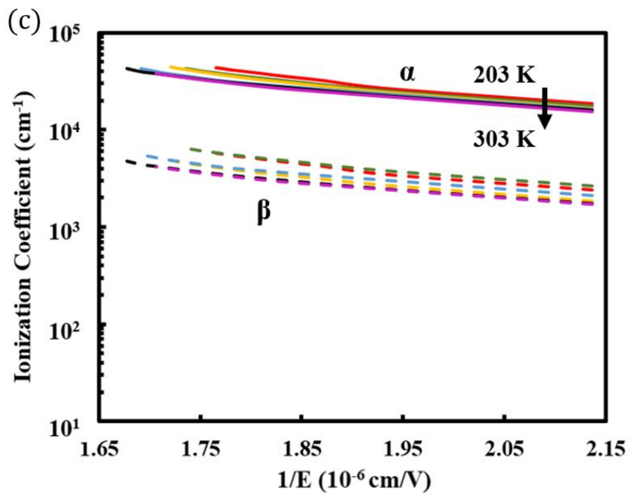

Figure 5-8. Ionization coefficients of (a) InAlAs random alloy, (b) InAlAs digital alloy, and (c) AlGaAs digital alloy at different temperatures.

In all three plots, the electron ionization coefficients exhibit modest decreases with temperature owing to increased phonon scattering. However, the most significant change is that of the hole ionization coefficient in the InAlAs digital alloy, which decreases with decreasing temperature. This is due, primarily to the presence of the mini-gap in the valence band, and explains the reduction in *k* and excess noise with decreasing temperature. By fitting the experimental ionization coefficients of InAlAs digital alloy, the relationship between the electric field, *E*, temperature, *T,* and the ionization coefficients can be expressed as:

$$\alpha\left(T,E\right)=2.2\times10^{7}\times\exp\left[-0.004\times T-\left(\frac{3.5\times10^{6}}{E}\right)^{0.9}\right], \tag{5.4}$$

$$\beta\left(T,E\right)=2.5\times10^{4}\times\exp\left[0.011\times T-\left(\frac{3.5\times10^{6}}{E}\right)^{0.9}\right]. \tag{5.5}$$

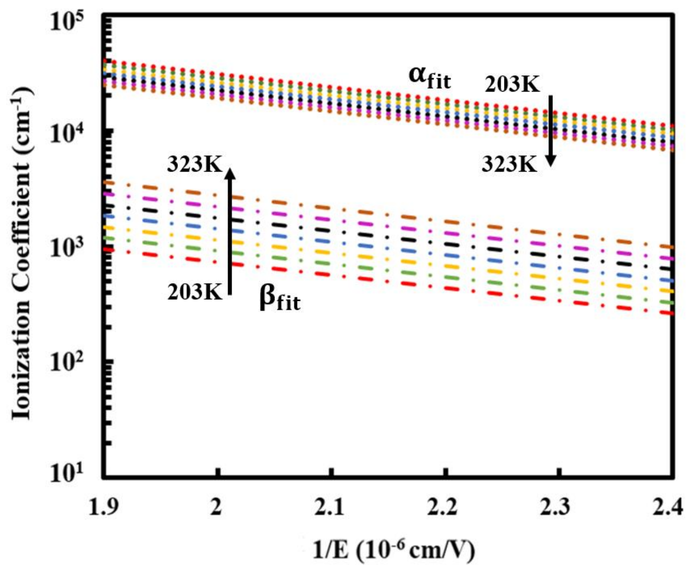

Figure 5-9. The fitting ionization coefficients of InAlAs digital alloy.

In summary, the ionization characteristics of InAlAs random alloy, InAlAs digital alloy, AlGaAs digital alloy have been investigated at different temperatures. The k values of the InAlAs digital alloy APDs decrease exponentially with decreasing temperature, owing to the suppression of hole ionization, which, in turn is due to a mini-gap in the valence band. The experimental results are consistent with the simulated band structures, and provide insight into the low excess noise exhibited by the InAlAs digital alloy and the absence of noise suppression in the AlGaAs digital alloy.

5.2.3 Breakdown voltage variation

In Chapter 3 it was shown that the digital alloy $Al_xInAsSb$ APDs exhibit much smaller $\Delta V_{bd}/\Delta T$ than other semiconductor materials. However, we do not know if this is a characteristic of digital alloys or the AlInAsSb material itself. Since the InAlAs digital alloy also exhibits noise suppression compared to the InAlAs random alloy, the breakdown voltage variation with temperature has been explored. I measured the gain curves of the 8ML InAlAs digital alloy APD from 223 K (-50 ℃) to 363 K (90 ℃) with a step of 20 K. These are plotted in Fig. 5-10(a). By fitting 1/gain versus bias voltage curves, the breakdown voltages can be estimated as the bias where 1/gain equals 0, i.e., infinite gain. Figure 5-10(b) illustrates the temperature dependent breakdown voltage, and the slope is the breakdown voltage temperature coefficient, $\Delta V_{bd}/\Delta T$, which is ~ 10 mV/K. The $\Delta V_{bd}/\Delta T$ values of different multiplication thickness are shown in Fig. 5-10(c). Compared with the random alloy InAlAs APDs [45], $\Delta V_{bd}/\Delta T$ of the 8ML digital alloy InAlAs APD 600 nm thick multiplication region falls on the same line as the random alloy.

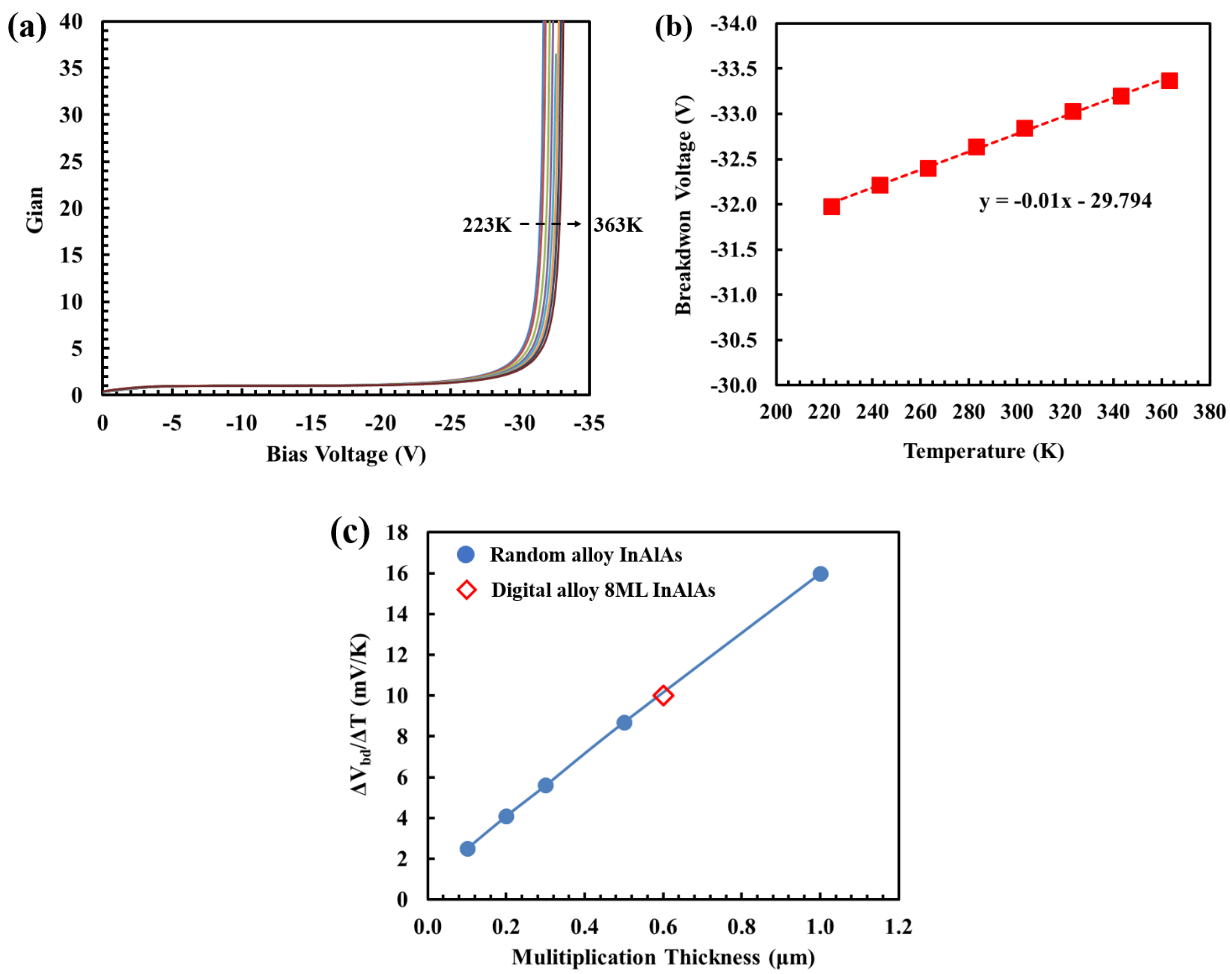

Figure 5-10. Temperature dependent (a) gain curves, (b) breakdown voltages, and (c) breakdown voltage temperature coefficient of InAlAs 8ML digital alloy and different thickness of the random alloy [45].

5.3 Stark-localization limited Franz-Keldysh effect

The influence of an electric field on the optical absorption edge in semiconductors has been studied both theoretically and experimentally [72-74]. For random alloys, which are classified as bulk semiconductors, the conduction and valence band widths $\Delta E_{c,v}$ are of the order of a few eV [76]. An applied electric field gives rise to the Franz-Keldysh effect; the optical absorption coefficient exhibits an exponential tail below the bandgap [75-77]. Typically, for multi-quantum-well (MQW) semiconductors, the wells are relatively independent and the energy levels are discrete, i.e., $\Delta E_{c,v} \sim 0$. An applied electric field leads to the quantum-confined Stark effect (QCSE), which is observable as a red shift in the optical absorption edge. However, for digital alloys, the extremely thin periods, only a few MLs, allow wave functions to couple through several wells by the resonant tunneling effect [79]. This results in a structure in which there is a quasicontinuum of energy levels, i.e., minibands with finite ΔE_c, as shown in Fig. 5-11(a). The widths of the conduction and valence minibands are typically tens of meV, an order of magnitude less than that of random alloys. Therefore, a moderate electric field, *F*, along the digital alloy growth direction can achieve $eFd \sim \Delta E_{c,v}$, where d is the digital alloy period thickness. In this case, the relative energy misalignment reduces the tunneling effect and splits the quasicontinuum of states into discrete energy levels [80], as illustrated in Fig. 5-11(b). In a random alloy it is difficult to achieve this condition before avalanche breakdown because $\Delta E_{c,v}$ ~ few eV and the lattice constant is a few Å ($F = \Delta E_{c,v}/ed \sim 10^7 V/cm$).

The threshold energy for optical absorption is determined by the energy difference from the top of the valence band state to bottom of conduction band. For digital alloys, the electric-field-induced Stark localization of carriers to isolated quantum wells causes the energy difference to be reduced by $\frac{1}{2}(\Delta E_c + \Delta E_v)$. Different from the random alloy and MQWs, the optical absorption edge of a digital alloy semiconductor is expected to exhibit a blue shift with applied electric field [81].

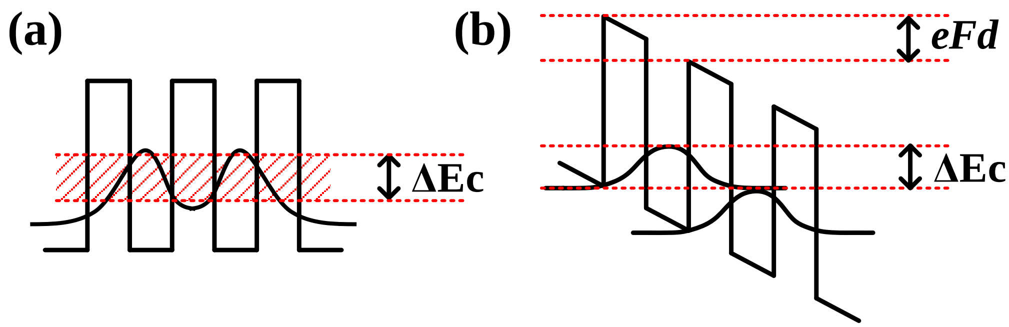

Figure 5-11. The overlap of wave functions throughout digital alloys with (a) small, and (b) $F \sim \Delta E_c / ed$ electric field.

In this project I studied the electric-field-induced Stark localization of 8ML InAlAs digital alloys. The digital alloy period consists of 4 ML InAs and 4 ML AlAs; the total thickness of a period is ~ 24 Å. The absorption coefficients of the digital alloy and the random alloy have been determined by measuring the external quantum efficiency of p-i-n photodiodes under different bias voltages. Both types of photodiodes have 600 nm depletion width; a schematic cross section is shown in Figs. 5-1(a) and 5-1(b). The three InAlAs layers are all either digital alloy or random alloy. In order to distinguish the Stark localization in the digital alloy from the Franz-Keldysh effect in the InAlAs random alloy, their absorption characteristics are compared as functions of the electric field. The external quantum efficiency was measured using a SPEX 1681 spectrometer with 1 nm wavelength resolution. The measured quantum efficiencies of the digital and random alloys for reverse voltages from 0 V to 12 V are shown in Figs. 5-12(a) and 5-12(b), respectively. Similar to a GaAs- $Ga_{0.7}Al_{0.3}As$ superlattice with a well width of 50 Å and a barrier width of 50 Å, which is shown in Fig. 5-12(c) [81], the quantum efficiency of the InAs-AlAs digital alloy, increases from 0 V to 4 V and saturates at higher voltages. Whereas, the quantum efficiency of the InAlAs random alloy for photon energy > 1.5 eV is almost independent of bias voltage.

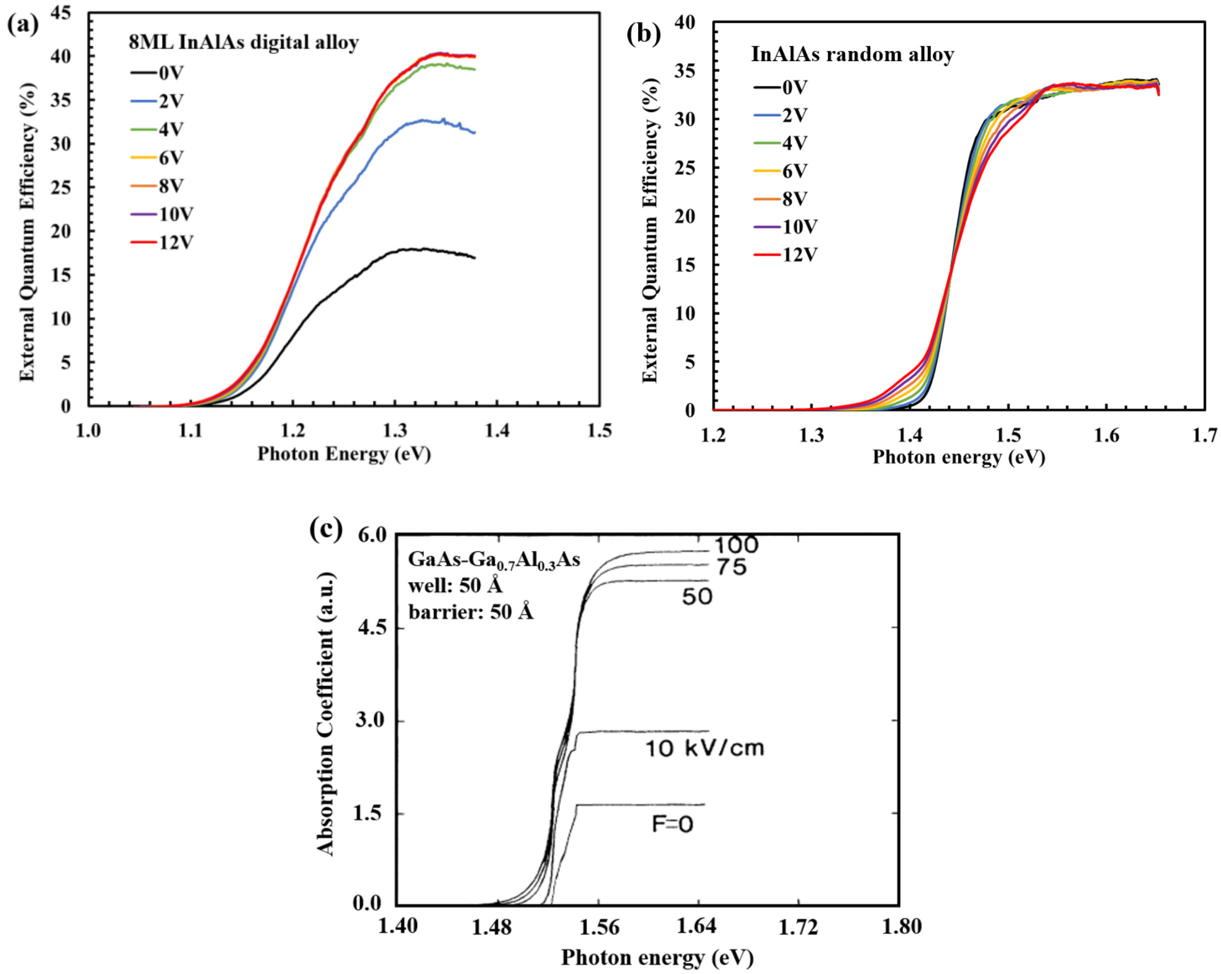

Figure 5-12. The external quantum efficiency (EQE) of (a) 8ML InAs-AlAs with digital alloy a well width of 12 Å and a barrier width of 12 Å and (b) InAlAs random alloy. (c) The absorption coefficient of a GaAs-$Ga_{0.7}Al_{0.3}As$ superlattice with a well width of 50 Å and a barrier width of 50 Å [81].

This electric field dependence of the quantum efficiency for the digital alloy can be explained by Fig. 5-13. For simplicity, we assume there is only one miniband in each digital alloy potential [82]. At 0 V, the wave functions extend throughout the digital alloys, as illustrated in Fig. 5-13(a). The interband transitions are delocalized. At intermediate electric field, in this case 2 V to 4V, the digital alloy energy states in the valence band still exhibit some delocalization. The eigenfunction of each quantum well is a Bessel function [76], as shown in Fig. 5-13(b). Additional increase in the electric field will restrict the eigenfunction further in the quantum well, and after Fourier transform there are more valance band energy states in the q space, where q is the wave vector in the digital alloy growth direction [81], which leads to a higher quantum efficiency. At high electric field, $F > \Delta E_{v,1}/ed$, the tunneling effect in the valence band is quenched. The valence band eigenfunctions are completely localized in the InAs quantum wells, as Fig. 5-13(c) shows, and the energy states in the q space no longer increase. Therefore, the quantum efficiencies saturate.

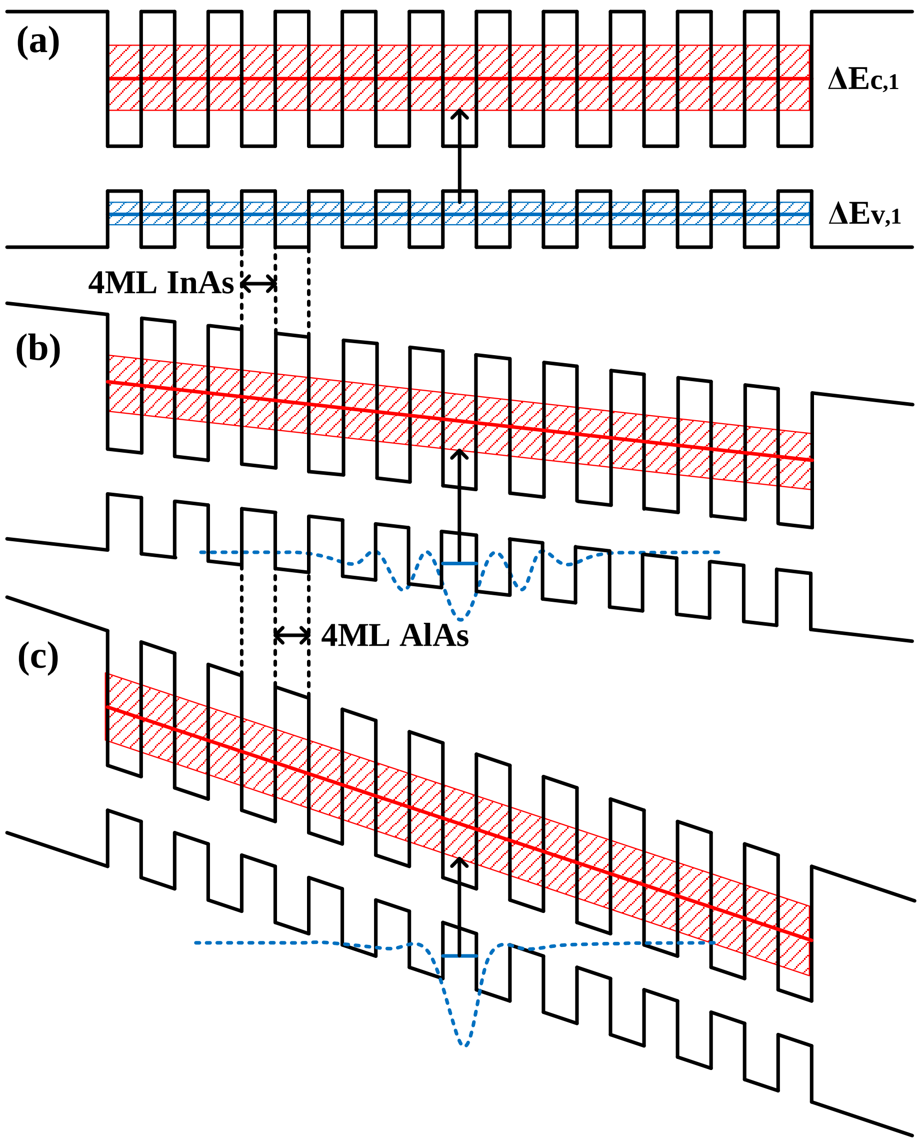

Figure 5-13. The conduction band and valence band potential profiles for InAs-AlAs digital alloys under (a) small, (b) moderate and (c) high electric field.

My colleague Dr. Jiyuan Zheng has calculated the density of states for the InAs-AlAs digital alloy using an environment-dependent tight binding model [70]. Figure 5-14 shows the band gap $E_g \sim 1.13\ eV$, the first miniband in the conduction band $\Delta E_{c,1} \sim 400\ meV$, and the first miniband in the valence band $\Delta E_{v,1} \sim 46\ meV$. The order of magnitude difference between ΔE_c and ΔE_v is caused by the higher effective mass in the valence band, $m_v^* \sim 0.75 m_0 > m_c^* \sim 0.09 m_0$. Therefore, for the InAs-AlAs digital alloy, only the energy states in the valence band exhibit localization. Based on this calculation, the effective blue shift is expected to be $\sim \frac{1}{2}\Delta E_{v,1}$.

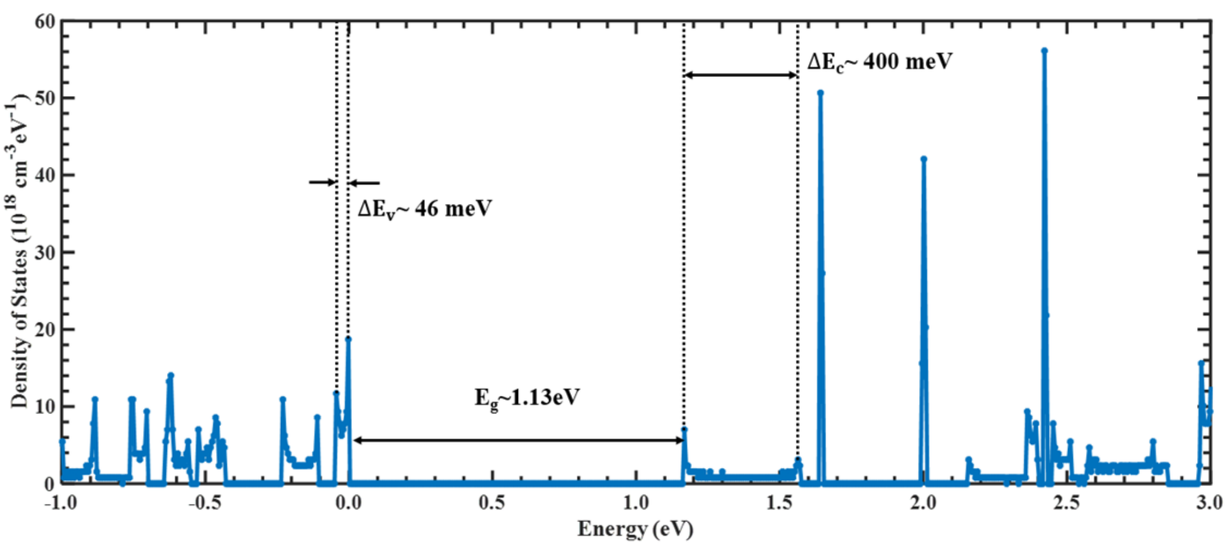

Figure 5-14. The density of states for InAs-AlAs digital alloy.

In order to verify the blue shift prediction for the digital alloy, the measured external quantum efficiencies are plotted with log-scale in Fig. 5-15. The absorption edge of the InAs-AlAs digital alloy changes ~ 15 nm from 0 V to 12 V, while that of the InAlAs random alloy is ~ 52 nm. The red shift in the random alloy is due to the well-known Franz-Keldysh effect. The energy band profile tilts along the direction of the electric field, and a photon with energy slightly below the bandgap can be absorbed by photon-assisted interband tunneling. The absorption coefficient exhibits an exponential tail below the bandgap, $\alpha(\hbar\omega) \propto \sqrt{\hbar\theta_F}[-\eta Ai^2(\eta) + Ai'^2(\eta)]$, where

$\hbar\theta_F = (\hbar^2 e^2 F^2/2m_r^*)^{1/3}$, m_r^* is the reduced mass, $\eta = (E_g - \hbar\omega)/\ \hbar\theta_F$, $Ai(\eta)$ is the Airy function and $Ai'(\eta)$ is the divative of $Ai(\eta)$ with respect to η [83]. The Franz-Keldysh effect in the random alloy has ~76 meV red shift from 0 V to 12 V. However, since m_r^* of the InAs-AlAs digital alloy (~ $0.08m_0$) is larger than that of the InAlAs random alloy (~ $0.06m_0$), the red shift of the digital alloy caused by the Franz-Keldysh effect should be smaller, ~ 40 meV. The measured red shift of the digital alloy is only ~ 14 meV. Although, the cut-off wavelength still extends to longer wavelengths with increasing field, the absorption edge is effectively blue shifted. At zero electric field, the InAs-AlAs digital alloy bandgap energy corresponds to the difference between the bottom of the conduction miniband and the top of the valence miniband, ~ 1.13 eV, and at high bias voltage, this energy gap is reduced the half of the valence miniband ~ 23 meV by the Stark localization effect, which results in the blue shift.

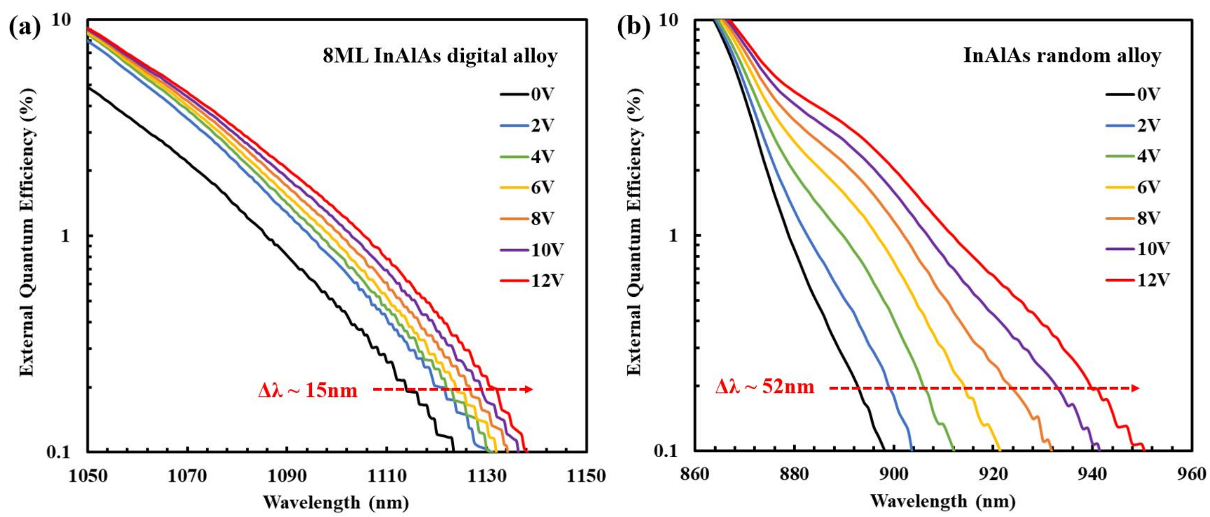

Figure 5-15. The absorption edge of (a) 8ML InAs-AlAs digital alloy and (b) InAlAs random alloy.

5.4 Conclusion

In this Chapter, the ionization characteristics of InAlAs random alloy, InAlAs digital alloy, and AlGaAs digital alloy have been investigated at different temperatures. The k values of the

InAlAs digital alloy APDs decrease exponentially with decreasing temperature, owing to the suppression of hole ionization, which in turn is due to a mini-gap in the valence band. The experimental results are consistent with the simulated band structures and provide insight into the low excess noise exhibited by the InAlAs digital alloy and the absence of noise suppression in the AlGaAs digital alloy. Meanwhile, the breakdown voltage temperature coefficient of 8ML InAlAs digital alloy is similar to InAlAs random alloy.

By measuring the external quantum efficiencies of an 8ML InAlAs digital alloy and an InAlAs random alloy under different voltages, the absorption characteristics of these two semiconductors was investigated. Owing to the Franz-Keldysh effect, both absorption edges exhibit a red shift. However, electric-field-induced Stark localization of the digital alloy results in an electric field dependent quantum efficiency and an effective blue shift.

Chapter 6. Single photon detection

6.1 Introduction

Single photo detection has been widely used in many applications, such as LIDAR, quantum communication, quantum computing, flow cytometry, and photoluminescence measurements [83, 84]. There are three principal categories of single photon detection devices: photomultiplier tubes (PMTs), superconducting single-photon detectors (SSPDs), and single-photon avalanche diodes (SPADs) [86].

The PMTs, a vacuum tube with anodes and a photocathode (Fig. 6-1(a)) were the first photodetectors to achieve single photon detection [86, 87]. PMTs have internal gain, low noise, and large active area; however, they suffer from the bulky volume, high operation voltage, fragility and low dynamic range. SSPDs are nano detectors based on a superconducting mechanism, which includes superconducting nanowire detectors [89], superconducting tunnel junction [90], and transition edge sensors [91]. Figure 6-1(b) is a picture of the superconducting nanowire detector [92]. Single-photon detection is based on the formation of a “hot spot”. When a photon is absorbed at temperature below superconductor critical temperature, it will break a Cooper pair and generate a hot electron, and then results in more Cooper pair dissociation to form the hotspot. The hotspot changes the resistivity, which can be detected by an external circuit. SSPDs exhibit the best detection performance: high detection efficiency, low dark counts, and low timing jitter. However, due to their extremely low critical temperatures (< 4 K), SSPDs need large, expensive cryogenic systems. A schematic of a SPAD is shown in Fig. 6-1(c) [93]. The SPAD is an APD that operates in the Geiger mode. A single absorbed photon can trigger a self-sustaining avalanche event. Different from the other two devices, SPAD is a solid-state device, which can be fabricated in standard complementary metal-oxide-semiconductor (CMOS) technology. It has the advantage of having all the quenching, control, and the read-out circuit integrated on a chip. SPADs have small size, relatively high detection efficiency, low jitter, and can work at relatively high temperature; however, relative to PMTs and SSPDs they exhibit high dark counts. The performance comparison of the three single-photon detectors is plotted in Fig. 6-1(d).

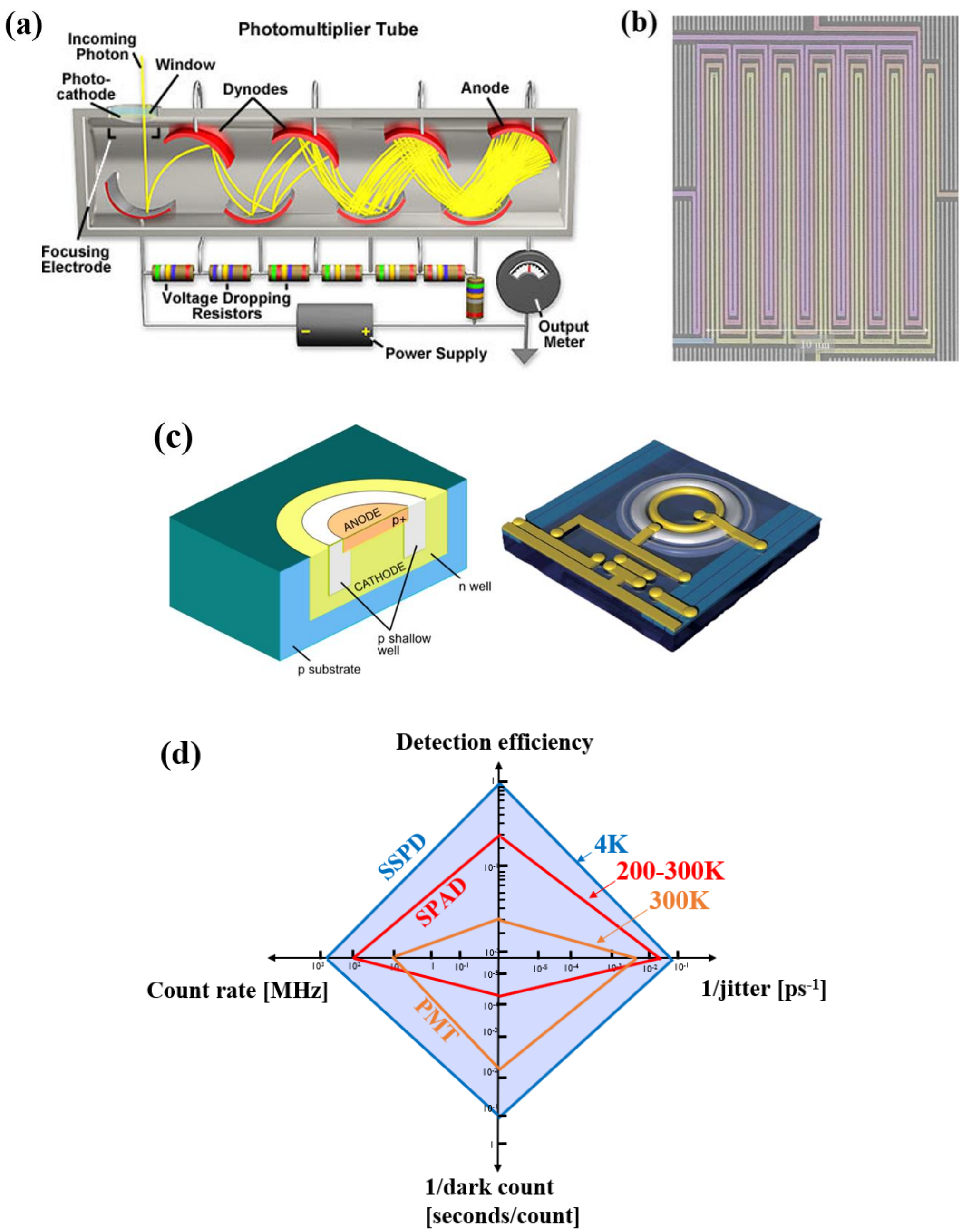

Figure 6-1. Image of (a) a photomultiplier tube, (b) a superconducting nanowire detector, and (c) a single-photon avalanche diode. (d) Performance comparison of the PMT, SSPD, and SPAD [87, 91, 92].

6.2 Figures of merit

Several figures of merit are used to evaluate the performance of SPADs. These include single photon detection efficiency (SPDE), dark count rate (DCR), timing resolution, afterpulse rate, and noise equivalent power. The definitions of these figures of merit are introduced in this section [94].

6.2.1 Single photon detection efficiency

Single photo detection efficiency (SPDE) describes the probability that an incident photon will be successfully detected by a SPAD. The probability is a product of two independent probability, one is the probability that an incident photon generates an electron-hole pair, which is the definition of external quantum efficiency; the other is the probability that an electron-hole pair triggers a breakdown avalanche, i.e., the avalanche process is self-sustaining. Therefore, the SPDE can be calculated as:

$$SPDE = \eta_{external} \times P_{bd} , \tag{6.1}$$

where $\eta_{external}$ is the external QE, which can be defined by Eq. 2.12; and P_{bd} is the breakdown probability. Accordingly, SPDE is always smaller than external QE.

In one laser pulse window, the number of photon-generated carriers should have a Poisson distribution. Thus, the probability of generating n_{e-h} number of electron-hole pairs is given by:

$$g(n_{e-h}) = \frac{\left(\eta_{external}\overline{n_{photon}}\right)^{n_{e-h}} \exp\left(-\eta_{external}\overline{n_{photon}}\right)}{n_{e-h}!} , \tag{6.2}$$

where $\overline{n_{photon}}$ is the average photon number per laser pulse. Thus $\eta_{external}\overline{n_{photon}}$ is the average number of photo-generated electron-hole pairs. The different n_{e-h} numbers lead to different probability of triggering an avalanche. Here I use $P_a(n_{e-h})$ to describe the detection probability given n_{e-h}:

$$P_a\left(n_{e-h}\right) = 1 - \left(1 - P_d\right)\left(1 - P_{bd}\right)^{n_{e-h}} , \tag{6.3}$$

where P_d is the probability of triggering an avalanche in the dark, $P_d = \#\, of\ dark\ counts/(time \times repetition\ rate)$. By combining Eqs. 6.2 and 6.3, the total probability of triggering an avalanche is the sum of all n_{e-h}:

$$P_t = \sum_{n_{e-h}=0}^{\infty} \left[P_a\left(n_{e-h}\right) g\left(n_{e-h}\right)\right] = 1 - \left(1 - P_d\right) \exp\left(-\eta_{external}\, \overline{n_{photon}} P_{bd}\right). \tag{6.4}$$

Hence, the SPDE is given by:

$$SPDE = \frac{1}{\overline{\overline{n_{photon}}}} \ln\left(\frac{1 - P_d}{1 - P_t}\right). \tag{6.5}$$

Using Eq. 6.5, the SPDE can be calculated by simply measuring the dark counting probability, P_d and the total count probability, P_t. Similar to P_d, P_t can be calculated from the $\#\, of\ total\ counts/(time \times repetition\ rate)$. Additionally, the breakdown probability, P_{bd}, can be calculated by Eq. 6.1. The breakdown probability increases with the excess voltage, V_{ex}, which is the voltage above the breakdown voltage:

$$V_{ex} = V - V_{bd} , \tag{6.6}$$

where V is the applied voltage when detection single photon, and V_{bd} is the breakdown voltage. Note that SPDE only depends on the external quantum efficiency and breakdown probability. T measured SPDE at different $\overline{n_{photon}}$ per laser pulse should be same.

6.2.2 Dark count rate

Similar to SPDE, the dark count rate (DCR) is the rate of triggering an avalanche by dark carriers instead of photon-generated carriers. As described in Section 2.1.1, there are several components of the dark current, such as the diffusion, internal G-R, and surface G-R dark current. All these dark carriers have the potential to trigger an avalanche event. The dark carriers generated in the multiplication layer have a position-dependent breakdown probability, due to the different acceleration lengths. For gated-quenching mode measurements, if the generated dark carriers during an electrical pulse width, τ_p, also have a Poisson distribution, then the dark count probability, P_d, can be written as:

$$P_d = 1 - \exp(-DCR \times \tau_p) \,. \tag{6.7}$$

It follows that the DCR can be expressed as:

$$DCR = \frac{-\ln\left(1 - P_d\right)}{\tau_p} \,. \tag{6.8}$$

When $P_d \ll 1$, this relation can be approximated as:

$$DCR \approx \frac{P_d}{\tau_p} \,. \tag{6.9}$$

To ensure the calculation of the DCR using Eq. 6.9 is accurate, the electric pulse width, τ_p, should much longer than the avalanche build-up time. This is due to the fact that the dark carriers need time to obtain sufficient energy to ionize. The build-up time is determined by material type and the excess voltage value. As long as the build-up time is negligible compared to the electric pulse with, the DCR should be independent of the pulse width; in this case the dark count probability, P_d, is proportional to τ_p.

6.2.3 Timing resolution

Timing resolution reflects the variation in the occurrence of the avalanche event relative to the arrival time of the incident photon. This is typically referred to as jitter. There are three factors that give rise to jitter [95]. The first arises from the absorption process. The photon-generated carriers are created at different points in the absorber, which results in variation in the transit time. A narrow absorber has a smaller jitter time. The second process is the impact ionization process, which is a well-known stochastic process. The location of the initial impact ionization varies. The degree depends on the excess voltage and multiplication thickness. A higher excess voltage and narrower multiplication layer can reduce the uncertainty. The third factor is the time required for the seed avalanche to spread laterally across the whole deice area. The lateral position of the initial avalanche will affect the spreading time. As a result, a small size SPAD have a better time resolution. The jitter time can be directly measured by a time-correlated single photo counting analyzer. The full-width-at-half-maximum (FWHM) of the total counting histograms is the jitter time.

6.2.4 Afterpulsing

Afterpulsing is a significant figure of merit, which determines the frequency operation of SPADs. Afterpulsing is one kind of dark count that is caused by emitted carriers that were trapped in deep levels, such as defects or impurities, during pervious avalanche events. Figure 6-2 illustrates the afterpulsing phenomena at different operation frequency. The trapped carriers gradually release over time, as Fig. 6-2(a) shows. At high operation frequency, the released carriers from the primary avalanche event can trigger another avalanche event during subsequent pulses. When the frequency is low as in Fig. 6-2(b), there is less probability to trigger a false avalanche event in subsequent pulses. Therefore, the dark count rate caused by afterpulsing decreases with the lower repetition rate. In order to reduce the dark count from afterpulsing, a long hold-off time is needed in order to release all trapped carriers.

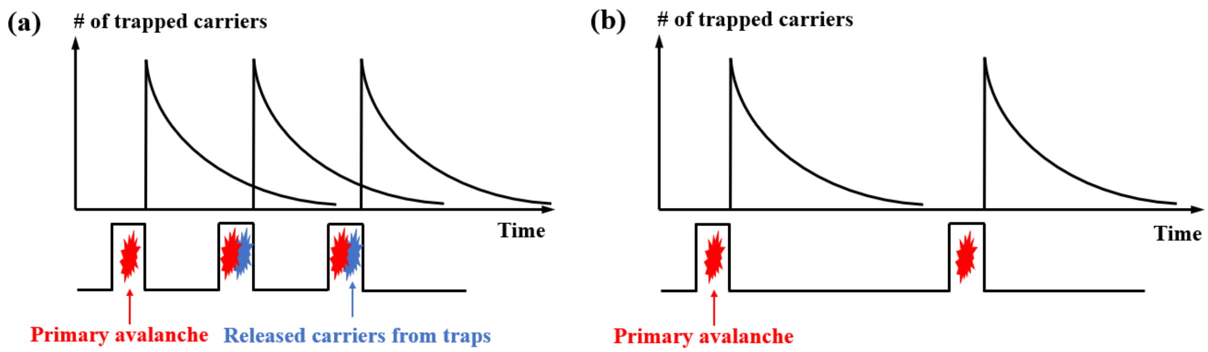

Figure 6-2. Schematic image of afterpulsing at two different frequency.

There are several factors that affect afterpulsing, i.e., the afterpulsing probability. The first is temperature. High temperature can effectively reduce the lifetime of traps, so that carriers are released faster. The second is the DC bias voltage. In gated-quenching mode measurements, there are two components of total voltage, the DC bias and the AC bias. For fixed excess voltage, a higher DC bias with a lower AC bias can also reduce afterpulsing. Carriers can escape from deep levels more easily at higher electric field. The third factor is the excess voltage. A higher excess voltage leads to higher avalanche current with the result of more carrier trapping and higher afterpulsing probability. The width of electrical pulse will also affect afterpulsing. Longer electrical pulses result in a higher breakdown probability and thus increased afterpulsing. The third and last factors can be combined as total charge flow. If the total charge flow for excess voltage and pulse width are the same, the afterpulsing probability should also be the same.

The method to measure the afterpulsing probability is shown in Fig. 6-3. We only introduce one laser pulse during the first electrical pulse in order to trigger the primary avalanche event. We then measure the count probability in the second electrical pulse. The afterpulsing probability equals the measured counting probability in second pulse after subtracting the dark count probability. By varying the hold-off time, $t_{hold-off}$, between the first and second electrical pulses, the afterpulsing probability for different delays can be measured.

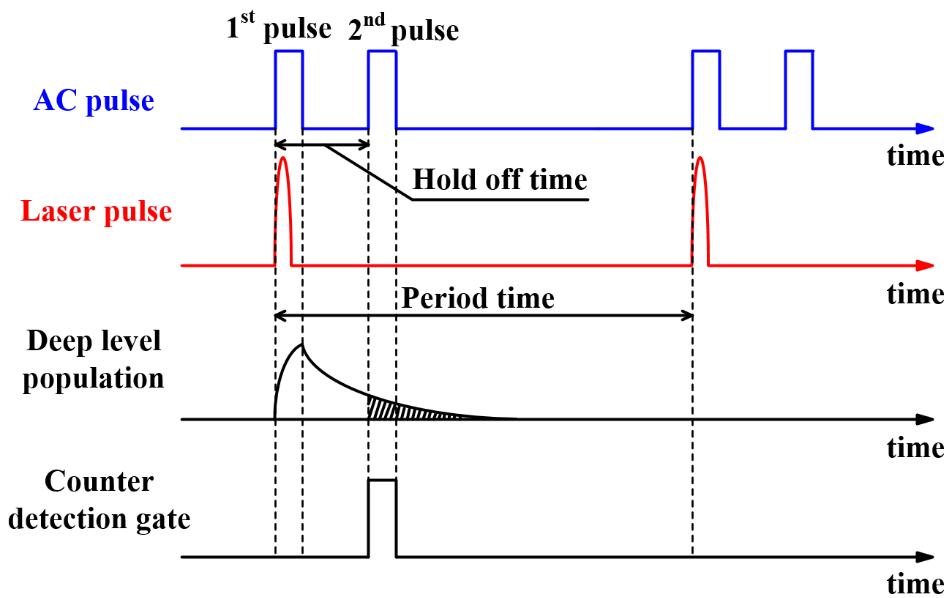

Figure 6-3. Illustration of afterpulsing probability measurement.

6.2.5 Noise equivalent power

Noise equivalent power (NEP) represents the sensitivity of SPADs, which is defined as the optical power that produces a SNR equal to one during one second. NEP can be simply calculated by the measured DCR and SPDE, which is given by:

$$NEP = \frac{h\nu\sqrt{2DCR}}{SPDE}, \tag{6.10}$$

which is related to the injected photon energy, $h\nu$.

6.3 Measurement techniques

As we mentioned before, SPADs work in the Geiger-mode region. This is illustrated in Fig. 6-4. In Geiger mode, a single initial carrier can trigger a self-sustaining avalanche event. The increased current can be detected with a counter. However, the SPAD remain in the high current "on" state until the self-sustaining avalanche is quenched to "off" state. Therefore, a DC bias plus

AC bias are needed to arm and quench the SPAD; typically, this DC bias is slightly below the breakdown voltage, V_{bd}, and an AC bias is adjusted to achieve suitable excess voltage, V_{ex}.

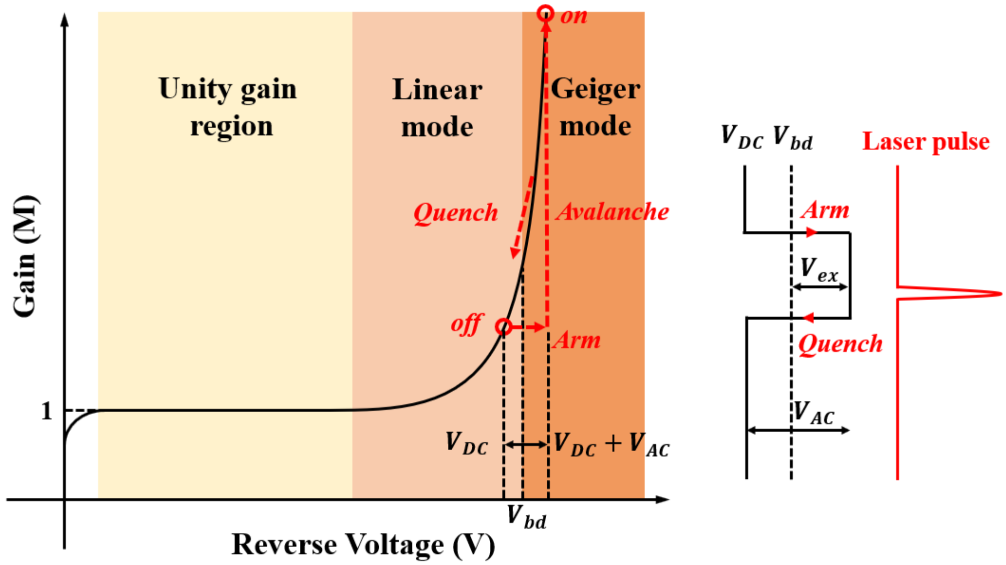

Figure 6-4. Illustration of SPAD work mechanism.

6.3.1 Quenching methods

In order to arm and quench SPADs, readout and quenching circuits are necessary components for single-photon detection. There are three primary types of quenching circuits: passive quenching, active quenching, and gated quenching.

Passive quenching, the simplest method to realize quenching, is implemented by adding a large resistive load in series with the SPAD. Figure 6-5 displays the passive quenching circuit with the SPAD, where R_L is the large resistor that is typically a few hundred kilohms, R_{out} is the 50 Ω load impendence, and C_{stray} is the stray capacitance. A comparator is connected to the anode of the SPAD to count the avalanche events. By applying a DC voltage, $V_{bd} + V_{ex}$, the device works in Geiger mode. When an avalanche event is triggered, the current increases to I_{av}, the bias on the SPAD will drop by $I_{av}R_L$ to a voltage lower than the breakdown voltage; the SPAD is quenched. The SPAD the begins to recharge through R_L. This is a slow process, whose time constant is:

$$t_{recharge} = R_L\left(C_{SPAD} + C_{stray}\right), \tag{6.11}$$

which depends on stray capacitance and the SPAD capacitance. These two capacitances are determined by the device structure, size, and materials; assuming total capacitance ~ 1pF, then the recharge time is several hundred nanoseconds. Passive quenching circuits have been widely applied since the quenching resistor can be directly integrated on the top of SPAD and only one DC voltage supply is required. However, it also suffers from the long reset time, which limits the high-speed operation.

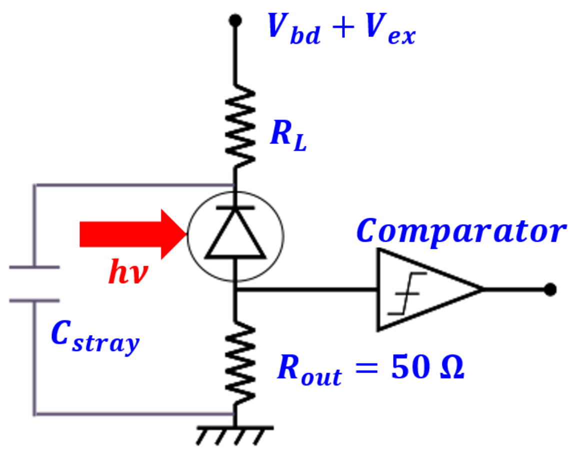

Figure 6-5. Passive quenching circuit [96].

To reduce the long reset time of passive quenching, active quenching is used to control the bias voltage on the SPADs to a few nanoseconds. Figure 6-6 is an active quenching circuit. When an avalanche event is detected, the quench driver switches into V_q to rise the anode voltage. Here V_q is higher than V_{ex}, and so that the voltage on the SPAD is less than V_{bd}, the SPAD is quenched. After a certain hold-off time, it switches back and recharge the SPAD for the subsequent detection. Typically, a CMSO integrated circuit is used to rise and drop the bias voltage. Compared with passive quenching, active quenching has better defined "on" and "off" bias voltage, an adjustable hole-off time, and shorter quenching time. In many application, especially to Si SPADs, integrated active quenching circuits have replaced the passive quenching method due to its superior performance [96-98].

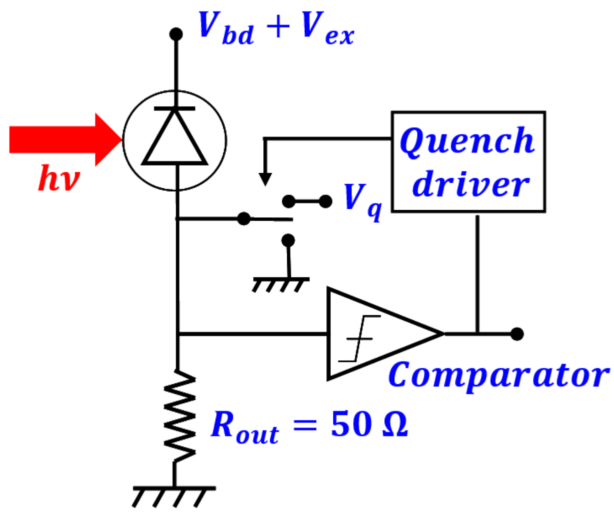

Figure 6-6. Active quenching circuit.

Another quenching method is gated quenching, which is regularly utilized in synchronized applications. In this thesis, I use gated quenching to determine the performance of SPADs. The SPAD is biased under a DC voltage, V_{DC}, which is lower than V_{bd}. An AC voltage, V_{AC}, is applied through a large capacitance to make total bias higher than V_{bd}. When an avalanche event is detected, the current increases and saturates due to R_L. Later, this avalanche current is quenched with the falling edge of the AC pulse voltage. The gated quenching circuit is shown in Fig. 6-7. A narrow-width AC pulse is need to reduce and dark counts and afterpulsing.

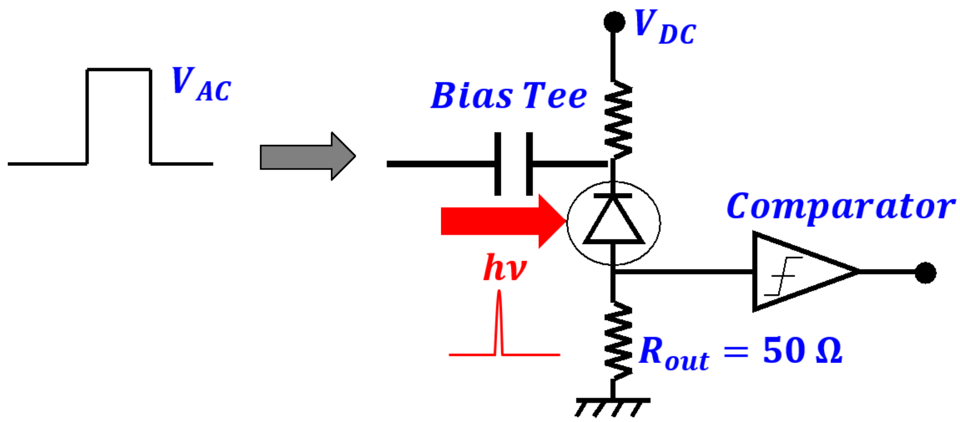

Figure 6-7. Gated quenching circuit.

6.3.2 Measurement setup

The detailed measurement setup for gated quenching in our lab is shown in Fig. 6-8, where the blue lines are electrical paths and the green lines are light paths. The SPAD is inside a continuous-flow cryostat, and the light is coupled into the cryostat through a fiber. There are a couple of advantages to placing the SPAD in the cryostat: first, it provides the capability to measure the performance at different temperatures; second, there is no background light to affect the SPAD due to the completely dark environment inside the cryostat; finally, the metal chamber can shield all RF crosstalk from the pattern generator and laser driver.

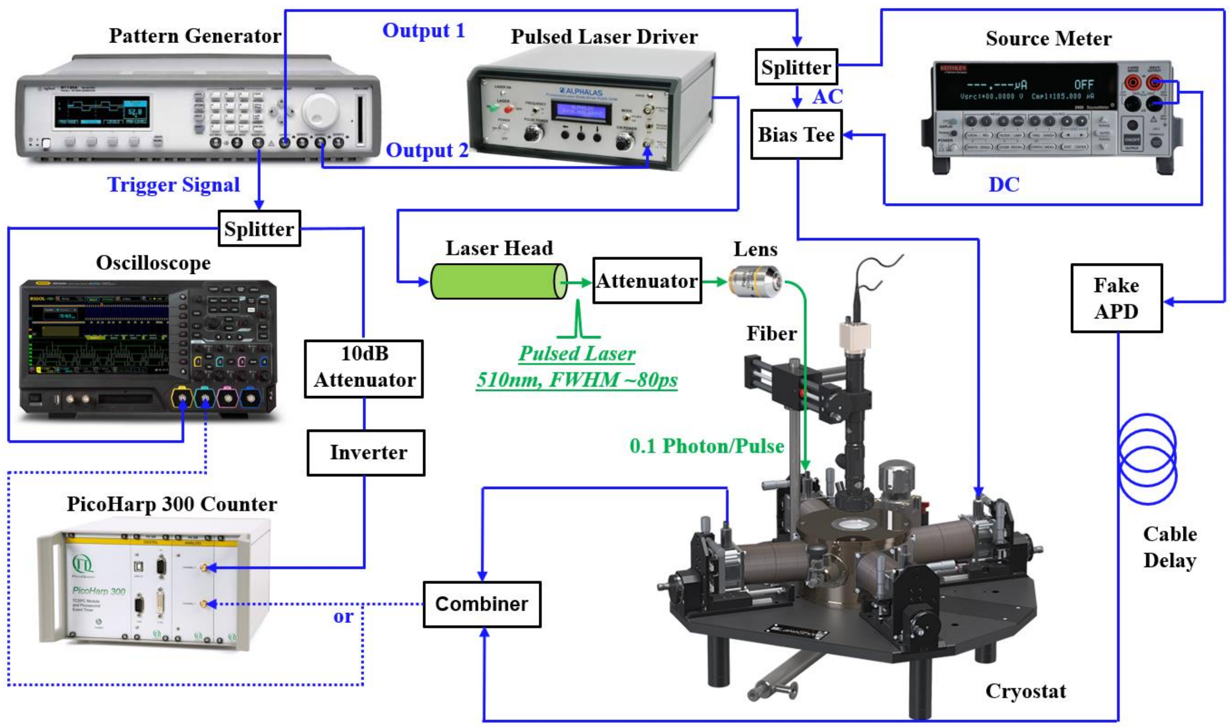

Figure 6-8. Single photon detection setup of gated quenching.

The SPAD is biased a little bit lower than V_{bd} with a DC power supply. I used a Keithley 2400 source meter. A pattern generator, Agilent 81110A, is used to supply the AC voltage pulses. Its trigger signal is used to synchronize the oscilloscope and photon counter. The output 1 signal splits into two paths, one provides a bias to the SPAD through a bias tee. The other biases a "fake" APD, which is a capacitor that is used to eliminate capacitance transients at the beginning and end of the gate pulse. This is a simple RC circuit similar to that in Fig. 2-2. The motivation for using an inactive APD is to isolate the light signal from the capacitive response noise. This is similar to the approach in Ref. [100]. The result is that there are no dark counts from electrical background noise. The combined electrical signal from the SPAD and the fake APD is shown in Fig. 6-9. By adjusting the cable delay of the fake APD, the peak voltage position of the combined electrical signals can be adjusted to the same position as the avalanche event (marked with BX label). The pulsed laser signal can also be adjusted into this time position, such that a clear difference can be seen between

Figs. 6-9(a) and 6-9(b) before attenuation.

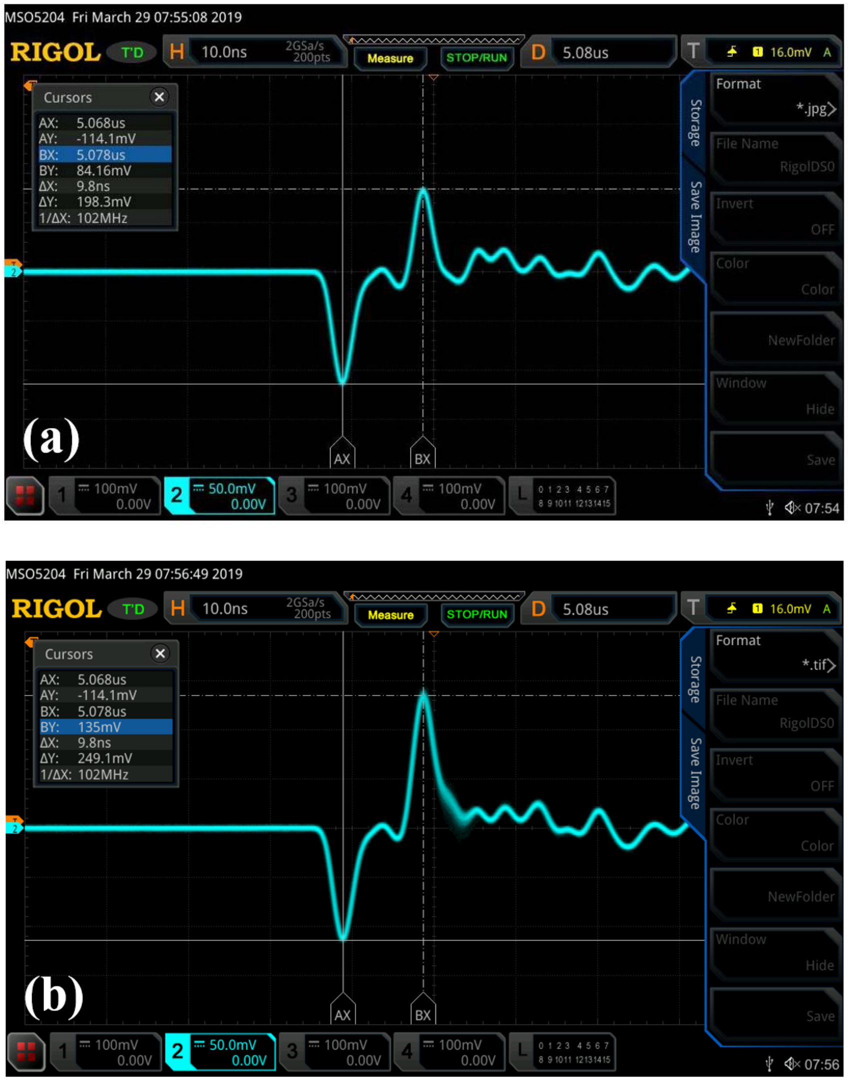

Figure 6-9. Combined electrical signal from the SPAD and fake APD at (a) dark and (b) light.

The output 2 signal of the pattern generator is used as an external trigger signal for the pulsed laser driver. I used an ALPHALAS picosecond laser diode driver PLDD-100M that can drive the laser head to generate a 510 nm optical pulse ~ 80 ps FWHM. The optical pulse can be adjusted by changing the relative time delay between the outputs 1 and 2 in the pattern generator. The output laser is coupled into the fiber through an optical lens, and the fiber is introduced into the cryostat. The fiber and fiber lens head inside the cryostat are shown in Fig. 6-10(a). The lateral and vertical laser coupling setups are shown in Figs.6-10(b) and 6-10(c), respectively. After coupling the laser into the fiber core, the optical pulse is injected into the center of APDs to achieve the highest responsivity and avoid mixed injection from the mesa edge. An attenuator is used to reduce the light intensity to single-photon level per pulse.

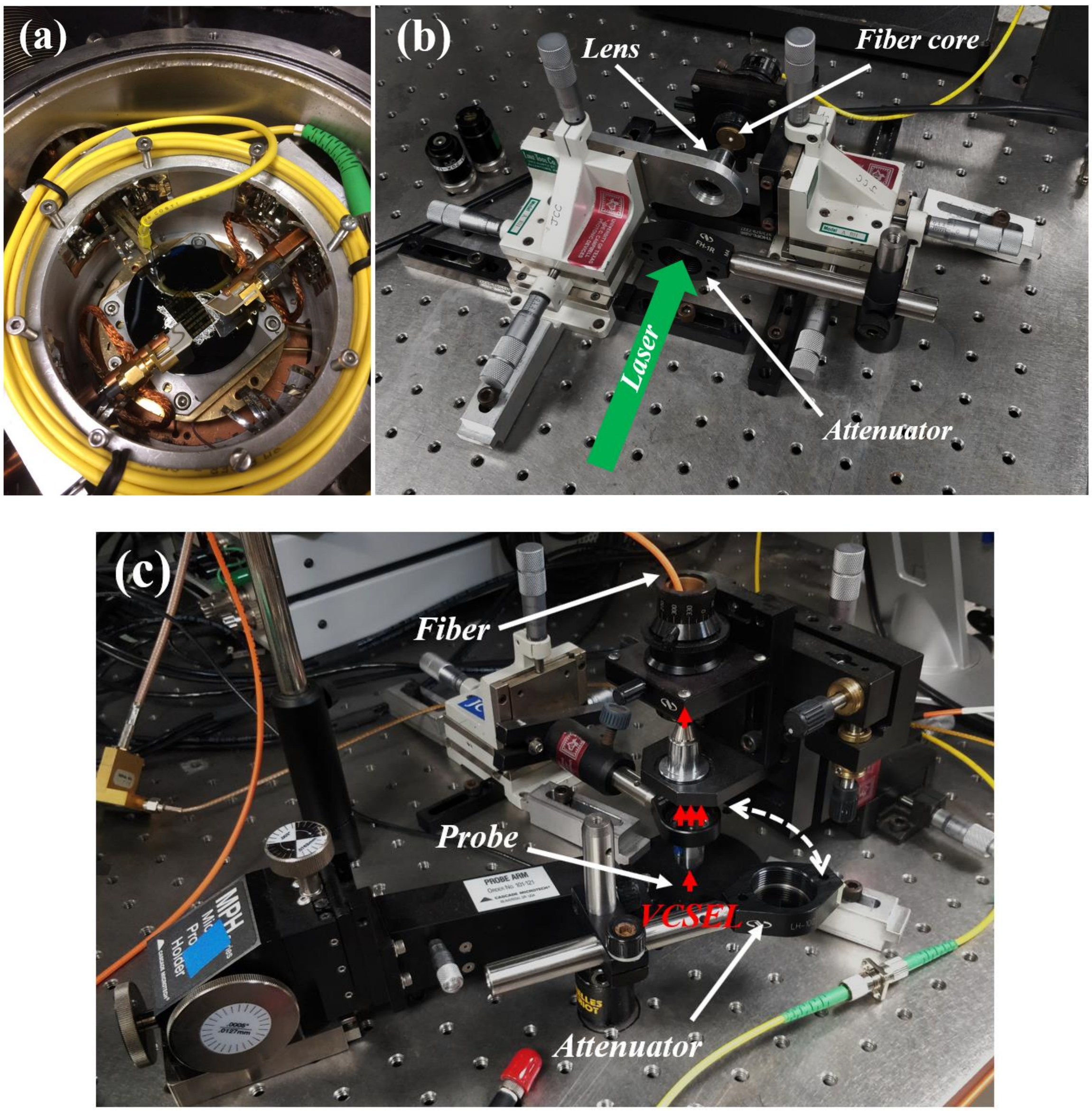

Figure 6-10. (a) SPADs in the cryostat, (b) lateral laser coupling, and (c) vertical laser coupling.

The counting results are detected by the time-correlated single photon counting (TCSPC) system, PicoHarp 300. It has a high-resolution bandwidth up to 4 ps. The channel 0 is used for synchronization, and channel 1 is connected to the combined signal of the SPAD and “fake” APD. Both input signals should at the range from 0 to -1 V. By adjusting the discriminate voltage level, the counts profile of the SPAD can be accurate.

6.4 $Al_{0.7}InAsSb$ SPADs

Due to the excellent performance of the $Al_{0.7}InAsSb$ APD, I studied it in Geiger mode for single-photon detection. The device cross section is shown in Fig. 6-11(a) which is a simple p-i-n structure with 1000 nm $Al_{0.7}InAsSb$ multiplication layer. As described in Chapter 3, the devices are passivated with SU8 2000.5 to further suppress the surface dark current. Figure 6-11(b) shows the photocurrent, dark current, and gain curve under 543 nm CW laser; this 100 μm-diameter APD achieves a high gain > 100 when dark current ~ 2 nA. The capacitance versus reverse bias is shown in Fig. 6-11(c), which illustrates that the APD is fully depleted at low reverse bias.

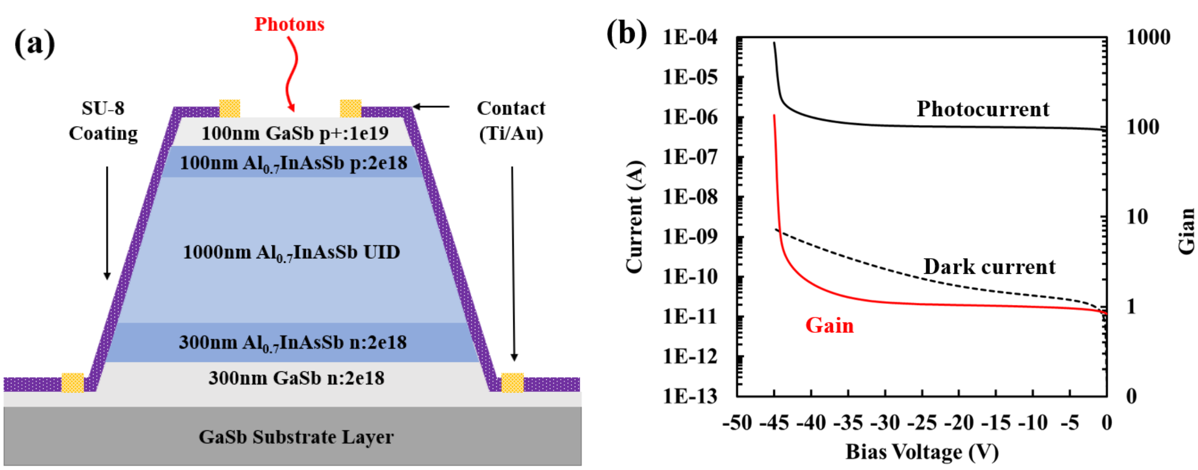

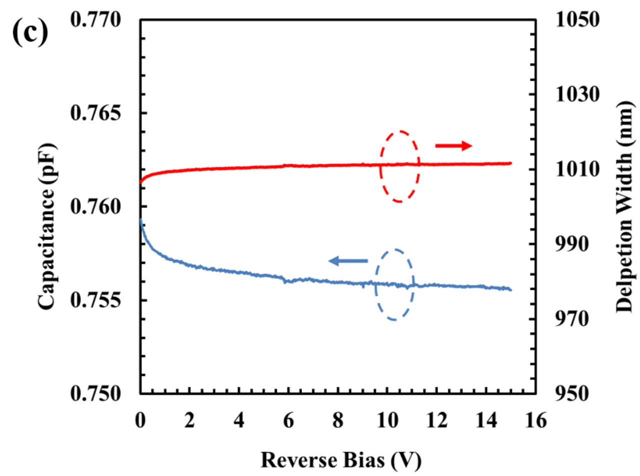

Figure 6-11. (a)Schematic cross section, (b) photocurrent, dark current, and gain, and (c) capacitance and depletion versus bias voltage width of a 100 μm-diameter $Al_{0.7}InAsSb$ p-i-n APD.

The dark currents versus device diameters were measured to analysis the source of dark current. Figure 6-12(a) shows the dark current versus bias voltage of 50 μm, 100 μm, 150 μm, and 250 μm diameter $Al_{0.7}InAsSb$ APDs. The dark current increases with diameter. The dark currents of these different size APDs at -10 V, -20 V, -30 V, -35 V, and -40 V are shown in Fig. 6-12(b), they exhibit a linear increase with size at all bias voltages; therefore, the dominate dark current mechanism is the surface leakage current.

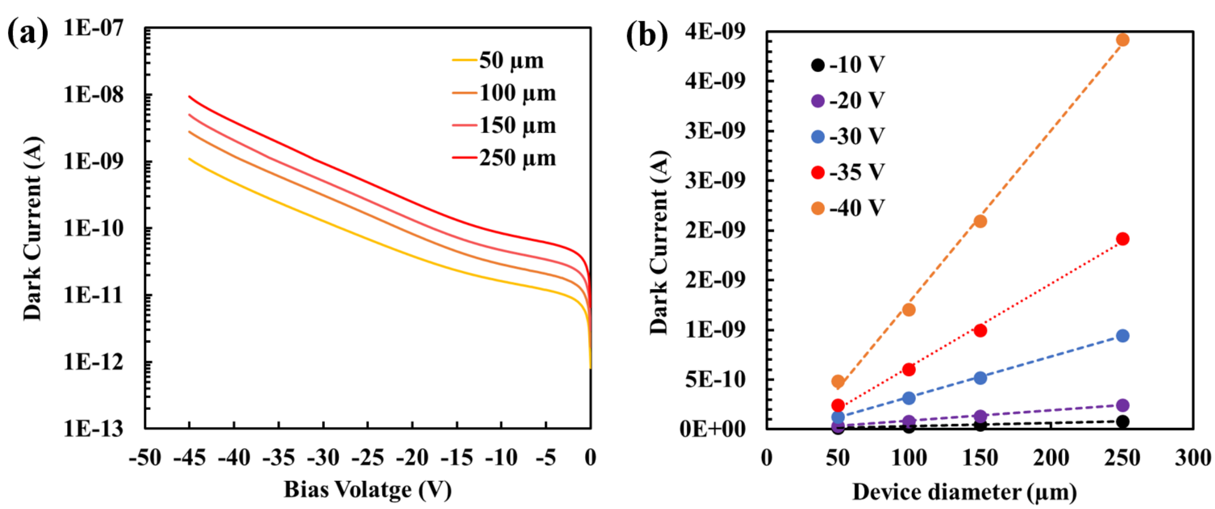

Figure 6-12. Dark currents versus (a) bias voltage and (b) device diameter of $Al_{0.7}InAsSb$ p-i-n APDs.

In order to reduce the dark current, this APD was measured at low temperature. The temperature dependent current-voltage and gain characteristics are shown in Fig. 6-13. The temperature was varied from 200 K to 340 K in steps of 10 K. The gain shifts to higher bias voltage with temperature due to increased phonon scattering. At all different temperatures, the $Al_{0.7}InAsSb$ APD can achieve a high gain > 10,000. Moreover, when the temperature is lower than 230 K, the dark current of it is very low < 1 pA, which limited by the noise floor of the semiconductor parameter analyzer (HP4145).

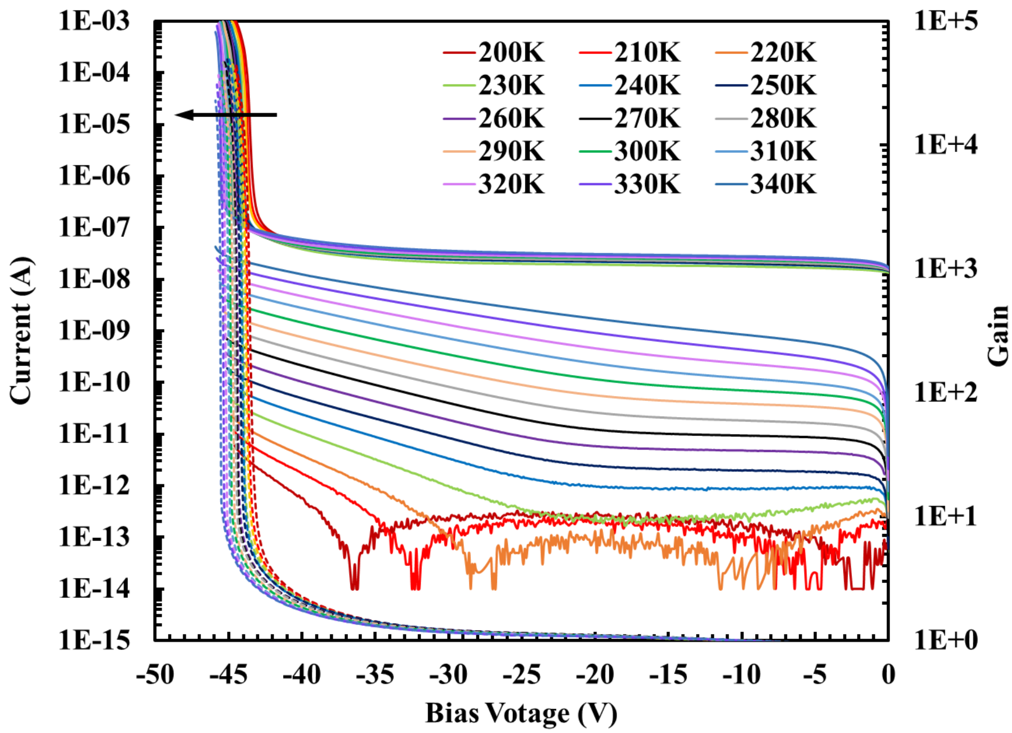

Figure 6-13. I-V and gain curves of the $Al_{0.7}InAsSb$ APD from 200 K to 340 K.

From the temperature characteristics in Fig. 6-13, the dark current near breakdown is ~ 0.1 pA when the temperature lower than 240K, which is suitable SPAD operation. Therefore, I measured the single-photon detection of the $Al_{0.7}InAsSb$ SPAD at 200 K, 220 K, and 240 K. All the measurements used a high-speed 850 nm VCSEL as the optical source. The count numbers at 240 K with 42.5 V DC bias and 6 V AC pulse are shown in Fig. 6-14. Fig. 6-14(a) shows the total and dark counts with 100 KHz repetition rate and 10 s integration. The photon counts are obtained from the difference between the total counts and the dark counts. As shown in Fig. 6-14(b), the FWHM is ~ 190 ps, which is the jitter time.

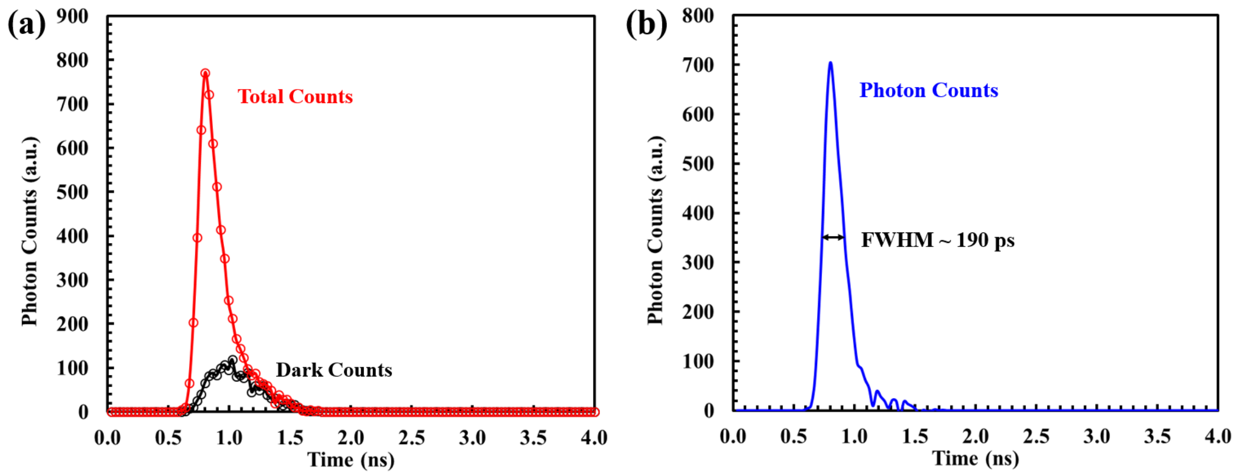

Figure 6-14. (a) Total and dark counts, (b) photon counts for 100 KHz repetition rate of the $Al_{0.7}InAsSb$ SPAD at 240 K.

The single photon detection efficiency (SPDE) and breakdown probability versus dark count probability (DCP) are shown in Fig. 6-15. The SPDE increases with higher DCP. The higher excess voltage enables higher probability to trigger avalanche events for both photon-generated carriers and dark carriers. At low temperature, the SPAD can achieve same SPDE with lower DCP, as a result of the lower dark current. The external quantum efficiency of the $Al_{0.7}InAsSb$ SPAD is 36% at 850 nm wavelength, due to absorption in the GaSb top contact layer. Thus, by using Eq. 6.1, the $Al_{0.7}InAsSb$ SPAD exhibits ~ 92.5% breakdown probability at 200 K, while the dark count probability is ~ 1%. Compared with the best InGaAs/InP SPAD [4], it has almost two orders magnitude higher DCP. The primary reason is the dark current. The $Al_{0.7}InAsSb$ SPAD has more than 10× higher dark current than the InGaAs/InP SPAD.

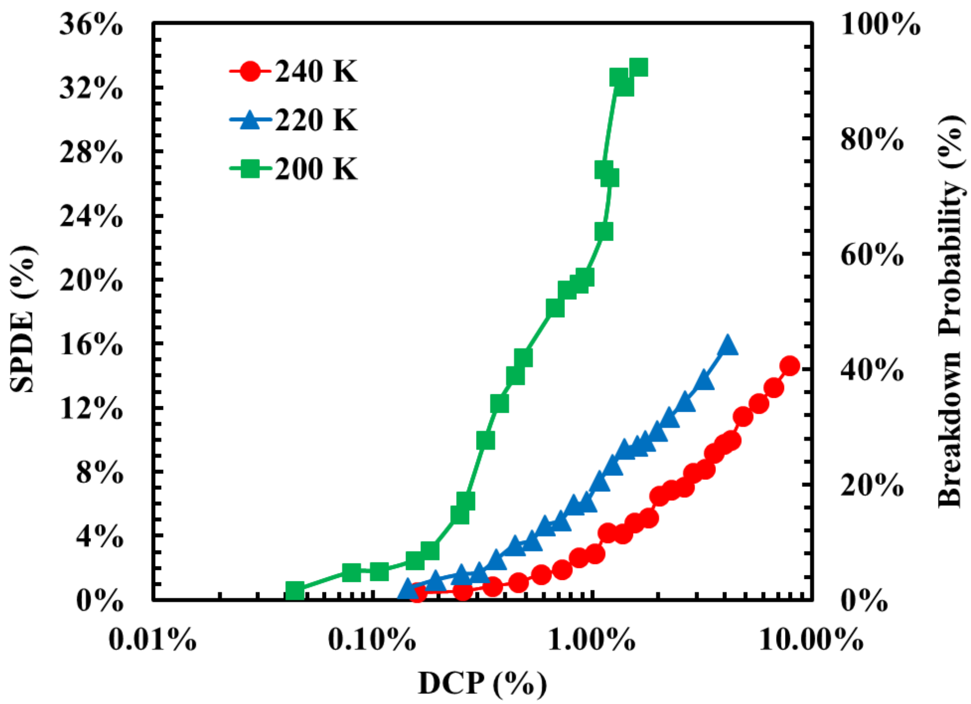

Figure 6-15. SPDE and breakdown probability versus DCP of the $Al_{0.7}InAsSb$ SPAD.

Another possible reason for high dark count probability may be afterpulsing. In order to verify this, the dark count rate (DCR) versus SPDE was measured at a lower repetition rate of 10 KHz. Figure 6-16 compares the measurements as 100 kHz and 10 kHz repetition rates. As noted in Section 6.2.4, the trapped carrier population decays with time, and a longer hold-off time can reduce the avalanche events caused by released carriers from deep levels. At both 200K and 220K, the DCR for the 10 KHz repetition rate (□， △) is much lower than the DCR of the 100 KHz repetition rate (■， ▲).

Based on Eq. 6.10, the noise equivalent power (NEP) at different excess voltages can be calculated. The results are shown in Fig. 6-17. The NEP at 10 KHz repetition rate is lower than that at 100 KHz. The 10 kHz the NEP is ~ $4.1 \times 10^{-15}\ W/Hz^{1/2}$ at 220 K and ~ $1.4 \times 10^{-15}\ W/Hz^{1/2}$ at 200 K. At 100 kHz the NEP is ~ $9.2 \times 10^{-15}\ W/Hz^{1/2}$ at 220 K and ~ $2.8 \times 10^{-15}\ W/Hz^{1/2}$ at 200 K. The average NEP at 10 kHz repetition rate is approximately half that at 100 kHz.

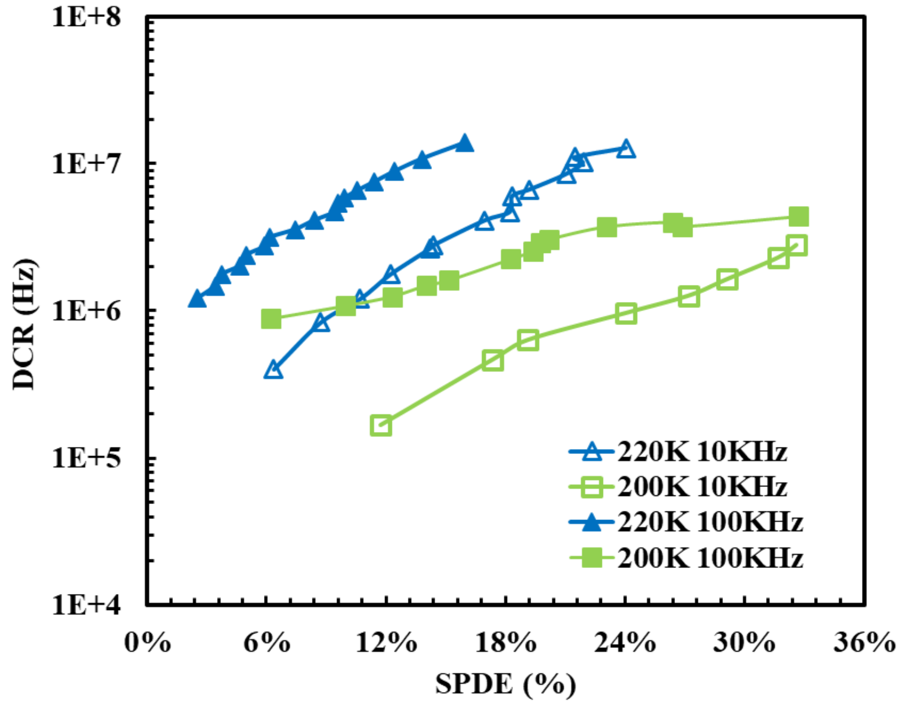

Figure 6-16. DCR versus SPDE with 10 KHz and 100 KHz repetition rate.

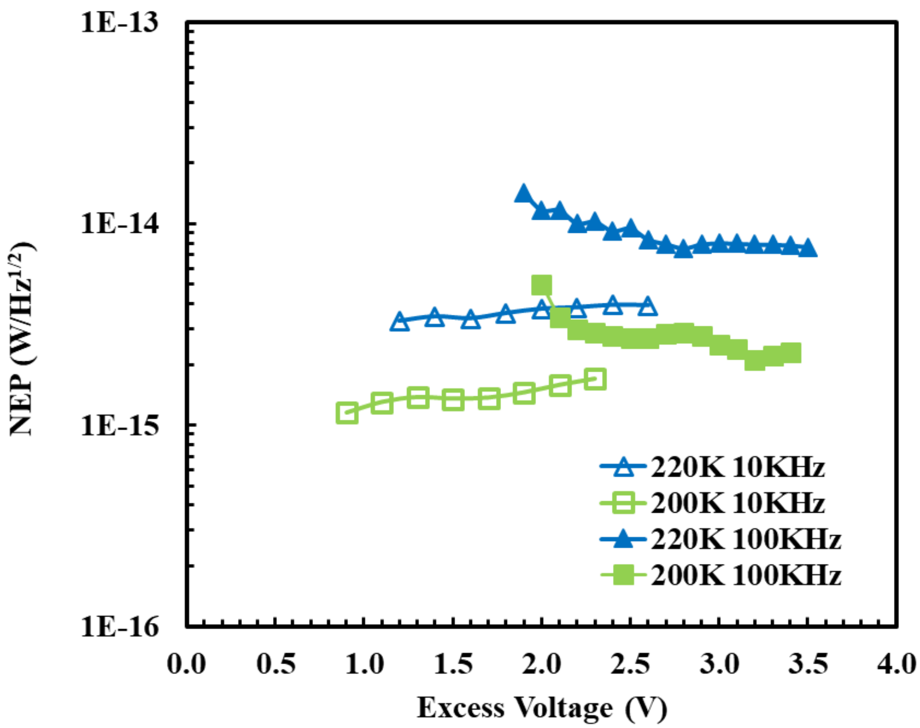

Figure 6-17. NEP versus excess voltage with 10 KHz and 100 KHz repetition rate.

One possible reason for this level of afterpulsing may be the high Al composition in the $Al_{0.7}InAsSb$ SPAD. Al oxidizes easily which might create deep level traps during crystal growth. There are numerous reports on InGaAs/InP and InGaAs/InAlAs SPADs. The InGaAs/InAlAs SPADs have magnitudes higher dark count rate than InGaAs InP SPADs [101]. We had secondary ion mass spectrometry (SIMS) done to measure the oxygen concentration. The SIMS results for this $Al_{0.7}InAsSb$ wafer and an InP wafer are shown in Fig. 6-18. The oxygen concentration in the $Al_{0.7}InAsSb$ wafer is nearly two orders of magnitude higher than that in the InP wafer, an indication of higher trap concentration and, thus, higher dark count rate.

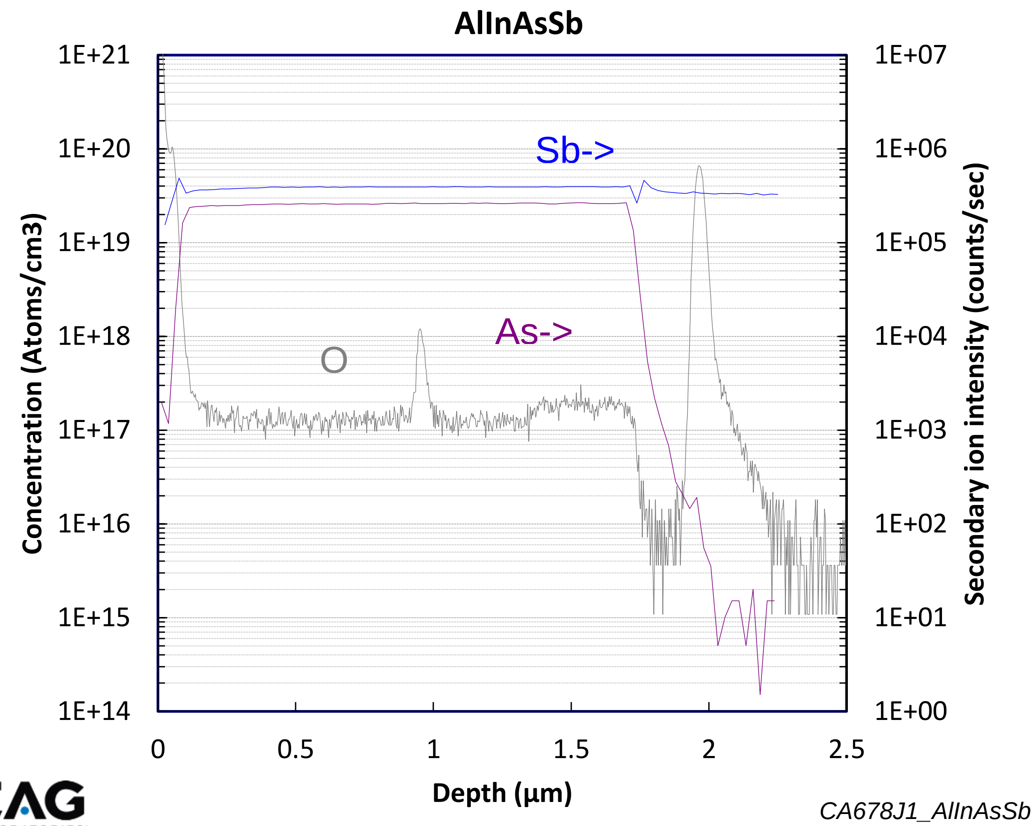

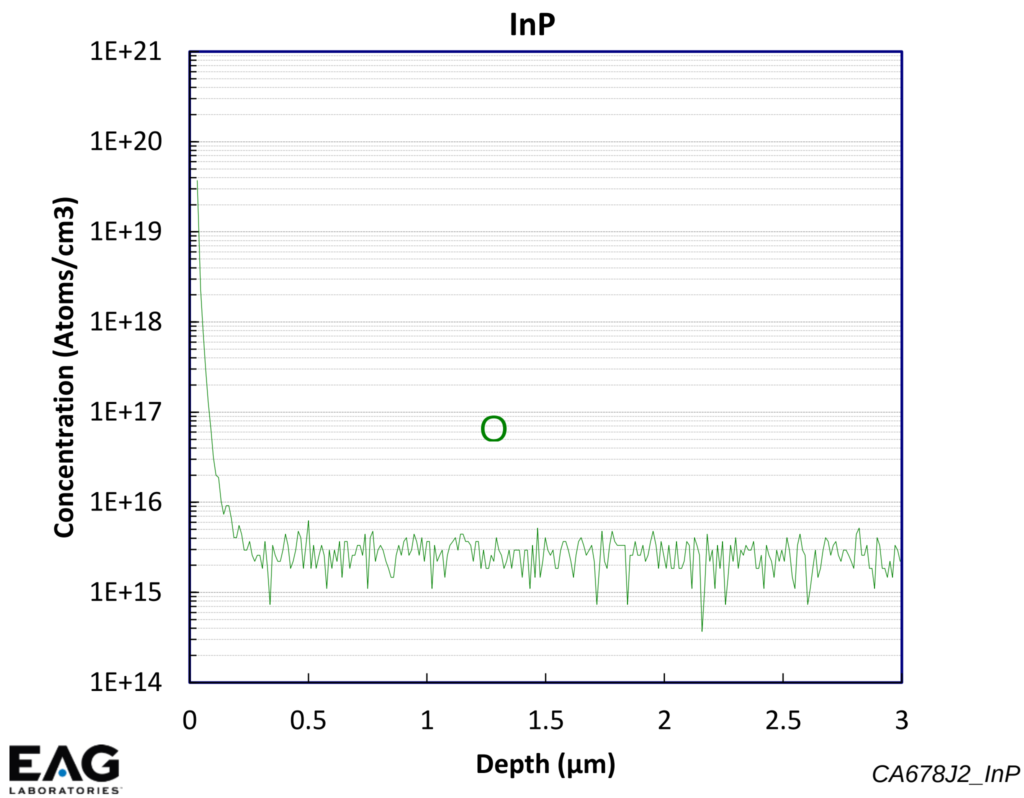

Figure 6-18. The SIMS results for $Al_{0.7}InAsSb$ and InP wafers.

However, compared with other SPADs with Al, such as InGaAs/InAlAs SPADs, the $Al_{0.7}InAsSb$ SPAD has a better performance. A comparison of InGaAs/InAlAs, InGaAs/InP, and $Al_{0.7}InAsSb$ SPADs is shown in Fig. 6-19, where the InGaAs/InAlAs SPADs are blue closed symbols, the InGaAs/InP SPADs are black open symbols, and the $Al_{0.7}InAsSb$ SPADs are red closed symbols. The $Al_{0.7}InAsSb$ SPADs achieve higher SPDE with a relatively small DCR [12, 85, 100-105].

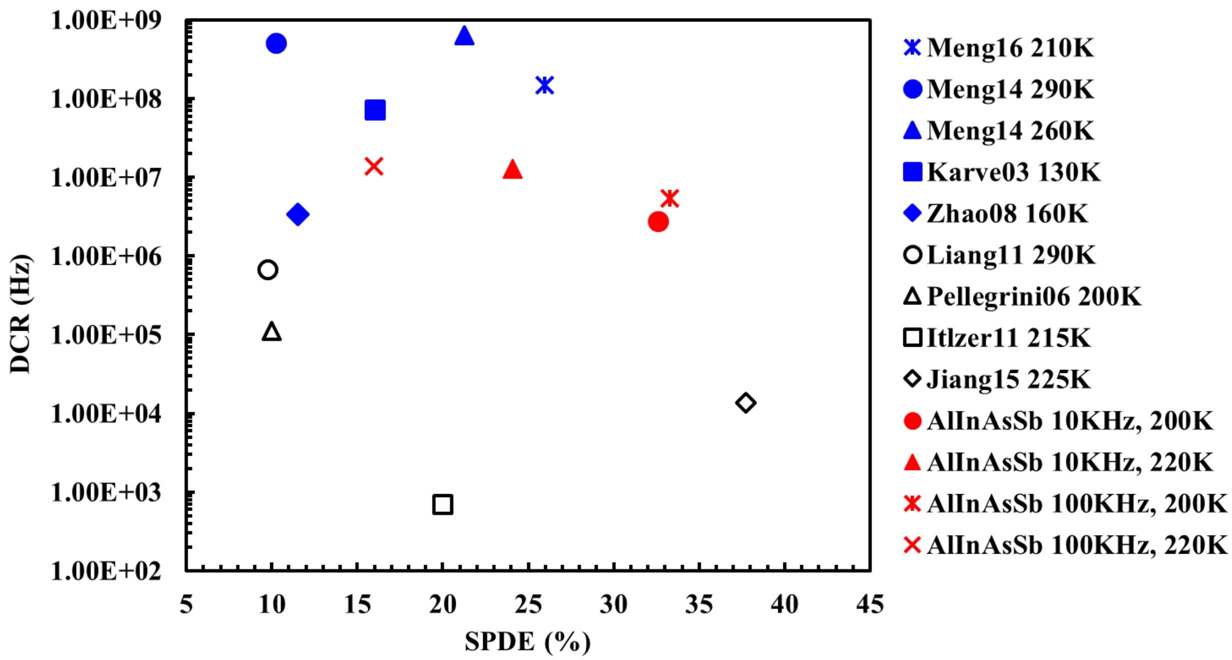

Figure 6-19. DCR versus SPDE in this work compared with previous reports of InGaAs/InAlAs (blue closed symbols) and InGaAs/InP (black open symbols) SPADs [12, 85, 100-105].

6.5 GaInP SPAD arrays

The performance of GaInP SPAD arrays is reported in this section. This work was a collaboration with LightSpin Technology. The devices were designed by Dr. Eric Harmon. Figure 6-20(a) is the mask design of the GaInP SPAD arrays. The epitaxial wafers were grown in a commercial foundry and fabricated in another foundry. I measured the SPADs arrays in the red block, which is a 50×50 array with bypass capacitance. Each device is $8\ \mu m \times 8\ \mu m$, and the pitch is 10 µm. The current versus bias voltage is displayed in Fig. 6-20(b). It was measured with a 543 nm laser. Low intensity light achieved higher gain without gain saturation. The highest gain obtained was ~ 1.1×10^4. The external quantum efficiency for the GaInP SPAD array is shown in Fig. 6-20(c). The peak QE is ~ 33% at 610 nm. The bandwidths of the array at gains of 1, 10, and 50 are shown in Fig. 6-20(d). All are near 130 MHz, which is the RC limit. These measurements were carried out with a relatively large light spot in order to cover the whole area of the array.

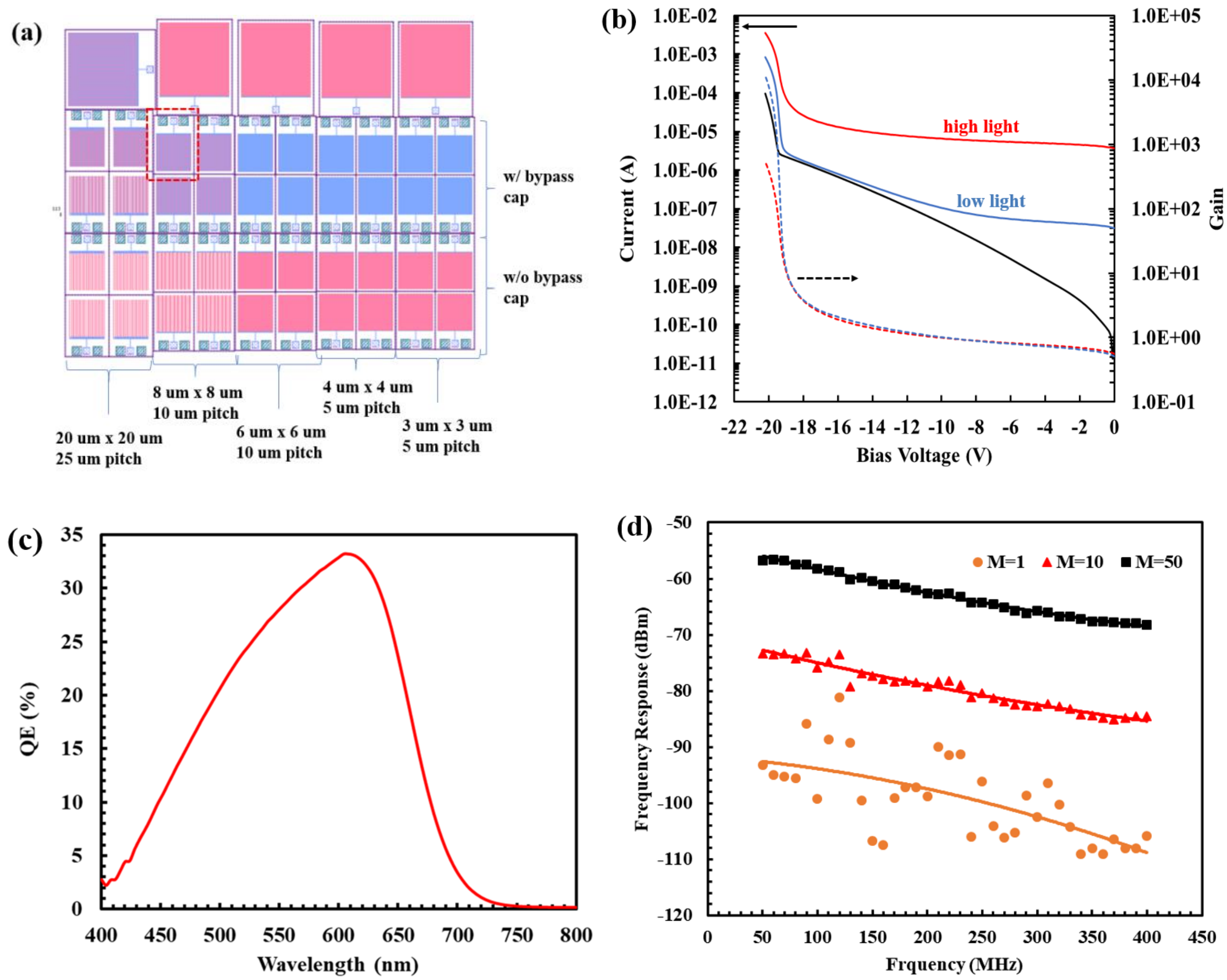

Figure 6-20. (a) Mask design of GaInP SPAD arrays, (b) current and gain versus bias voltage, (c) quantum efficiency versus wavelength, and (d) bandwidth measurements of the 50×50 GaInP SPAD array.

For the SPAD array, the isolation between devices is very improtant in order to aviod crosstalk. In order to determine the isolation these arrays, i measured the 2D spatial scan of a 3 × 3 SPAD array with a small 543 nm laser beam. Fig. 6-21 shows that there is very good isolation between the devices. During fabrication three things were done to achieve isolation, including implant isolation, a p-layer etch, and a deep etch.

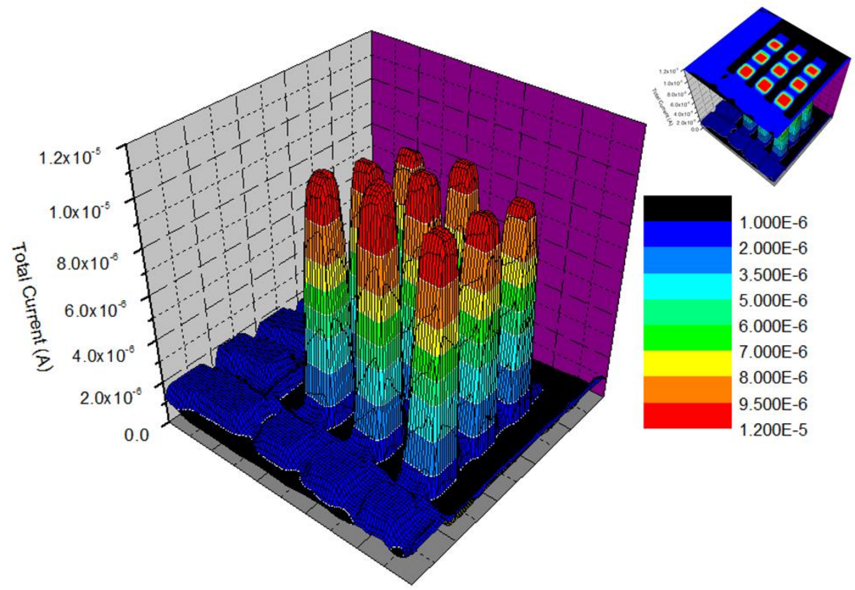

Figure 6-21. The 2D spatial scan of a 3 × 3 GaInP SPAD array.

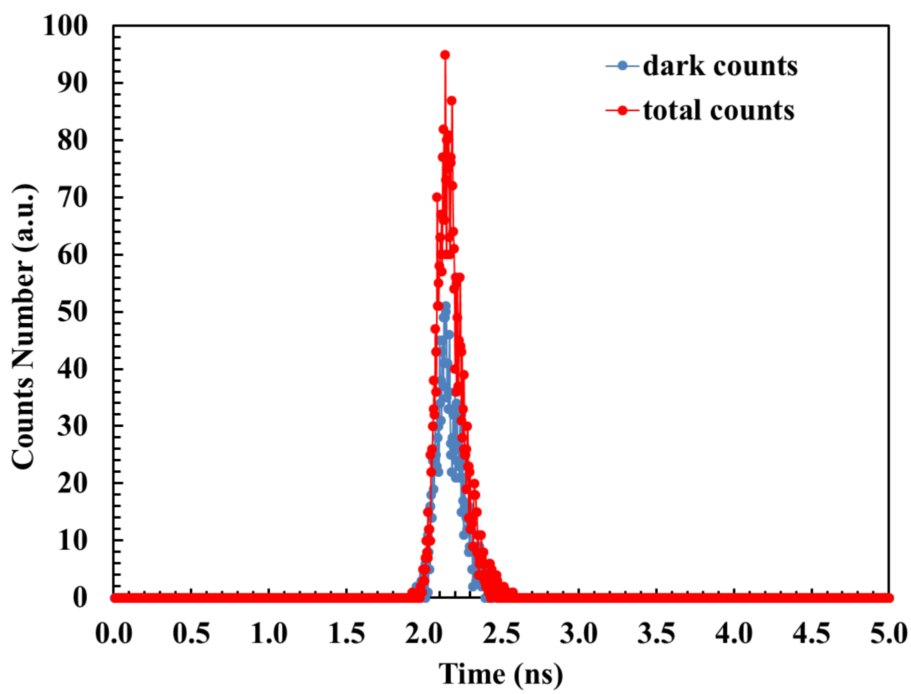

Figure 6-22. Total and dark counts number of a 50 × 50 GaInP SPAD array.

I used a 510 nm pulsed laser to measure the single photon detetcion of this 50 × 50 GaInP SPAD array. The pulsed laser has narrow width of FWHM ~ 80 ps, which enables an accurate jitter measurement. I attenuated the energy level to ~ 0.1 photon/pulse and the gated-mode repetition rate was 10 kHz. The array was measured at room temperature with 19.9 V DC bias plus 2.5 V AC bias. The results are shown in Fig. 6-22. By using the equations in Section 6.2, it was determined that the SPAD array achieved jitter ~ 120 ps, SPDE ~ 16.3%, and dark count probability ~ 2.0%.

6.6 Conclusion

In this chapter, the figures of merit and techniques to measure the characteristics of SPADs have been discussed. An $Al_{0.7}InAsSb$ SPAD has been measured. For 10 kHz gated mode operation it exhibits jitter time ~ 190 ps, SPDE ~ 32.6%, and DCR ~ 2.8 MHz at 200 K. At 100 kHz it achieved SPDE ~ 33.3% and DCR ~ 5.4 MHz at 200 K. Compared to conventional InGaAs/InAlAs SPADs, the $Al_{0.7}InAsSb$ SPADs achieved higher SPDE with a relatively smaller DCR. A GaInP SPAD array has also been measured. At room temperature and 10 kHz gated mode, it achieved jitter ~ 120 ps, SPDE ~ 16.3%, and dark count probability ~ 2.0%.

Chapter 7. Triple-mesa APDs

7.1 Introduction

As described in Section 2.1.1, it is beneficial to reduce the dark current of APDs in order to achieve high SNR for high sensitivity. For single-photon detection in Chapter 6, low dark current is desirable because it is the primary source of dark counts. Low dark current is also an important factor in characterizing the uniformity of APD arrays. The dark current of APDs is frequently described in terms of the bulk and surface components, which scale with area and perimeter, respectively. The bulk portion is primarily related to the material quality. The dark current that originates at the surface depends on fabrication processing, a critical aspect of which passivation of surface defects from dangling bonds, crystalline defects, and impurities is essential. This is especially true for mesa-structure detectors that tend to have relatively large exposed surfaces. APDs have the additional issue of high electric fields at the surface. Many passivation methods have been explored to reduce surface leakage, however, these passivation methods have proved to be only partially successful in reducing surface-related dark current [107]. Recently, Nada et al. [6, 7, 101] reported a triple-mesa-structure InGaAs/InAlAs SACM APDs that achieved high bandwidth with small active areas. The low dark current exhibited by these APDs was attributed to suppression of surface leakage by the triple mesa [109]. In this chapter, different from the structures in pervious references, we report a reach-through APD with modified charge layer doping. The reach-through structure can achieve better restriction of the electric field in the center of the multiplication region, which results in a relatively low electric field at the surface. This approach is approximately equivalent to passivation with the same semiconductor material, which effectively eliminates surface dangling bonds. Moreover, it is easily extended to different semiconductors.

7.2 Device structure

A schematic diagram of the triple-mesa structure is shown in Fig. 7-1(a). It consists of three mesas with increasing area from top to bottom. Figure 7-1(b) is an SEM picture of a fabricated triple mesa APD. The epitaxial layers of the triple-mesa reach-through APD are shown in Fig. 7-1(c). From the top to bottom, the structure consists a 100 nm InAlAs P-type contact layer, an 80 nm InAlAs unintentionally-doped buffer layer, an 80 nm InAlAs P-type charger layer, an 800 nm InAlAs unintentionally-doped multiplication layer, a 160 nm InAlAs N-type contact layer, and an InP N-type substrate. This wafer is grown by Thorlab Quantum Electronics. The mesas of the triple-mesa APDs were defined with standard photolithography and formed by wet etching. The lowest mesa was etched with a solution of H_2SO_4: H_2O_2: H_2O, which has a fast etch rate and good anisotropy. The second and third mesas were etched with a solution of $C_6H_8O_7$: H_3PO_4: H_2O_2: H_2O, which has a stable slow etch rate. Top and bottom contacts were deposited by evaporation and lift-off of Ti/Au.

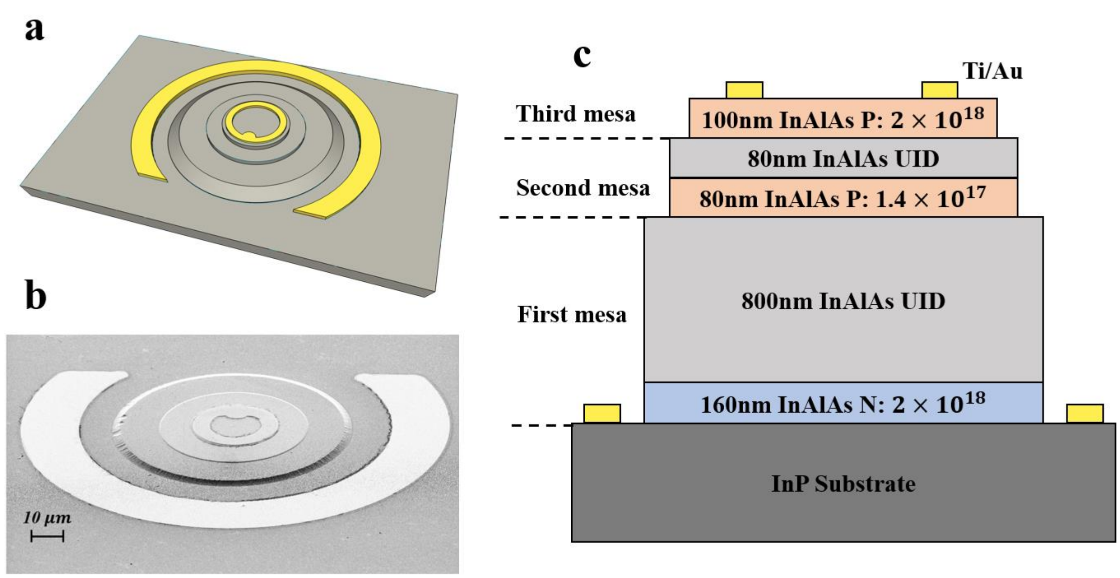

Figure 7-1. (a) Schematic diagram of triple-mesa APDs. (b) SEM picture of one fabricated triple-mesa APD. (c) Cross sections of triple-mesa reach-through InAlAs APDs.

The triple-mesa structure can restrict the surface electric field more than a double-mesa [110]. The purpose of the charge layer is to tailor the vertical electric field profile, and the triple-mesa structure performs a similar function laterally. Therefore, the electric field can be precisely controlled in the center of the multiplication region. The simulated electric field at - 40 V bias of an InAlAs double-mesa APD and a triple-mesa (reach-through) APD are shown in Fig. 7-2. In the double-mesa structure, the electric field in the multiplication layer is influenced by the first mesa region, however, electric-field crowding is observed at the foot of the first mesa sidewall, as shown in Fig. 7-2(a). This can cause premature breakdown at the edge [111]. The electric field profile of the triple-mesa APD is shown in Fig. 7-2(b).

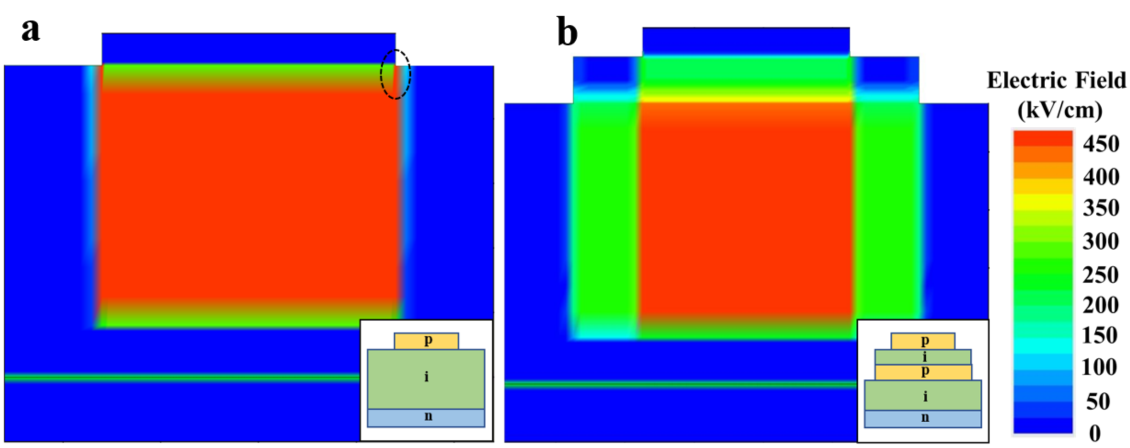

Figure 7-2. Simulated electric field profiles of (a) double-mesa and (b) triple-mesa APDs.

7.3 Results and discussions

The gain versus bias voltage of the InAlAs reach-through APD is shown in Fig. 7-3(a), and the excess noise of this APD is shown in Fig. 7-3(b). The InAlAs reach-through APDs have similar avalanche characteristics as that of InAlAs p-i-n APDs.

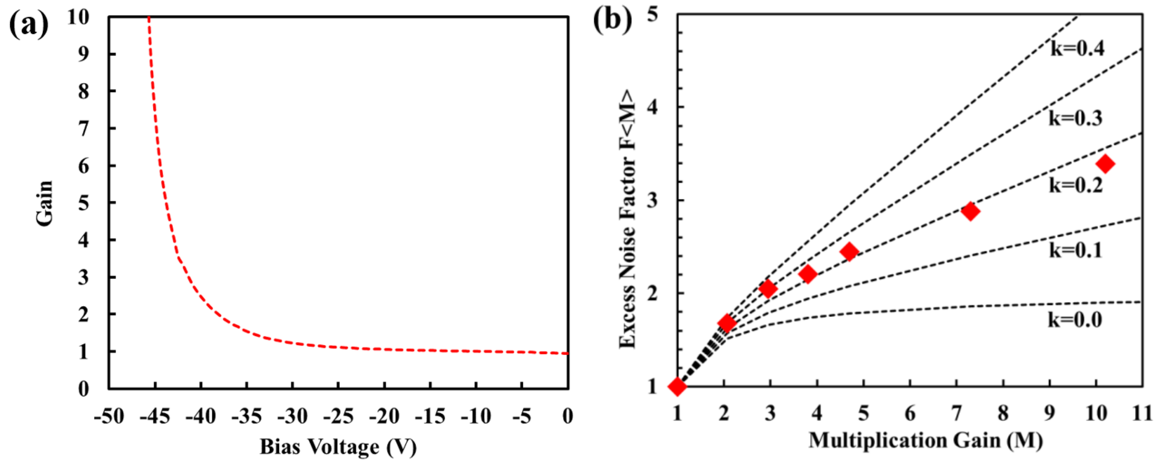

Figure 7-3. Gain versus bias voltage, and (b) excess noise of InAlAs reach-through APD.

In order to verify that the triple-mesa structure can suppress surface leakage, single-mesa and triple-mesa APDs were fabrication from the same InAlAs reach-through wafer. Figure 7-4(a) shows the dark currents of both structures for different mesa diameters. The diameters of the single mesas were 55 µm, 75 µm, and 135 µm. For the triple-mesa, we used the effective diameters, which were estimated to be 50 µm, 70 µm, and 124 µm. The dark current of the 50 µm-diameter triple-mesa device is < 1 pA at - 45 V. The dark current densities of the single-mesa and triple-mesa are plotted in Fig. 7-4(b). For bias > - 15 V, the dark current density of the single-mesa APDs is ~ 1.5 $\mu A/cm^2$, while that of the triple-mesa is ~ 30 nA/cm^2, i.e., ~ 50 times lower than the single-mesa.

By plotting dark current versus diameter, it is possible to determine the relative magnitudes of the bulk and surface components of the dark current. As Figures 7-5(a) and (b) show, the dark current of the single-mesa APDs varies linearly with mesa diameter, which indicates that surface leakage dominates. However, the quadratic relationship of the triple-mesa devices indicates that bulk leakage is the most significant dark current component. It follows that the triple-mesa design can effectively suppress surface leakage.

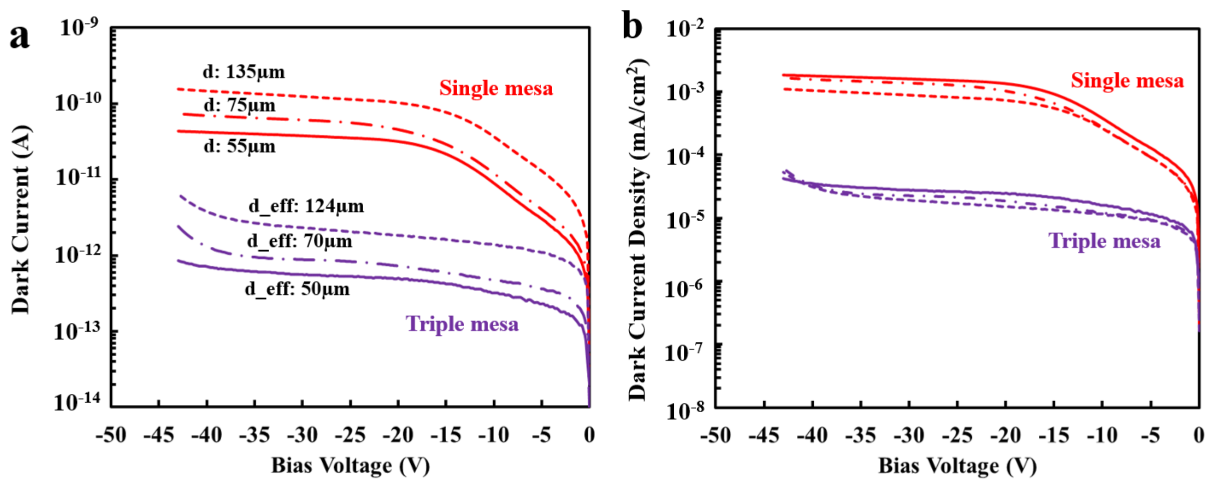

Figure 7-4. Comparison of single-mesa and triple-mesa InAlAs reach-through APDs: (a) dark current, and (b) dark current density.

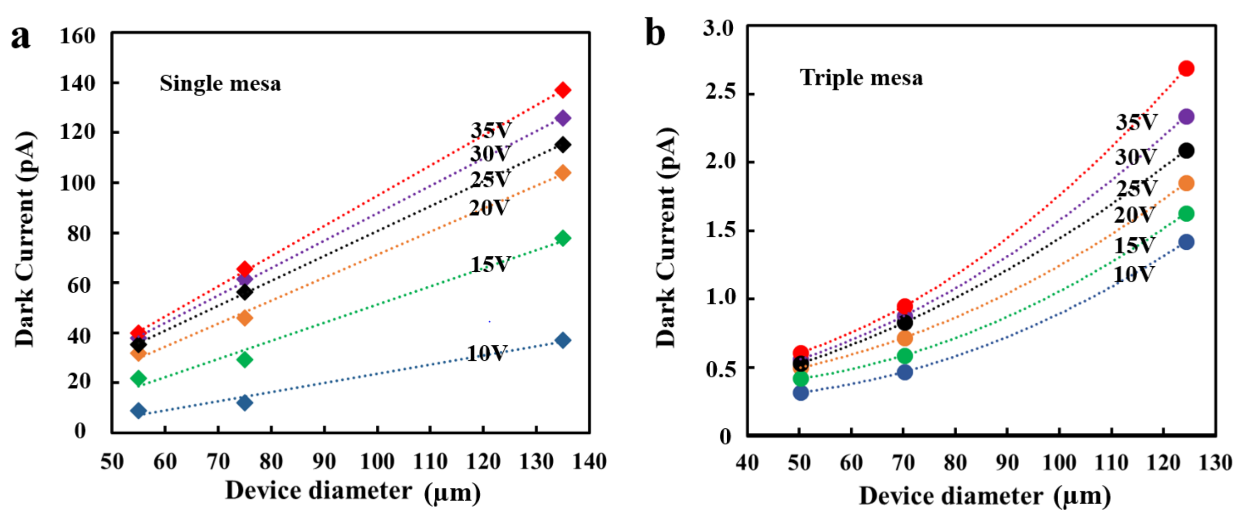

Figure 7-5. Dark current versus device diameter: (a) single-mesa, and (b) triple-mesa APDs.

To measure the spatial uniformity of the photo-response of the triple-mesa APDs, two-dimensional scans were carried out. Figure 7-6 shows the unity gain response of a triple-mesa APD under 543 nm CW laser illumination. Nearly all the response current is confined in the third mesa (smallest one). There is almost no photo-response in the second and first mesa. The circular top contact blocks light and creates a valley between the edge and the center.

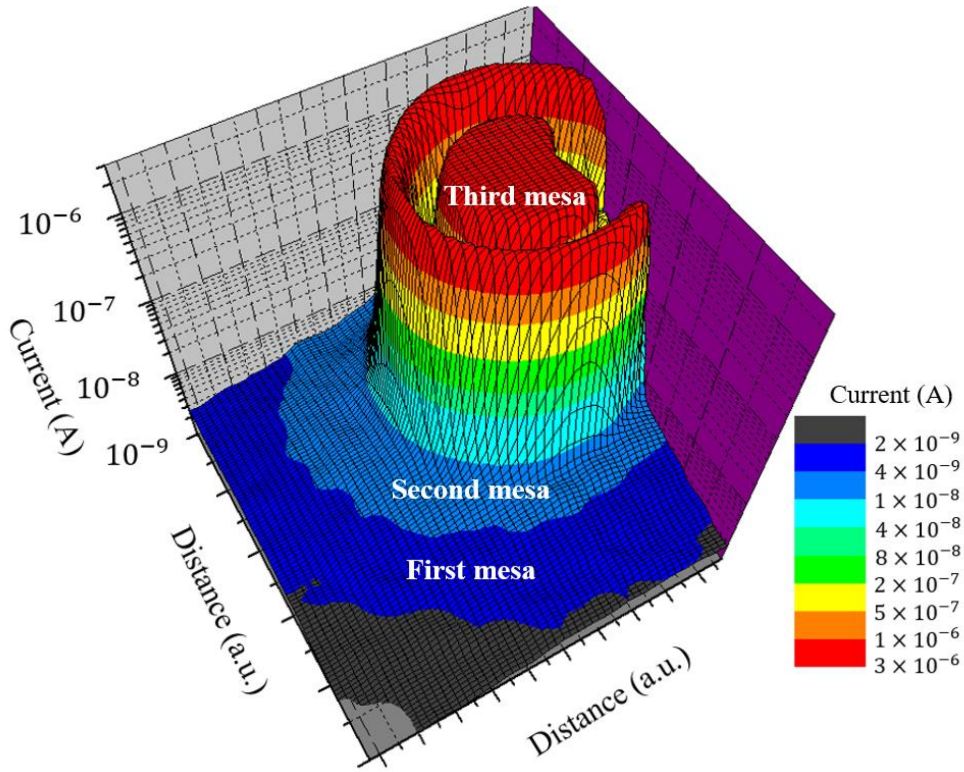

Figure 7-6. Two-dimensional photo response of the InAlAs triple-mesa APDs.

While the triple-mesa structure can suppress the surface leakage better than the single-mesa, this comes at the cost of more complex design and fabrication. One issue is radii of the first and second mesas. Figure 7-7 illustrates the electric field distributions of different radii. As shown in Fig. 7-7(a), when the radial difference between the first and second mesas are both 1 μm, at the foot of each mesa there is electric-field crowding similar to that in the double-mesa. Increasing the radial difference of the second mesa to 3 μm while keeping that of the first mesa at 1 μm, eliminates the electric-field crowding. This represents the smallest triple-mesa radius tolerance; the radius of the first mesa should be at least 1 μm bigger than that of the second mesa, and the second mesa should be more than 3 μm larger than the third mesa.

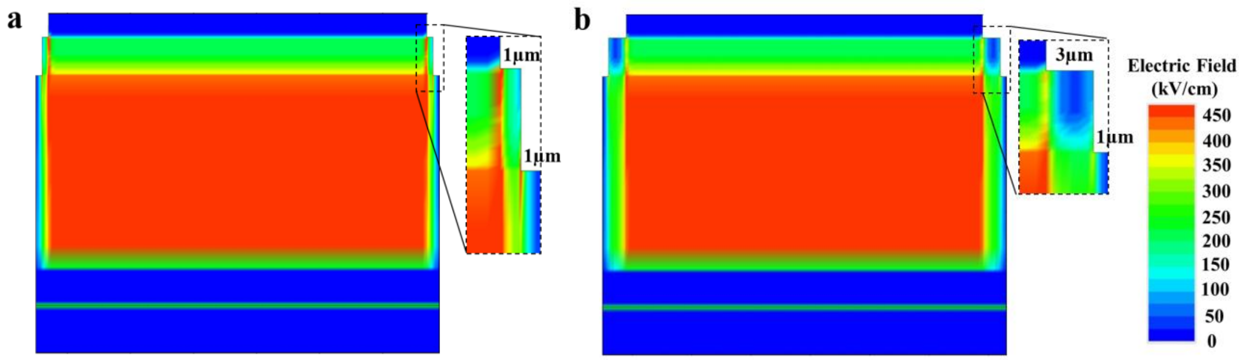

Figure 7-7. Comparison of electric field distribution of triple-mesa InAlAs reach-through APDs with (a) 1 μm and 1 μm surplus radiuses, and (b) 3 μm and 1 μm surplus radiuses.

Another important point is that the triple-mesa requires that etching terminate at the interfaces of layers. If this is not achieved, the electric field distribution will be changed, and may adversely affect the dark current performance, especially at high reverse bias voltage. Figure 7-8(a) illustrates the electric field distribution when the third mesa is over-etched. The electric field on the top mesa sidewall is much higher than that when the etch stops at the interface (i.e. Fig. 7-2(b)). This is confirmed by the measurements of the dark current shown in Fig 7-8(b). At low bias, < -15 V, the over-etched triple-mesa APDs exhibits similar low dark current density of ~ 30 $\mathrm{nA/cm^2}$. However, the dark current increases abruptly at high bias, owing to the high surface electric field around the top mesa.

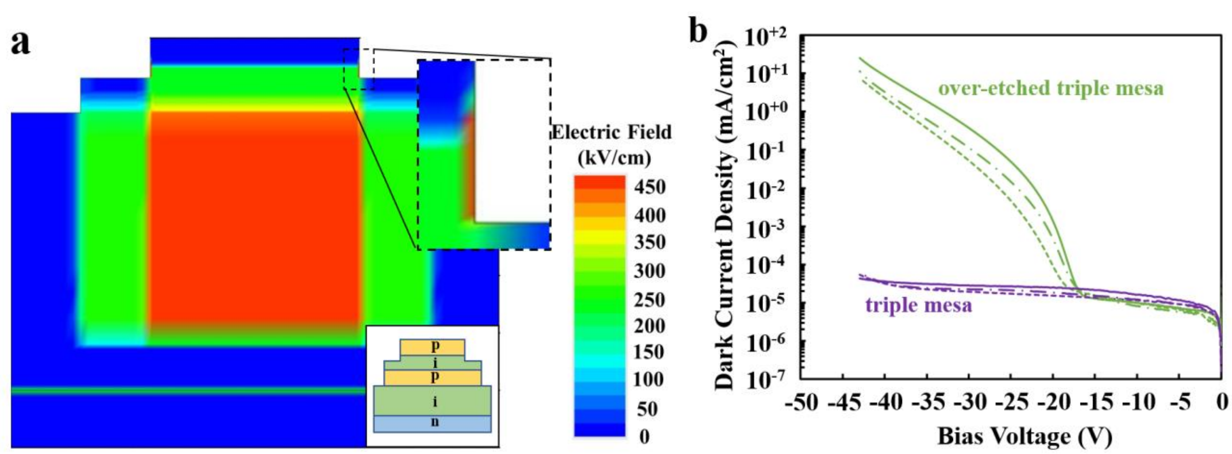

Figure 7-8. Over-etched triple-mesa APDs: (a) electric field distribution, and (b) comparison of dark current density.

7.4 Conclusion

In this chapter, I report triple-mesa reach-through APDs in which the surface-related dark current is effectively suppressed by reducing the surface electric field. The InAlAs triple-mesa APDs exhibit ~ 50 times lower dark current density than single-mesa APDs fabricated from the same wafer. The bulk dark current dominates for the triple mesa devices while that of the single mesa is surface leakage. Two-dimensional scans show almost no photo-response from the wider mesas. Tolerances of triple-mesa design and fabrication have also been discussed.

Chapter 8. III-V on Si APDs

8.1 Introduction

Heterogeneous silicon photonics has drawn significant interest due to its potential for large-scale photonics integration [112]. Integration of III-V compound semiconductors with silicon photonics can reduce cost owing to economy of scale and provide high-performance III-V semiconductor devices that are compatible with Si-CMOS circuits [113]. Recently, there have been numerous reports of heterogeneous silicon photonics, such as waveguides [114], couplers, multiplexers, splitters [115], quantum dot lasers [116], distributed feedback lasers [117], ring cavities [117, 118], modulators [120], and photodiodes [121]. However, there are no silicon photonics-compatible III-V APDs, which play an important role in telecommunication systems [2], owing to their high bandwidth and high sensitivity at 1550 nm. The high bandwidth enables fewer lanes in wavelength-division multiplexing or pulse amplitude modulation, which simplifies the transmission system and results in lower launch power [122]. Another potential impact area of III-V APDs is optical interconnects, a promising approach to solve the bandwidth limitation in the post-Moore's law era. High-speed, high-efficiency, and low-cost heterogeneous silicon photonics optical interconnects have the potential to meet the tremendous data transmission demand in modern processors [123]. The high sensitivity of APDs can permit lower laser power available in optical interconnects and could improve energy efficiency by reducing the power consumption of the lasers, a key metric in future high-bandwidth-density interconnect applications, such as data centers [124]. Integrating III-V APDs with silicon photonics can also expand and improve performance of existing applications such as time-of-flight based light detection and ranging (LIDAR) [124, 125]. In order to integrate single-photon avalanche diodes (SPADs) with CMOS-based front-end circuits and digital signal processors (DSP), LIDAR typically uses Si SPADs arrays, which are referred to as silicon photomultipliers [127]. The integration of III-V APDs on Si substrates with CMOS front-end circuits and DSPs could extend the wavelength beyond the Si response spectrum [127, 128]. Another promising application is next generation access network with optical fiber to the x (FTTx) [130]. Heterogeneously integrated III-V APDs on Si can reduce cost dramatically, thereby alleviating the conflict between data capacity and cost.

8.2 Device structure

There are several approaches to integrate III-V components on silicon, such as hybrid integration and wafer bonding [118, 130]; but heteroepitaxial growth is the only wafer-level solution [132]. In this work, we report the first III-V APDs grown directly on InP/Si templates. The APD reported here is a separate absorption, charge, and multiplication (SACM) structure with an InGaAs absorber and an InAlAs multiplication region. A cross-sectional schematic of the InGaAs/InAlAs SACM APD is shown in Fig. 8-1(a). From top to bottom, the structure consists of a 200 nm InGaAs p-type top contact layer, a 400 nm InGaAs p-type graded-doping absorption layer, a 700 nm InGaAs unintentionally-doped absorption layer, three 30 nm $Al_xInGaAs$ grading layers, an 80 nm InAlAs charge layer, a 250 nm InAlAs unintentionally-doped multiplication layer, a 65 nm InAlAs n-type layer, a 250 nm InAlAs n-type buffer layer, and a 400 nm InAlAs n-type bottom contact layer. The APD sample was grown on a 3.4 × 3.4 cm2 InP/Si template piece by Prof. Bowers' group in UCSB. After 10 min of oxide desorption on the InP surface under As2 overpressure, the growth temperature was set at 500 °C measured by a pyrometer for the entire SACM APD structure. The structure of the InP/Si template is shown in Fig. 8-1(b) consists of a 500 nm Ge layer, 1000 nm GaAs layer, 1100 nm InAlAs linearly graded buffer layer, and 1000 nm InP layer grown by molecular beam epitaxy (MBE) [121]. The InP/Si template was grown on a full 6-inch Si wafer without using selective area growth technique.

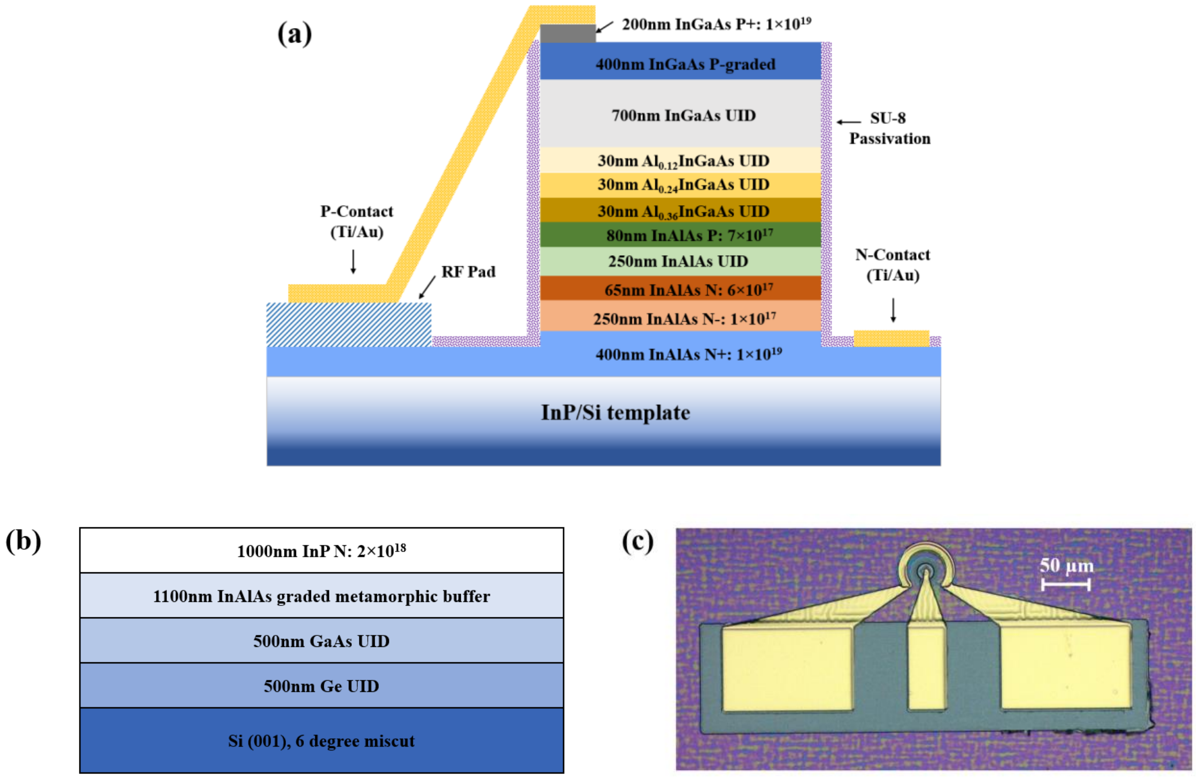

Figure 8-1. (a) Schematic cross section of the InGaAs/InAlAs SACM APD on InP/Si template; (b) Schematic cross section of the InP/Si template; (c) Optical image of a 20 µm-diameter InGaAs/InAlAs SACM APD.

The mesas were formed by standard dry etching with RIE and ICP. Ti/Au was deposited as the top and bottom contacts by electron-beam evaporation. After lift-off of the metals, SU-8 was spun on the sidewall as a surface passivation. Then, an airbridge and GSG pads were plated. Finally, recessed windows were formed by wet etching to increase external quantum efficiency. An optical image of a 20 µm-diameter InAlAs/InGaAs APD is shown in Fig. 8-1(c). The remaining region is cover by SU-8 passivation.

8.3 Results and discussions

The photocurrent, dark current, and gain versus bias voltage characteristics of a 20 µm-diameter InGaAs/InAlAs SACM APD under 1550 nm are shown in Fig. 8-2. The punch-through point is approximately -14 V. The photocurrent remains flat when the bias is slightly higher than -

14 V. This enables straightforward identification of the unity gain point, which was selected at -15 V. Gain > 20 was achieved. Due to the three grading layers, the electrons in the InGaAs absorber can transport into InAlAs multiplication layer, which leads to a relatively high photocurrent before punch-through point.

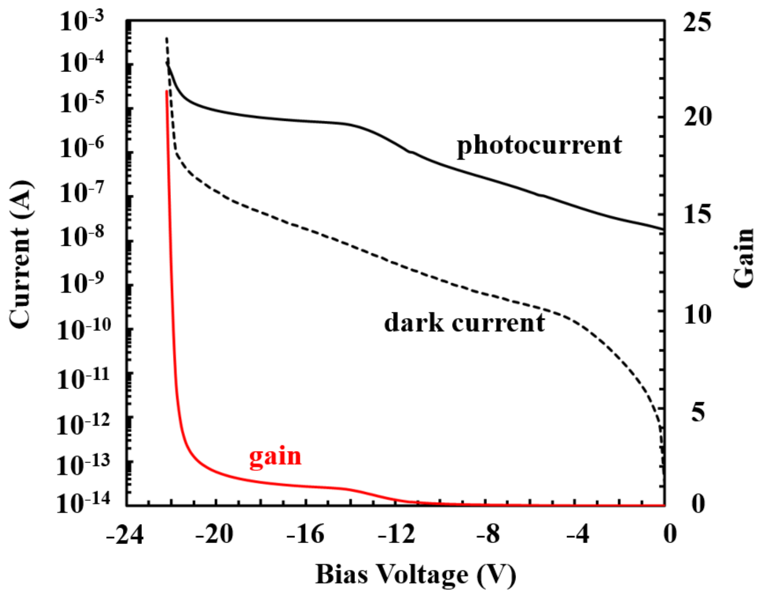

Figure 8-2. Photocurrent (black solid line), dark current (black dash line), and gain (red line) versus bias voltage of a 20 μm-diameter InGaAs/InAlAs SACM APD on silicon under 1550 nm laser.

The circular data points in Fig. 8-3 show the photocurrent versus the incident power at 1550 nm (●) and 1310 nm (▲) at -15 V. These photocurrent points were measured at the unity gain point, and by linear fitting, the responsivities and the external quantum efficiencies at unity gain were calculated. For this device, the responsivity is ~ 0.54 A/W and 0.48 A/W, which corresponds to an external quantum efficiency of ~ 43 % and 46% for 1550 nm and 1310 nm, respectively. The absorption region is the combination of the 400 nm InGaAs p-type graded-doping layer and the 700 nm InGaAs unintentionally-doped absorption layer. Therefore, the total absorption thickness is estimated to be ~1.1 μm. The absorption coefficient of InGaAs at 1550 nm is 0.82 μm^{-1}, and at

1310 nm is 1.0 μm^{-1} [133]. If we assume that the top reflectivity without an anti-reflection coating is R = 0.3, it follows that the calculated external quantum efficiencies at 1550 nm and 1310 nm are $0.7 \times [1 - \exp(-0.82 \times 1.1)] \sim 42$ % and $0.7 \times [1 - \exp(-1.0 \times 1.1)] \sim 46$ %, which are close to the measured results.

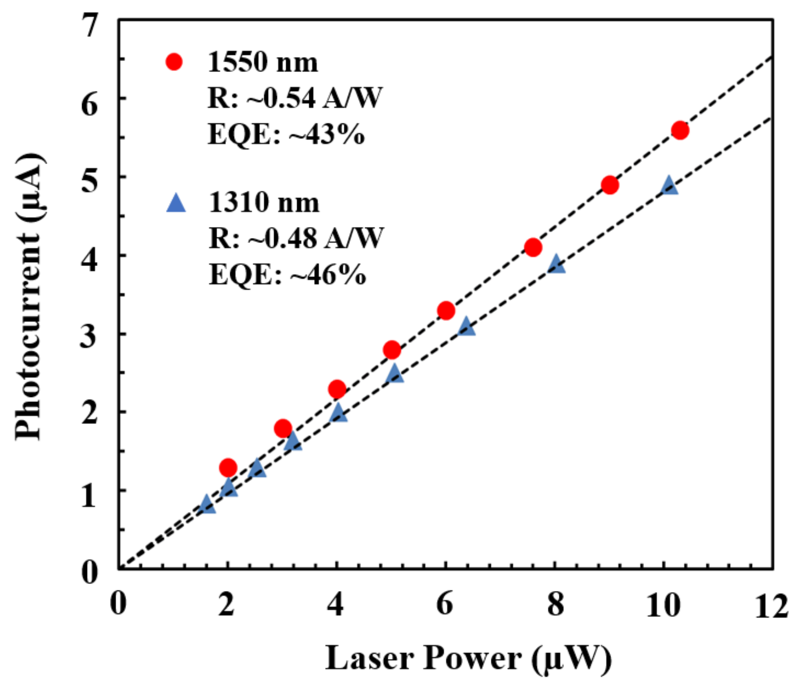

Figure 8-3. The photocurrent of the InGaAs/InAlAs SACM APD on silicon versus the incident power of 1550 nm and 1310 nm laser.

The excess noise characteristics were measured at 1550 nm wavelength using a noise figure meter. Since the InAlAs layers are transparent at 1550 nm, all of the photon-generated carriers are created in the two absorption layers. This results in pure electron injection into the multiplication layer, i.e., the excess noise performance will not be affected by mixed injection. The excess noise versus gain is shown in Fig. 8-4. The k value, which is the ratio of hole to electron ionization coefficients, β/α, is ~ 0.2, which is consistent with reports on similar thickness InAlAs multiplication region APDs [134]. The InGaAs/InAlAs SACM APD grown on silicon exhibits the same excess noise as that based on InP substrate [135].

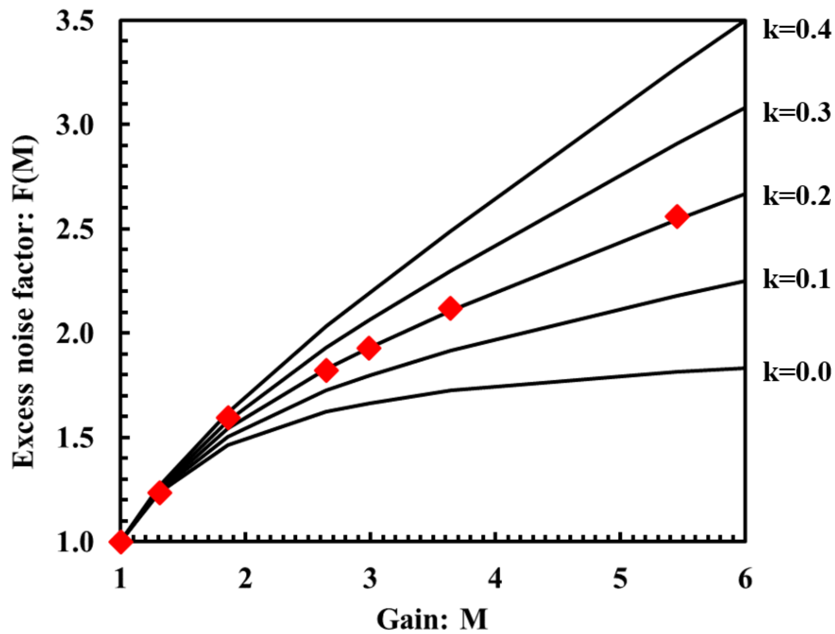

Figure 8-4. Excess noise of the InGaAs/InAlAs SACM APD on silicon.

One of the primary challenges in heteroepitaxial integration is the large lattice mismatch (7.5%) and the concomitant defects in the III-V semiconductor layers, such as threading dislocations, antiphase domains, and cracks [135, 136]. The issue of defects is particularly important for APDs since they operate at high electric field ($10^5 \sim 10^6$ V/cm). Defects can lead to high dark current and limit the performance of APDs. In order to characterize the dark current of this APD on Si, another InGaAs/InAlAs APD on InP substrate with same epilayers was grown for comparison. The dark current densities at room temperature of both APDs are shown in Fig. 8-5(a). The one grown on InP has about an order of magnitude lower dark current density than the one on Si. Figures 8-5(b) and (c) illustrate the dark current from 223 K to 323 K with a step of 20 K for the 20 µm-diameter APD on Si and a 50 µm-diameter APD on InP, respectively. At low bias, both dark currents show significant temperature dependence, the dark currents decrease with temperature. However, different from the APD on InP, the temperature dependence of the APD on

Si is weaker at high bias due to trap-assisted tunneling. Unlike the generation-recombination current, the trap-assisted tunneling current is relatively independent of temperature [31].

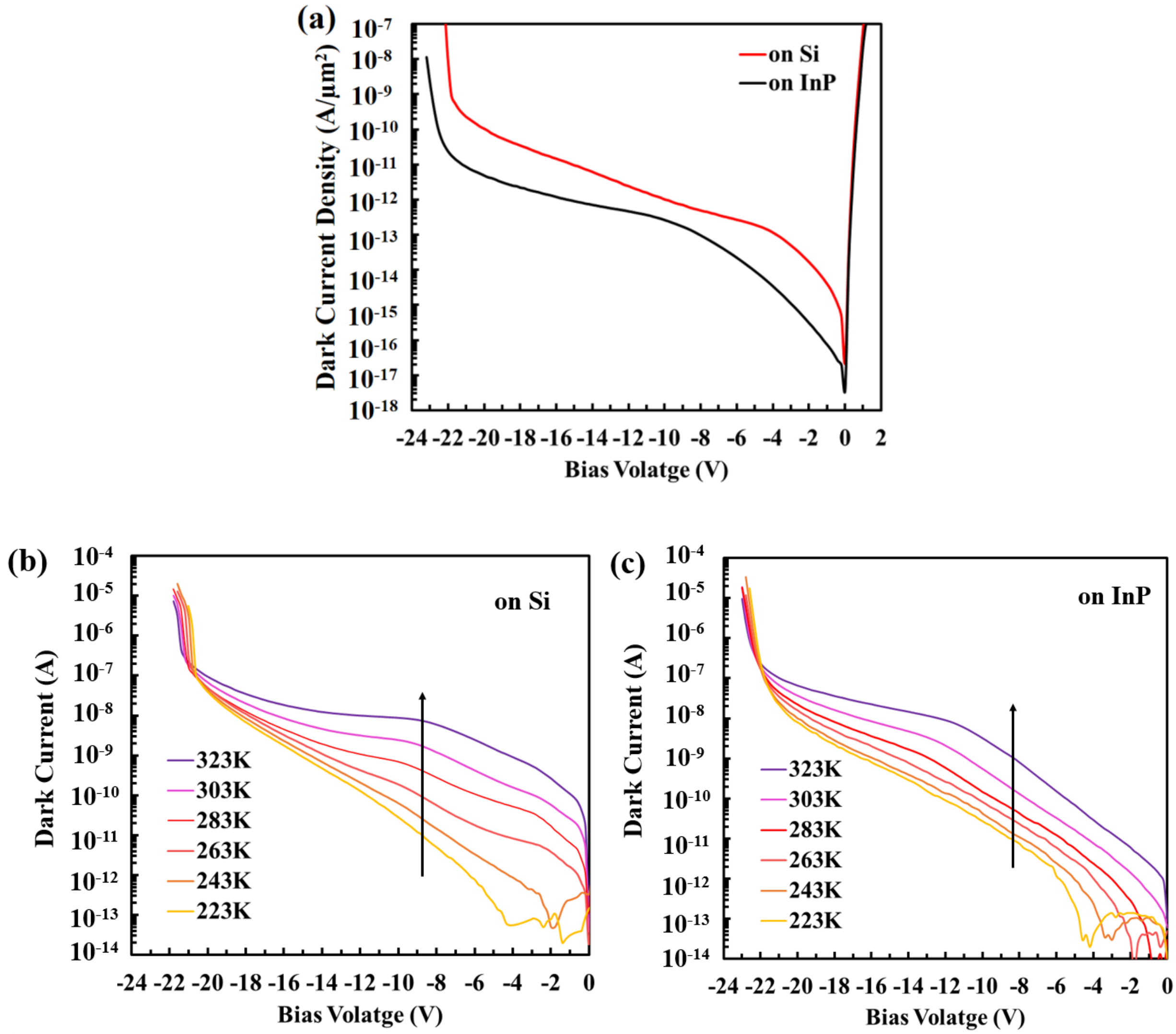

Figure 8-5. (a) Dark current density at room temperature of APDs on Si and InP; temperature dependent dark current versus bias voltage of the (b) 20 µm-diameter APD on Si and (c) 50 µm-diameter APD on InP.

The temperature variation of the dark current a function of the thermal activation energy is expressed as Eq. 2.6. Figure 8-6 shows the dark current fits using this equation at -5 V bias, for the APDs on Si and InP, respectively. At low bias, such as -5 V, the primary source of dark current is generation-recombination, and the activation energies are ~ 0.5 eV and ~ 0.3 eV for the APDs on

Si and InP, respectively. Compared to the APD on InP, the APD on Si has a deeper generation-recombination defect center.

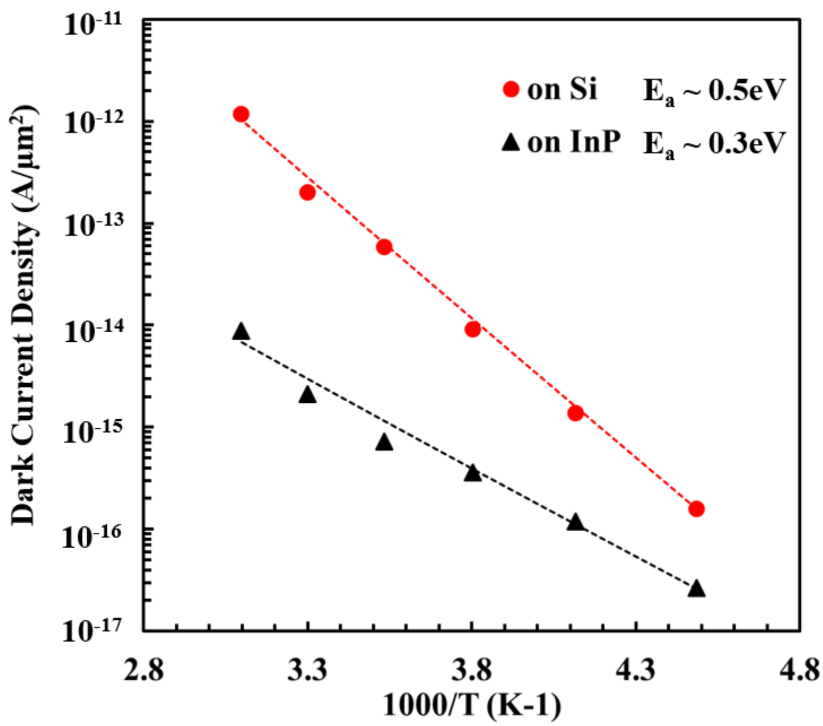

Figure 8-6. The activation energies at -5 V from dark current density versus temperature for APDs grown on Si (●) and InP (▲).

8.4 Conclusion

In this chapter, I have demonstrated the first III-V APD grown by heteroepitaxy on silicon. This InGaAs/InAlAs APD exhibits low dark current, gain > 20, external quantum efficiency > 40%, and similar low excess noise, k ~0.2, as InAlAs APDs on InP. However, owing to the large lattice mismatch between III-V and Si, the InGaAs/InAlAs APD on Si substrate exhibits a higher dark current than that of same structure APD on InP, it also has a deeper generation-recombination defect center.

Chapter 9. Si-Ge waveguide APDs

9.1 Introduction

Silicon photonics technology has become a potential solution for the tremendous data transmission in modern processors, data centers, and high-performance computers (HPCs) [137-140]. The explosive growth of the data traffic will reach > 2.2 zettabytes/year in 2020 as Cisco excepted [141, 142], however, the data transmission through electrical wires has a performance bottleneck in bandwidth and power density. The optical interconnectors with silicon photonics integration have the capability to overcome the limitation in the new zettabyte era. Moreover, owing to the compatibility with complementary metal-oxide-semiconductor (CMOS) chips and low cost, the optical interconnectors have many promising applications, such as next generation optical fiber to the x (FTTx) and light detection and ranging (LIDAR) [124, 129].

In the future, high-bandwidth-density optical interconnects, high bandwidth and high sensitivity receivers are desirable owing to the requirement of high data rates and low power consumption. APDs on silicon-on-insulator (SOI) is a potential choice owing to its internal gain. Compared to conventional p-i-n photodiodes, APDs have a higher sensitivity which permits lower laser power, and, thus, an improvement of link power consumption. Recently, Si-Ge based APDs have drawn significant interest as a result of the compatibility of Si photonics and CMOS circuit integration. There have been numerous efforts to improve the bandwidth, sensitivity, and gain-bandwidth product (GBP) [14, 18, 143-147]. For applications such as data centers and HPCs, the operating temperature is higher than room temperature. However, there is roughly no research on Si-Ge APDs at high temperature. At present, global data centers use approximately 4.16×10^{11} watts, equaling > 3% of the total electricity consumption, and this will increase with the explosive growth in the new zettabyte era. More than a third of this electricity consumption is used for cooling. One degree temperature increase in data centers can save ~ 4% of the energy cost [149]. Google, Microsoft, Intel, and Hewlett Packard Enterprise are raising the thermostats in their data centers. In order to satisfy the higher work temperature in future data centers, the temperature dependence of Si-Ge waveguide APDs have been investigated in this chapter.

9.2 Device structure

The Si-Ge based waveguide SACM APD operates at telecommunication wavelengths. The photo and a cross sectional schematic the Si-Ge APD is shown in Fig. 9-1. The 1550 nm input laser signal is coupled through the grading coupler. The structure of the Si-Ge SACM APD, from the top to bottom, consists of 400 nm p^+-type Ge absorb layer, 50 nm p^--type Si charge layer, 100 nm UID Si multiplication layer, and 220 nm n^+-type Si contact layer. In this APD, a p^+-p^--i-n^+ SACM structure offers the following advantages: the doped Ge absorber ensures the small electrical field in absorber, which reduces the probability of high field tunneling, and further slacken the rigorous requirement of a charge layer; moreover, p^+-type doping in Ge absorber can effectively reduce the relaxation time of photon-generated holes, therefore, the device will exhibit higher speed [15].

Si-Ge SACM APDS were designed by Dr. Zhihong Huang at HP Labs. I carried out these measurements while an intern at HP Labs. The Si-Ge SACM APD was grown on a 220 nm SOI substrate with 3 μm buried SiO_2, which was implanted with arsenic to form an n^+-type Si contact layer. Then the rest of the 150 nm Si was grown by selective growth. The top 50 nm Si was followed by Boron implantation to form a p^-charge layer. After that, a 400 nm Ge absorber was grown with boron to create the p^+-type doping. The whole wafer was covered with SiO_2 as passivation, and Al contacts were deposited through the opened holes. The fabrication process was finished by the Institute of Microelectronics (IME), Singapore.

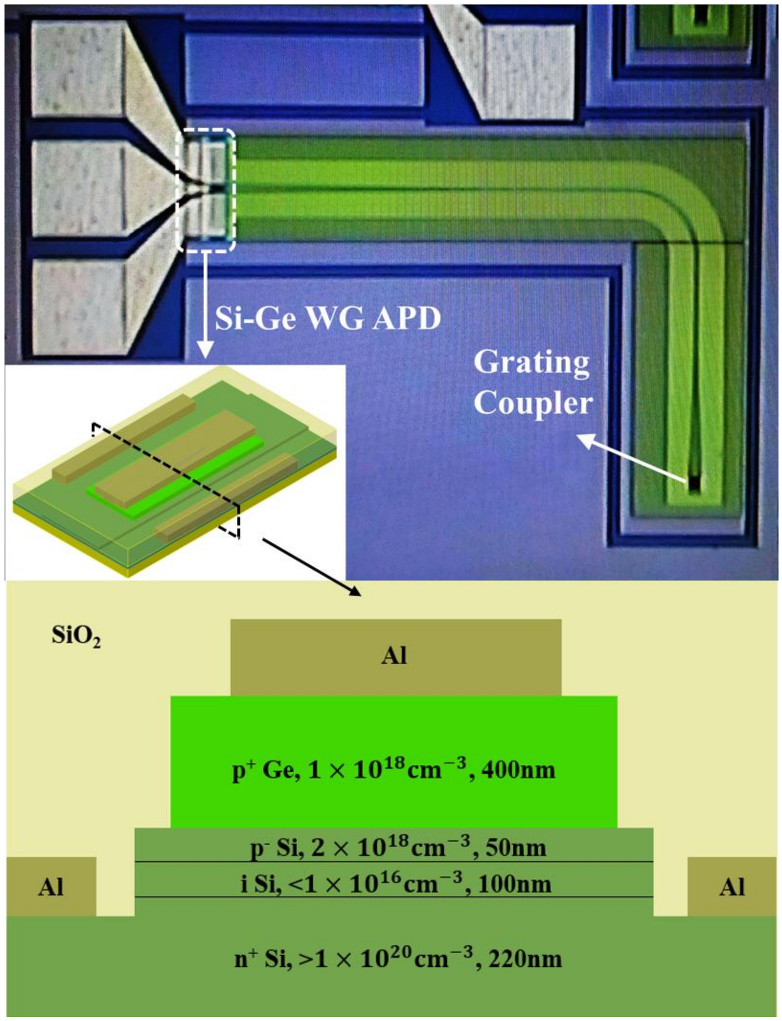

Figure 9-1. Photo and schematic diagram of the Si-Ge waveguide SACM APD.

9.3 Temperature dependent characteristics

9.3.1 Multiplication gain and breakdown voltage

All measurements were carried out with 4 μm-width and 10 μm-length APDs, which is defined by the Ge layer dimension. The gain-temperature stability is a significant figure of merit for APDs, especially for the APDs used in dynamic ambient temperature environments. Owing to higher phonon scattering rates with increasing temperature the impact ionization rates decrease with temperature [27]. Therefore, with increasing temperature APDs require higher electrical field to maintain constant gain value. The gain-temperature characteristics for the Si-Ge SACM APD are shown in Fig. 9-2(a). Gain > 15 was achieved from 23 °C to 90 °C at fixed bias voltage. The gain-temperature stability of APDs can be characterized by the breakdown voltage variations with temperature, $\Delta V_{bd}/\Delta T$ [20], which is determined by plotting 1/gain versus voltage, as shown in Fig. 9-2(b). The intersection of linear fits lines along the voltage-axis are the breakdown voltages where 1/gain = 0, and gain = ∞ as discussed in Section 3.2 and 5.2.3. The breakdown voltages are ~ 10 V, which is low enough to meet the highest computer architecture supplied voltage, 12 V [150]. By plotting these calculated breakdown voltages versus temperature as illustrated in Fig. 9-2(c), it was determined that the temperature dependent breakdown coefficient $\Delta V_{bd}/\Delta T$ = 4.2 mV/°C.

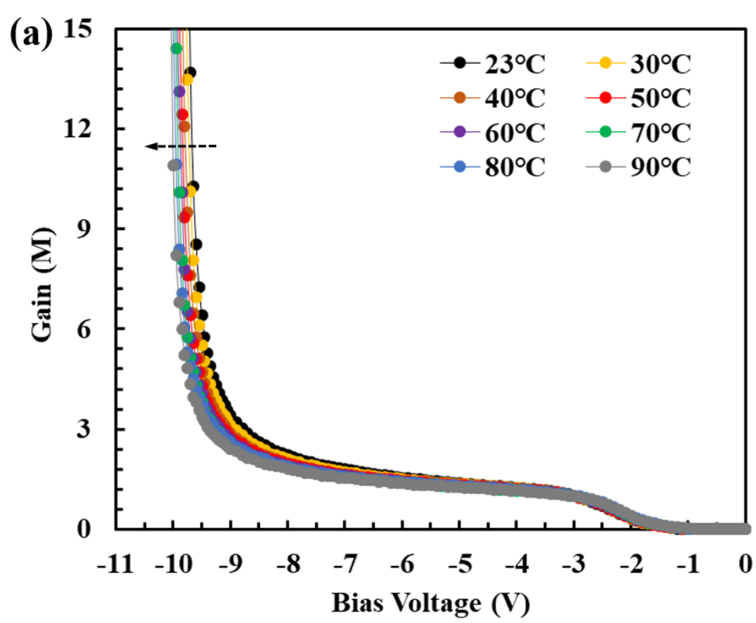

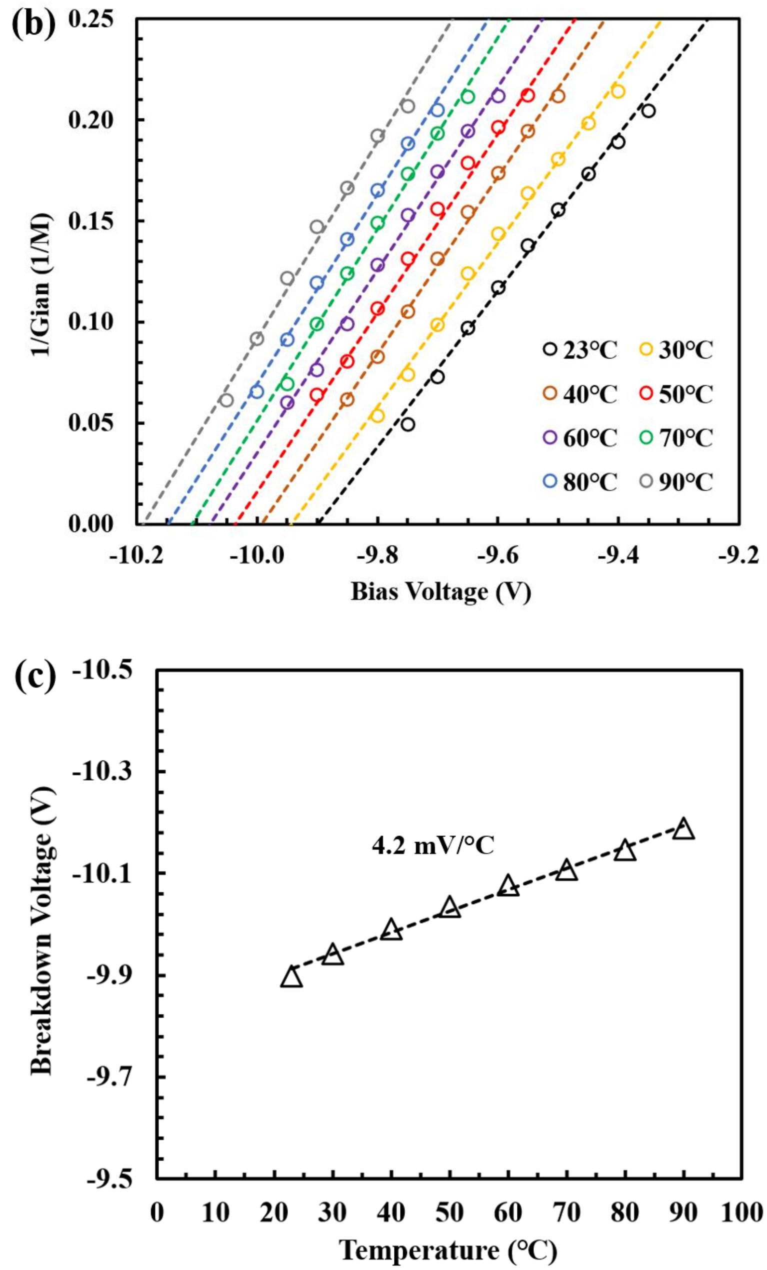

Figure 9-2. (a) Multiplication gain versus bias voltage, (b) 1/gain versus bias voltage, and (c) breakdown voltages for Si-Ge waveguide SACM APD under different temperatures.

The gain-temperature stability of APDs not only depends on the semiconductor materials, but also depends on the device thickness. For SACM APDs, this includes the mulitiplication region width, w_m, and the depletion region width, $w_{depletion}$. The $\Delta V_{bd}/\Delta T$ for SACM APDs can be expressed as [45]:

$$\frac{\Delta V_{bd}}{\Delta T}(SACM) = \frac{\Delta V_{bd}}{\Delta T}(pin) \times \frac{w_{depletion}}{w_m}, \tag{9.1}$$

where $\Delta V_{bd}/\Delta T\ (pin)$ is the coefficient of a p-i-n APD with the same w_m thickness of the multiplication region. In Table 9-1, I compared $\Delta V_{bd}/\Delta T$ values of several SACM APDs for telecommunication wavelength [44, 150-156]. Figure 9-3(a) shows the data in Table 9-1, compared to different thickness InAlAs-InGaAs and InP-InGaAs SACM APDs. The Si-Ge SACM has much smaller $\Delta V_{bd}/\Delta T$ value, owing to the thin w_m and $w_{depletion}$.

Waveguide APDs can effectively decouple the bandwidth and quantum efficiency. In APDs with thin multiplication layers, the electric field required to achieved a specific gain is higher than that in with thick multiplication regions. Therefore, carriers in thin APDs acquire the ionization threshold energy in a shorter distance, which means carriers experience fewer phonon scattering events before ionization. As a result, the ionization coefficients of carriers are more insensitive to temperature, which yields small $\Delta V_{bd}/\Delta T$ [72]. $\Delta V_{bd}/\Delta T\ (SACM)$ for InP, InAlAs, and Si SACM APDs can be calculated by substituting $\Delta V_{bd}/\Delta T\ (pin)$ values into Eq. 9.1. For these three semiconductor APDs, empirical fitting of $\Delta V_{bd}/\Delta T\ (pin)$ yields the following relations [43, 44]:

$$\frac{\Delta V_{bd}}{\Delta T}(pin - InP) = 42.5 \times w_m + 0.5, \tag{9.2}$$

$$\frac{\Delta V_{bd}}{\Delta T}(pin - InAlAs) = 15.3 \times w_m + 1.0, \tag{9.3}$$

$$\frac{\Delta V_{bd}}{\Delta T}(pin - Si) = 32.2 \times w_m - 0.6, \tag{9.4}$$

where the w_m unit is μm, and that of $\Delta V_{bd}/\Delta T\ (pin)$ is $mV/°C$. Figure 9-3(b)-9-3(d) illustrate the relationship of $\Delta V_{bd}/\Delta T\ (SACM)$, w_m, and $w_{depletion}$, which exhibit good agreement with the reported data in Fig. 9-3(a). The low coefficient, $\Delta V_{bd}/\Delta T = 4.2\ mV/°C$, for Si-Ge waveguide SACM APDs is desirable for diminishing the price and complexity of the temperature control system in many applications, such as data centers, HPCs.

Table 9-1. $\Delta V_{bd}/\Delta T$ of different types SACM APDs [44, 150-156].

SACM APD Types	Multiplication Width (μm)	Depletion Width (μm)	$\Delta V_{bd}/\Delta T$ (mV/°C)	Ref.
InAlAs-InGaAs	0.13	0.75	15	Levine06
	0.15	1.15	23	Tan10
	0.2	1.1	21	Ishimura07
	0.2	1.4	25	Rouvie08
	1	2.7	40	Goh09
InP-InGaAs	0.2	1.2	46	Tan10
	0.4	3.27	150	Zhao18
	0.5	3.5	150	Ma95
	0.8	2.4	100	Sidhu06
Si-Ge	0.1	0.15	4.2	This work

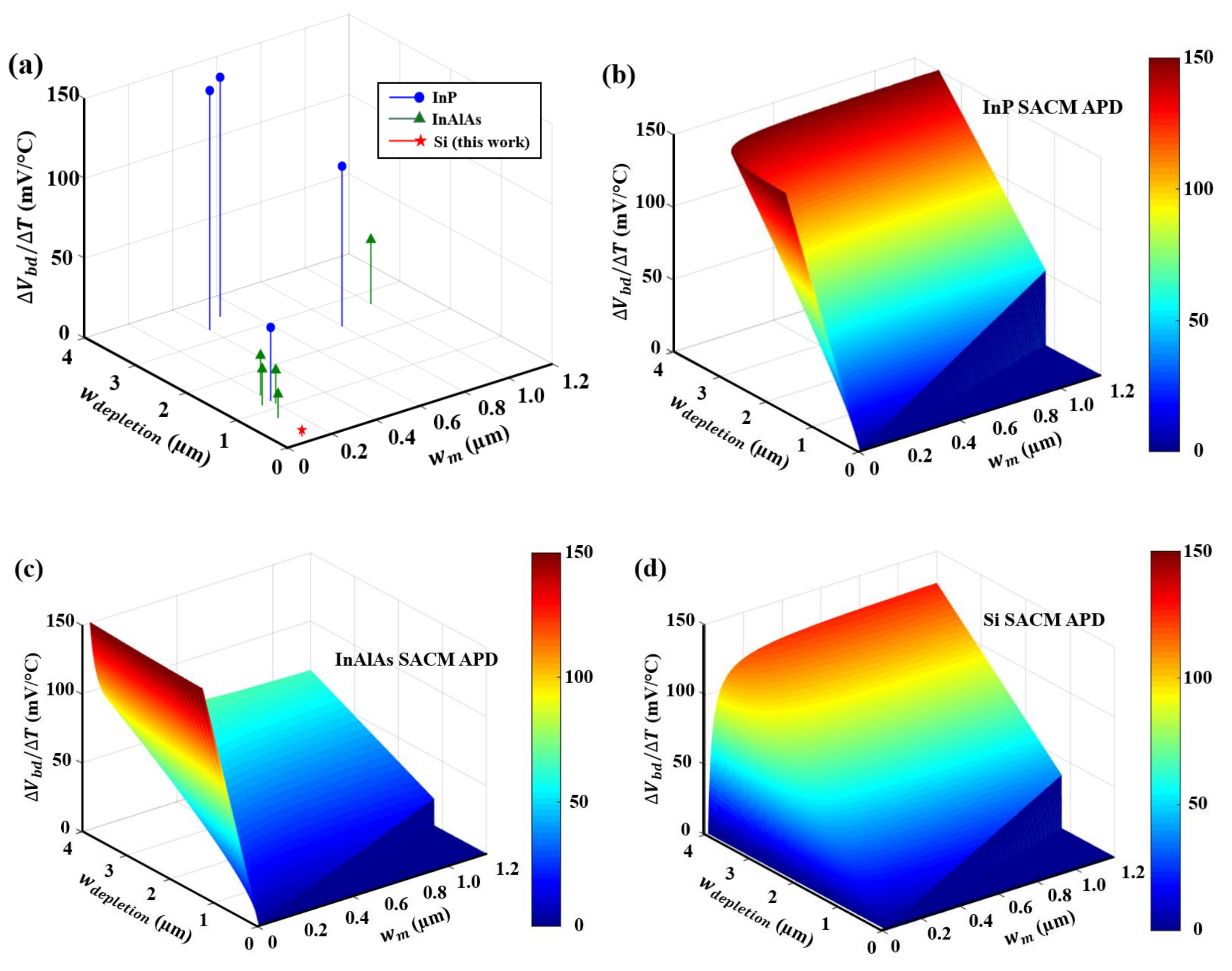

Figure 9-3. Relationship of $\Delta V_{bd}/\Delta T$ $(SACM)$, multiplication width, and depletion width for (a) experimental

data of InP, InAlAs, and Si SACM APDs; calculated data of (b) InP, (c) InAlAs, and (d) Si SACM APDs [44, 150-156].

9.3.2 Dark current and activation energy

The dark current at different temperature is shown in Fig. 9-4(a). The dark current increases uniformly with temperature. At bias voltage near -10 V, the dark current also shows a slight shift to higher voltage with temperature due to the temperature dependent gain. The relationship of APD dark current and temperature is given by Eq. 2.6, and the activation energy of the Si-Ge SACM APD can be extracted. I chose the dark current at -1 V, -2 V, and -3 V to prevent interference factors, such as temperature dependent gain and tunneling dark current [29]. At this low bias region, generation-recombination (G-R) is the primary source of dark current, and an accurate activation energy can be obtained. Figure 9-4(b) indicates that for all three biases, the activation energy is, $E_a = 0.4\ eV$. This value means the Ge absorption layer dominates the dark current, and $E_a = 0.4\ eV$ is also consist with the Si-Ge APDs in Ref. [158].

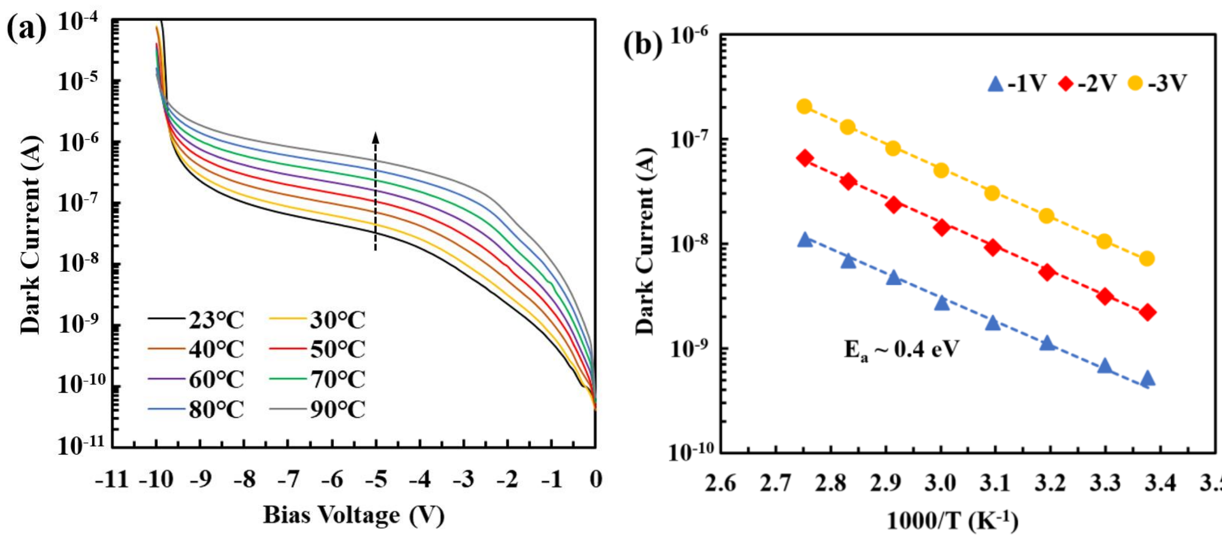

Figure 9-4. (a) Dark current versus bias voltage, and (b) activation energy for different bias voltages for Si-Ge waveguide SACM APD.

9.3.3 Bandwidth and gain-bandwidth product

The temperature dependent bandwidths of the Si-Ge SACM APD were measured with a 1550 nm femtosecond pulse laser and an Agilent DCA86100C sampling scope [159]. The system excess loss is ~ -0.5 dB at 25 GHz. By using the Fourier transform and considering the system loss, the frequency domain results can be extracted Figs. 9-5(a) to 9-5(g) demonstrate the bandwidths at temperature from 30 °C to 90 °C with 10 °C step. Fig. 9-5(h) displays the raw measured pulse responses at 90 °C with the APD gain of 1, 5, 10 and 12. It has a full width at half maximum (FWHM) of ~ 14.5 ps.

The bandwidth increases with gain in the low gain region owing to the shorter carrier transit time at higher electrical field. In the medium gain regime, M = 6 ~ 9, the bandwidth is constant. As the gain increases further, the bandwidth drops owing to the longer multiplication time, which results in the gain-bandwidth product (GBP). However, in the higher gain regime, the bandwidth increases again, yielding an enhanced GBP of ~ 300 GHz. The similar enhanced GBP phenomenon has been observed in Ref. [159-161]. The primary reason for this is the space charge effect caused by the high dark and photo currents at high bias voltage. The space charge effect introduces an electrical field collapse in the Si multiplication region, while the total bias voltage across the APD is constant, the electric field in the Ge absorber raises and the carrier transit time decreases.

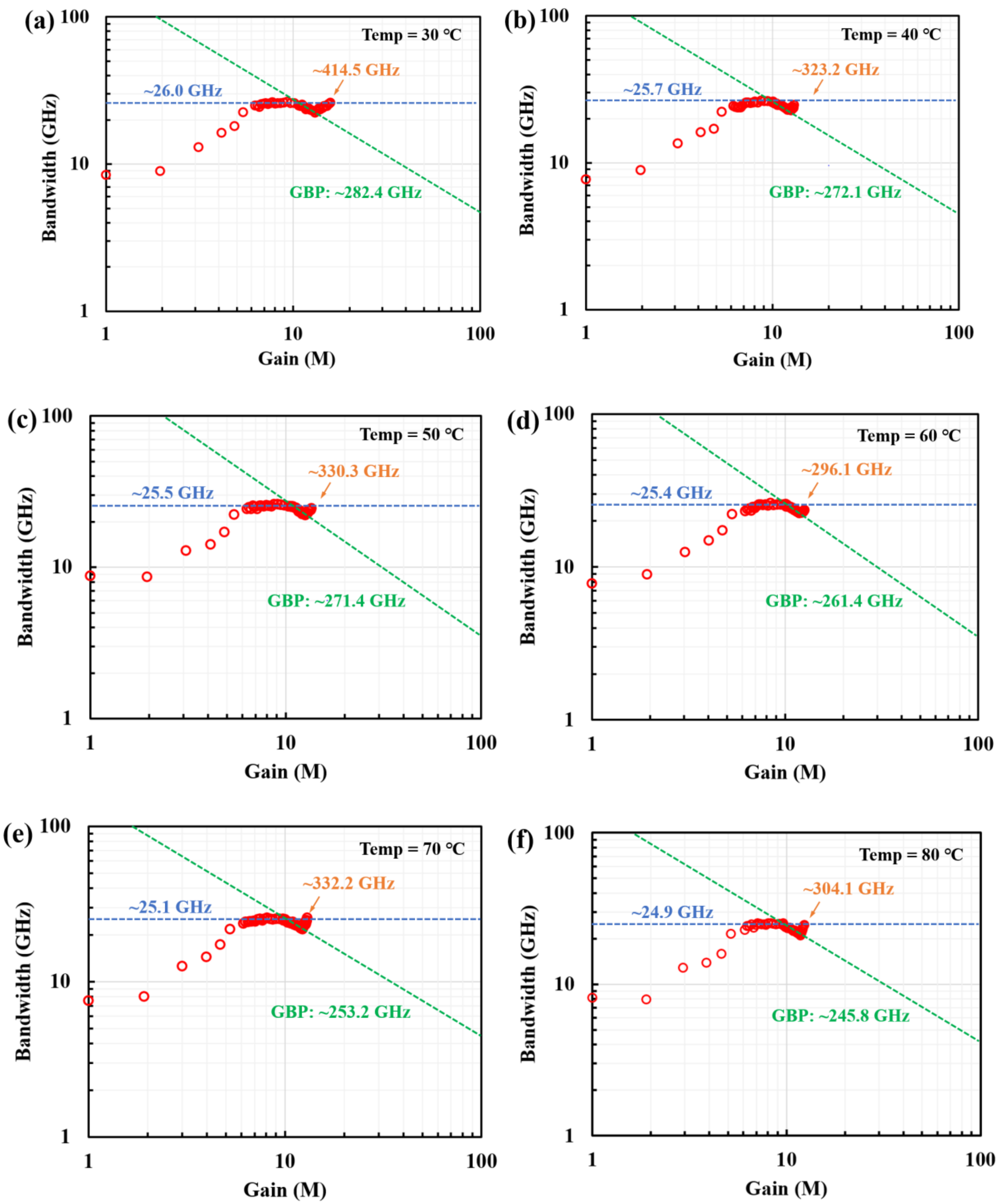

(a)
Temp = 30 °C
~26.0 GHz
~414.5 GHz
GBP: ~282.4 GHz
(b)
Temp = 40 °C
~25.7 GHz
~323.2 GHz
GBP: ~272.1 GHz
(c)
Temp = 50 °C
~25.5 GHz
~330.3 GHz
GBP: ~271.4 GHz
(d)
Temp = 60 °C
~25.4 GHz
~296.1 GHz
GBP: ~261.4 GHz
(e)
Temp = 70 °C
~25.1 GHz
~332.2 GHz
GBP: ~253.2 GHz
(f)
Temp = 80 °C
~24.9 GHz
~304.1 GHz
GBP: ~245.8 GHz
Bandwidth (GHz)
Gain (M)

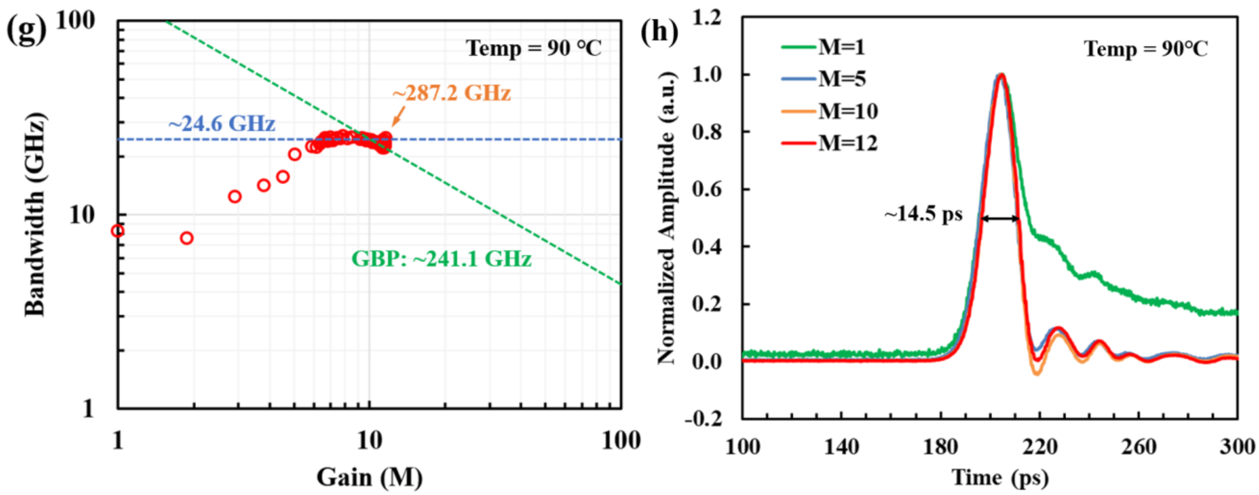

Figure 9-5. Measured bandwidth versus gain at (a) temp = 30 °C, (b) temp = 40 °C, (c) temp = 50 °C, (d) temp = 60 °C, (e) temp = 70 °C, (f) temp = 80 °C, (g) temp = 90 °C, and (h) impulse response at temp = 90 °C of the 4 μm × 10 μm Si-Ge SACM APD.

By plotting the constant bandwidth in the medium gain regime, the frequency response at different temperature can be determined. Fig. 9-6(a) shows that the 3-dB bandwidth decreases slightly with temperature. Figure 9-6(b) shows the temperature dependence of the bandwidth and GBP. They both exhibit a negative linear relationship with temperature. The 3-dB bandwidth decreases from 26.0 GHz at 30 °C to 24.6 GHz at 90 °C, a decrease of ~ 22 MHz/°C (~ 0.09% /°C). The GBP decreases from 282.4 GHz to 241.1 GHz when temperature raises 60 °C, a decrease of ~ 0.695 GHz/°C (~ 0.24% /°C).

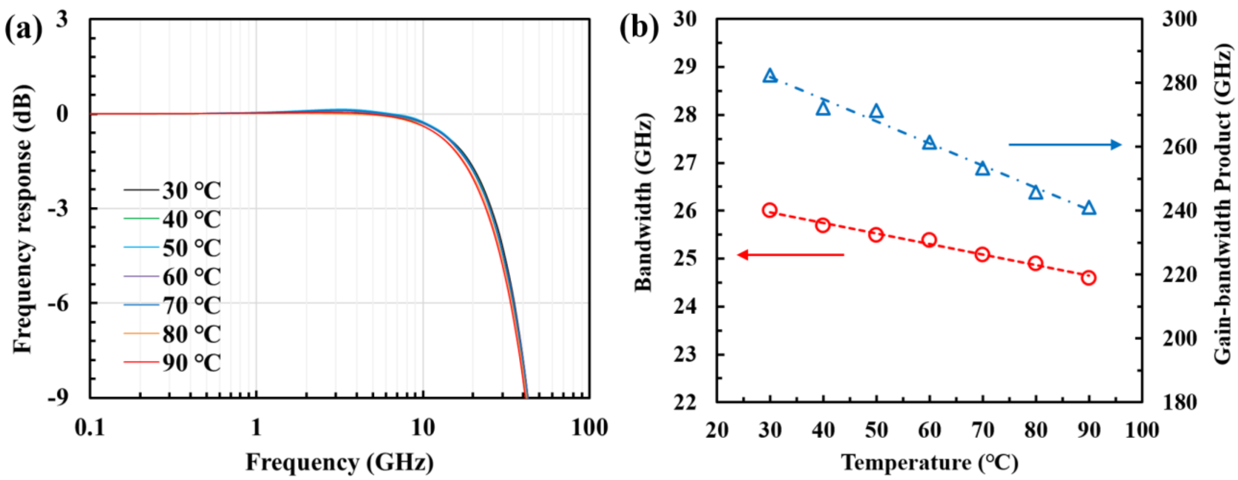

Figure 9-6. (a) Frequency response at different temperature, and (b) bandwidth and gain-bandwidth product versus temperature of the 4 µm × 10 µm Si-Ge SACM APD.

9.3.4 Quantum efficiency and responsivity

Increased temperature also introduces a decrease in the bandgap due to thermal expansion. The lattice constant expands with temperature, and hence shifts the semiconductor band structure. The temperature dependence of the bandgap can be expressed as [163]:

$$E_g(T) = E_g(0K) - \frac{AT^2}{T+B}, \tag{9.5}$$

where $E_g(0K)$ is the bandgap at 0 K, A and B are empirical fitting parameters. Since the bandgap of the Ge absorber decreases with temperature, the absorption coefficient at 1550 nm increases. Figure 9-8(a) shows the photocurrent at unity gain versus 1550 nm for the 4 µm × 10 µm Si-Ge waveguide SACM APD. The photocurrent increases with temperature as expected. By linear fitting, the internal quantum efficiency and responsivity at 1550 nm can be obtained. The measured data versus temperature is shown in Fig. 9-7(b). At room temperature, T ~ 23 °C, the internal quantum efficiency ~ 56%, which is consistent with a previous report in Ref. [15]. As the temperature increases, the Si-Ge APD can achieve higher quantum efficiency. It saturates to 100%

for temperature > 80 °C. From Ref. [164], the square root of the Ge absorption coefficient is almost proportional to the temperature, i.e. $\Delta\alpha^{\frac{1}{2}} \propto T$, as shown in Fig. 9-7. Therefore, the temperature dependent absorption coefficient and quantum efficiency yield the following equations:

$$\alpha(T) = \left[C \times (T - T_0)\right]^2 + \alpha(T_0)\,, \tag{9.6}$$

$$QE = 1 - \exp\left[-\left[\left[C \times (T - T_0)\right]^2 + \alpha(T_0)\right] \times L\right], \tag{9.7}$$

where α is the absorption coefficient, C is a fitting parameter obtained from the measurements, T_0 is the initial temperature (here it is 23 °C), and L is the Ge absorber length (here it is 10 μm). The fitted quantum efficiency at different temperatures is shown as the dash lines in Fig. 9-8(b). Good agreement with experiment is observed.

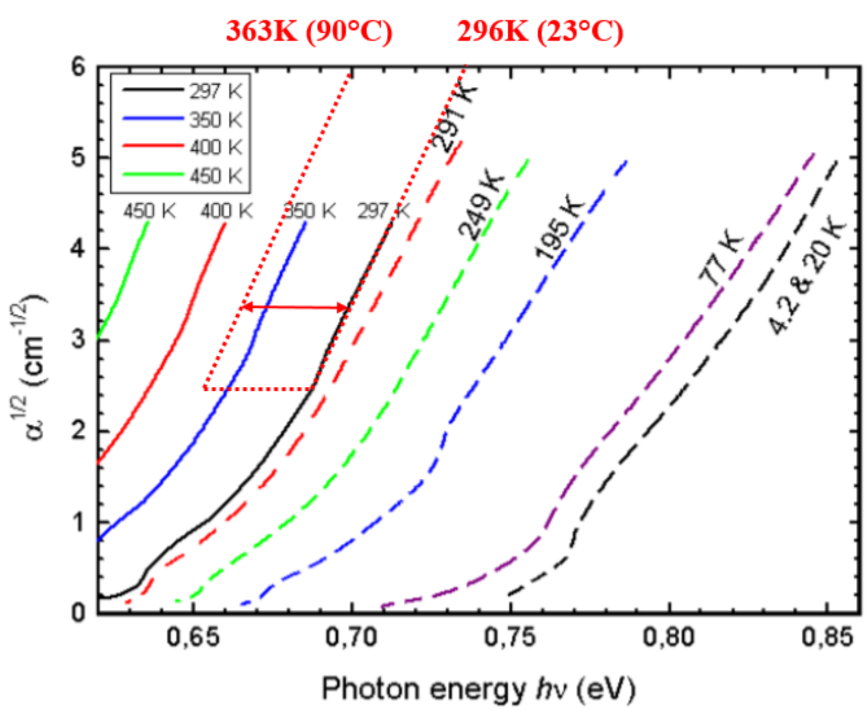

Figure 9-7. Low level absorption edge in Ge at various temperatures [164].

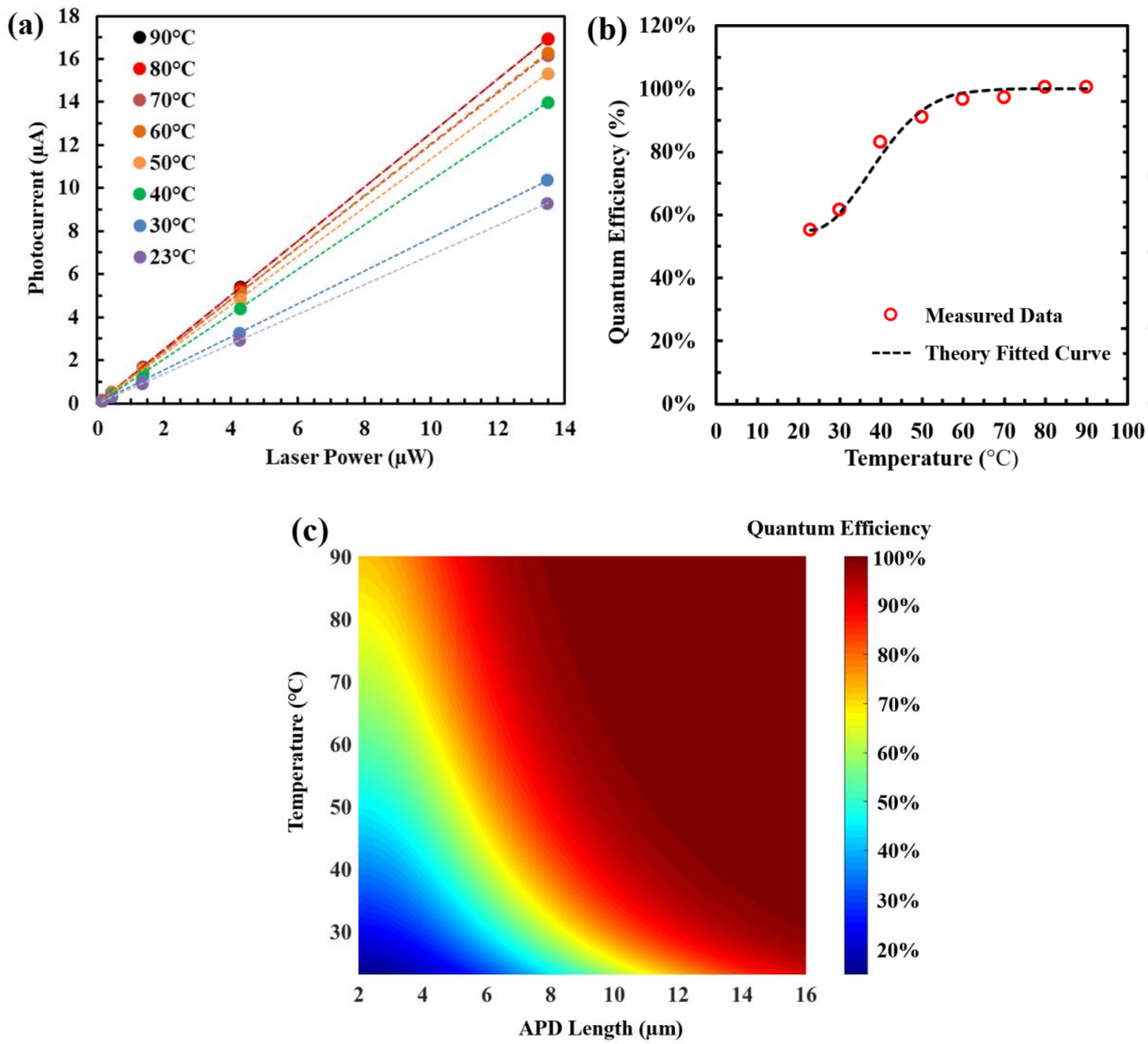

Figure 9-8. (a) Photocurrent versus 1550 nm laser power, and (b) quantum efficiency and responsivity of the 4 μm × 10 μm Si-Ge SACM APDs at different temperatures; (c) 2D color map of calculated quantum efficiency versus temperature and length of APD.

A 2D color map of the calculated quantum efficiency versus temperature and APD length based on Eq. 9.7 is plotted in Fig. 9-8(c). When the temperature > 60 °C, the Si-Ge SACM APD can achieve quantum efficiency > 70% with only 6 μm APD length, which results in a higher speed by reducing the RC time limitation.

9.3.5 Eye diagrams

The NRZ and PAM4 eye diagrams of the 4 μm × 10 μm Si-Ge waveguide APD were measured at 30 °C, 60 °C, and 90 °C, respectively. I used a 96 GSa/s arbitrary waveform generator (AWG) to produce 2^9-1 pattern length NRZ and PAM4 PRBS9 (Pseudo Random Binary Sequence) signals. A sampling scope was used to record the output electrical signal of the APDs. At each temperature, I measured the electrical eye diagrams with gain of M=6, 8, and 11.5, as shown in Fig. 9-9(a) to 9-9(c). The Si-Ge waveguide APD exhibits clear open eye diagrams from 30 °C to 90 °C at data rates of 32 Gbps (NRZ) and 64 Gbps (PAM4). As temperature increases, the openings in the eye diagrams become larger due to the higher temperature-dependent quantum efficiency, however, they also become noisier as a result of higher dark current.

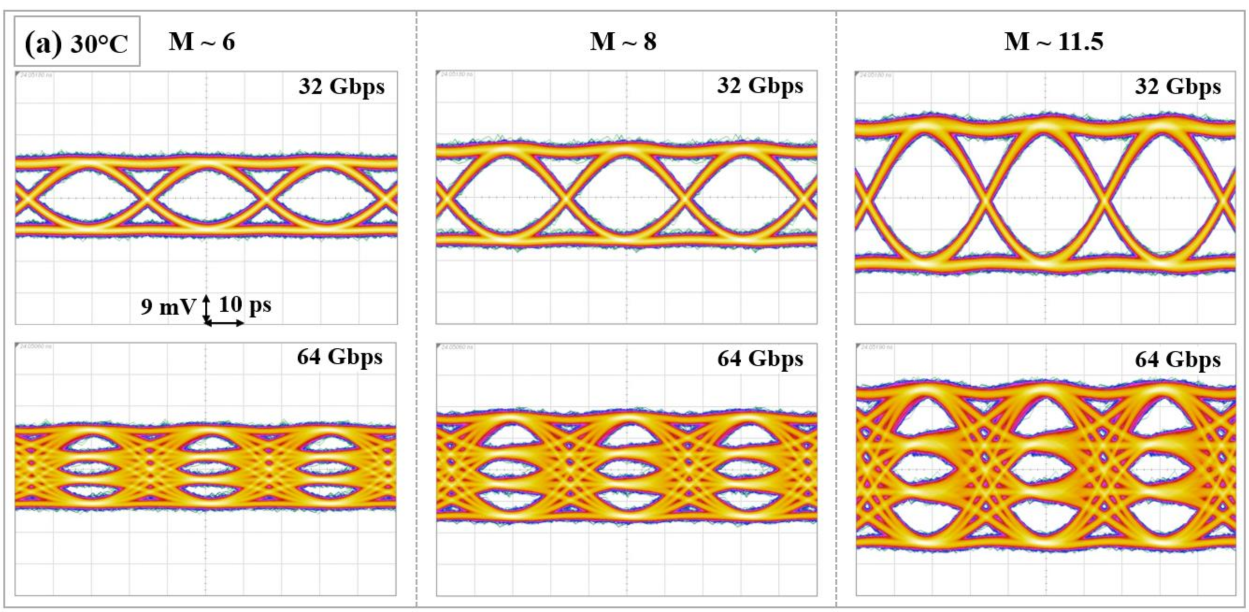

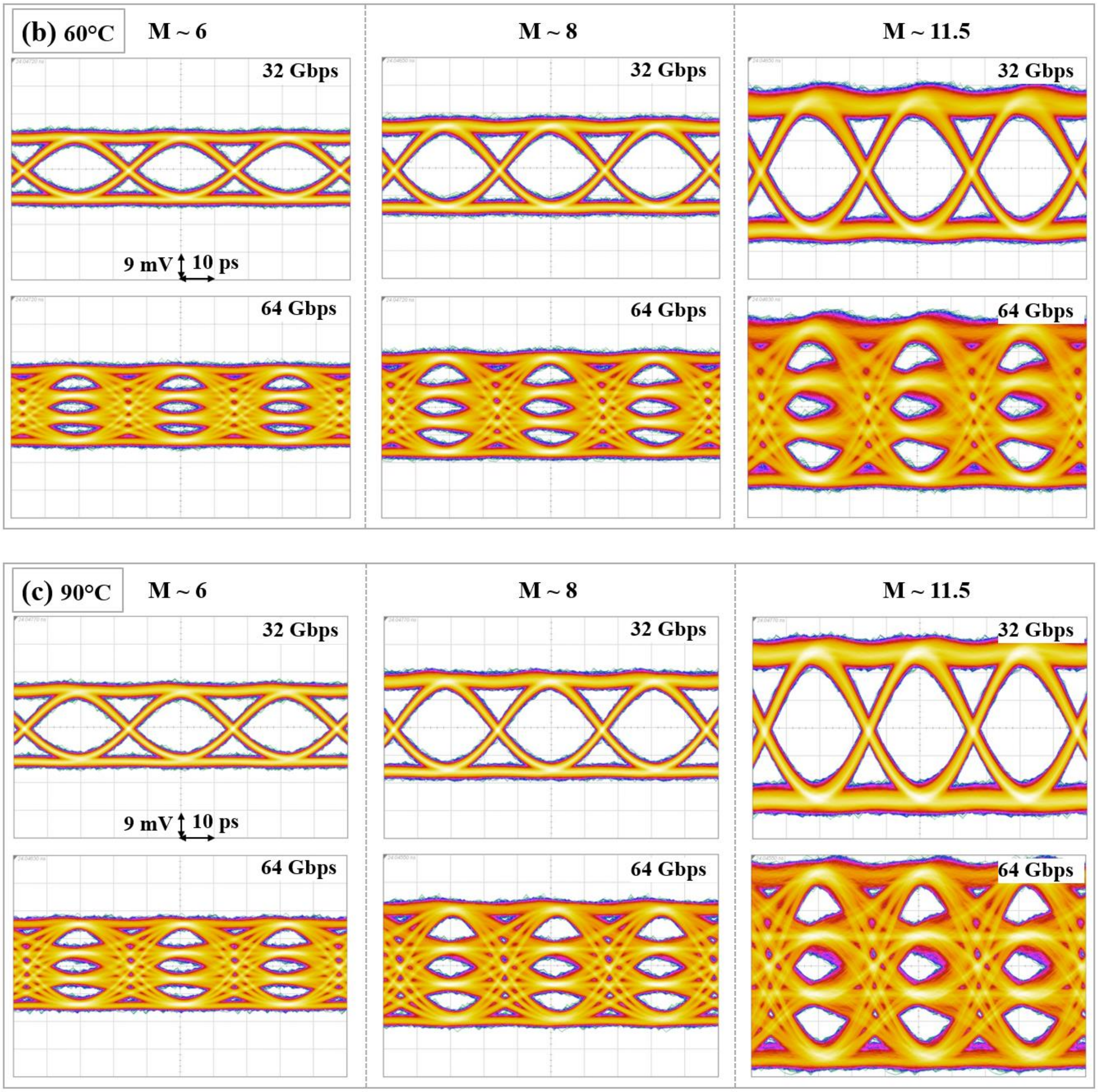

Figure 9-9. Electrical eye diagram at 32 Gbps NRZ and 64 Gbps PAM4 with M=6, 8, and 11.5 at (a) temp = 30 °C, (b) temp = 60 °C, and (c) temp = 90 °C of the 4 μm × 10 μm Si-Ge SACM APD.

The setup for the eye diagram measurements is shown in Fig. 9-10. A thermoelectric cooler (TEC) was put under the APDs, and it controlled the wafer temperature from 30 °C to 90 °C. The 96 GSa/s AWG generated a PRBS9 data stream to drive a 25 GHz Mach-Zehnder modulator (MZM). A modulated 1550 nm laser was coupled into a grating coupler of Si-Ge WG APDs after an erbium-doped fiber amplifier (EDFA) and bandpass filter (BPF) in order to compensate the system loss and coupling loss. All signal distortion caused by the MZM, TIA, and cables was calibrated with the internal calibration tool of the AWG. The NRZ and PAM4 eye diagrams at different temperature and different gain bias were directly recorded with a 65 GHz Agilent DCA86100C digital communication analyzer oscilloscope.

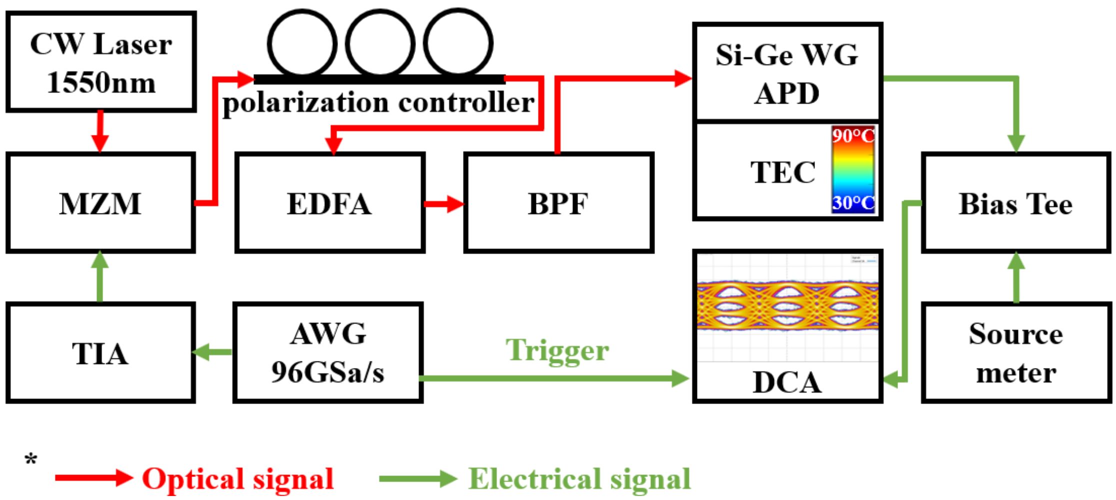

Figure 9-10. Eye diagram measurement setup, where CW is continuous wave, MZM is Mach-Zehnder modulator, EDFA is erbium-doped fiber amplifier, BPF is bandpass filter, TEC is thermoelectric cooler, TIA is transimpedance amplifier, AWG is arbitrary waveform generator, and DCA is digital communication analyzer oscilloscope.

9.4 Ge/Si APDs with distributed Bragg reflector

In order to obtain high-speed, it is beneficial to reduce the length of waveguide APD to decrease the RC time constant. However, that can decrease the quantum efficiency if some of the incident signal is transmitted without being absorbed. In this section, a distributed Bragg reflector (DBR) incorporated at the end to the Si-Ge APD to improve the sensitivity. The DBR structure reflects the unabsorbed light forming a dual-path absorption. Therefore, DBR structure can further decouple the quantum efficiency and bandwidth, which increases the quantum efficiency and the effective APD length. An illustration of the waveguide Si-Ge with DBR is shown in Fig. 9-11.

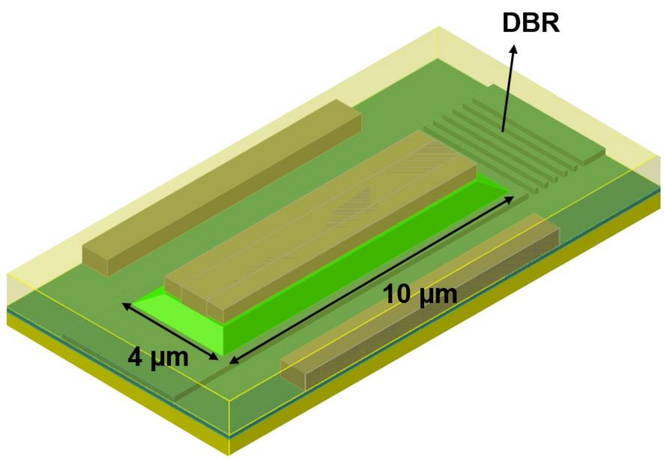

Figure 9-11. Schematic diagram of the Si-Ge waveguide SACM APD with DBR.

Two DBR designs, by Dr. Di Liang at HP Labs, were used for this work. Details for DBR1 and DBR2, are shown in Table 9-2. The DBRs were designed to operate in TM mode at 1550 nm. The thickness of Si is 320 nm, the thickness of slab Si is 70 nm, and SiO_2 is used as a cladding layer.

Table 9-2. DBR structures design.

Design Type	Period Width (nm)	Groove Width (nm)	Teeth Width (nm)	Period Number
DBR1	695	267	428	6
DBR2	384	211	173	6

The reflection for the two DBR designs can be calculated by the transfer matrix method [165]. The transfer matrix is defined as:

$$\begin{bmatrix} A_1 \\ B_1 \end{bmatrix} = \begin{bmatrix} T_{11} & T_{12} \\ T_{21} & T_{22} \end{bmatrix} \begin{bmatrix} A_2 \\ B_2 \end{bmatrix}, \tag{9.8}$$

where the parameters are shown in Fig. 9-12 for homogeneous and heterogeneous sections, respectively.

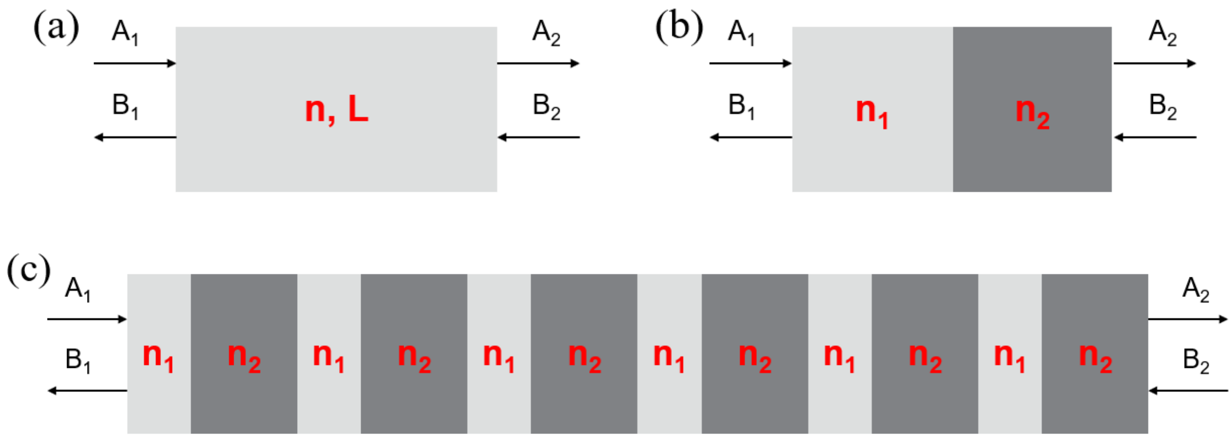

Figure 9-12. Illustration of the transfer matrices for (a) homogeneous, (b) heterogeneous section, and (c) total DBR structure.

The transfer matrices for the homogeneous section of a waveguide, which is shown in Fig. 9-12(a), are given by:

$$T_{homo} = \begin{bmatrix} e^{j\beta L} & 0 \\ 0 & e^{-j\beta L} \end{bmatrix}, \tag{9.9}$$

where L is the propagation length in the homogeneous section waveguide; β is the complex propagation constant, which includes the effective refraction index, n_{eff}, and the propagation loss, α, as:

$$\beta = \frac{2\pi n_{eff}}{\lambda} - i\frac{\alpha}{2}. \tag{9.10}$$

The transfer matrices for the heterogeneous section, which is expressed in Fig. 9-12(b), is given by:

$$T_{heter,1\to 2} = \begin{bmatrix} \frac{n_1+n_2}{2\sqrt{n_1 n_2}} & \frac{n_1-n_2}{2\sqrt{n_1 n_2}} \\ \frac{n_1-n_2}{2\sqrt{n_1 n_2}} & \frac{n_1+n_2}{2\sqrt{n_1 n_2}} \end{bmatrix}. \tag{9.11}$$

Based on the equations above, the DBR structure can be treated as a cascaded network of homogeneous and heterogeneous sections, as shown in Fig. 9-12(c). For this work, the period number is 6, thus:

$$T_{total} = \left(T_{homo,1} T_{heter,1\to 2} T_{homo,2} T_{heter,2\to 1}\right)^6 . \tag{9.12}$$

The effective refractive index, n_{eff}, for the 1550 nm TM0 mode wave is 1.452761 in the groove, and 2.711785 in the teeth. If we assume there is no propagation loss in the DBR, i.e. $\alpha = 0.$, the DBR1 can reflect ~ 95.75% light, and the DBR2 can reflect ~ 99.47%.

The photocurrent versus input laser power at 1550 nm for the 4 μm × 10 μm APDs with DBR1, DBR2. The internal quantum efficiencies and responsivities were extracted by linear fitting. For the APD with DBR1, the QE is ~ 71 % and the responsivity is ~ 0.89 A/W; for the devices with DBR2, the QE is ~ 76% and the responsivity is ~ 0.95 A/W; for no DBR the QE is ~ 55% and the responsivity is ~ 0.69 A/W. The DBR1 and DBR2 structure can improve QE ~ 30% and 38%, respectively. The improvements are lower than the ideal reflection calculation at $\alpha = 0.$ If all light is reflected by the DBR, the QE can improve up to 45%, which in practice is not realizable. If $\alpha = 0.17\ \mu m^{-1}$, the calculated QEs agree well with experiment results as shown in Fig. 9-14.

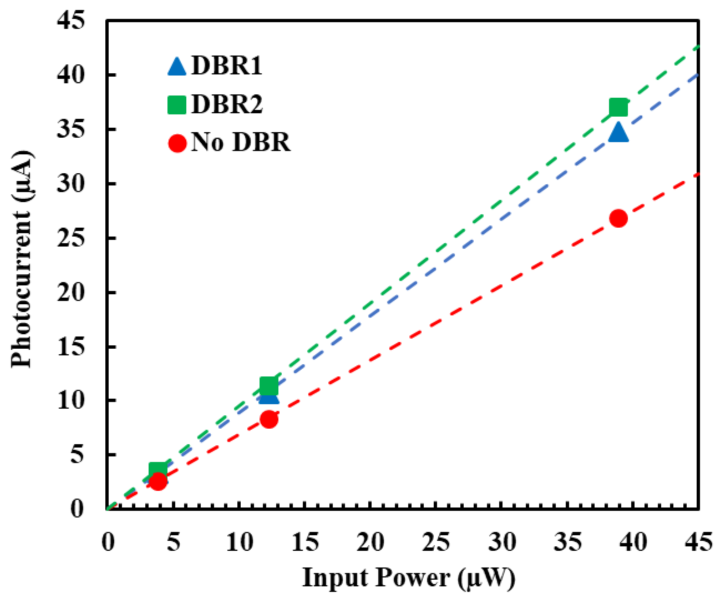

Figure 9-13. Photocurrent versus input laser power at 1550 nm laser for APDs with DBR1, DBR2, and without DBR structure.

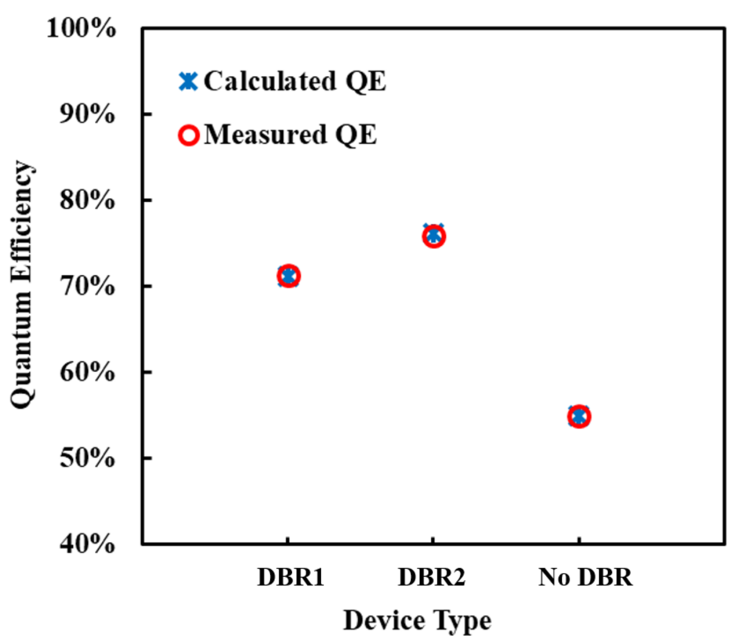

Figure 9-14. Comparsion of calculated and measured quantum efficiencies.

FDTD simulation by Lumerical was also used to study the quantum efficiency improvement. The material library in Lumerical only has the absorption coefficients of bulk Ge, which are not suitable for the strained Ge in these APDs. The strained Ge has a higher absorption coefficient at 1550 nm, as illustrated in Fig. 9-15 [166]. Thus, the κ was modified to 0.012. Also, in Lumerical the z-max, x-min, and x-max FDTD boundary conditions should be set to metal, i.e., all electromagnetic waves are totally reflected, because these surfaces are covered with metal. Other surfaces were set to perfectly matched layer (PML) boundaries, which absorb the electromagnetic waves incident upon them, i.e. model open (reflectionless) boundaries.

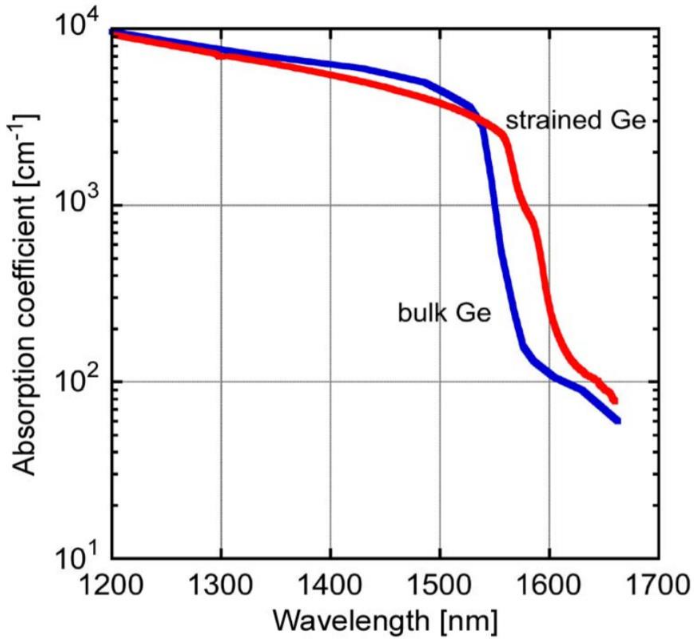

Figure 9-15. Optical absorption spectra for bulk Ge and tensile strained Ge on Si [166].

The FDTD simulation of the absorption profile for the 4 μm × 10 μm APDs with DBR1, DBR2, and without DBR structure are shown is Fig. 9-16. The absorption profiles confirm that the APDs with DBR structure have higher absorption than the APD without a reflector. The simulated quantum efficiencies are 67% for DBR1, 68.5% for DBR2, and 54% for no DBR; which are a little bit lower than the measured data. As with the measurement and matrix calculation, the FDTD simulation also shows that DBR2 achieves higher quantum efficiency than the DBR1.

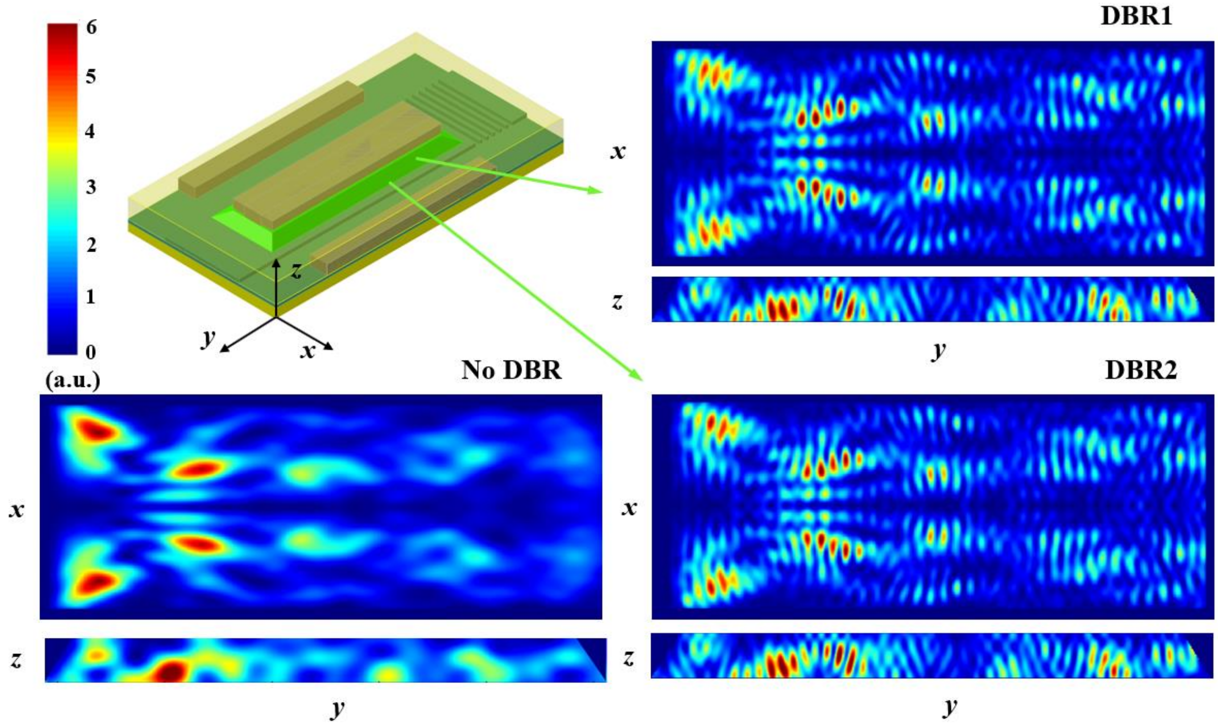

Figure 9-16. FDTD simulation of absorption profile for 4 μm × 10 μm Si-Ge waveguide APDs with DBR1, DBR2, and without DBR structure.

The bandwidth and eye diagrms for the 4 μm × 10 μm APDs with DBR1 and DBR2 are shown in Figs. 9-17 and 9-18, respectively. Both DBR1 and DBR2 APDs have bandwidth ~ 25 GHz, similar to those in Section 9.3.3, i.e., the bandwidth is not be affected by adding a DBR after waveguide APDs.

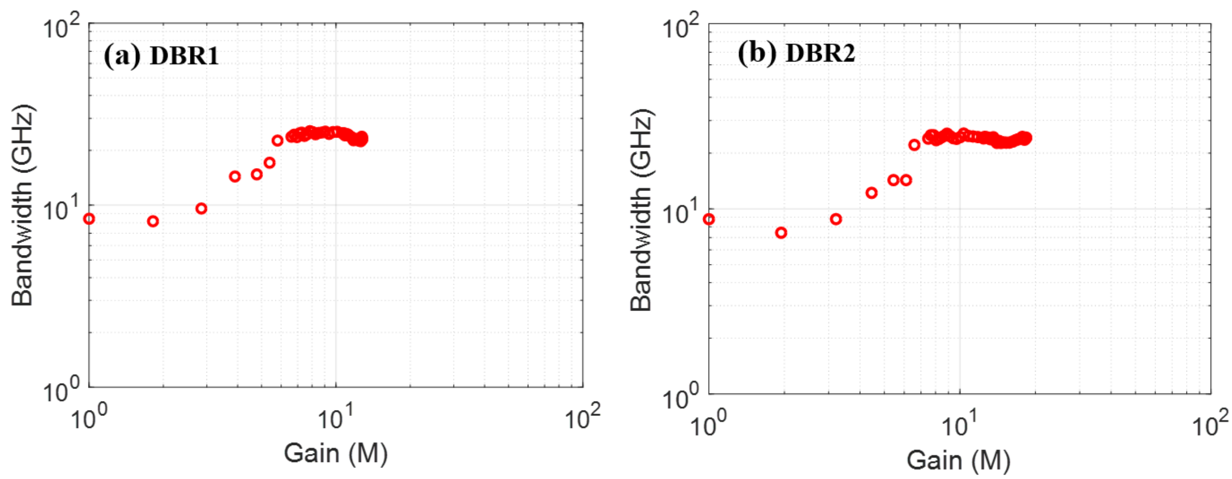

Figure 9-17. Bandwidth versus gain for (a) DBR1 and (b) DBR2 APDs.

The clear open eye diagrams also illustrate that the bandwidth is not decreases by using DBRs. The eye diagrams were measured at 30 ℃ for all three APDs. Fig. 9-18(b) and (c) have a larger eye openings for both 32 Gpbs NRZ and 64 Gpbs PAM4 modulation than Fig. 9-18(a), as a result of higher quantum efficiency in APDs with DBR.

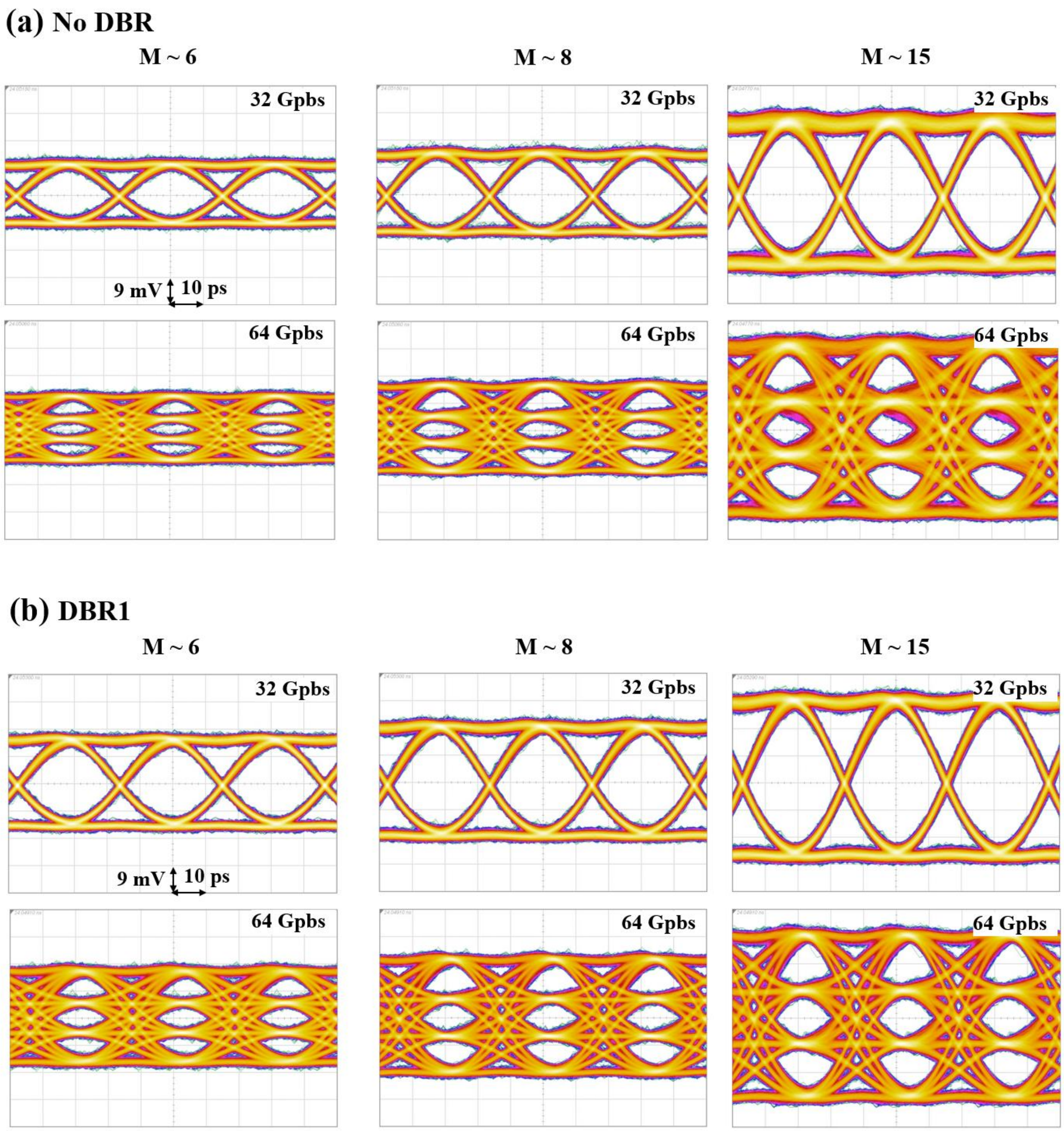

(c) DBR2

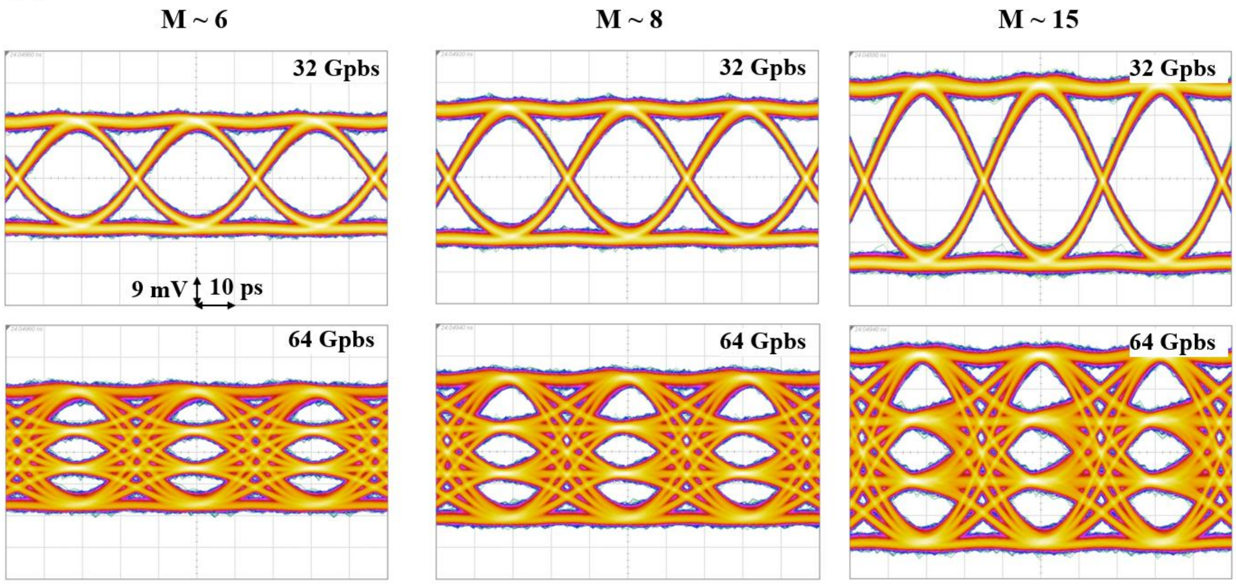

Figure 9-18. Electrical eye diagram at 32 Gbps NRZ and 64 Gbps PAM4 with M=6, 8, and 15 for 4 μm × 10 μm Si-Ge waveguide APDs with (a) no DBR, (b) DBR1, and (c) DBR2.

9.5 Conclusions

The temperature dependent characteristics of 4 μm × 10 μm Si-Ge waveguide APDs have been investigated from 30 °C to 90 °C. Owing to the thin epitaxial layers, the Si-Ge APDs have a low breakdown voltage ~ 10 V, and exhibit high temperature stability. As temperature increases, the breakdown voltage increases $4.2\ mV/℃$, the bandwidth decreases ~ 0.09% /°C, and the gain-bandwidth product decreases ~ 0.24% /°C. The activation energy of the Si-Ge APD is similar to a pervious report, $E_a = 0.4\ eV$. A high-performance Si-Ge waveguide APD for future high temperature optical interconnect applications has been demonstrated, which has high multiplication gain > 15, high speed ~ 24.6 GHz, high GBP > 240 GHz, high internal quantum efficiency ~ 100%, and clearly open eye diagrams with 64 Gbps PAM4 at 90 °C.

Also, a new design with two DBR structures was used to improve the quantum efficiency of the Si-Ge waveguide APDs. The DBR1 structure exhibited 71% quantum efficiency, which is ~

30% higher than without the DBR. The DBR2 achieved even higher improvement ~ 38% with quantum efficiency up to ~ 76%. A matrix theory calculation and an FDTD simulation have been demonstrated to verify the measured results. Moreover, the DBR structure does not degrade the APD bandwidth (~ 25 GHz) and open eye diagrams are observed for 64 Gbps PAM4.

Chapter 10. Conclusions and future work

10.1 Conclusions

This thesis focused on low-noise avalanche photodiodes, including $Al_{0.7}InAsSb$ digital alloy APDs, $Al_{0.8}InAsSb$ digital alloy APDs, InAlAs digital alloy APDs, $Al_{0.7}InAsSb$ SPADs, triple-mesa InAlAs APDs, InGaAs-InAlAs SACM APDs on Si, and Si-Ge APDs.

For $Al_{0.7}InAsSb$ digital alloy APDs, I compared two different periods, binary and ternary structures. Both exhibit very low excess noise and high thermal stability. The excess noise performance at different temperatures exhibits an exponential relation with temperature. For the first time, we determined the impact ionization coefficients of this low-noise material by pure carrier injection and mixed injection methods. It was found that the hole ionization coefficient exhibits significant reduction at lower temperature, while that of the electron is relatively independent of temperature. This is a clue as to why $Al_{0.7}InAsSb$ digital alloy APDs achieve low excess noise.

For $Al_{0.8}InAsSb$ digital alloy APDs, I report the first $Al_{0.8}InAsSb$ p-i-n structure APDs. These APDs exhibit high multiplication gain up to 489, low excess noise corresponding to $k = 0.05{\sim}0.07$, and external quantum efficiency of 30% at 850 nm wavelength. Furthermore, a new method is proposed to determine the unity gain point for the APDs with bias-dependent responsivity, which can be used for different APD structures, such as undeleted APDs and SACM APDs.

I am also the first to report the low-noise performance in the InAlAs digital alloy APDs. In order to understand the low-noise mechanism, the ionization characteristics of InAlAs random alloy, InAlAs digital alloy, and AlGaAs digital alloy have been investigated at different temperatures. The k values of the InAlAs digital alloy APDs decrease exponentially with decreasing temperature, owing to the suppression of hole ionization, which in turn is due to a mini-gap in the valence band. The experimental results are consistent with the simulated band structures and provide insight into the low excess noise exhibited by the InAlAs digital alloy and the absence of noise suppression in the AlGaAs digital alloy. I also found that the breakdown voltage temperature coefficient of 8ML InAlAs digital alloy is similar to that of the InAlAs random alloy. This has yet to be explained. By measuring the external quantum efficiencies of an 8ML InAlAs digital alloy and an InAlAs random alloy under different voltages, the absorption characteristics of these two semiconductors were investigated. Owing to the Franz-Keldysh effect, both absorption edges exhibit a red shift. However, electric-field-induced Stark localization of the digital alloy results in an electric field dependent quantum efficiency and an effective blue shift.

I showed that the $Al_{0.7}InAsSb$ digital alloy can also be used as single-photon avalanche diodes. The jitter time is ~ 190 ps. At 200 K and 10 kHz gated mode quenching, the highest SPDE is ~ 33% and DCR is ~ 2.8 MHz; for 100 kHz gated mode, the highest SPDE is ~ 33% and DCR is ~ 5.4 MHz at 200K. Compared to conventional InGaAs/InAlAs SPADs, the $Al_{0.7}InAsSb$ SPADs can obtain higher SPDE with a relatively smaller DCR.

The APDs discussed above use low-excess-noise materials, i.e., digital alloys, to improve the noise performance. I also investigated reducing the noise by reducing the dark current. In Chapter 7, a random InAlAs reach-through APD with triple-mesa structure has been demonstrated. The surface-related dark current is effectively suppressed by reducing the surface electric field. The InAlAs triple-mesa APDs exhibits ~ 50 times lower dark current density than single-mesa APDs fabricated from the same wafer. The bulk dark current dominates for the triple mesa devices while that of the single mesa is surface leakage. Tolerances of triple-mesa design and fabrication have also been discussed.

Silicon photonics has drawn significant interest due to its potential for large scale photonics integration and compatibility with CMOS circuits. Low-noise APDs are an important component in silicon photonics, due to their higher sensitivity. Chapter 8 and 9 focus on low-noise APDs on Si platform. Chapter 8 reported the first III-V APD grown by heteroepitaxy on Si. This InGaAs/InAlAs APD exhibits low dark current, gain > 20, external quantum efficiency > 40%, and similar low excess noise, k ~ 0.2, as InAlAs APDs on InP. However, owing to the large lattice mismatch between III-V and Si, the InGaAs/InAlAs APD on Si substrate exhibits a higher dark current than that of same structure APD on InP. It also has a deeper generation-recombination defect center.

Chapter 9 focuses on improving existing Si-Ge APDs on silicon photonics. The temperature dependent characteristics of 4 μm $\times$ 10 μm Si-Ge waveguide APDs have been investigated from 30 °C to 90 °C. Owing to the thin epilayers, the Si-Ge APDs have a low breakdown voltage ~ 10 V, and exhibit good temperature stability. As temperature increases, the breakdown voltage increases $4.2\ mV/°\mathrm{C}$, the bandwidth decreases ~ 0.09% /°C, and the gain-bandwidth product decreases ~ 0.24% /°C. The activation energy of the Si-Ge APD is similar to pervious report for Ge, $E_a = 0.4\ eV$. A high-performance Si-Ge waveguide APD for future high-temperature optical interconnect applications has been demonstrated, which has high multiplication gain > 15, high speed ~ 24.6 GHz, high GBP > 240 GHz, high internal quantum efficiency ~ 100%, and open eye diagrams with 64 Gbps PAM4 at 90 °C. A new design with a DBR has demonstrated improved quantum efficiency relative to a similar device without the DBR. The DBR1 structure achieved 71% quantum efficiency, which is ~ 30% higher than that with no DBR structure. The DBR2 structure exhibited even higher improvement of ~ 38% and quantum efficiency up to ~ 76%. A matrix theory calculation and an FDTD simulation have been demonstrated to verify the measured results. The DBR structure does not degrade the bandwidth (~ 25 GHz) and open eye diagrams are observed for 64 Gbps PAM4.

10.2 Future works

10.2.1 High-speed III-V APD on Si

Chapter 8 demonstrates the first III-V APDs on Si with relatively high gain, low dark current, and low noise. However, these APDs did not achieve high bandwidth. To determine the reason, I measured the capacitance versus the reverse voltage, as shown in Fig. 10-1. There is no step in the capacitance sudden before avalanche gain is observed, which means the charge layer is not fully depleted. The punch-through point in Fig. 8-2 is due to the fact that the carriers can the conduction band barriers when bias > -14 V.

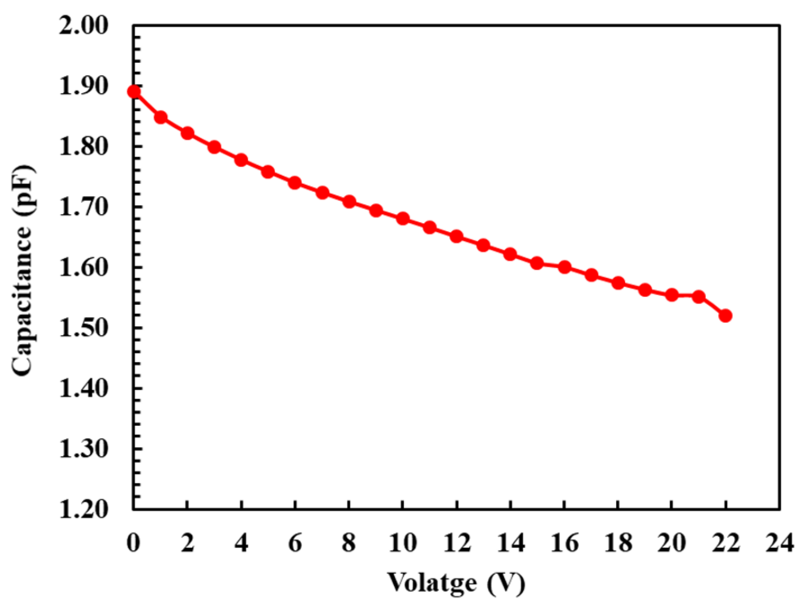

Figure 10-1. Capacitance versus reverse voltage of the InGaAs/InAlAs APD on Si.

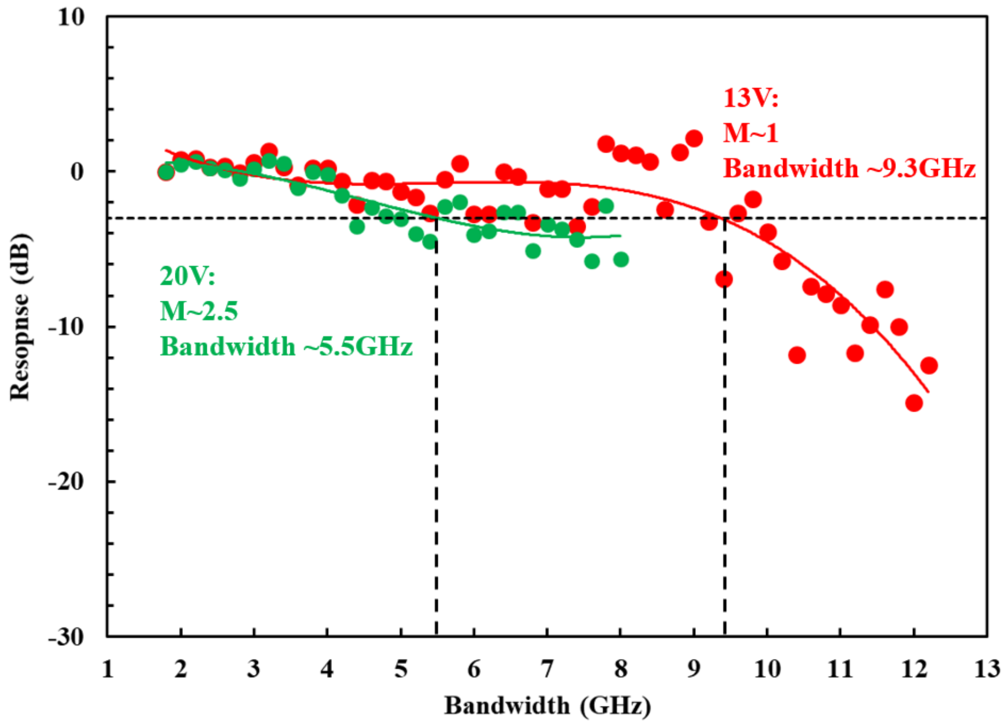

Figure 10-2. Bandwidth measurement at gain euqals 1 and 2.5.

The undepleted charge layer can also be verified by bandwdith measurement. Figure 10-2 illustrates the bandwdith at M ~ 1 and 2.5. The bandwdith is ~ 9.3 GHz when there is no gain, and it reduces to 5.5 GHz when gain euqals 2.5. The impact-ionization-generated holes in the InAlAs multiplication layer take a long time to transit through InGaAs absorber, since there is effectively no electric field in the aborber. Therefore, when the APD has a slight gain, the bandwdith rapidly decreases. In order to slove this problem, the doping in the InAlAs charger layer should be reduced. By simulation with BandProf, the new doping in the charge layer should be reduced from $7 \times 10^{17}\ cm^{-3}$ to $3.4 \times 10^{17}\ cm^{-3}$, which is shown in Fig. 10-3, and this new design should punch-through around -14 V.

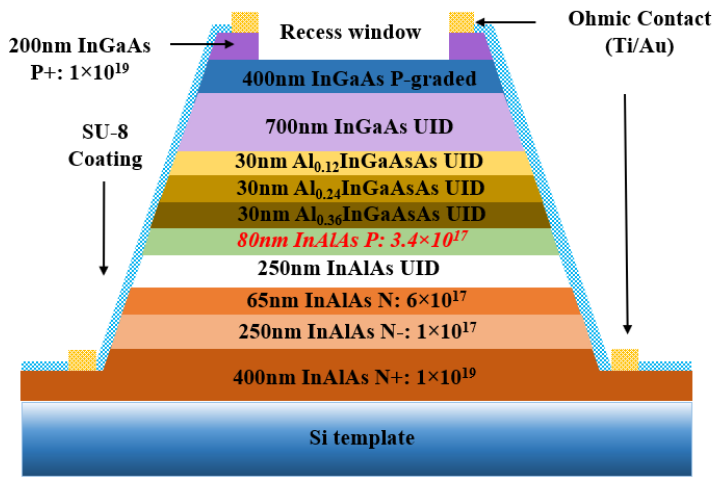

Figure 10-3. New III-V APD design with lower charger layer doping.

10.2.2 InGaAs/InAlAs digital alloy SACM APDs

InGaAs/InAlAs SACM APDs are widely used in optical telecommunication systems. In Chapter 5, I demonstrated that 8ML InAlAs digital alloy APDs have lower *k* value than random alloy InAlAs APDs. By replacing the InAlAs random alloy with a digital alloy, the SACM APDs could achieve lower excess noise and higher sensitivity. Also, the InAlAs digital alloy as multiplication region should also have higher gain-bandwidth product.

Compared to the random alloy, the InGaAs digital alloy does not exhibit lower *k* value. However, from the quantum efficiency measurement shown in Fig. 10-4, a 10ML digital alloy InGaAs could extend the cut-off wavelength to ~ 2 μm [167]. By using a digital alloy InGaAs as absorption layer and a digital alloy InAlAs as multiplication layer, an SACM APD with lower excess noise, higher sensitivity, higher gain-bandwidth product, and longer response spectrum can be achieved. Figure 10-5 is the design of the a 10ML InGaAs and 8ML InAlAs digital alloy SACM APD. I used Crosslight to simulate the electric field of the SACM APD. At -15 V, the electric filed extends into the InGaAs absorber, i.e., punch-through. At -21V, the electric filed in the InAlAs multiplication layer is ~ 576 KV/cm, which is high enough for avalanche gain. For the same bias the electric field in the InGaAs absorber is much lower than 100 KV/cm. As a result, no tunneling dark current in the InGaAs absorber is expected.

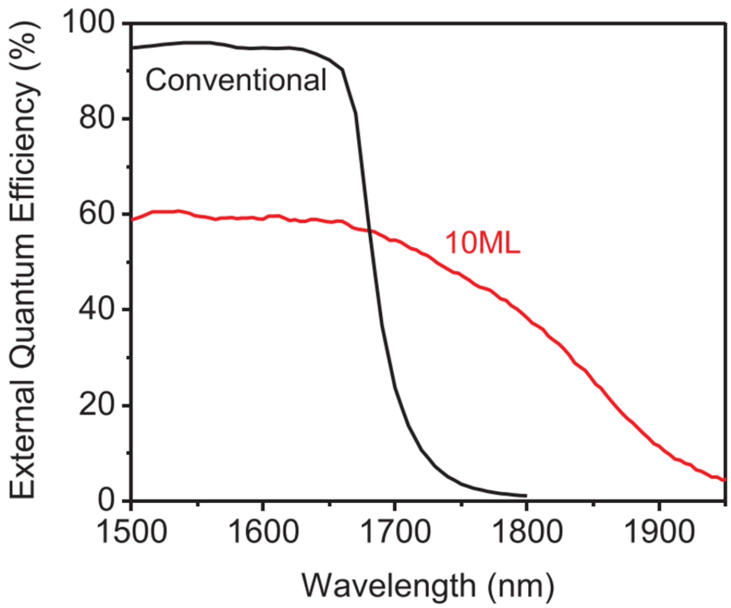

Figure 10-4. External quantum efficiency of conventional random alloy (black line) and 10ML digital alloy (red line) InGaAs APDs [167].

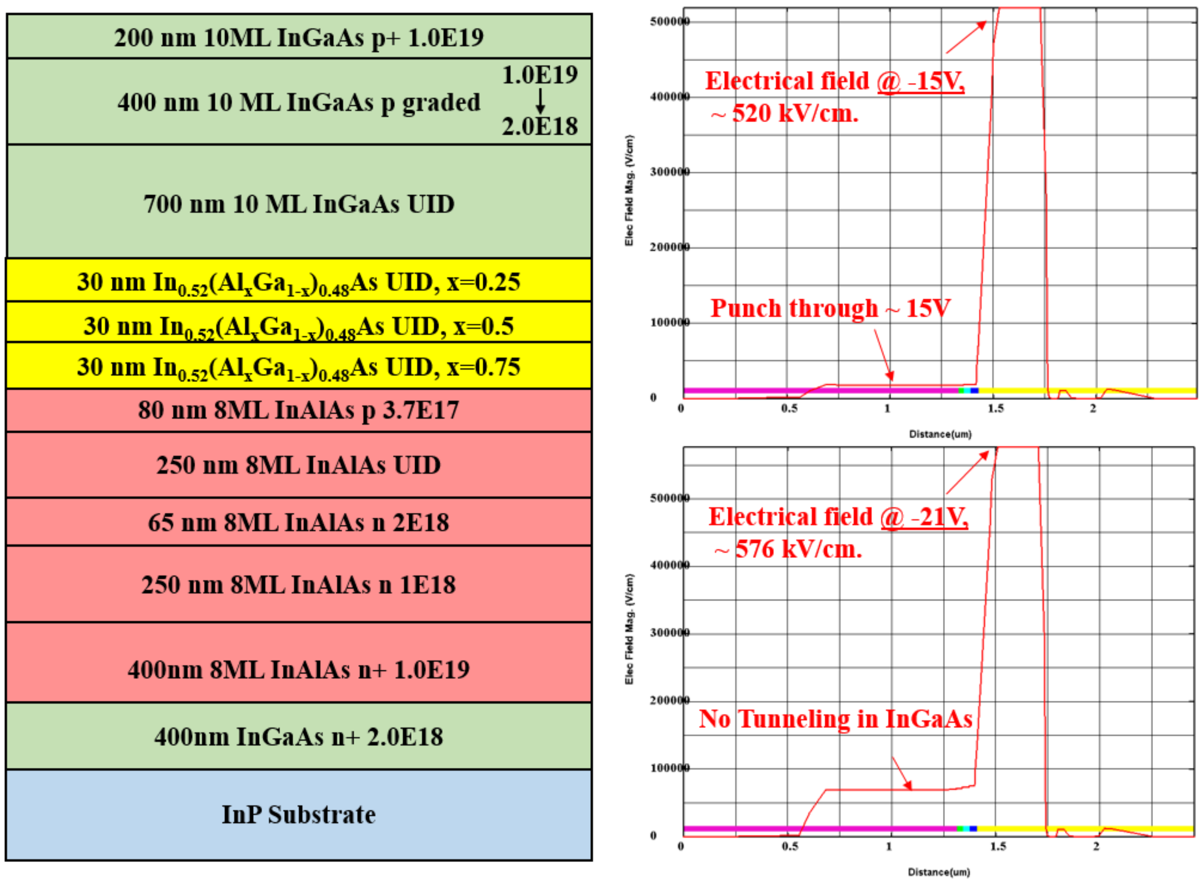

Figure 10-5. Design of the InGaAs/InAlAs digital alloy SACM APD.

10.2.3 Passive quenching with memristor

The passive quenching circuit has been widely integrated in SPAD arrays, because it is the simplest method to realize quenching by adding a large resistive load in series with the SPAD. However, as Eq. 6.11 shows, the recharge time is proportional to the large resistive load, R_L. Recently, the memristor has drawn significant interest because of its insulator-to-metal transition behavior. Figure 10-6 shows the insulator-to-metal transition of a HfO_2 device [168]. It has ~ 100 times resistance difference between insulator phase and metal phase. As shown in Fig. 10-6(b), the low resistance is ~ 100 Ω while the high resistance ~ 10 kΩ. The high resistance can be used to quench the self-sustaining avalanche event. During quenching the avalanche current will set the memristor to the metal phase, and the low resistance will reduce recharge time. In addition, this HfO_2 device has a short switch time of < 300 ps.

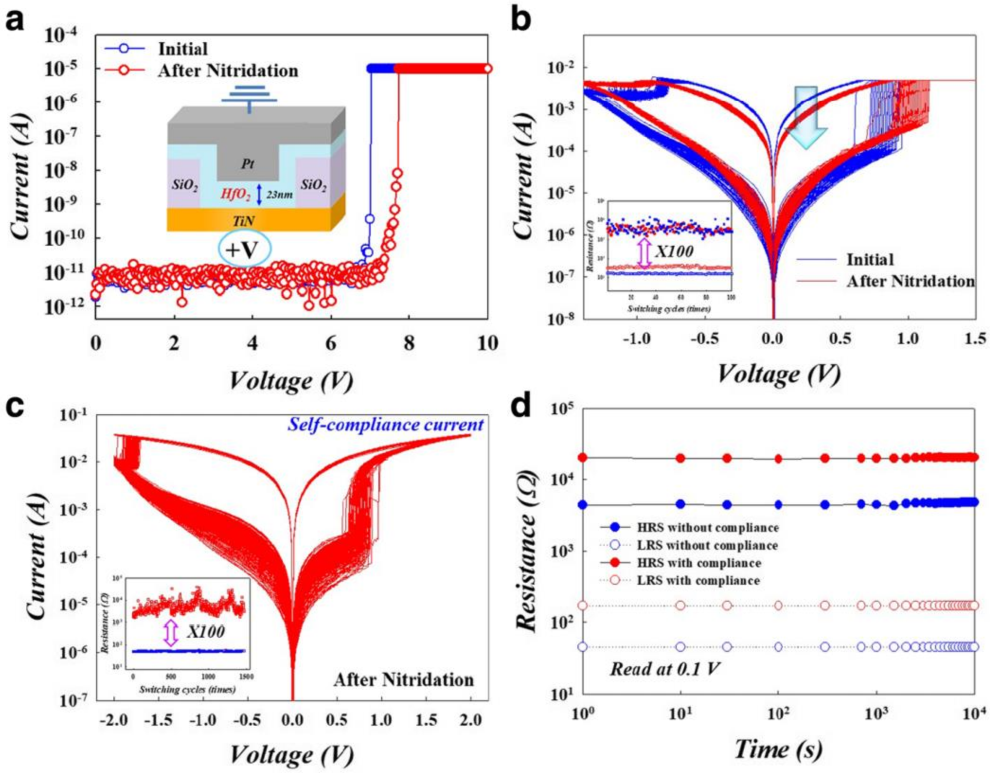

Figure 10-6. (a) The forming current curves of a HfO_2 device. (b) Comparison of DC sweep cycles at a 5 mA compliance current between initial and after nitridation treatment of HfO_2. (c) DC sweep cycles without external current compliance of the HfO_2 device after nitridation treatment. (d) Retention time of the HfO_2-based RRAM devices at 85 °C with and without compliance current after nitridation treatment [168].

The integration of a memristor quench circuit and APD is shown in Fig. 10-7. Typically, the dimension of the memristor is tens of nm, which makes it easy to integrate with the APD mesa. The dimension of the memristor is designed so that its threshold voltage is a little lower than the maxmium voltage across it during the avalanche event. Then using atomic layer deposition (ALD) to deposition memristor on the top of ring contact. Finally, an airbridge GSG pad is desosited to connect the SPAD and memristor in series.

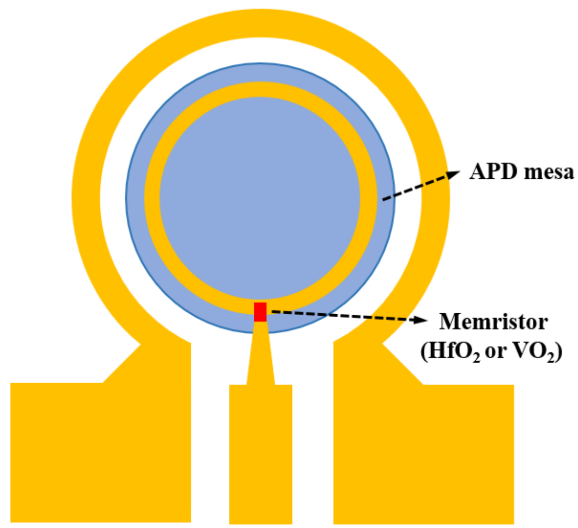

Figure 10-7. Integrated memristor quench circuit with the APD.

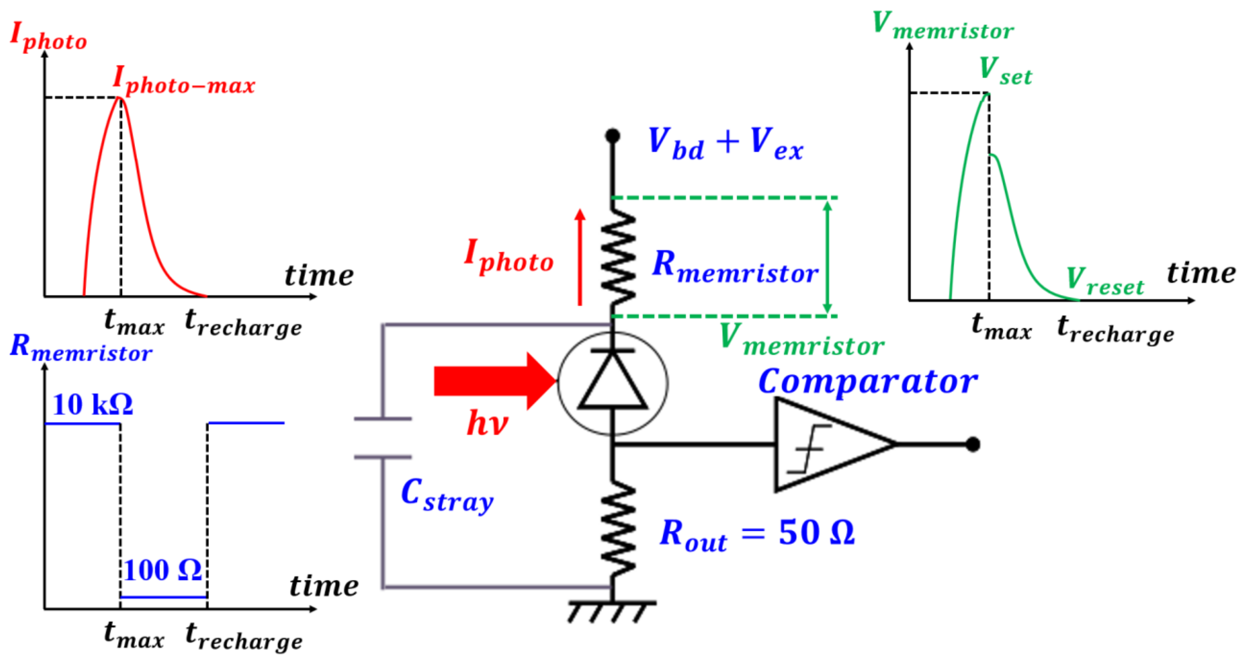

Figure 10-8. Passive quenching ciruit with memristor as the quenching resistor.

The passive quenching circuit is shwon in Fig. 10-8. When the photon triggers an avalanche, the SPAD switches into "on" status, and thus photocurrent increases. The memristor in the insulator phase, which exhibits a high resistance ~ 10 kΩ, so that the voltage across the memristor increases rapidly to quench the voltage over the SPAD lower than breakdown voltage. By designing the memristor set voltage equals the highest voltage across the memristor, the memristor can be set at t_{max}, and it results in a low resistance is ~ 100 Ω. The low resistance enables a fast recharge time by reducing the RC time constant. And when the capacitances are fully recharged, the memristor is reset at $t_{recharge}$ to wait next detection. By integrating the memristor as the quenching resistor, the passive quenching circuit can achieve shorter recharge time with a rapid quenching time.

References

[1] X. Yi *et al.*, “Extremely low excess noise and high sensitivity AlAs0.56Sb0.44 avalanche photodiodes,” *Nat. Photonics*, vol. 13, no. 10, pp. 683–686, Oct. 2019.
[2] J. C. Campbell, “Recent Advances in Avalanche Photodiodes,” *J Light. Technol*, vol. 34, no. 2, pp. 278–285, Jan. 2016.
[3] F. Laforce, “Low noise optical receiver using Si APD,” presented at the SPIE OPTO: Integrated Optoelectronic Devices, San Jose, CA, 2009, p. 721210.
[4] M. Liu *et al.*, “High-Performance InGaAs/InP Single-Photon Avalanche Photodiode,” *IEEE J. Sel. Top. Quantum Electron.*, vol. 13, no. 4, pp. 887–894, 2007.
[5] Y. Zhao *et al.*, “InGaAs–InP avalanche photodiodes with dark current limited by generation-recombination,” *Opt. Express*, vol. 19, no. 9, p. 8546, Apr. 2011.
[6] N. Li *et al.*, “InGaAs/InAlAs avalanche photodiode with undepleted absorber,” *Appl. Phys. Lett.*, vol. 82, no. 13, pp. 2175–2177, Mar. 2003.
[7] M. Nada, M. Nakamura, and H. Matsuzaki, “25-Gbit/s burst-mode optical receiver using high-speed avalanche photodiode for 100-Gbit/s optical packet switching,” *Opt. Express*, vol. 22, pp. 443–449, 2014.
[8] M. Nada, H. Yokoyama, Y. Muramoto, T. Ishibashi, and H. Matsuzaki, “50-Gbit/s vertical illumination avalanche photodiode for 400-Gbit/s ethernet systems,” *Opt. Express*, vol. 22, pp. 14681–14687, 2014.
[9] F. Capasso, “Physics of avalanche photodiodes,” in *Semiconductors and semimetals*, vol. 22, Elsevier, 1985, pp. 1–172.
[10] J. C. Campbell, “Advances in photodetectors,” in *Optical Fiber Telecommunications VA*, Elsevier, 2008, pp. 221–268.
[11] M. A. Albota *et al.*, “Three-dimensional imaging laser radar with a photon-counting avalanche photodiode array and microchip laser,” *Appl. Opt.*, vol. 41, no. 36, p. 7671, Dec. 2002.
[12] B. F. Aull, E. K. Duerr, J. P. Frechette, K. A. McIntosh, D. R. Schuette, and R. D. Younger, “Large-Format Geiger-Mode Avalanche Photodiode Arrays and Readout Circuits,” *IEEE J. Sel. Top. Quantum Electron.*, vol. 24, no. 2, pp. 1–10, Mar. 2018.
[13] X. Jiang *et al.*, “InP-Based Single-Photon Detectors and Geiger-Mode APD Arrays for Quantum Communications Applications,” *IEEE J. Sel. Top. Quantum Electron.*, vol. 21, no. 3, pp. 5–16, May 2015.
[14] B. E. Kardynał, Z. L. Yuan, and A. J. Shields, “An avalanche-photodiode-based photon-number-resolving detector,” *Nat. Photonics*, vol. 2, no. 7, pp. 425–428, Jul. 2008.
[15] Z. Huang *et al.*, “25 Gbps low-voltage waveguide Si–Ge avalanche photodiode,” *Optica*, vol. 3, no. 8, p. 793, Aug. 2016.
[16] R. J. McIntyre, “Multiplication noise in uniform avalanche diodes,” *IEEE Trans. Electron Devices*, vol. ED-13, no. 1, pp. 164–168, Jan. 1966.
[17] W. Sun, “Theoretical Study and Monte Carlo Simulation of III-V Compound Low-Noise Photodiodes,” University of Virginia, 2014.
[18] R. B. Emmons, “Avalanche-Photodiode Frequency Response,” *IEEE Trans. Electron Devices*, vol. 38, no. 9, pp. 3705–3714, 1967.
[19] Y. Kang *et al.*, “Monolithic germanium/silicon avalanche photodiodes with 340 GHz gain–bandwidth product,” *Nat. Photonics*, vol. 3, no. 1, pp. 59–63, Jan. 2009.
[20] X. Zhou, L. L. G. Pinel, S. J. Dimler, S. Zhang, J. S. Ng, and C. H. Tan, “Thin Al1-xGaxAs0.56Sb0.44 Diodes With Low Excess Noise,” *IEEE J. Sel. Top. Quantum Electron.*, vol. 24, no. 2, pp. 1–5, Mar. 2018.
[21] S. Xie *et al.*, “InGaAs/AlGaAsSb avalanche photodiode with high gain-bandwidth product,” *Opt. Express*, vol. 24, no. 21, p. 24242, Oct. 2016.
[22] S. R. Bank *et al.*, “Avalanche Photodiodes Based on the AlInAsSb Materials System,” *IEEE J. Sel. Top. Quantum Electron.*, vol. 24, no. 2, pp. 1–7, Mar. 2018.
[23] M. E. Woodson, M. Ren, S. J. Maddox, Y. Chen, S. R. Bank, and J. C. Campbell, “Low-noise AlInAsSb avalanche photodiode,” *Appl. Phys. Lett.*, vol. 108, no. 8, p. 081102, Feb. 2016.
[24] M. Ren, S. J. Maddox, M. E. Woodson, Y. Chen, S. R. Bank, and J. C. Campbell, “Characteristics of AlxIn1−xAsySb1−y (x:0.3−0.7) Avalanche Photodiodes,” *J. Light. Technol.*, vol. 35, no. 12, pp. 2380–2384,

Jun. 2017.
[25] M. Ren, S. J. Maddox, M. E. Woodson, Y. Chen, S. R. Bank, and J. C. Campbell, "AlInAsSb separate absorption, charge, and multiplication avalanche photodiodes," *Appl. Phys. Lett.*, vol. 108, no. 19, p. 191108, May 2016.
[26] A. Rockwell, Y. Yuan, A. H. Jones, S. D. March, S. R. Bank, and J. C. Campbell, "Al0.8In0.2As0.23Sb0.77 Avalanche Photodiodes," *IEEE Photonics Technol. Lett.*, vol. 30, no. 11, pp. 1048–1051, Jun. 2018.
[27] Y. Yuan *et al.*, "Temperature dependence of the ionization coefficients of InAlAs and AlGaAs digital alloys," *Photonics Res.*, vol. 6, no. 8, p. 794, Aug. 2018.
[28] J. Zheng *et al.*, "Digital Alloy InAlAs Avalanche Photodiodes," *J. Light. Technol.*, vol. 36, no. 17, pp. 3580–3585, Sep. 2018.
[29] Y. Yuan *et al.*, "III-V on silicon avalanche photodiodes by heteroepitaxy," *Opt. Lett.*, vol. 44, no. 14, pp. 3538–3541, Jul. 2019.
[30] Y. Yuan *et al.*, "III-V Compound Avalanche Photodiodes on Silicon," in *OSA Advanced Photonics Congress (AP) 2019 (IPR, Networks, NOMA, SPPCom, PVLED) (2019), paper IW3A.4*, 2019, p. IW3A.4.
[31] X. Li, H. Tang, T. Li, P. Wei, H. Gong, and J. Fang, "Study on dark current of extended wavelength InGaAs detectors," in *International Symposium on Photoelectronic Detection and Imaging 2013: Infrared Imaging and Applications*, 2013, vol. 8907, p. 890703.
[32] S. M. Sze and K. K. Ng, *Physics of Semiconductor Devices*. John Wiley & Sons, 2006.
[33] P. J. Ker, A. R. J. Marshall, C. H. Tan, and J. P. R. David, "Surface passivation of InAs avalanche photodiodes for low-noise infrared imaging," in *2016 IEEE 6th International Conference on Photonics (ICP)*, Kuching, Sarawak, Malaysia, 2016, pp. 1–3.
[34] C. Lenox *et al.*, "Resonant-cavity InGaAs-InAlAs avalanche photodiodes with gain-bandwidth product of 290 GHz," *IEEE Photonics Technol. Lett.*, vol. 11, no. 9, pp. 1162–1164, Sep. 1999.
[35] K. Kato, S. Hata, K. Kawano, and A. Kozen, "Design of ultrawide-band, high-sensitivity pin protodetectors," *IEICE Trans. Electron.*, vol. 76, no. 2, pp. 214–221, 1993.
[36] R. Miglierina, M. Norgia, G. Giuliani, and S. Donati, "High-bandwidth photodiode frequency-response characterization method based on the photomixing technique," in *Microwave and Terahertz Photonics*, 2004, vol. 5466, pp. 54–60.
[37] S. J. Maddox, S. D. March, and S. R. Bank, "Broadly Tunable AlInAsSb Digital Alloys Grown on GaSb," *Cryst. Growth Des.*, vol. 16, no. 7, pp. 3582–3586, Jul. 2016.
[38] "WSI Research Groups." [Online]. Available: https://www.wsi.tum.de/views/sub_group.php?group=Amann. [Accessed: 05-Oct-2019].
[39] L. G. Vaughn, L. Ralph, H. Xu, Y. Jiang, and L. F. Lester, "Characterization of AlInAsSb and AlGaInAsSb MBE-grown Digital Alloys," *MRS Proc.*, vol. 744, p. M7.2, 2002.
[40] D. M. Kim, D. H. Kim, and S. Y. Lee, "Characterization and modeling of temperature-dependent barrier heights and ideality factors in GaAs Schottky diodes," *Solid-State Electron.*, vol. 51, no. 6, pp. 865–869, Jun. 2007.
[41] Z. Hu *et al.*, "Near unity ideality factor and Shockley-Read-Hall lifetime in GaN-on-GaN p-n diodes with avalanche breakdown," *Appl. Phys. Lett.*, vol. 107, no. 24, p. 243501, Dec. 2015.
[42] A. H. Jones, Y. Yuan, M. Ren, S. J. Maddox, S. R. Bank, and J. C. Campbell, "AlxIn1-xAsySb1-y photodiodes with low avalanche breakdown temperature dependence," *Opt. Express*, vol. 25, no. 20, p. 24340, Oct. 2017.
[43] M. Ren *et al.*, "Operation stability study of AlInAsSb avalanche photodiodes," in *2017 IEEE Photonics Conference (IPC)*, 2017, pp. 159–160.
[44] D. J. Massey, J. P. R. David, and G. J. Rees, "Temperature Dependence of Impact Ionization in Submicrometer Silicon Devices," *IEEE Trans. Electron Devices*, vol. 53, no. 9, pp. 2328–2334, Sep. 2006.
[45] L. J. J. Tan *et al.*, "Temperature Dependence of Avalanche Breakdown in InP and InAlAs," *IEEE J. Quantum Electron.*, vol. 46, no. 8, pp. 1153–1157, Aug. 2010.
[46] L. L. G. Pinel *et al.*, "Effects of carrier injection profile on low noise thin $Al_{0.85}Ga_{0.15}As_{0.56}Sb_{0.44}$ avalanche photodiodes," *Opt. Express*, vol. 26, no. 3, pp. 3568–3576, Feb. 2018.
[47] J. Xie, S. Xie, R. C. Tozer, and C. H. Tan, "Excess Noise Characteristics of Thin AlAsSb APDs," *IEEE Trans. Electron Devices*, vol. 59, no. 5, pp. 1475–1479, May 2012.
[48] P. Yuan *et al.*, "Impact ionization characteristics of III-V semiconductors for a wide range of multiplication

region thicknesses," *IEEE J. Quantum Electron.*, vol. 36, no. 2, pp. 198–204, Feb. 2000.
[49] Y. L. Goh *et al.*, "Excess Avalanche Noise in In0.52Al0.48As," *IEEE J. Quantum Electron.*, vol. 43, no. 6, pp. 503–507, Jun. 2007.
[50] C. H. Tan *et al.*, "Avalanche noise measurement in thin Si p+-i-n+ diodes," *Appl. Phys. Lett.*, vol. 76, no. 26, pp. 3926–3928, Jun. 2000.
[51] G. J. Rees and J. P. R. David, "Nonlocal impact ionization and avalanche multiplication," *J. Phys. Appl. Phys.*, vol. 43, no. 24, p. 243001, Jun. 2010.
[52] M. M. Hayat, B. E. A. Saleh, and M. C. Teich, "Effect of dead space on gain and noise of double-carrier-multiplication avalanche photodiodes," *IEEE Trans. Electron Devices*, vol. 39, no. 3, pp. 546–552, Mar. 1992.
[53] Xiaowei Li, Xiaoguang Zheng, Shuling Wang, Feng Ma, and J. C. Campbell, "Calculation of gain and noise with dead space for GaAs and AlxGa1-xAs avalanche photodiode," *IEEE Trans. Electron Devices*, vol. 49, no. 7, pp. 1112–1117, Jul. 2002.
[54] "NSM Archive - Gallium Indium Arsenide Antimonide (GaInAsSb) - Band structure." [Online]. Available: http://www.ioffe.ru/SVA/NSM/Semicond/GaInAsSb/bandstr.html. [Accessed: 06-Oct-2019].
[55] H. Fujiwara, *Spectroscopic Ellipsometry: Principles and Applications*. John Wiley & Sons, 2007.
[56] W. S. Weiglhofer, A. Lakhtakia, and B. Michel, "Maxwell Garnett and Bruggeman formalisms for a particulate composite with bianisotropic host medium," *Microw. Opt. Technol. Lett.*, vol. 15, no. 4, pp. 263–266, 1997.
[57] G. E. Bulman, L. W. Cook, and G. E. Stillman, "Electroabsorption produced mixed injection and its effect on the determination of ionization coefficients," *Solid-State Electron.*, vol. 25, no. 12, pp. 1189–1200, Dec. 1982.
[58] M. H. Woods, W. C. Johnson, and M. A. Lampert, "Use of a Schottky barrier to measure impact ionization coefficients in semiconductors," *Solid-State Electron.*, vol. 16, no. 3, pp. 381–394, Mar. 1973.
[59] X. Yi *et al.*, "Demonstration of large ionization coefficient ratio in AlAs 0.56 Sb 0.44 lattice matched to InP," *Sci. Rep.*, vol. 8, no. 1, pp. 1–6, Jun. 2018.
[60] J. Zheng *et al.*, "Low-temperature-dependent property in an avalanche photodiode based on GaN/AlN periodically-stacked structure," *Sci. Rep.*, vol. 6, p. 35978, Oct. 2016.
[61] G. E. Stillman and C. M. Wolfe, "Chapter 5 Avalanche Photodiodes.," in *Semiconductors and Semimetals*, vol. 12, R. K. Willardson and A. C. Beer, Eds. Elsevier, 1977, pp. 291–393.
[62] J. S. Ng, C. H. Tan, J. P. R. David, G. Hill, and G. J. Rees, "Field dependence of impact ionization coefficients in In/sub 0.53/Ga/sub 0.47/As," *IEEE Trans. Electron Devices*, vol. 50, no. 4, pp. 901–905, Apr. 2003.
[63] R. Van Overstraeten and H. De Man, "Measurement of the ionization rates in diffused silicon p-n junctions," *Solid-State Electron.*, vol. 13, no. 5, pp. 583–608, May 1970.
[64] L. W. Cook, G. E. Bulman, and G. E. Stillman, "Electron and hole impact ionization coefficients in InP determined by photomultiplication measurements," *Appl. Phys. Lett.*, vol. 40, no. 7, pp. 589–591, Apr. 1982.
[65] J. Zheng *et al.*, "A PMT-like high gain avalanche photodiode based on GaN/AlN periodically stacked structure," *Appl. Phys. Lett.*, vol. 109, no. 24, p. 241105, Dec. 2016.
[66] D. Martín and C. Algora, "Temperature-dependent GaSb material parameters for reliable thermophotovoltaic cell modelling," *Semicond. Sci. Technol.*, vol. 19, no. 8, pp. 1040–1052, Jul. 2004.
[67] H.-D. Liu *et al.*, "Avalanche photodiode punch-through gain determination through excess noise analysis," *J. Appl. Phys.*, vol. 106, no. 6, p. 064507, Sep. 2009.
[68] C. Lenox *et al.*, "Thin multiplication region InAlAs homojunction avalanche photodiodes," *Appl. Phys. Lett.*, vol. 73, no. 6, pp. 783–784, Aug. 1998.
[69] X. Zheng, "Long-wavelength, high-speed avalanche photodiodes and APD Arrays," PhD Thesis, 2004.
[70] Y. Tan, M. Povolotskyi, T. Kubis, T. B. Boykin, and G. Klimeck, "Transferable tight-binding model for strained group IV and III-V materials and heterostructures," *Phys. Rev. B*, vol. 94, no. 4, p. 045311, Jul. 2016.
[71] X. G. Zheng *et al.*, "Temperature dependence of the ionization coefficients of AlxGa1-xAs," *IEEE J. Quantum Electron.*, vol. 36, no. 10, pp. 1168–1173, Oct. 2000.
[72] C. N. Harrison, J. P. R. David, M. Hopkinson, and G. J. Rees, "Temperature dependence of avalanche multiplication in submicron Al0.6Ga0.4As diodes," *J. Appl. Phys.*, vol. 92, no. 12, pp. 7684–7686, Nov.

2002.
[73] D. A. B. Miller *et al.*, "Electric field dependence of optical absorption near the band gap of quantum-well structures," *Phys. Rev. B*, vol. 32, no. 2, pp. 1043–1060, Jul. 1985.
[74] D. A. B. Miller *et al.*, "Band-Edge Electroabsorption in Quantum Well Structures: The Quantum-Confined Stark Effect," *Phys. Rev. Lett.*, vol. 53, no. 22, pp. 2173–2176, Nov. 1984.
[75] D. A. B. Miller, D. S. Chemla, and S. Schmitt-Rink, "Relation between electroabsorption in bulk semiconductors and in quantum wells: The quantum-confined Franz-Keldysh effect," *Phys. Rev. B*, vol. 33, no. 10, pp. 6976–6982, May 1986.
[76] J. Bleuse, G. Bastard, and P. Voisin, "Electric-Field-Induced Localization and Oscillatory Electro-optical Properties of Semiconductor Superlattices," *Phys. Rev. Lett.*, vol. 60, no. 3, pp. 220–223, Jan. 1988.
[77] W. Franz, "Einfluß eines elektrischen Feldes auf eine optische Absorptionskante," *Z. Für Naturforschung A*, vol. 13, no. 6, pp. 484–489, 1958.
[78] L. Keldysh, "The effect of a strong electric field on the optical properties of insulating crystals," *Sov Phys JETP*, vol. 7, no. 5, pp. 788–790, 1958.
[79] J. Zheng, Y. Tan, Y. Yuan, A. W. Ghosh, and J. C. Campbell, "Strain effect on band structure of InAlAs digital alloy," *J. Appl. Phys.*, vol. 125, no. 8, p. 082514, 2019.
[80] E. E. Mendez and G. Bastard, "Wannier-Stark Ladders and Bloch Oscillations in Superlattices," *Phys. Today*, vol. 46, no. 6, p. 34, Jan. 2008.
[81] B. Jogai and K. L. Wang, "Interband optical transitions in GaAs-Ga1-xAlxAs superlattices in an applied electric field," *Phys. Rev. B*, vol. 35, no. 2, pp. 653–659, Jan. 1987.
[82] P. Tronc, C. Cabanel, J. F. Palmier, and B. Etienne, "Stark localization in GaAs-GaAlAs superlattices under a low electric field," *Solid State Commun.*, vol. 75, no. 10, pp. 825–829, Sep. 1990.
[83] S. L. Chuang, *Physics of Photonic Devices*. John Wiley & Sons, 2012.
[84] J. L. O'Brien, A. Furusawa, and J. Vučković, "Photonic quantum technologies," *Nat. Photonics*, vol. 3, no. 12, pp. 687–695, Dec. 2009.
[85] *Single-Photon Generation and Detection: Physics and Applications*. Academic Press, 2013.
[86] J. Zhang, M. A. Itzler, H. Zbinden, and J.-W. Pan, "Advances in InGaAs/InP single-photon detector systems for quantum communication," *Light Sci. Appl.*, vol. 4, no. 5, pp. e286–e286, May 2015.
[87] "Photomultiplier Tubes: Basics and Applications," *Hamamatsu Hamamatsu Photonics*, p. 323, 2006.
[88] "Molecular Expressions Microscopy Primer: Digital Imaging in Optical Microscopy - Concepts in Digital Imaging - Photomultiplier Tubes." [Online]. Available: https://micro.magnet.fsu.edu/primer/digitalimaging/concepts/photomultipliers.html. [Accessed: 07-Oct-2019].
[89] G. N. Gol'tsman *et al.*, "Picosecond superconducting single-photon optical detector," *Appl. Phys. Lett.*, vol. 79, no. 6, pp. 705–707, Aug. 2001.
[90] A. Peacock *et al.*, "Single optical photon detection with a superconducting tunnel junction," *Nature*, vol. 381, no. 6578, pp. 135–137, May 1996.
[91] D. Rosenberg, A. E. Lita, A. J. Miller, and S. W. Nam, "Noise-free high-efficiency photon-number-resolving detectors," *Phys. Rev. A*, vol. 71, no. 6, p. 061803, Jun. 2005.
[92] "Superconducting nanowire single photon detectors — Department of Physics." [Online]. Available: https://www.physics.utoronto.ca/dept-items/colloquium/physics-colloquium-nov-6-2008. [Accessed: 08-Oct-2019].
[93] "CMOS Single-Photon Avalanche Diodes (SPADs): Technology and Applications – AQUA." .
[94] L. Mingguo, "Infrared Single Phgoton Avalanche Diodes," University of Virginia, 2008.
[95] A. Spinelli and A. L. Lacaita, "Physics and numerical simulation of single photon avalanche diodes," 1997.
[96] S. Cova, M. Ghioni, A. Lacaita, C. Samori, and F. Zappa, "Avalanche photodiodes and quenching circuits for single-photon detection," *Appl. Opt.*, vol. 35, no. 12, p. 1956, Apr. 1996.
[97] A. Tosi, A. Della Frera, A. Bahgat Shehata, and C. Scarcella, "Fully programmable single-photon detection module for InGaAs/InP single-photon avalanche diodes with clean and sub-nanosecond gating transitions," *Rev. Sci. Instrum.*, vol. 83, no. 1, p. 013104, Jan. 2012.
[98] F. Zappa, A. Lotito, A. C. Giudice, S. Cova, and M. Ghioni, "Monolithic active-quenching and active-reset circuit for single-photon avalanche detectors," *IEEE J. Solid-State Circuits*, vol. 38, no. 7, pp. 1298–1301, Jul. 2003.

[99] C. L. Niclass, A. Rochas, P. A. Besse, and E. Charbon, "A CMOS single photon avalanche diode array for 3D imaging," in *2004 IEEE International Solid-State Circuits Conference (IEEE Cat. No.04CH37519)*, 2004, pp. 120-517 Vol.1.
[100] Z. Lu, W. Sun, Q. Zhou, J. Campbell, X. Jiang, and M. A. Itzler, "Improved sinusoidal gating with balanced InGaAs/InP Single Photon Avalanche Diodes," *Opt. Express*, vol. 21, no. 14, pp. 16716–16721, Jul. 2013.
[101] X. Meng, C. H. Tan, S. Dimler, J. P. R. David, and J. S. Ng, "1550 nm InGaAs/InAlAs single photon avalanche diode at room temperature," *Opt. Express*, vol. 22, no. 19, pp. 22608–22615, Sep. 2014.
[102] G. Karve *et al.*, "Origin of dark counts in In0.53Ga0.47As⁄In0.52Al0.48As avalanche photodiodes operated in Geiger mode," *Appl. Phys. Lett.*, vol. 86, no. 6, p. 063505, Feb. 2005.
[103] K. Zhao, S. You, J. Cheng, and Y. Lo, "Self-quenching and self-recovering InGaAs⁄InAlAs single photon avalanche detector," *Appl. Phys. Lett.*, vol. 93, no. 15, p. 153504, Oct. 2008.
[104] Y. Liang, Y. Jian, X. Chen, G. Wu, E. Wu, and H. Zeng, "Room-Temperature Single-Photon Detector Based on InGaAs/InP Avalanche Photodiode With Multichannel Counting Ability," *IEEE Photonics Technol. Lett.*, vol. 23, no. 2, pp. 115–117, Jan. 2011.
[105] S. Pellegrini *et al.*, "Design and performance of an InGaAs-InP single-photon avalanche diode detector," *IEEE J. Quantum Electron.*, vol. 42, no. 4, pp. 397–403, Apr. 2006.
[106] X. Meng *et al.*, "InGaAs/InAlAs single photon avalanche diode for 1550 nm photons," *R. Soc. Open Sci.*, vol. 3, no. 3, Mar. 2016.
[107] Y. Ma *et al.*, "Impact of etching on the surface leakage generation in mesa-type InGaAs/InAlAs avalanche photodetectors," *Opt. Express*, vol. 24, no. 7, pp. 7823–7834, Apr. 2016.
[108] M. Nada, Y. Muramoto, H. Yokoyama, T. Ishibashi, and H. Matsuzaki, "Triple-mesa Avalanche Photodiode With Inverted P-Down Structure for Reliability and Stability," *J. Light. Technol.*, vol. 32, no. 8, pp. 1543–1548, Apr. 2014.
[109] B. Li, Q. Lv, R. Cui, W. Yin, X. Yang, and Q. Han, "A Low Dark Current Mesa-Type InGaAs/InAlAs Avalanche Photodiode," *IEEE Photonics Technol. Lett.*, vol. 27, no. 1, pp. 34–37, Jan. 2015.
[110] H. Liu, X. Zheng, Q. Zhou, X. Bai, D. C. Mcintosh, and J. C. Campbell, "Double Mesa Sidewall Silicon Carbide Avalanche Photodiode," *IEEE J. Quantum Electron.*, vol. 45, no. 12, pp. 1524–1528, Dec. 2009.
[111] E. Kamrani, F. Lesage, and M. Sawan, "Efficient premature edge breakdown prevention in SiAPD fabrication using the standard CMOS process," *Semicond. Sci. Technol.*, vol. 28, no. 4, p. 045008, Feb. 2013.
[112] J. E. Bowers *et al.*, "Recent advances in silicon photonic integrated circuits," in *Next-Generation Optical Communication: Components, Sub-Systems, and Systems V*, 2016, vol. 9774, p. 977402.
[113] J. E. Bowers, J. E. Bowers, J. T. Bovington, A. Y. Liu, A. C. Gossard, and A. C. Gossard, "A Path to 300 mm Hybrid Silicon Photonic Integrated Circuits," in *Optical Fiber Communication Conference (2014), paper Th1C.1*, 2014, p. Th1C.1.
[114] F. Xia, L. Sekaric, and Y. Vlasov, "Ultracompact optical buffers on a silicon chip," *Nat. Photonics*, vol. 1, no. 1, pp. 65–71, Jan. 2007.
[115] D. Dai and J. E. Bowers, "Silicon-based on-chip multiplexing technologies and devices for Peta-bit optical interconnects," *Nanophotonics*, vol. 3, no. 4–5, pp. 283–311, 2013.
[116] A. Y. Liu, R. W. Herrick, O. Ueda, P. M. Petroff, A. C. Gossard, and J. E. Bowers, "Reliability of InAs/GaAs Quantum Dot Lasers Epitaxially Grown on Silicon," *IEEE J. Sel. Top. Quantum Electron.*, vol. 21, no. 6, pp. 690–697, Nov. 2015.
[117] A. W. Fang, E. Lively, Y.-H. Kuo, D. Liang, and J. E. Bowers, "A distributed feedback silicon evanescent laser," *Opt. Express*, vol. 16, no. 7, pp. 4413–4419, Mar. 2008.
[118] P. Rabiei, J. Ma, S. Khan, J. Chiles, and S. Fathpour, "Heterogeneous lithium niobate photonics on silicon substrates," *Opt. Express*, vol. 21, no. 21, pp. 25573–25581, Oct. 2013.
[119] S. Srinivasan, M. Davenport, T. Komljenovic, J. Hulme, D. T. Spencer, and J. E. Bowers, "Coupled-Ring-Resonator-Mirror-Based Heterogeneous III–V Silicon Tunable Laser," *IEEE Photonics J.*, vol. 7, no. 3, pp. 1–8, Jun. 2015.
[120] L. Chen, Q. Xu, M. G. Wood, and R. M. Reano, "Hybrid silicon and lithium niobate electro-optical ring modulator," *Optica*, vol. 1, no. 2, pp. 112–118, Aug. 2014.
[121] K. Sun *et al.*, "Low dark current III-V on silicon photodiodes by heteroepitaxy," *Opt. Express*, vol. 26, no. 10, pp. 13605–13613, May 2018.

[122] M. Nada, T. Yoshimatsu, Y. Muramoto, T. Ohno, F. Nakajima, and H. Matsuzaki, "106-Gbit/s PAM4 40-km Transmission Using an Avalanche Photodiode With 42-GHz Bandwidth," in *2018 Optical Fiber Communications Conference and Exposition (OFC)*, 2018, pp. 1–3.
[123] T. Komljenovic *et al.*, "Heterogeneous Silicon Photonic Integrated Circuits," *J. Light. Technol.*, vol. 34, no. 1, pp. 20–35, Jan. 2016.
[124] C. Zhang and J. E. Bowers, "Silicon photonic terabit/s network-on-chip for datacenter interconnection," *Opt. Fiber Technol.*, vol. 44, pp. 2–12, Aug. 2018.
[125] B. Schwarz, "Mapping the world in 3D," *Nat. Photonics*, vol. 4, no. 7, pp. 429–430, Jul. 2010.
[126] G. Adamo and A. Busacca, "Time Of Flight measurements via two LiDAR systems with SiPM and APD," in *2016 AEIT International Annual Conference (AEIT)*, 2016, pp. 1–5.
[127] F. Powolny *et al.*, "Time-Based Readout of a Silicon Photomultiplier (SiPM) for Time of Flight Positron Emission Tomography (TOF-PET)," *IEEE Trans. Nucl. Sci.*, vol. 58, no. 3, pp. 597–604, Jun. 2011.
[128] M. Seifried *et al.*, "Monolithically Integrated CMOS-Compatible III–V on Silicon Lasers," *IEEE J. Sel. Top. Quantum Electron.*, vol. 24, no. 6, pp. 1–9, Nov. 2018.
[129] J. E. Bowers, "Heterogeneous III-V / Si photonic integration," in *2016 Conference on Lasers and Electro-Optics (CLEO)*, 2016, pp. 1–2.
[130] A. Mitcsenkov, G. Paksy, and T. Cinkler, "Geography- and infrastructure-aware topology design methodology for broadband access networks (FTTx)," *Photonic Netw. Commun.*, vol. 21, no. 3, pp. 253–266, Jun. 2011.
[131] Q. Yu *et al.*, "High-performance InGaAs/InP photodiodes on silicon using low-temperature wafer-bonding," in *2018 Conference on Lasers and Electro-Optics (CLEO)*, 2018, pp. 1–2.
[132] B. Shi, Q. Li, and K. M. Lau, "Epitaxial growth of high quality InP on Si substrates: The role of InAs/InP quantum dots as effective dislocation filters," *J. Appl. Phys.*, vol. 123, no. 19, p. 193104, May 2018.
[133] H. Riechert, "Physical properties of III-V semiconductor compounds—InP, InAs, GaAs, GaP, InGaAs and InGaAsP. By Sadao Adachi, John Wiley & Sons, Chichester, UK 1992, XVIII, 318 pp., hardcover, £ 55, ISBN 0-471-57329-9," *Adv. Mater.*, vol. 6, no. 1, pp. 86–86, 1994.
[134] T. Nakata, J. Ishihara, K. Makita, and K. Kasahara, "Multiplication Noise Characterization of InAlAs-APD With Heterojunction," *IEEE Photonics Technol. Lett.*, vol. 21, no. 24, pp. 1852–1854, Dec. 2009.
[135] Ning Duan *et al.*, "Detrimental effect of impact ionization in the absorption region on the frequency response and excess noise performance of InGaAs-InAlAs SACM avalanche photodiodes," *IEEE J. Quantum Electron.*, vol. 41, no. 4, pp. 568–572, Apr. 2005.
[136] J. C. Norman *et al.*, "A Review of High-Performance Quantum Dot Lasers on Silicon," *IEEE J. Quantum Electron.*, vol. 55, no. 2, pp. 1–11, Apr. 2019.
[137] D. Jung, P. G. Callahan, B. Shin, K. Mukherjee, A. C. Gossard, and J. E. Bowers, "Low threading dislocation density GaAs growth on on-axis GaP/Si (001)," *J. Appl. Phys.*, vol. 122, no. 22, p. 225703, Dec. 2017.
[138] R. Soref, "The Past, Present, and Future of Silicon Photonics," *IEEE J. Sel. Top. Quantum Electron.*, vol. 12, no. 6, pp. 1678–1687, Nov. 2006.
[139] C. Sun *et al.*, "Single-chip microprocessor that communicates directly using light," *Nature*, vol. 528, no. 7583, pp. 534–538, Dec. 2015.
[140] D. Thomson *et al.*, "Roadmap on silicon photonics," *J. Opt.*, vol. 18, no. 7, p. 073003, Jun. 2016.
[141] A. H. Atabaki *et al.*, "Integrating photonics with silicon nanoelectronics for the next generation of systems on a chip," *Nature*, vol. 556, no. 7701, pp. 349–354, Apr. 2018.
[142] Q. Cheng, M. Bahadori, M. Glick, S. Rumley, and K. Bergman, "Recent advances in optical technologies for data centers: a review," *Optica*, vol. 5, no. 11, pp. 1354–1370, Nov. 2018.
[143] "VNI Global Fixed and Mobile Internet Traffic Forecasts," *Cisco*. [Online]. Available: https://www.cisco.com/c/en/us/solutions/service-provider/visual-networking-index-vni/index.html. [Accessed: 12-Oct-2019].
[144] S. Assefa, F. Xia, and Y. A. Vlasov, "Reinventing germanium avalanche photodetector for nanophotonic on-chip optical interconnects," *Nature*, vol. 464, no. 7285, pp. 80–84, Mar. 2010.
[145] J. Michel, J. Liu, and L. C. Kimerling, "High-performance Ge-on-Si photodetectors," *Nat. Photonics*, vol. 4, no. 8, pp. 527–534, Aug. 2010.
[146] R. Soref, "Mid-infrared photonics in silicon and germanium," *Nat. Photonics*, vol. 4, no. 8, pp. 495–

497, Aug. 2010.
[147] P. Vines *et al.*, “High performance planar germanium-on-silicon single-photon avalanche diode detectors,” *Nat. Commun.*, vol. 10, no. 1, p. 1086, Dec. 2019.
[148] M. Huang *et al.*, “56GHz Waveguide Ge/Si Avalanche Photodiode,” in *2018 Optical Fiber Communications Conference and Exposition (OFC)*, 2018, pp. 1–3.
[149] N. El-Sayed, I. Stefanovici, G. Amvrosiadis, A. A. Hwang, and B. Schroeder, “Temperature Management in Data Centers: Why Some (Might) Like It Hot,” p. 12.
[150] M. Ware *et al.*, “Architecting for power management: The IBM® POWER7™ approach,” in *HPCA - 16 2010 The Sixteenth International Symposium on High-Performance Computer Architecture*, 2010, pp. 1–11.
[151] B. F. Levine *et al.*, “A New Planar InGaAs–InAlAs Avalanche Photodiode,” *IEEE Photonics Technol. Lett.*, vol. 18, no. 18, pp. 1898–1900, Sep. 2006.
[152] E. Ishimura *et al.*, “Degradation Mode Analysis on Highly Reliable Guardring-Free Planar InAlAs Avalanche Photodiodes,” *J. Light. Technol.*, vol. 25, no. 12, pp. 3686–3693, Dec. 2007.
[153] A. Rouvie, D. Carpentier, N. Lagay, J. Decobert, F. Pommereau, and M. Achouche, “High Gain x Bandwidth Product Over 140-GHz Planar Junction AlInAs Avalanche Photodiodes,” *IEEE Photonics Technol. Lett.*, vol. 20, no. 6, pp. 455–457, Mar. 2008.
[154] Y. L. Goh, D. S. G. Ong, S. Zhang, J. S. Ng, C. H. Tan, and J. P. R. David, “InAlAs avalanche photodiode with type-II absorber for detection beyond 2 μm,” in *Infrared Technology and Applications XXXV*, 2009, vol. 7298, p. 729837.
[155] Y. Zhao *et al.*, “Temperature dependence simulation and characterization for InP/InGaAs avalanche photodiodes,” *Front. Optoelectron.*, vol. 11, no. 4, pp. 400–406, Dec. 2018.
[156] C. L. F. Ma, M. J. Deen, L. E. Tarof, and J. C. H. Yu, “Temperature dependence of breakdown voltages in separate absorption, grading, charge, and multiplication InP/InGaAs avalanche photodiodes,” *IEEE Trans. Electron Devices*, vol. 42, no. 5, pp. 810–818, May 1995.
[157] R. Sidhu *et al.*, “2.4 μm cutoff wavelength avalanche photodiode on InP substrate,” *Electron. Lett.*, vol. 42, no. 3, pp. 181–182, Feb. 2006.
[158] D. Dai, J. E. Bowers, Z. Lu, J. C. Campbell, and Y. Kang, “Temperature dependence of Ge/Si avalanche photodiodes,” in *68th Device Research Conference*, 2010, pp. 231–232.
[159] B. Wang *et al.*, “A Compact Model for Si-Ge Avalanche Photodiodes Over a Wide Range of Multiplication Gain,” *J. Light. Technol.*, vol. 37, no. 13, pp. 3229–3235, Jul. 2019.
[160] H.-S. Kang, M.-J. Lee, and W.-Y. Choi, “Si avalanche photodetectors fabricated in standard complementary metal-oxide-semiconductor process,” *Appl. Phys. Lett.*, vol. 90, no. 15, p. 151118, Apr. 2007.
[161] J.- Shi, Y.- Wu, Z.- Li, and P.- Chen, “Impact-Ionization-Induced Bandwidth-Enhancement of a Si ndash;SiGe-Based Avalanche Photodiode Operating at a Wavelength of 830 nm With a Gain-Bandwidth Product of 428 GHz,” *IEEE Photonics Technol. Lett.*, vol. 19, no. 7, pp. 474–476, Apr. 2007.
[162] W. S. Zaoui *et al.*, “Frequency response and bandwidth enhancement in Ge/Si avalanche photodiodes with over 840GHz gain-bandwidth-product,” *Opt. Express*, vol. 17, no. 15, pp. 12641–12649, Jul. 2009.
[163] Y. P. Varshni, “Band-to-Band Radiative Recombination in Groups IV, VI, and III-V Semiconductors (I),” *Phys. Status Solidi B*, vol. 19, no. 2, pp. 459–514, 1967.
[164] T. R. Harris, “Optical properties of Si, Ge, GaAs, GaSb, InAs, and InP at elevated temperatures,” AIR FORCE INST OF TECH WRIGHT-PATTERSON AFB OH SCHOOL OF ENGINEERING AND …, 2010.
[165] L. Chrostowski and M. Hochberg, *Silicon Photonics Design: From Devices to Systems*. Cambridge University Press, 2015.
[166] L. Colace and G. Assanto, “Germanium on Silicon for Near-Infrared Light Sensing,” *IEEE Photonics J.*, vol. 1, no. 2, pp. 69–79, Aug. 2009.
[167] A. K. Rockwell *et al.*, “Toward deterministic construction of low noise avalanche photodetector materials,” *Appl. Phys. Lett.*, vol. 113, no. 10, p. 102106, 2018.
[168] F.-Y. Yuan *et al.*, “Conduction Mechanism and Improved Endurance in HfO2-Based RRAM with Nitridation Treatment,” *Nanoscale Res. Lett.*, vol. 12, no. 1, p. 574, Dec. 2017.

A. List of publications

Journals:

1. J. Zheng, **Y. Yuan**, Y. Tan, Y. Peng, A. K. Rockwell, S. R. Bank, A. W. Ghosh, and J. C. Campbell. "Simulations for InAlAs digital alloy avalanche photodiodes." *Applied Physics Letters* 115, no. 17 (2019): 171106.
2. A. H. Jones, A. K. Rockwell, S. D. March, **Y. Yuan**, S. R. Bank, and J. C. Campbell. "High gain, low dark current $Al_{0.8}In_{0.2}As_{0.23}Sb_{0.77}$ avalanche photodiodes." *Photonics Technology Letters* (2019).
3. **Y. Yuan**, Y. Li, J. Abell, J. Zheng, K. Sun, C. Pinzone, and J. C. Campbell. "Triple-mesa avalanche photodiodes with very low surface dark current." *Optics Express* 27, no. 16 (2019): 22923-22929.
4. **Y. Yuan**, D. Jung, K. Sun, J. Zheng, A. H. Jones, J. E. Bowers, and J. C. Campbell. "III-V on silicon avalanche photodiodes by heteroepitaxy." *Optics Letters* 44, no. 14 (2019): 3538-3541.
5. J. Zheng, Y. Tan, **Y. Yuan**, A. W. Ghosh, and J. C. Campbell. "Tuning of energy dispersion properties in InAlAs digital alloys." *Journal of Applied Physics* 125, no. 24 (2019): 245702.
6. **Y. Yuan**, A. K. Rockwell, Y. Peng, J. Zheng, S. D. March, A. H. Jones, S. R. Bank, and J. C. Campbell. "Comparison of different period digital alloy $Al_{0.7}InAsSb$ avalanche photodiodes." *Journal of Lightwave Technology* (2019).
7. **Y. Yuan**, J. Zheng, K. Sun, A. H. Jones, A. K. Rockwell, S. D. March, Y. Shen, S. R. Bank, and J. C. Campbell. "Stark-Localization-Limited Franz–Keldysh Effect in InAlAs Digital Alloys." *Physica Status Solidi (RRL)–Rapid Research Letters*: 1900272 (2019).

8. **Y. Yuan**, J. Zheng, A. K. Rockwell, S. D. March, S. R. Bank, and J. C. Campbell. "AlInAsSb Impact Ionization Coefficients." *Photonics Technology Letters* 31, no. 4 (2019):315-318.
9. J. Zheng, Y. Tan, **Y. Yuan**, A. W. Ghosh, and J. C. Campbell. "Strain effect on band structure of InAlAs digital alloy." *Journal of Applied Physics* 125, no. 8 (2019): 082514.
10. A. K. Rockwell, M. Ren, M. Woodson, A. H. Jones, S. D. March, Y. Tan, **Y. Yuan**, Y. Sun, R. Hool, S. J. Maddox, M. L. Lee, A. W. Ghosh, J. C. Campbell and S. R. Bank. "Toward deterministic construction of low noise avalanche photodetector materials." *Applied Physics Letters* 113, no. 10 (2018): 102106.
11. **Y. Yuan**, J. Zheng, Y. Tan, Y. Peng, A. K. Rockwell, S. R. Bank, A. Ghosh, and J. C. Campbell. "Temperature dependence of the ionization coefficients of InAlAs and AlGaAs digital alloys." *Photonics Research* 6, no. 8 (2018): 794-799.
12. J. Zheng, **Y. Yuan**, Y. Tan, Y. Peng, A. K. Rockwell, S. R. Bank, A. Ghosh, and J. C. Campbell. "Digital Alloy InAlAs Avalanche Photodiodes." *Journal of Lightwave Technology* (2018).
13. A. K. Rockwell*, **Y. Yuan***, A. H. Jones, S. D. March, S. R. Bank, and J. C. Campbell. "$Al_{0.8}In_{0.2}As_{0.23}Sb_{0.77}$ Avalanche Photodiodes." *Photonics Technology Letters* 30, no. 11 (2018): 1048-1051.
14. A. H. Jones, **Y. Yuan**, M. Ren, S. J. Maddox, S. R. Bank, and J. C. Campbell. "$Al_xIn_{1-x}As_ySb_{1-y}$ photodiodes with low avalanche breakdown temperature dependence." *Optics Express* 25, no. 20 (2017): 24340-24345.

Conferences:

1. **Y. Yuan**, D. Jung, K. Sun, J. Zheng, A. H. Jones, J. E. Bowers, and J. C. Campbell. "III-V Compound Avalanche Photodiodes on Silicon." *Integrated Photonics Research, Silicon and Nanophotonics*, pp. IW3A-4. OSA, 2019.

2. **<u>Y. Yuan</u>**, J. Zheng, Y. Tan, Y. Peng, A. K. Rockwell, S. R. Bank, A. Ghosh, and J. C. Campbell. "Comparison of excess noise in InAlAs and AlGaAs digital and random alloy avalanche photodiodes." *IEEE Photonics Conference (IPC), 2018.*
3. J. Zheng, **<u>Y. Yuan</u>**, Y. Tan, Y. Peng, A. K. Rockwell, S. R. Bank, A. Ghosh, and J. C. Campbell. "Digital alloy-based avalanche photodiodes." *IEEE Photonics Conference (IPC), 2018.*
4. S. R. Bank, J. C. Campbell, S. J. Maddox, A.K. Rockwell, M. E. Woodson, M. Ren, A. H. Jones, S. D. March, J. Zheng, and **<u>Y. Yuan</u>**. "Digital Alloy Growth of Low-Noise Avalanche Photodiodes." *IEEE Research and Applications of Photonics In Defense Conference (RAPID), pp. 1-3, (2018).*
5. M. Ren, **<u>Y. Yuan</u>**, A. H. Jones, S. J. Maddox, M. E. Woodson, S. R. Bank, and J. C. Campbell. "Operation stability study of AlInAsSb avalanche photodiodes." *IEEE Photonics Conference (IPC), 2017 IEEE*, pp. 159-160.

B. Vita

Yuan Yuan (袁源), son of Guobiao Yuan (袁国标) and Hongmei Sun (孙红梅), was born on September 9th, 1994 in City of Yancheng, Jiangsu Province, China. After completing his study at Sheyang middle school in 2012, he began his undergraduate study at Automation College in Nanjing University of Aeronautics and Astronautics (NUAA), majoring in Electrical engineering. After graduation in 2016, he joined Dr. Joe. C. Campbell's group as a Ph.D. student. His current research focuses on the design, fabrication and characterization of low-noise avalanche photodiodes and single photon avalanche diodes.

This dissertation has been typed by the author.